Dissertation presented to the Instituto Tecnológico de Aeronáutica, in partial fulfillment of the requirements for the degree of Master of Science in the Program of Aeronautics and Mechanical Engineering of Materials, Manufacturing and Automation Field.

Matheus Rubik

SHOT PEENING-BASED STRATEGY FOR DENSIFICATION AND RESIDUAL STRESS ENHANCEMENT IN BINDER JETTING

Dissertation approved in its final version by the signatories below:

Prof. Dr. Ronnie Rodrigo Rego
Advisor

Campo Montenegro
São José dos Campos, SP – Brasil
2025

Cataloging-in Publication Data
Documentation and Information Division

Rubik, Matheus
Shot Peening-Based Strategy for Densification and Residual Stress Enhancement in Binder Jetting / Matheus Rubik
São José dos Campos, 2025.
175f.

Dissertation of Master of Science – Aeronautics and Mechanical Engineering Program, Materials, Manufacturing and Automation Field – Instituto Tecnológico de Aeronáutica, 2025. Advisor: Prof. Dr. Ronnie Rodrigo Rego

1. Gears 2. Shot Peening 3.Binder Jetting 4. Manufacturing 6. Mechanical Engineering I. Instituto Tecnológico de Aeronáutica. II. Shot Peening-Based Strategy for Densification and Residual Stress Enhancement in Binder Jetting

BIBLIOGRAPHIC REFERENCE

RUBIK, Matheus. **Shot Peening-Based Strategy for Densification and Residual Stress Enhancement in Binder Jetting**. 2025. 175f. Dissertation in Aeronautics and Mechanical Engineering – Instituto Tecnológico de Aeronáutica, São José dos Campos, 2025.

CESSION OF RIGHTS

AUTOR NAME: Matheus Rubik
PUBLICATION TITLE: Shot Peening-Based Strategy for Densification and Residual Stress Enhancement in Binder Jetting
PUBLICATION KIND/YEAR: Dissertation / 2025

_____

Matheus Rubik
Rua José Machado Faria, 415
CEP: 12227-730, São José dos Campos - SP

SHOT PEENING-BASED STRATEGY FOR DENSIFICATION AND RESIDUAL STRESS ENHANCEMENT IN BINDER JETTING

Matheus Rubik

Thesis Committee Composition:

Prof. Dr.	Gilmar Patrocínio Thim	Chairperson	-	ITA
Prof. Dr.	Ronnie Rodrigo Rego	Advisor	-	ITA
Prof. Dr.	Kahl Dick Zilnyk	Internal Member	-	ITA
Prof. Dr.	Izabel Fernanda Machado	External Member	-	USP

ITA

Dedico este trabalho à minha família,
que sempre me apoiou e inspirou em
cada etapa da minha jornada.

Agradecimentos

Este trabalho só foi possível graças ao apoio, à orientação e à colaboração de diversas pessoas ao longo do meu percurso acadêmico, às quais expresso meus sinceros agradecimentos.

Aos meus pais, Roger e Rosângela, pela dedicação incansável e pelos sacrifícios muitas vezes silenciosos, que foram determinantes para que eu chegasse até aqui. Cada conquista ao longo desta jornada carrega a marca do apoio, dos valores e da força que recebi. De vocês, minha mais profunda gratidão.

Ao meu irmão, Eduardo, pela amizade, parceria e por sempre estar presente nos momentos importantes.

Ao meu orientador, Prof. Ronnie, que dedicou inúmeras horas me orientando ao longo de toda esta pesquisa. Sou grato pela oportunidade, pelas discussões e pelos ensinamentos que me permitiram concluir este trabalho.

Aos meus colegas do Grupo de Inovação em Engrenagens, pela cooperação, suporte e compreensão. Em especial ao Guilherme Guimarães, Bruno Oliveira e Matheus Fernandes, que me apoiaram durante toda a escrita e o aprendizado nos últimos anos.

Ao ITA, ao CCM e ao CNPq pelos recursos disponibilizados, que foram essenciais para a conclusão desta pesquisa.

"Pois quem espera sempre alcança."

(Lamartine Babo)

Resumo

A manufatura aditiva por *binder jetting* surgiu como uma tecnologia promissora para a produção de componentes metálicos complexos, com potencial para reduzir custos, desperdício de material e promover escalabilidade. No entanto, os desafios relacionados à alta porosidade limitam sua aplicação em sistemas sujeitos a fadiga por contato, como engrenagens. Nesse contexto, o objetivo deste estudo foi investigar a aplicação sequencial de *shot peening* como estratégia de pós-processamento para otimizar a integridade da superfície e melhorar o desempenho de fadiga de componentes fabricados por *binder jetting*. A investigação se concentrou na caracterização detalhada da integridade de superfície resultante do *shot peening* aplicado em duas etapas: a primeira dedicada à densificação da superfície e a segunda à indução de tensões residuais compressivas. Foram avaliados parâmetros como dureza, porosidade, rugosidade e estado de tensão residual. A primeira etapa de *shot peening* promoveu 99% de densidade superficial até uma profundidade de 350 μm, acompanhada por um aumento de 37% na dureza superficial e uma melhoria notável nos parâmetros de rugosidade, estabelecendo uma condição favorável para tratamentos subsequentes. A segunda etapa induziu tensões residuais compressivas superiores a –900 MPa em profundidades de aproximadamente 100 μm, alinhadas com perfis tipicamente associados à resistência à fadiga aprimorada. Testes de fadiga de contato por rolamento mostraram que ambos os tratamentos prolongaram significativamente a vida útil à fadiga. A combinação de densificação e indução de tensão residual levou a um aumento de até 54% na vida útil à fadiga em comparação com a condição original. Os ganhos mais significativos foram associados à supressão de poros superficiais críticos e à estabilização de campos de tensão residual compressiva. Esses resultados indicam que a combinação de estratégias de densificação e modificação de tensão residual é essencial para mitigar as limitações intrínsecas do *binder jetting*, promovendo melhorias na resistência à fadiga sem comprometer a geometria da peça. Este estudo contribui para o avanço de rotas de fabricação integradas, combinando processos aditivos e tratamentos mecânicos, com potencial aplicação na produção de engrenagens e outros componentes críticos, incluindo aplicações emergentes em eletromobilidade, como em setores como o automotivo, bem como em aplicações aeroespaciais. Como continuação, propõe-se a validação dessas estratégias em geometrias reais sob condições operacionais representativas.

Abstract

Additive manufacturing by binder jetting has emerged as a promising technology to produce complex metal components, with the potential to reduce costs, material waste, and promote scalability. However, challenges related to high porosity limit its application in systems subject to contact fatigue, such as gears. In this context, the objective of this study was to investigate the sequential application of shot peening as a post-processing strategy to optimize surface integrity and improve the fatigue performance of components manufactured by binder jetting. The investigation focused on the detailed characterization of the surface integrity resulting from shot peening applied in two stages: the first dedicated to surface densification and the second to the induction of compressive residual stresses. Parameters such as hardness, porosity, roughness, and residual stress state were evaluated. The first shot peening stage promoted 99% surface density up to a depth of 350 µm. It was accompanied by a 37% increase in surface hardness and a notable improvement in roughness parameters, establishing a favorable condition for subsequent treatments. The second stage induced compressive residual stresses exceeding –900 MPa at depth levels of approximately 100 µm, aligned with profiles typically associated with improved fatigue resistance. Rolling contact fatigue tests showed that both treatments significantly extended fatigue life. The combination of densification and stress induction led to an increase of up to 54% in fatigue life compared to the as-built condition. The most significant gains were associated with the suppression of critical surface pores and the stabilization of compressive stress fields. These results indicate that combining densification and residual stress modification strategies is essential to mitigate the intrinsic limitations of binder jetting, promoting improvements in fatigue resistance without compromising part geometry. This study contributes to the advancement of integrated manufacturing routes, combining additive processes and mechanical treatments, with potential application in the production of gears and other critical components, including emerging applications in electromobility, as in sectors such as automotive, as well as in aerospace applications. As a continuation, the validation of these strategies in real geometries under representative operating conditions is proposed.

List of Figures

List of Tables

List of Abbreviations and Acronyms

AM	Additive manufacturing
EV	Electric vehicle
BJT	Binder Jetting
CAGR	Compound Annual Rate of Growth
DED	Direct Energy Deposition
HIP	Hot Isostatic Pressing
iSLS	Indirect Selective Laser Sintering
L-PBF	Laser Powder Bed Fusion
OM	Optical microscopy
RCF	Rolling Contact Fatigue
ITA	Aeronautics Institute of Technology
SEM	Scanning electron microscopy
SP	Shot Peening
SS	Stainless steel

Contents

1 Introduction

The new industrial revolution and electrification drive, largely in the automotive sector, have changed the face of manufacturing. Electric vehicles (EV) are among the most critical drivers for this change and require leading-edge manufacturing technologies to produce high-performance components and meet the ever-increasing demand. Over 26 million EV's were on the road in 2022, 60% more than in 2021 and more than 5 times the stock in 2018, as shown in Figure 1-1. This trend is expected to continue as governments and industries worldwide seek more sustainable technologies for the energy transition and the reduction of carbon emissions (IEA, 2023).

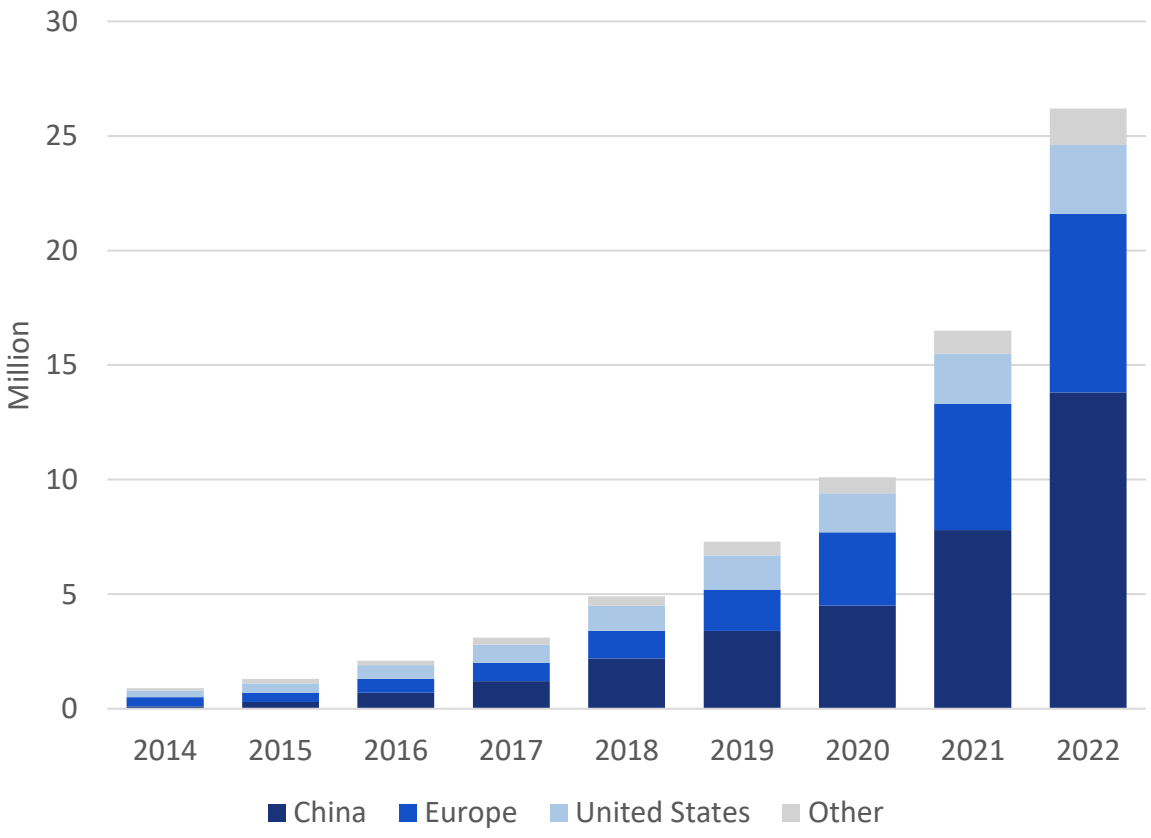

Figure 1-1 - Global electric car sock (IAE, 2023).

The increasing demand, particularly within the EV market, has provided further motivation for developing gears and other drivetrain components capable of tolerating higher power densities (IEA, 2021). Furthermore, transmissions with compact envelopes and high-

efficiency gears that are capable of transmitting high torque and high speeds without compromising durability are of critical importance for EV transmissions. Binder Jetting (BJT), a rising technique of additive manufacturing (AM), shows considerable potential in this field due to its high productivity potential, which enables the creation of intricate designs while minimizing material use (Ziaee; Crane, 2019).

The BJT process is an indirect AM method. As opposed to direct methods, such as the direct laser powder bed fusion (L-PBF) technique, no powder particles get melted in the BJT process. Instead, the powder particles are bound in successive layers with a liquid binding agent to build up the component by the BJT process, followed by the post-processing steps of debinding and sintering to get the final part (Ziaee; Crane, 2019). The process inherently leads to higher porosity compared to direct methods. It is, therefore, essential to ensure an adequate understanding and control of porosity to guarantee the optimal mechanical performance of the parts produced (Liu *et al.,* 2017).

Despite the advantages provided by BJT, this technique presents several challenges, primarily related to the structural integrity of the manufactured parts due to inherent porosity and irregular pore shapes (Dahmen *et al.,* 2021). These characteristics significantly impact fatigue life, especially in applications subjected to cyclic and high-load conditions, such as automotive gears. Fatigue failure in gears is often initiated at the surface or subsurface regions due to defects that act as stress concentrators, facilitating crack initiation and propagation, which can result in catastrophic failure (Alban, 2002). The presence of inclusions or porosity exacerbates these defects, significantly impacting the mechanical performance and reliability of gears (Alban, 2002). In the context of EV's, reliability and longevity are of paramount importance due to the high demands for performance and the need to reduce maintenance costs over the vehicle's lifetime (Emadi, 2014). Understanding and mitigating such failure mechanisms is therefore critically important.

BJT components present unique challenges in this regard. The inherent porosity and irregular pore shapes in BJT parts act as stress concentrators where crack initiation occurs under cyclic loading conditions (Dahmen *et al*., 2021). Unlike pores from L-PBF components, which are more uniform and nearly spherical, pores created by BJT are irregular and anisotropic. These pores result from the way the binder agent infiltrates the powder bed and the subsequent thermal processes used to solidify the structure (Dahmen *et al.*, 2021). The anisotropy in pore shapes leads to uneven stress distribution within the material, resulting in localized stress concentrations that are more severe than those in materials with isotropic pore structures. This

stress distribution is a critical factor in fatigue performance, as it can significantly accelerate crack initiation and propagation under cyclic loading conditions (Dunstan; Paramore; Fang, 2018).

Finishing processes offer a promising solution to mitigate these issues by modifying the surface and subsurface characteristics of BJT components. Processes such as shot peening (SP) and grinding can significantly alter surface integrity, defining the final state of roughness, residual stresses, hardness, and pore morphology. SP, in particular, modifies pore morphology through plastic deformation of the surface layer. The high-velocity impact of shots induces localized plastic flow, collapsing surface-connected pores and reducing surface porosity (Almangour; Yang, 2016; Guagliano, 2001). This plastification leads to surface densification, decreasing the number and size of stress concentrators where cracks can initiate. If its energy is not entirely consumed in densification, SP will introduce beneficial compressive residual stresses into the surface layer, counteracting tensile stresses during operation and further enhancing fatigue life (Guagliano, 2001).

In BJT components, the effect of SP-induced plastification is particularly significant due to the irregular and anisotropic nature of the pores. The plastification process can effectively modify the pore morphology from irregular and open to more closed configurations, improving resistance to fatigue failure (Luo *et al.,* 2018). By reducing the size and number of surface-connected pores and inducing compressive residual stresses, the SP enhances the overall structural integrity of the part.

Anisotropic pores not only initiate cracks but also facilitate their propagation between pores, following paths over regions of maximum equivalent stresses (Holmberg *et al.*, 2019). Therefore, controlling surface integrity like pore morphology, along with inducing compressive residual stresses, is of great importance in improving fatigue performance. This approach aligns with the benefits observed in other AM processes, where surface treatments have been shown to significantly improve mechanical properties (Martin *et al*., 2022; Nicoletto, 2019).

Moreover, Criscuolo *et al.* (2023) have demonstrated that densification and modifications in surface integrity can play a crucial role in the performance of parts under fatigue loading, highlighting the potential of integrating post-processes within the manufacturing chain. Despite these insights, the interaction between post-processes, residual stress and pore morphology in BJT components is not fully understood. There is a lack of comprehensive research focusing on BJT parts and the specific mechanisms by which finishing processes alter pore characteristics. Most existing literature addresses porosity reduction in

processes like L-PBF, where pores are typically spherical and uniformly distributed (Nicoletto, 2019; Martin *et al.,* 2022). In contrast, the irregular and anisotropic pores in BJT components require specialized approaches for modification and control (Dahmen *et al.,* 2021).

Understanding how post-processes can be optimized to modify pore morphology in BJT components is essential for improving their fatigue strength and expanding their applicability in high-performance applications (Mostafaei *et al.,* 2018). By thoroughly investigating how SP influence the internal and surface structures of BJT parts, particularly through plasticizing mechanisms, this research addresses the identified gap in literature. Such an understanding is crucial for developing optimized post-processing strategies that enhance the mechanical performance of BJT components. It is particularly justified in applications where mechanical performance and durability are critical, such as electric vehicle drivetrains (Emadi, 2014).

This Master thesis explores the potential benefits of integrating post-processes into the BJT manufacturing chain. In this light, the objective of this study is the characterization of the effects of SP on surface integrity and fatigue behavior of BJT components. Specifically, this study will address the following research questions:

1st Research question: How does shot peening for densification modifies the surface integrity properties of BJT parts?

2nd Research question: How does shot peening as a finishing stage modifies the rolling contact fatigue behavior of BJT parts?

By examining these questions, this research seeks to establish a clear correlation between surface integrity modifications and fatigue performance. Although the specimens tested are not actual gears, they were printed, post-processed and tested to replicate the surface integrity conditions and operational requirements typically encountered in gear applications. Employing experimental analyses such as surface integrity examination and mechanical testing, the insights gained will contribute to optimizing the post-processing chain for BJT components, providing a framework for enhancing surface integrity in AM. Ultimately, this optimization is expected to enhance the reliability and applicability of BJT in high-performance applications such as electric vehicle drivetrains, advancing its adoption in industries where mechanical performance and durability are critical.

Furthermore, this research provides valuable insights into the fundamental mechanisms of fatigue failure in porous materials. These insights can be extrapolated to other AM techniques

facing similar porosity-related challenges, such as the indirect selective laser sintering (iSLS) process. By deepening the understanding of how porosity influences fatigue behavior, the findings help bridge the gap between conventional and AM methods. This advancement fosters innovation and increases reliability in the production of high-performance components, contributing to the wider adoption of AM technologies in sectors such as automotive and aerospace.

The structure of this Master thesis is oriented to answer the research questions related to its objective logically and comprehensively. In Chapter 2, the fundamentals that were used to develop the thesis are presented. This chapter is divided into three areas of basic knowledge: gear technology and failure mechanisms, gear manufacturing methods and surface integrity and performance enhancement. The last section of Chapter 2 presents the state of the art related to pore morphology in BJT. This section provides up-to-date knowledge of what has been developed in scientific and industrial in recent years. The final section of Chapter 2 provides comprehensive information about the potential for studying the subject.

Subsequently, the established objective is suitably structured in Chapter 3. It presents the technology gap, upon which the hypothesis, objective, and two research questions are elaborated to encompass the entirety of the thesis development content.

Chapter 4 expounds this study's materials, experimental, and analytical methods. An overview of the experimental scope is initially provided, describing the post-processing techniques, the fatigue testing campaign, the methodologies utilized for surface integrity inspection and the pore morphology investigation.

The findings of this study are presented in Chapter 5, which is divided into two sections to address each of the research questions. The first section is devoted to elucidating the impact of SP for densification on the surface integrity of parts produced by BJT, specifically analyzing its effects on porosity morphology, with complementary assessment of residual stresses and mechanical properties. The second section examines how SP for finishing influences the fatigue behavior of BJT components, emphasizing the role of surface integrity modifications in enhancing fatigue performance. A summary of the results is provided after each section.

In the concluding chapter, the thesis reaffirms its stated objective and research questions while emphasizing the technological contributions of the study concerning those questions. The findings are extended to suggest opportunities for further predictive studies. As a result, this Master thesis contributes to the expanding body of knowledge on AM and its potential applications in electrification. The structure of this study is summarized in Figure 1-2.

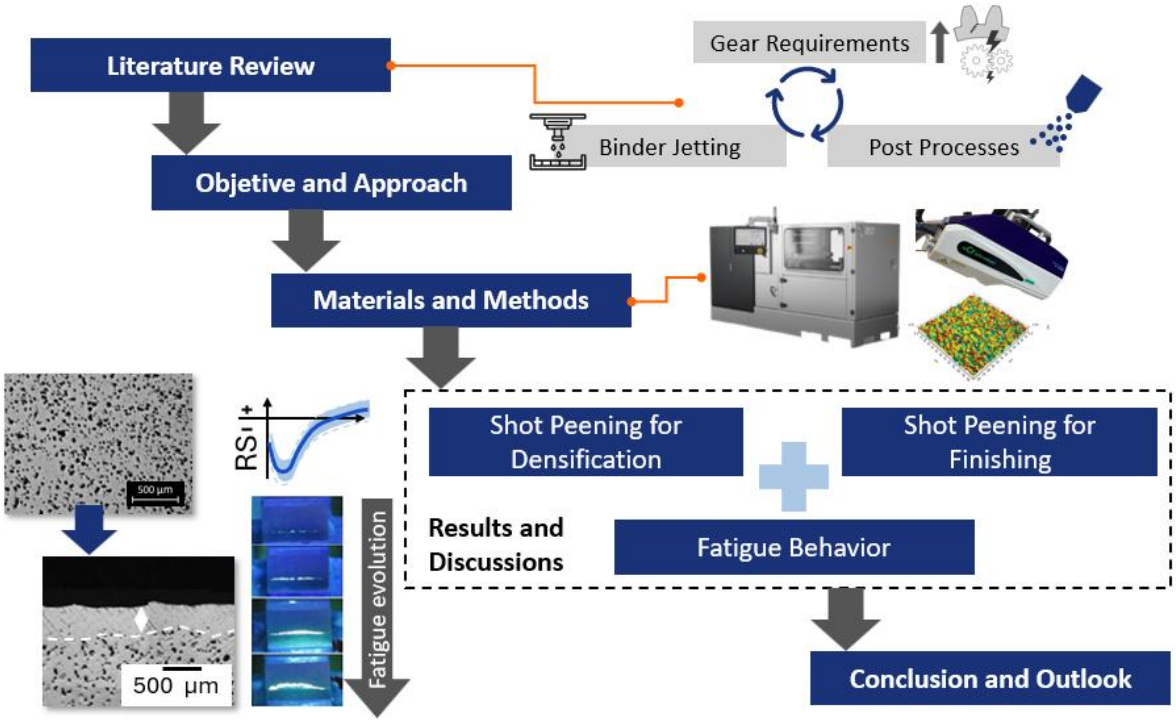

Figure 1-2 - The summarized structure of this study (Author).

2 Literature Review

2.1 Gear Technology and Failure Mechanisms

Gears are essential components in the transmission of mechanical power, playing a critical role in several industrial, automotive and aerospace applications. The performance and durability of gears depend on several factors, including material, manufacturing processes, operating conditions and load regimes. However, due to the cyclical nature of the stresses to which they are subjected, gears are susceptible to different failure mechanisms that can compromise their functionality and service life (Shigley; Mischke, 2014).

In recent years, developments in materials and manufacturing processes have enabled significant advances in fatigue resistance and gear performance. The introduction of techniques such as AM, surface treatments and residual stress engineering has shown a direct impact on improving the service life of these components, enabling the development of gears that are more resistant to failures due to contact and bending fatigue (Mostafaei *et al*., 2018; Schoinochoritis; Chatzis; Salonitis, 2017).

Consequently, technological advances in gear engineering have enabled not only more effective failure mitigation strategies, but also the design of components suited to the requirements of new mobility technologies. These developments aim to improve torque efficiency and load-carrying capacity in increasingly variable and demanding operating conditions.

2.1.1 Gear Demands for the Industry of the Future

The industry is undergoing profound transformations driven by technological advances, evolving consumer expectations and strict environmental regulations, which has a significant impact on gear manufacturing. The rise of EVs requires the development of gears that are efficient, quiet and capable of handling the increased torque of electric motors. By 2035, electric vehicles (EVs) are projected to account for 60% of new vehicle sales globally. This shift necessitates changes in gear design and production approaches to reduce noise and improve efficiency. Significant investments support this market transition, with the EV market anticipated to experience financial growth and considerable development and manufacturing expenditures, as industries respond to evolving consumer demands and regulatory standards (Boston Consulting Group, 2023).

At the same time, the emergence of autonomous vehicles (AVs) increases the need for durable and precise gears capable of operating in varying conditions and managing the complexities of automated systems, emphasizing robustness and technological compatibility (J.P. Morgan, 2023). In addition, the integration of big data and artificial intelligence (AI) is revolutionizing gear production by enhancing predictive maintenance capabilities, enabling real-time monitoring and data analysis to proactively predict wear and schedule maintenance, thereby improving gear reliability and manufacturing efficiency (StartUs Insights, 2024).

Changes in consumer behavior further influence gear demands, with an increasing preference for personalized and sustainable mobility solutions such as car-sharing and mobility-as-a-service, impacting vehicle design and gear manufacturing (McKinsey, 2023). This dynamic environment presents challenges and opportunities for innovation in gear design and manufacturing, driving the development of more sophisticated, durable, and efficient gear systems. As gear manufacturers continue to adapt to these rapid changes, the industry is poised to meet the advanced requirements of next-generation vehicles, ensuring continued growth and technological progression in gear manufacturing.

Changes in consumer behavior further influence gear demands, with a growing preference for personalized and sustainable mobility solutions, such as car sharing and mobility-as-a-service, impacting vehicle design and gear manufacturing (McKinsey, 2023). This dynamic environment presents challenges and opportunities for innovation in gear design and manufacturing, driving the development of more sophisticated, durable and efficient gear systems. As gear manufacturers continue to adapt to these rapid changes, the industry is prepared to meet the advanced requirements of next-generation vehicles, ensuring continued growth and technological progression in gear manufacturing (Boston Consulting Group,2025).

In 2023, the global gear manufacturing market was valued at approximately $80.0 billion. This sector is expected to witness a compound annual growth rate (CAGR) of 5.5%, potentially reaching around $131.4 billion by 2032. This expansion is being driven by several factors, including the increasing demand for industrial high-performance gears and the growth of the automotive industry, which remains a major end-user segment for gear products. Investments in the sector are robust, as evidenced by detailed economic analyses provided for setting up specific types of gear manufacturing plants. These reports highlight the capital investments, operating costs, and expected income and expenditure projections. For instance, the automotive gear manufacturing segment has been elaborated with insights into various

financial aspects such as capital costs, revenue projections, and profitability (IMARC Group, 2024; Market Research Future, 2024).

The future expenses in the gear industry are connected to advancements in automotive technologies, especially as the market shifts towards electric. Electrification will cause a major shift in the entire supply chain, including dedicated hybrid transmissions as shown in Figure 2-1. This transition will likely influence the types of gear required, with a possible increase in demand for more sophisticated and high-performance gears to accommodate new vehicle technologies (McKinsey, 2021).

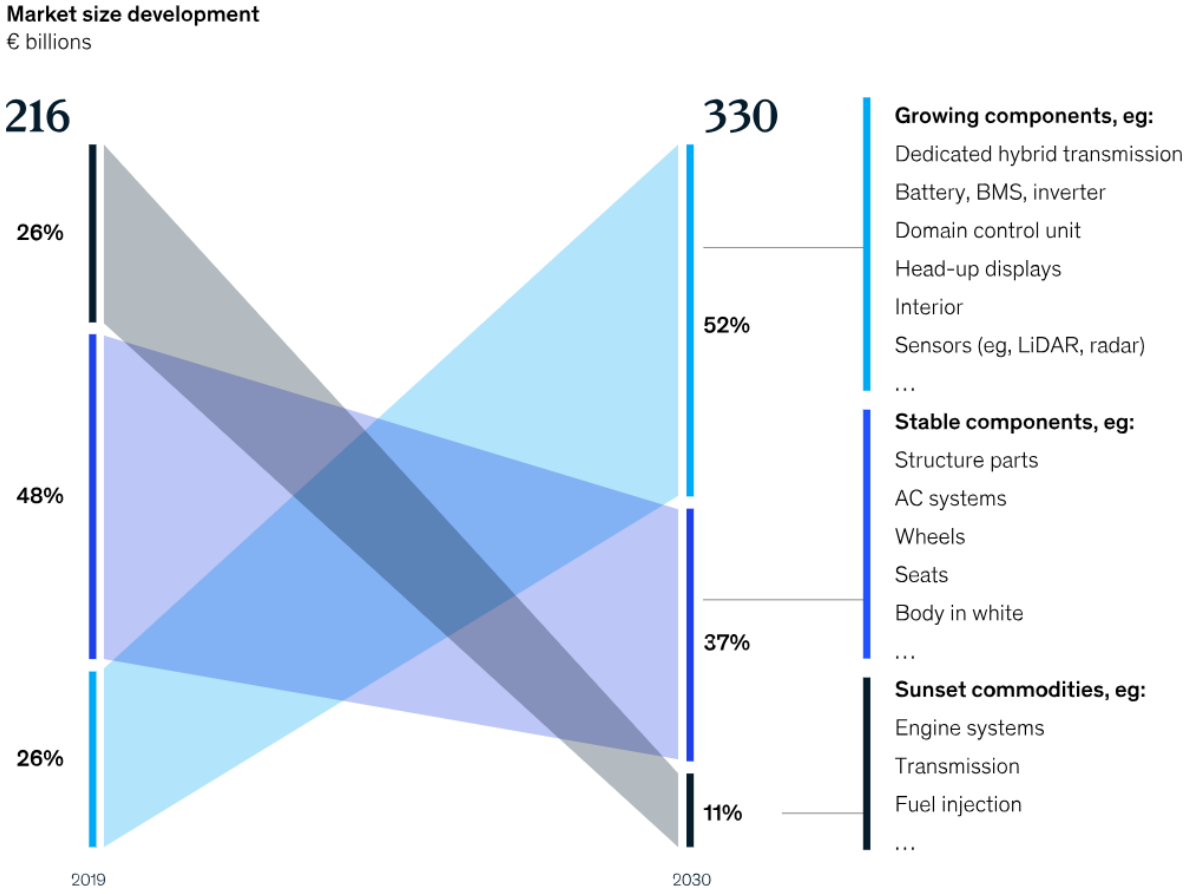

Figure 2-1- Market size development: from €216B (2019) to €330B (2030). Electrification-related components grow from 26% to 52%, combustion engine components decline from 26% to 11%, and structural parts remain stable (McKinsey, 2021).

Additive Manufacturing (AM) has significant potential to meet the growing demand for advanced gear systems in the evolving automotive industry. This technology enables the production of complex and precise gear geometries that are difficult to achieve with traditional manufacturing methods, improving performance and efficiency (NGO *et al.,* 2018). AM enables rapid prototyping and customization, reducing development time and costs, while

promoting innovation in gear design to meet the specific requirements of electric vehicles, including the need for reduced noise emission and high torque transmission efficiency (Schoinochoritis; Chantzis; Salonitis, 2017). It also supports sustainable manufacturing practices, minimizing material waste and energy consumption, in line with the industry's shift towards environmentally friendly solutions (Ford; Despeisse, 2016). The integration of AM into gear production increases the ability to meet market demands for high-performance, reinforced and efficient gear systems, ensuring competitiveness and growth in a rapidly changing market (McKinsey, 2022).

2.1.2 Rolling Contact Fatigue in Gears

Gears play a crucial role in the transmission of mechanical power and, due to high cyclic loads and operational demands, are subject to several failure modes throughout their useful life. Identifying and understanding the main failure mechanisms is essential to improve the performance and increase the reliability of mechanical systems. Among the main failure modes, fatigue, wear, overload fracture and surface degradation stand out. These phenomena can be influenced by factors such as material microstructure, residual stress distribution, inadequate lubrication and adverse operating conditions (Alban, 1993; Wulpi, 2013; Rego, 2016).

Fatigue is one of the most critical failure modes in gears, as it occurs under cyclic loading, even when the applied stresses are lower than the material's yield strength. This failure results from the initiation and propagation of cracks due to the continuous repetition of mechanical stresses, eventually leading to complete fracture of the component. Fatigue can be classified into bending fatigue and contact fatigue, both influenced by factors such as tooth geometry, *Hertzian* stresses in contact and the presence of residual stresses (Alban, 2002).

When a gear is subjected to cyclic loading, the induced microstrains promote the relaxation of compressive residual stresses and localized strain hardening, favoring the nucleation of cracks. Crack initiation can be originated at the surface or subsurface and is often invisible until the failure reaches an advanced stage (Dalaei; Karlsson; Svensson, 2011).

Rolling contact fatigue is a phenomenon associated with cyclic compression and shear stresses at the interface between gear teeth. This failure mode usually occurs in the region of greatest acting stress, due to repetitive loading in the contact region, and may manifest as superficial or subsurface, depending on the origin and propagation mode of the cracks (Fajdiga et al., 2006; Olver, 2005). Figure 2-2 illustrates the acting stress profiles related to superficial and subsurface stresses.

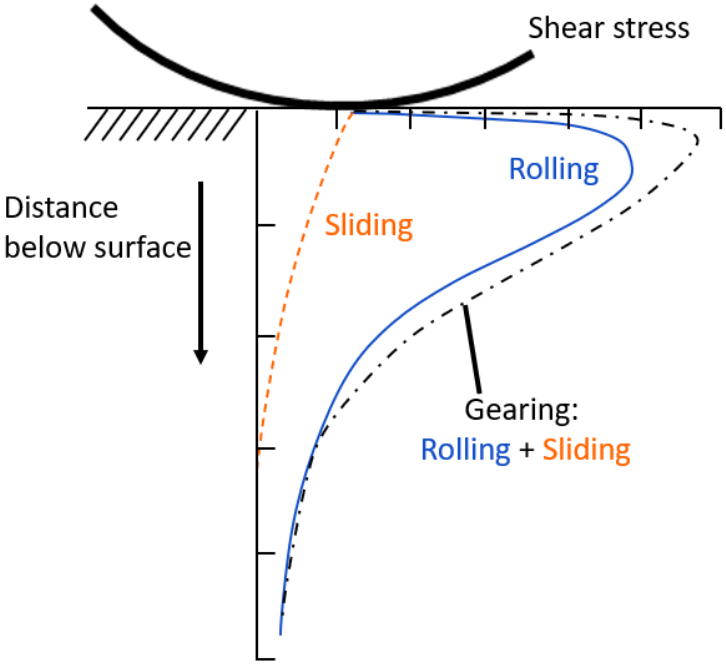

Figure 2-2 - Acting stress in superficial and subsurface stresses (Alban, 2002).

Surface failure is characterized by the formation of cavities originating on the surface due to the propagation of microcracks that begin at the contact interface. These cracks generally grow at an angle of 20° to 40° in relation to the surface, originating due to the combination of rolling and sliding (Antoine; Besson, 2002; Olver et al, 2004; Zafošnik et al, 2007).

Subsurface failure occurs due to the nucleation of cracks below the surface, in the region of maximum shear stress, associated with *Hertzian* contact. These cracks initially grow parallel to the surface, then at angles between 18° and 33° against the rolling direction and finally at 50°, in the same rolling direction. They have dimensions larger than surface failure, reaching up to 180 µm, resulting in the removal of larger fragments of material and significantly compromising the functionality of the gear (Sadeghi *et al*., 2009; Rego, 2011).

Table 2-1 contains a summary of the main points between pitting and spalling.

Table 2-1 - Comparative analysis between surface and subsurface failure. (Rego, 2011)

Feature	**Surface Failure**	**Subsurface Failure**
Dimension	Typically up to 10µm. Maximum 20µm.	Typically between 20µm and 100µm. Maximum 180µm.
Crack origin	Surface	Under surface
Gear kinetics associated	Combined rolling and sliding	Pure rolling
Fracture Region	Dedendum	Pitch diameter, or at dedendum but close to pitch diameter
Crack direction	From surface to core, in an angle of 20° to 40° with surface	1- Parallel to surface; 2- 18º to 33º with surface, against rolling direction; 3- 50º with surface, following rolling direction
Major crack propagation mode	Opening (mode I) and shear (mode II) together.	Shear mode (mode II)

Rolling contact fatigue (RCF) is one of the main failure mechanisms in gears, resulting from the repetitive application of cyclic loads on contacting surfaces. This phenomenon is directly related to *Hertzian* stresses and can be influenced by factors such as material microstructure, lubrication, and the presence of non-metallic inclusions (Sadeghi *et al.,* 2009). Porosity plays a critical role in RCF resistance, as it acts as a stress concentration factor, reducing the mechanical strength of the material and favoring crack nucleation under cyclic loading (Mostafaei *et al.*, 2018). This mechanism can significantly compromise the durability of mechanical systems, making its detailed study essential to optimize component reliability (Olver, 2005).

Crack nucleation in RCF, as seen in

Table 2-1, occurs predominantly in the subsurface of the gear. Subsurface nucleation is associated with the *Hertzian* mechanism, in which maximum stresses occur below the contact surface due to the distribution of normal loads in the elastic contact between two bodies. When two bodies having at least one of them a non-flat surface are in contact, as in gears and bearings, the real contact area is much smaller than the apparent area, generating a three-dimensional stress field in the region close to the interface. *Hertz's* theory describes the distribution of these stresses for elastic contacts, considering parameters such as the radius of curvature of the surfaces, the stiffness of the materials and the applied load. As a result, the maximum shear stress does not occur directly at the surface, but rather at a certain depth below it, depending on the loading conditions and the properties of the materials involved. (Sadeghi, *et al*. 2009.)

Residual stress gradients from AM or heat treatment can accelerate crack nucleation and propagation under cyclic loading (Sadeghi *et al*., 2009). Inherent porosity intensifies this effect by acting as a stress concentration site, facilitating crack initiation (Almangour *et al*., 2016). In materials of high structural purity, meaning alloys that contain very few inclusions, low porosity and minimal surface irregularities as roughness or topographical defects, subsurface initiation is often associated with the accumulation of stresses at depth, resulting in the formation of internal flaws that eventually reach the surface, a phenomenon known as spalling (Olver, 2005).

Different manufacturing processes can significantly affect a component's resistance to RCF. Rego (2016) demonstrates that the state of residual stresses induced by treatments such as SP and carburizing directly influences the material's resistance to crack propagation. However, residual porosity from AM and powder metallurgy processes can reduce the effectiveness of these treatments, as it creates regions of lower density and mechanical continuity, favoring the propagation of premature failures (Mostafaei *et al*., 2018). The effect of the redistribution of residual stresses along the component's manufacturing chain can modify its resistance to contact fatigue, making strict control of the manufacturing and operating processes essential (Rego, 2011).

RCF can be described in three distinct stages. Initially, there is shakedown, in which the material responds elastically to the applied load. Then, there is a phase of stable elastic response, where stresses are distributed homogeneously along the contact surface (Sadeghi et al., 2009). In the final stage, the damage growth rate intensifies significantly, leading to component failure in less than one million cycles (Rego, 2016). Detailed analysis of this evolution allows correlating fatigue resistance with variables such as residual stress level and lubrication conditions (Mitsubayashi; Miyata; Aihara, 1994). The interaction between surface topography

and lubrication conditions plays a crucial role in the evolution of RCF, since irregularities in the contact surface can amplify local stresses, accelerating crack nucleation and reducing component life (Olver, 2005). The presence of porosity on the surface or in subsurface regions can act as a stress concentration point and reduce the material's ability to withstand load cycles, making it essential to apply densification processes to minimize this effect (Almangour *et al*., 2016).

Wulpi (2003), Aslantas and Tasgeriren (2004) shows that the RCF failure begins in the region of maximum shear stress, located below the contact surface due to the distribution of hertzian stresses. In this region, the interaction between mechanical loads, heterogeneous microstructures and residual stresses can result in the formation of microcracks, which initially grow parallel to the surface, following a shear propagation mode (Mode II), as shown in Figure 2-3. As cyclic loading progresses, the crack seeks a path of least resistance, changing its trajectory to a propagation in the opening mode (Mode I), growing towards the surface. This behavior is influenced by factors such as the presence of non-metallic inclusions, porosity and distribution of residual stresses. Upon reaching the surface, the crack can evolve to material removal. In more severe cases, successive detachment of fragments of the material occurs.

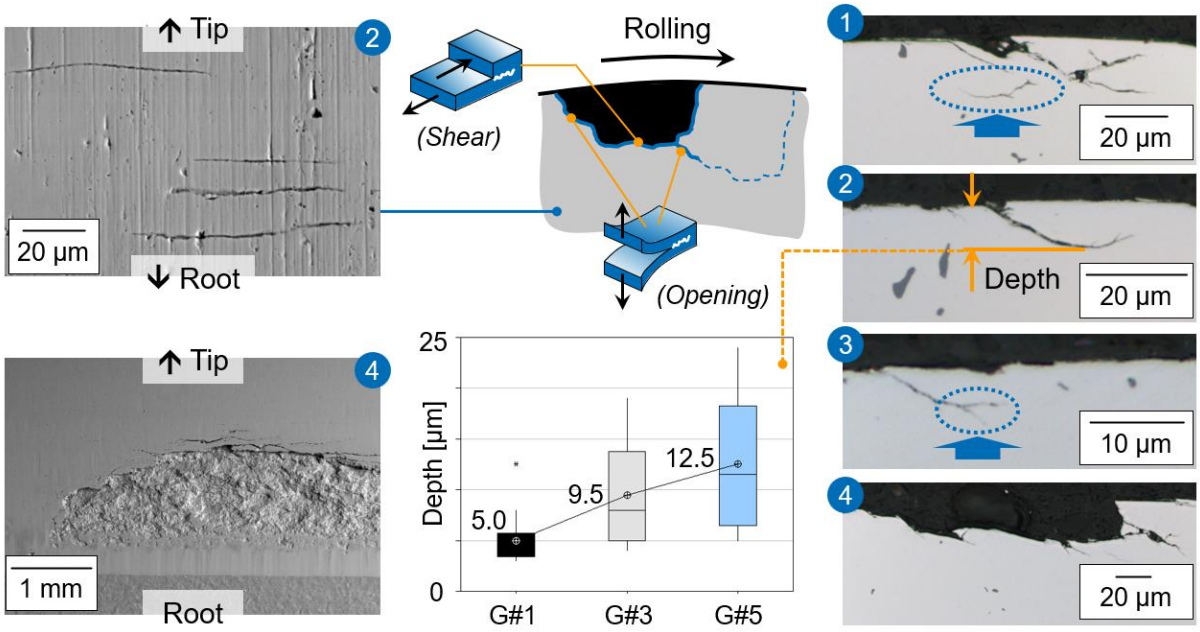

Figure 2-3 - The crack originates beneath the surface, propagates outward, and, upon the final collapse of the opposite extremity, leads to material removal. (Rego, 2016).

In the final stage of failure, material removal occurs by a mechanism known as ligament collapse, in which, instead of continuous crack propagation, material separation occurs due to the collapse of the ligament region at the crack tip. According to Ding (2009), this mechanism occurs when the average stress in this region exceeds the ultimate strength of the material, resulting in catastrophic failure. As a consequence, the fracture surface presents an irregular and fragmented profile, characteristic of the fusion of microcracks formed along the directions of maximum shear stress at the crack tip. Cracks remaining from the bifurcation in the previous stage can still propagate under the opening mode, promoting progressive material removal and increasing the extent of damage in the direction of the gear pitch circle Rego (2016). To isolate and reproduce this failure mechanism under controlled conditions, a rolling contact fatigue (RCF) test rig will be used with simplified specimens.

2.2 Gear Manufacturing Methods

2.2.1 Traditional Manufacturing Methods

Traditional manufacturing methods have long been the cornerstone of gear production, particularly machining, forging, and casting processes. While these techniques have proven effective over time, producing high-performance gears introduces several limitations and challenges that necessitate careful consideration (Groover, 2013).

Machining is a subtractive manufacturing process that removes material from a workpiece to obtain the desired shape and dimensions of the gear. This method is highly regarded for its precision and ability to produce gears with tight tolerances and excellent surface finishes (Kalpakjian; Schmid, 2014). Techniques such as gear milling, gear shaping and gear grinding are fundamental to gear machining. Gear milling uses a cutter to progressively cut the gear teeth and is efficient for producing medium to high volumes (Dudley, 1994). Gear shaping uses a reciprocating cutter that gradually forms the gear teeth through a continuous gearing action between the cutter and the gear blank. This process is advantageous for the production of internal gears and gears with limited access to machining tools, where methods such as gear milling are not feasible due to geometric restrictions. Gear shaping allows manufacturers to create precise gear profiles in situations where other machining processes cannot be applied effectively (Maitra, 1994). Grinding refines gear surfaces to achieve the surface integrity and precision required for high-performance applications (Marinescu *et al*., 2007).

Despite its advantages, machining faces challenges in the production of high-performance gears. One significant limitation is material waste, as machining involves cutting material, leading to inefficiencies and higher costs, especially when working with expensive alloys required for high-performance gears (Groover, 2013). In addition, machining complex gear geometries can be time-consuming and may require multiple setups and specialized tools, increasing production time and costs (Kalpakjian; Schmid, 2014). The machining process can also introduce residual stresses into the gear material, potentially affecting the performance and service life of the gear if not managed properly (Totten; Xie; Funatani, 2006).

Forging consists of shaping the metal using compressive forces, improving the mechanical properties of gears through refined grain structures and greater strength (Altan, Ngaile; Shen, 2005). Processes such as open die forging and closed die forging are commonly used in the manufacture of gears. Forged gears benefit from superior fatigue resistance and strength, which makes them suitable for high-stress applications (Behrens; Bouguecha; Bonk, 2010).

However, forging high-performance gears presents challenges. The process is less suitable for producing gears with complex geometries or internal features due to limitations in die design and material flow (Lange, 1985). The high initial costs of die production make forging less economical for small production runs or for customized gears, which are often required in high-performance applications (Altan *et al.,* 2005). In addition, achieving the necessary dimensional accuracy and surface finish usually requires additional machining operations, increasing production time and costs (Shivpuri; Hua, 2001).

Casting processes involve pouring molten metal into molds to create gears. Techniques such as sand casting, investment casting and die casting allow for the production of complex shapes and large components (Campbell, 2015). Casting is versatile and economical for high-volume production, and investment casting in particular can achieve excellent surface finishes and dimensional accuracy suitable for gear manufacturing (Rao, 2003).

The limitations of casting high-performance gears include the possibility of defects such as porosity, shrinkage and inclusions, which can compromise the mechanical properties and reliability of the gears (Stefanescu *et al.*, 2002). Cast gears may not achieve the same level of strength and fatigue resistance as forged or machined gears, making them less suitable for high-performance applications where durability is critical (Campbell, 2015). In addition, controlling the microstructure of cast gears to meet the stringent requirements of high-performance

applications can be challenging, often requiring heat treatments and inspections after casting (Davis, 1998).

The production of high-performance gears also involves several wide-ranging challenges, regardless of the manufacturing method. Material selection is crucial, as high-performance gears often require advanced alloys or composite materials to meet the demands of strength, wear resistance and lightweight characteristics (Budinski; Budinski, 2010). Working with these materials can be difficult due to their hardness, toughness or sensitivity to heat, affecting tool wear, machining parameters and overall process stability (Groover, 2013).

Another significant challenge is achieving the required precision and surface integrity. High-performance gears must meet strict dimensional tolerances and surface finish specifications to ensure efficient power transmission, minimize noise and avoid premature failure (Dudley, 1994). Manufacturing processes must be strictly controlled and quality assurance measures, such as non-destructive testing and surface inspections, are essential (Totten, 2003).

In addition, the growing demand for gears with complex geometries and lightweight designs presents challenges to traditional manufacturing methods. Complex gear designs, including those with internal cooling channels or non-standard tooth profiles, can be difficult or impossible to produce using conventional machining, forging or casting without significant investments in terms of cost and time (Debroy *et al*., 2018).

To solve these limitations and challenges, manufacturers are exploring advanced manufacturing technologies and hybrid processes. AM, for example, offers the ability to produce complex geometries with minimal material waste and can be combined with traditional methods to improve performance and efficiency (Thompson *et al*., 2016). Process innovations, including high-speed machining, precision forging and improved casting techniques are also being developed to overcome the limitations of traditional methods and meet the demands of high-performance gear production (Groover, 2013).

In summary, although traditional manufacturing methods such as machining, forging and casting are essential for gear production, they face limitations and challenges in the production of high-performance gears. Issues such as material waste, limitations in producing complex geometries, high tooling costs, potential defects and difficulties in achieving the required precision and mechanical properties require continuous advances in manufacturing technologies and processes. By understanding and addressing these challenges, manufacturers

can improve gear performance, reliability and production efficiency to meet the evolving demands of modern industries.

2.2.2 Additive Manufacturing in Gear Production

AM has established itself as a promising alternative for gear manufacturing, offering advantages as design freedom, reduced material waste, and the possibility of on-demand production. Unlike conventional methods as machining, forging, and casting, AM builds parts layer by layer from a digital model, allowing the creation of complex geometries optimized for specific performance (Thompson *et al*., 2016). This capability has attracted significant interest in gear manufacturing, especially for applications where weight reduction and customization are desirable (Frazier, 2014).

Among the main AM technologies applicable to gear production, the processes based on powder bed fusion (PBF), directed energy deposition (DED), and BJT stand out. Powder bed fusion includes techniques such as laser powder bed fusion (L-PBF) and Electron Beam Powder Bed Fusion (PBF-EB). In L-PBF, a high-power laser selectively melts metal powder particles, allowing the manufacture of parts with high density and geometric accuracy (DebRoy *et al*., 2018). However, this technique presents challenges. The need for structural support and the presence of residual stresses, which can affect the mechanical integrity of the part (Leuders *et al*., 2013). In PBF-EB, the use of an electron beam allows the powder to be melted in a vacuum environment, reducing residual stresses and minimizing the need for support, but resulting in rougher surface finishes compared to L-PBF (Strano *et al*., 2013; Yadroitsev *et al.*, 2021).

Directed energy deposition (DED) is a technique that uses a concentrated heat source, a laser or electron beam, to melt simultaneously added metal material. This process is particularly useful for gear recovery and repair, as it allows the deposition of material on pre-existing components, increasing their useful life and reducing replacement costs (DebRoy *et al.,* 2018). However, DED has limitations in terms of geometric resolution and surface finish, often requiring secondary machining operations to achieve the desired tolerances (Frazier, 2014).

Binder jetting (BJT) has also been explored in gear production as a viable alternative due to its high production rate and manufacturing capacity without the need for supports. Unlike PBF and DED, BJT uses a binding agent to join powder particles in successive layers, creating a preform that subsequently undergoes sintering processes to achieve the desired density (Frazier, 2014). Although this technology presents advantages in terms of scalability and cost,

challenges as the presence of residual porosity and shrinkage during sintering still need to be overcome to ensure the reliability of the gears produced (DebRoy *et al*., 2018).

Despite the advantages of AM in gear manufacturing, technical challenges persist and limit its large-scale adoption. The surface roughness of AM-manufactured parts can significantly impact the tribological performance of gears, increasing friction and wear during operation (Strano *et al*., 2013). In addition, the mechanical strength and fatigue life of printed gears can be influenced by factors as microstructure anisotropy and the presence of internal defects, making it essential to apply post-process thermal and mechanical treatments to ensure adequate performance (Leuders *et al*., 2013).

The economic viability of AM for gears should also be considered. Although the technology allows the production of complex geometries and the customization of components, the high costs of equipment and materials, as well as the need for post-processing, can limit its competitiveness in relation to conventional methods for mass production (Thompson *et al*., 2016). However, for applications where design flexibility, weight reduction and on-demand production are priorities, AM can represent a highly advantageous solution (DebRoy *et al*., 2018).

Recent research has sought to improve the reliability and efficiency of AM for gears, exploring the development of new materials, optimization of manufacturing parameters and integration with conventional processes, as machining and heat treatment (Frazier, 2014). The combination of AM with hybrid techniques can significantly improve the surface integrity and mechanical properties of manufactured gears, making this approach more attractive for demanding industrial applications (Leuders *et al*., 2013).

AM has the potential to transform gear manufacturing, offering benefits in terms of design and functionality. However, its successful implementation requires a multidisciplinary approach, involving the optimization of processes manufacturing processes, effective post-processing strategies and rigorous validation of the mechanical properties of the components produced (Thompson *et al*., 2016). With the continuous advancement of research and improvement of technologies, AM is expected to play a growing role in the production of gears for high-performance applications, expanding its acceptance in the industry (DebRoy *et al*., 2018).

2.2.3 Binder Jetting Process

BJT is an AM technology that offers significant advantages in the production of complex geometries, functional components, and scalable batch manufacturing. Unlike laser-based AM methods such as Selective Laser Melting and Electron Beam Melting, BJT does not require thermal energy to fuse particles. Instead, a liquid binder selectively bonds powder particles layer by layer, after which the part goes through post-processing steps such as binder removal and sintering, as the Figure 2-4 shown. (Mostafei *et al*., 2021).

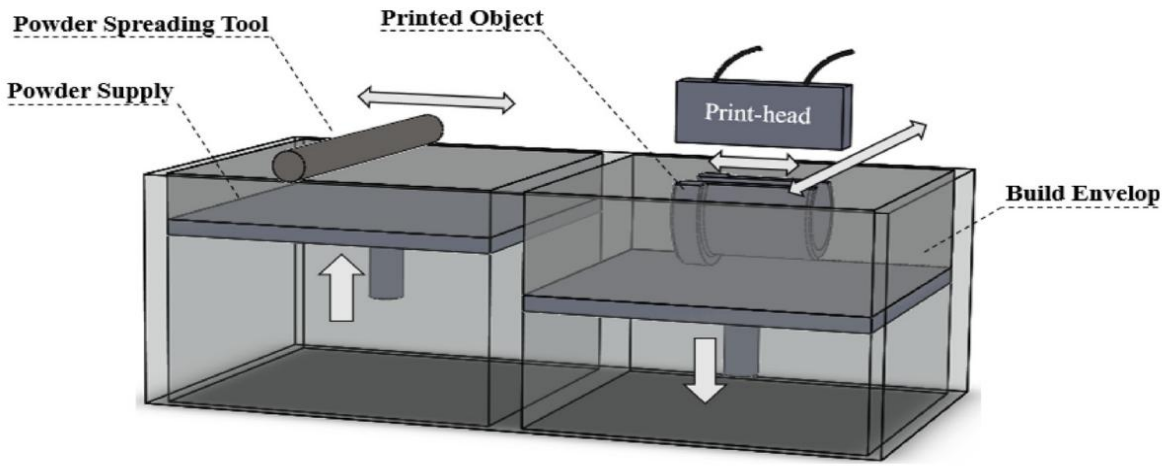

Figure 2-4 - BJT system schematic (Ziaee; Crane, 2019).

BJT has several advantages compared to other AM techniques. The unbound powder acts as a natural support during printing, eliminating the need for additional material, which simplifies post-processing and reduces material waste (Ziaee; Crane, 2019). It can process large batches in industrial sintering furnaces, making it an attractive option for mass production of components (Du *et al*., 2021). Because no melting occurs during the process, BJT manufactured parts exhibit a more homogeneous residual stress distribution, in the first stages of manufacturing, reducing the risk of warping and distortion compared to laser-based techniques (Mostafei *et al*., 2021). The process allows the fabrication of complex features, such as cooling channels and lightweight lattice structures, which are difficult to achieve using conventional manufacturing techniques (Del Giudice; Vassiliou, 2020).

To better understand the origin of the inherent porosity observed in BJT, it is essential to explore each stage of its process chain. Manufacturing begins with powder sieving, which ensures consistent particle size distribution by removing agglomerates and oversized particles that can compromise the powder's compaction density (Mostafaei *et al.,* 2019). This is followed by powder mixing, where flow enhancers or alloy blends can be added to improve deposition

uniformity (Mostafaei *et al.,* 2018). The powder drying step is then used to remove any residual moisture that could interfere with the saturation of the binder or create defects during curing and sintering (Muhammad *et al.,* 2022). Once the powder is properly conditioned, the printing step uses a head to selectively deposit a binder over each powder layer, creating a green part without the application of heat (Ziaee and Crane, 2019; Mostafaei *et al.,* 2019).

After printing, the part undergoes curing, usually in an oven below 220 °C, to polymerize or harden the binder and give the part sufficient strength for handling (Ziaee and Crane, 2019). The depowdering step removes the unbound powder, exposing the geometry of the part. Finally, sintering is carried out at high temperatures, usually between 1200-1400 °C, depending on the material, to promote diffusion bonding between the particles, densify the part and achieve metallurgical integrity (Dahmen *et al.,* 2021; Klee *et al.,* 2023). The complete sequence can be seen in Figure 2-5.

Figure 2-5: Binder Jetting process steps: powder preparation (sieving, mixing, drying), layer-by-layer printing with binder, thermal curing, depowdering, and final sintering. Each step directly influences the final part's density and integrity.

As the initial powder bed is loosely compacted and the binder holds the particles in place only temporarily, shrinkage and residual porosity are inherent to the process. Final porosity is influenced by powder characteristics, binder content, green density and sintering parameters

(Zago *et al.,* 2024; Mostafaei *et al.,* 2018). Therefore, understanding the complete manufacturing sequence is key to interpreting how defects are introduced and how post-processing strategies can mitigate their effects (Almangour *et al.,* 2016).

Despite its advantages, BJT has specific challenges that limit its mechanical performance. Green parts produced by BJT typically have a lower density than those manufactured by laser powder bed fusion, requiring extensive post-processing such as hot isostatic pressing (HIP) or infiltration to improve mechanical integrity (Bai *et al*., 2017). Shrinkage caused by sintering can lead to dimensional inaccuracies, and achieving full densification remains a challenge (Du *et al*., 2021). BJT parts, even after sintering, may exhibit lower fatigue resistance compared to forged or laser-based AM parts, requiring additional surface treatments such as shot peening (Zhou *et al*., 2024).

BJT is compatible with a wide range of materials, including metals, ceramics, and composites. The most common metals used in BJT are stainless steels, titanium alloys, and nickel-based superalloys (Del Giudice; Vassiliou, 2020). BJT is widely used for ceramic processing due to the lack of heat input during manufacturing, but obtaining high-density sintered parts is challenging and requires precise control of binder removal and sintering parameters (Bai *et al*., 2017).

The environmental impact and cost-effectiveness of BJT depends on multiple factors. Unlike L-PBF, where the powder can often be reused, BJT powders can degrade due to binder contamination, limiting their recyclability (Ziaee; Crane, 2019). BJT does not require high-energy lasers or electron beams, making it more energy-efficient during the printing phase. However, industrial sintering is energy-intensive and contributes to overall process costs (Mostafei *et al*., 2021). The absence of support structures leads to less material waste, improving the overall sustainability of the process (Zhou *et al*., 2024).

To improve BJT, current research focuses on advancing binder formulations to enable multi-material capabilities, enabling functional gradients and hybrid structures (Du *et al*., 2021). New sintering methods and surface treatments, such as laser-assisted sintering and densification through SP, are being explored to improve the final properties of the part (Bai *et al*., 2017). The development of next-generation binders that reduce contamination and increase the strength of the green part remains a key area of research (Ziaee; Crane, 2019).

BJT is a promising AM technology that offers high scalability, design freedom, and lower thermal stress compared to laser-based AM processes. On the other hand, one of its most critical challenges lies in the intrinsic porosity of green and sintered parts, which significantly

impacts surface integrity and mechanical performance. Unlike laser-based processes, BJT relies on subsequent debinding and sintering steps, during which incomplete densification or pore coalescence can occur. As a result, porosity becomes a limiting factor for high-performance applications, particularly in components subject to cyclic loading, such as gears. Understanding how porosity interacts with post-processing techniques is essential to improving part quality and enabling the wider adoption of BJT in structural applications.

2.2.4 17-4PH: Characteristics and Heat Treatment Behavior

17-4 PH stainless steel is a precipitation-hardened martensitic alloy widely used due to its excellent combination of strength, toughness, and corrosion resistance. Its hardening mechanism is mainly associated with the precipitation of copper-rich phases within a martensitic matrix after appropriate aging treatments (Viswanathan; Banerjee; Krishnan, 1988).

After solution treatment at temperatures above 1000 °C and rapid cooling, the alloy forms a martensitic structure supersaturated with alloying elements, particularly copper. Transmission electron microscopy confirms the presence of high dislocations densities within the martensite, which may exhibit micro-twinning depending on processing conditions (Hsiao; Chiou; Yang, 2002). Supersaturation provides the driving force for subsequent precipitation reactions during aging.

Solution treatment, typically performed at temperatures around 1040 °C, plays a crucial role in the heat treatment sequence of 17-4 PH stainless steel. Its main purpose is to completely dissolve alloying elements, such as copper and niobium, into the austenitic matrix, eliminating any preexisting precipitates formed during previous processing. This homogenization ensures a supersaturated solid solution after quenching, which is essential for the subsequent formation of finely distributed copper rich precipitates during aging (Viswanathan; Banerjee; Krishnan, 1988; Dossett; Totten, 2013). Incomplete solution treatment can result in non-uniform precipitation behavior and reduced hardening response, as undissolved particles can act as preferential sites for coarse precipitate growth, accelerating excessive aging and compromising mechanical performance (Hsiao; Chiou; Yang, 2002).

Aging at intermediate temperatures, typically 480–510 °C, promotes the nucleation of fine, coherent or semi-coherent, copper rich precipitates within the martensitic matrix. These precipitates are initially spherical and coherent, contributing significantly to the increase in hardness through precipitation hardening (Viswanathan; Banerjee; Krishnan, 1988). Optimal hardness is generally achieved after 1 to 2 hours at these temperatures, with the precipitates

adopting an FCC crystal structure consistent with copper and following a Nishiyama-Wasserman orientation relationship with the matrix (Hsiao; Chiou; Yang, 2002).

Prolonged exposure or higher aging temperatures, above 600°C, can lead to superaging, characterized by thickening of the precipitate and reversal of martensite to austenite, particularly along grain boundaries. This reversed austenite may retain the crystallographic memory of the original austenite grain, forming through diffusion processes facilitated by local enrichment of stabilizing elements such as copper and nickel (Viswanathan; Banerjee; Krishnan, 1988). Superaging is typically accompanied by a decline in hardness, although the microstructure may stabilize with a two-phase morphology, depending on cooling rates (Hsiao; Chiou; Yang, 2002).

The precipitation sequence in 17-4 PH is similar to that observed in iron-copper alloys, starting from coherent body-centered cubic copper clusters to incoherent face-centered cubic particles, through intermediate metastable phases, such as 9R structures (Hsiao; Chiou; Yang, 2002). The sequence and kinetics are influenced by the aging temperature, time, and initial microstructural conditions resulting from previous thermal or mechanical treatments.

Furthermore, understanding the evolution of residual stresses during aging is critical, especially in applications involving high mechanical loads or thermal cycling. The interaction between precipitation-induced hardening, dislocation recovery, and phase transformations underpins the mechanical behavior of the alloy in service environments (Rack; Kalish, 1974; Dossett; Totten, 2013).

2.3 Surface Integrity and Performance Enhancement

2.3.1 Porosity and Crack Initiation in AM

Porosity is a major challenge in components produced using indirect AM techniques as BJT. Unlike wrought steel, which is almost completely pore-free, BJT components often retain significant porosity after sintering, ranging between 0,9% and 57%, in stainless steel depending on process parameters, as shown in Table 2-2 (Dahmen *et al*., 2021). This porosity not only decreases the density of the parts but also compromises essential mechanical properties, such as fatigue resistance (Mostafaei *et al*., 2018). Zhu *et al*. (2020) further highlighted that the presence and evolution of porosity during sintering significantly affect the mechanical performance of AM components, with irregular pore morphology leading to higher stress concentrations.

Table 2-2 - Review of densities in stainless steels manufactured by BJT. Author.

Material	Sintered Density (%)	Density by Other Densification Techniques (%)	Reference
SS 17-4PH	43	~100	Seluga (2001)
	93.5 - 96	-	Zago *et al.* (2024)
	93.98	93.98	Klee *et al.* (2023)
	97.4	-	Klee *et al.* (2023)
	99	-	Klee *et al.* (2023)
	96 ± 0.6%	-	Huber, Vogel and Fischer (2021)
	97 ± 0.6%	-	Huber, Vogel and Fischer (2021)
	99 ± 0.2%	-	Huber, Vogel and Fischer (2021)
	97.8 ± 0.6%	-	Huber, Vogel and Fischer (2021)
	98.8 ± 0.2%	-	Huber, Vogel and Fischer (2021)
	98.9 ± 0.2%	-	Huber, Vogel and Fischer (2021)
	99.1 ± 0.2%	-	Huber, Vogel and Fischer (2021)
	-	99.99%	Nezhadfar *et al.* (2021)
	97%	-	Radhakrishnan *et al.* (2022)
	98.50%	-	Radhakrishnan *et al.* (2022)
	97%	99%	Radhakrishnan *et al.* (2022)
SS 316L	-	~99	Do, Kwon and Shin (2017)
	80	-	Miyanaji (2018)
	65 a 92	-	Michaels, Sachs and Cima (1992)
	88	-	Dourandish, Godlinski and Simchi (2007)
	93.9	-	Ziaeem Tridas and Crane (2016)
	97.5	-	Verlee, Dormal and Lecomte-Beckers (2013)
	50	-	Tang *et al.* (2016)
	52.4	-	Zhou *et al.* (2015)

Table 2-3 – Review of densities in stainless steels manufactured by BJT. Author. Continued from previous page

SS 316L	98.7	-	Verlee, Dormal and Lecomte-Beckers (2013)
	63.2 a 98.7	-	Verlee, Dormal and Lecomte-Beckers (2013)
	96	-	Ziaee, Tridas and Crane (2016)
	80.5	-	Dourandish, Godlinski and Simchi (2007)
	72	-	Miyanaji (2018)
	97.8 - 98.6	-	Muhammad *et al.*(2022)
	95.8 - 97.2	99.9	Muhammad *et al.*(2022)
	93.5 - 95.0	-	Muhammad *et al.*(2022)
	92.5 - 94.5	-	Zago *et al.* (2024)
SS 420	-	96.98	Do *et al.* (2015)
SS 420	-	99	Doyle *et al.* (2015)
SS 420	-	99.8	Sun, Kim and Kwon (2009)
SS 420	-	99.6	Do, Kwon and Shin (2017)

Zhu *et al*. (2020) classified porosity into four groups based on their morphology and distribution, as shown in Figure 2-6. Group 1 (isolated spherical pores), Group 2 (small elongated and interconnected pores), Group 3 (large, elongated pores), and Group 4 (highly irregular and networked pores). Among these, pores of Group 4 have the highest stress concentrations and are the most detrimental to fatigue strength. The transition of Group 4 porosity to Groups 3,2 and 1 during sintering significantly improves mechanical properties, reducing internal defects and increasing material integrity.

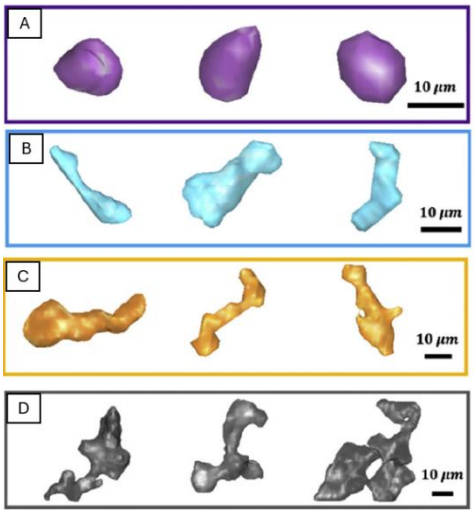

Figure 2-6 - Examples of representative pores in each group (Zhu et al., 2020). From top to bottom: A - Group 1 – quasi-spherical pores, B - Group 2 – small elongated pores, C - Group 3 – large elongated pores with low solidity, D - Group 4 – reticulated pores.

The evolution of porosity through different processing stages can be better understood by analyzing the pore number fraction and relative pore volume fraction . The pore number fraction refers to the proportion of pores belonging to a specific group in relation to the total number of pores, while the relative pore volume fraction expresses the volumetric contribution of a given group to the overall pore volume. These two metrics helps differentiate whether a group dominates in terms of quantity or volumetric impact (Zhu *et al*., 2020). The analysis shows that the total amount of pores does not decrease dramatically with sintering or HIP. However, their morphology changes significantly. Highly irregular and interconnected pores (Group 4) almost disappear after HIP, while isolated spherical pores (Group 1) become the dominant type. This suggests that although the absolute number of pores remains relatively constant, their transformation into less detrimental forms improves mechanical performance, as illustrated in Figure 2-7.

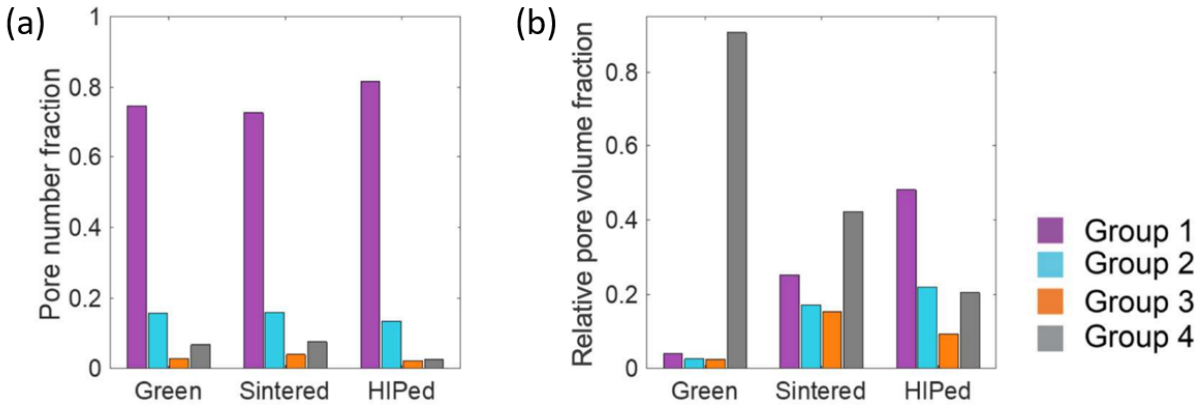

Figure 2-7 - Quantitative evolution of (a) pore number fraction and (b) relative volume. (Zhu et al., 2020)

Similarly, analysis of the relative pore volume fraction reveals a significant reduction in the total volume occupied by pores, particularly in Group 4. In the green state, large, interconnected pores represent the most substantial fraction of the total porosity. However, after sintering, the interconnectivity between pores is reduced, and after HIP, almost all large and interconnected pores are eliminated. This transition highlights the effectiveness of post-processing techniques in minimizing structural defects that could act as crack initiation sites (Zhu *et al*., 2020).

Therefore, pore closure through sintering and HIP is more efficient in volume than in number, which means that the processes used reduce the most critical defects, but still maintain some small pores (Zhu *et al*., 2020). However, it is important to note that HIP is ineffective at eliminating surface-connected pores, which are essential in gear applications, where fatigue cracks often start at or near the surface. When it comes to crack initiation, the pores in components manufactured by indirect AM act as stress concentrators, creating favorable conditions for the formation of cracks. These cracks typically originate in pores located at the surface or on sub surface, where shear stresses are intensified during cyclic rolling loads (Holmberg *et al*., 2019). Zhu *et al.* (2020) demonstrated that anisotropy and pore clustering further amplify local stress fields, accelerating crack propagation and reducing fatigue life. Dahmen et al. (2021) observed that pores tend to be irregularly shaped and are often located close to grain boundaries, with diameters ranging from 1 to 20 μm, which increases the local concentration of stresses and facilitates the initiation of microcracks as seen in Figure 2-8. Mostafaei et al. (2018) further confirmed that even subsurface pores smaller than 10 μm can critically impact fatigue life, especially when associated with rough surfaces, acting as effective

initiation sites under cyclic stresses. Thus, both the size and morphology of pores, particularly those located along grain boundaries, play a key role in accelerating crack propagation in BJT components.

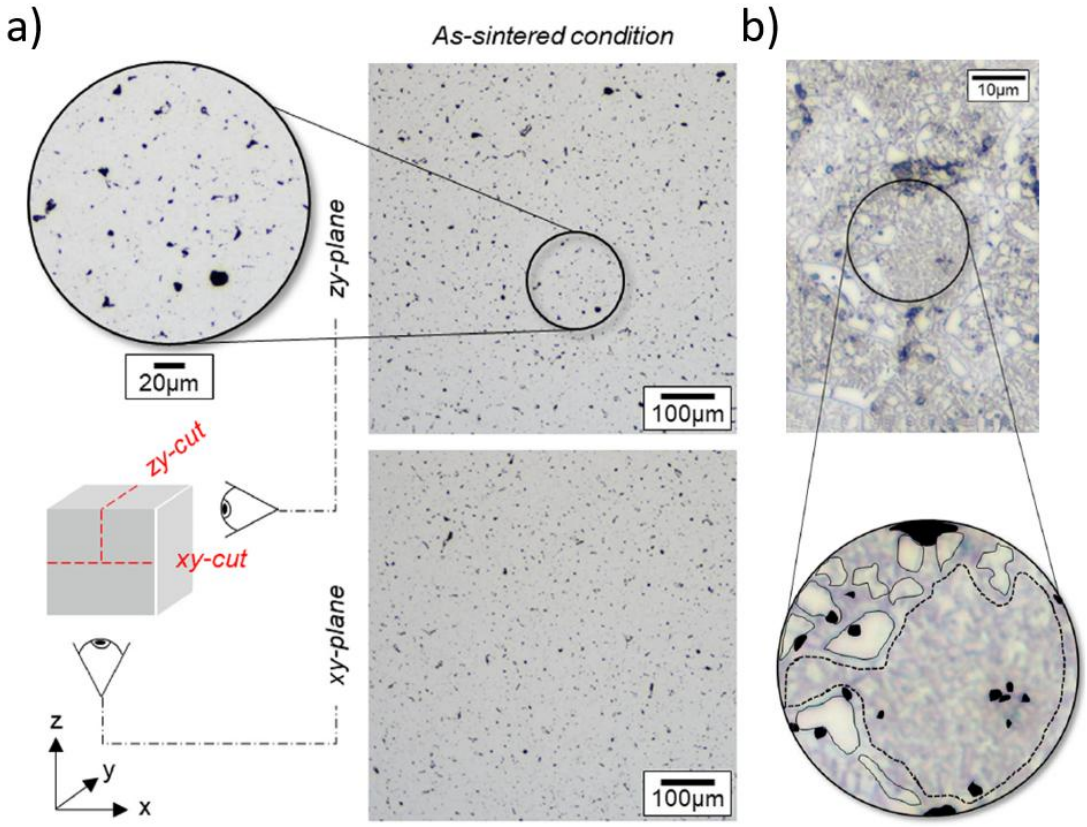

Figure 2-8: Micrographs of MAR-M247 made by Binder Jetting. (a) Polished view showing porosities and carbides; Z-direction indicates the build direction. (b) As-sintered condition with 2.4× magnification, highlighting pores near grain boundaries. (Dahmen et al., 2021)

This limitation of HIP reinforces the need for additional post-processing strategies. Shot peening can improve surface integrity by inducing compressive residual stresses and mitigating

the effect of remaining surface defects. Figure 2-9 illustrates how HIP effectively closes the internal pores, but fails to act on the porosity connected to the surface.

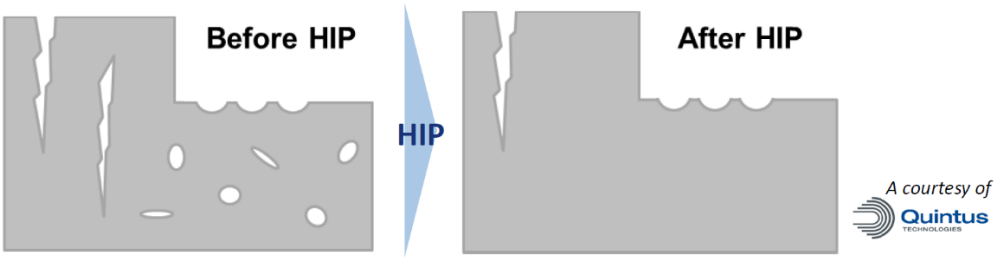

Figure 2-9: Effect of HIP on internal and surface defects. While HIP effectively closes internal pores, it does not remove surface-connected defects, which are critical for fatigue performance (Adapted from Quintus Technologies).

In contrast, wrought steel is almost full dense and shows uniform microstructures, which significantly minimize stress concentration points. As a result, wrought steel exhibits exceptional fatigue resistance, making it a preferred material for high-load applications that demand mechanical reliability and long service life (Bergman; Bergmark., 2003).

Despite the challenges with indirect AM, advancements in post-processing and finishing have shown promise results in reducing porosity. Techniques like SP and HIP have proven effective in densifying surfaces and inducing compressive residual stresses, improving fatigue life (Almangour; Yang, 2016). For instance, SP promotes surface plastic deformation, closing superficial pores and slowing crack propagation (Guagliano, 2001). Similarly, HIP facilitates the closure of internal pores, resulting in near-complete densification (Mostafaei *et al*., 2018).

Despite the challenges with indirect AM, porosity remains a critical factor influencing mechanical performance. Even after sintering, pores act as internal discontinuities that intensify local stress fields under cyclic loading, especially when located close to the surface or exhibiting irregular shapes. These conditions promote crack nucleation and early failure, particularly under contact fatigue. Post-processing techniques, such as shot peening and hot isostatic pressing, have shown promising results by densifying the surface, closing internal pores and inducing beneficial compressive residual stresses (Guagliano, 2001; Almangour; Yang, 2016; Mostafaei et al., 2018).

The interaction between pore morphology and these processing methods plays a critical role in determining the mechanical performance of indirect AM components. With optimized post-processing for a specific application, the performance of a BJT part can approach that of conventionally manufactured components (Holmberg *et al*., 2019).

2.3.2 Density Measurement Methods

Density measurement is one of the main parameters for characterizing metallic materials, especially those obtained by AM. The presence of porosity in materials manufactured by this method can significantly compromise their mechanical properties, affecting fatigue resistance and durability in structural applications (Mostafaei *et al*., 2018). Therefore, the appropriate choice of density measurement method is essential to ensure accurate characterization and avoid underestimation or overestimation of material quality.

Several methods are used for this purpose, ranging from direct approaches, as mass-by-volume measurement, to advanced techniques, as X-ray computed tomography. However, each technique has advantages and limitations, and some approaches may be ineffective when applied to highly porous materials, such as those sintered by BJT (Dahmen *et al*., 2021). In this section, the main density measurement methods will be critically reviewed, considering their applicability, limitations, and regulatory guidelines.

2.3.2.1 Density Measurement by Mass and Volume

The simplest method for determining the density of a material is the ratio between its mass and volume, according to the equation 4.1:

$$\rho = \frac{m}{V} \tag{4.1}$$

Where m represents the mass of the sample and V its volume. Mass can be determined with high precision using analytical balances, while volume is usually obtained by direct geometric measurements, such as using calipers, micrometers or three-dimensional measuring devices (ASTM B962-23, 2023).

This method is widely used in industry due to its simplicity and low cost. However, its accuracy is highly dependent on the uniformity of the material. For conventional processes, where the material is completely dense, the technique provides reliable results, but for materials with high porosity, such as those obtained by BJT, the volume measurement may be inaccurate (Ternero *et al.,* 2021). This is because conventional volumetric measurement methods cannot capture the complexity of internal voids, leading to overestimation of the true density.

Furthermore, variations in sample preparation may introduce uncertainties in the values obtained, since the presence of irregular surfaces and small variations in volume may generate significant errors. Therefore, this method should be used with caution for sintered materials, being more suitable for homogeneous and fully dense materials (ASTM B962-23, 2023).

2.3.2.2 Archimedes Method

The Archimedes method, standardized by ASTM B962-23 and ISO 3369, is one of the most widely used methods for measuring the density of sintered metallic materials and composites. The principle is based on measuring the buoyancy generated by a fluid on a submerged body, according to the equation 4.2:

$$\rho = \frac{m_s}{m_s - m_a} \cdot \rho_{fluid} \tag{4.2}$$

Where m_s represents the dry mass of the sample, m_a is the mass of the submerged sample, and ρ_{fluid} is the density of the liquid used.

According to ASTM B962-23, this method is highly reliable for materials that do not present significant interconnected porosity. However, the standard specifies that its accuracy may be compromised when the sample contains more than 2% of open porosity, since the infiltration of fluid into the connected pores may result in an overestimation of density. To minimize this problem, the standard recommends that the pores be sealed before the test, either by impregnation with oil or another suitable method.

In addition, the accuracy of the technique may be influenced by the adhesion of air bubbles in the sample, requiring rigorous procedures to eliminate these interferences. This can be done by adding humectant agents to the water, reducing the surface tension or removing bubbles by vacuum or ultrasound (Terneiro *et al*., 2021).

Although this method is widely used and accepted, its applicability to parts manufactured by BJT must be evaluated with caution, especially when there is the presence of interconnected open porosity, requiring combination with other techniques.

2.3.2.3 Density Measurement by Image Analysis

Image analysis is a widely used technique for characterizing the density of metallic materials manufactured by processes such as BJT. Unlike traditional volumetric methods, such as Archimedes' principle (ASTM B962-15), which only provide an estimate of the overall density of the material, image analysis allows direct visualization of pores, enabling the identification of their morphology, distribution, and evolution throughout the manufacturing chain (Mostafaei *et al*., 2018; Dahmen *et al*., 2021).

The method is based on the acquisition of high-resolution images obtained by Optical Microscopy (OM), which are digitally processed to segment the porous regions and quantify the volumetric fraction of porosity. The main advantage of this method is that, instead of simply providing a numerical value for density, it enables individual pore evaluation by measuring parameters such as diameter, area, shape factor, and location within the material (Zhu *et al*., 2020). This information is essential for understanding the behavior of the material, since the distribution and shape of the pores can directly affect their mechanical strength and durability in service (Muhammad *et al*., 2022).

Furthermore, the resolution of image analysis is essentially limited by the optical system and the magnification used. Most optical microscopes used in metallography can resolve features down to approximately 0.5 to 1.0 μm, depending on the quality of the optics and the illumination method (Mostafaei et al., 2018). This resolution is compatible with the typical pore sizes observed in BJT components, which typically range from a 1 to 20 microns (Dahmen et al., 2021), ensuring that the technique captures the most important features that influence mechanical performance.

In addition to static porosity measurement, image analysis also allows monitoring the evolution of pores throughout the manufacturing and post-processing chain. During sintering, for example, pores can undergo variations in size and connectivity, and image analysis makes it possible to document these changes at different stages of the process. This monitoring is essential for optimizing manufacturing parameters, as it allows identifying pore closure trends and evaluating the efficiency of thermal and mechanical treatments in densifying the material (Dahmen *et al*., 2021).

Automated image segmentation has been widely explored to increase the accuracy of the technique and eliminate operator subjectivity in quantifying porosity. Studies show that the use of software such as ImageJ, Avizo and MATLAB enables more refined pore segmentation, ensuring reproducible and reliable measurements (Mostafaei *et al*., 2018). Advanced algorithms allow not only the detection of pore contours, but also the differentiation between

interconnected and isolated pores, a crucial aspect for assessing the real density of the material (Ziaee; Crane, 2019).

Another significant advantage of image analysis is the possibility of identifying porosity distribution patterns, analyzing whether the pores are uniformly dispersed or whether there are specific regions of the material with a higher concentration of voids. This information is essential for applications that require high mechanical reliability, as it allows adjustments to the design of the manufacturing process to reduce critical defects. Muhammad *et al*. (2022) demonstrated that pore distribution analysis can be correlated with the material's fatigue strength, allowing more accurate predictions about its durability in service.

However, an inherent limitation of the technique is the fact that the images capture only a two-dimensional section of the material, which can lead to inaccuracies in the quantification of total porosity if the pore distribution is not uniform throughout the sample volume. To mitigate this limitation, it is recommended to acquire multiple images in different regions of the sample or to combine image analysis with computed tomography (Micro-CT), which allows a detailed three-dimensional reconstruction of the material's internal structure (Mostafaei *et al*., 2018; Muhammad *et al*., 2022).

Image analysis has been widely used in literature as an essential tool for measuring density in sintered and binder jetted materials, offering a level of detail that cannot be achieved by conventional volumetric methods. The possibility of directly visualizing and measuring pores, analyzing their distribution and monitoring their evolution throughout the process makes this technique one of the most promising for the study of porous materials and their optimization for high-performance applications (Dahmen *et al*., 2021).

2.3.2.4 Density Measurement by Computed Tomography

X-ray computed tomography (Micro-CT) is one of the most advanced methods for characterizing the density and distribution of porosity in metallic materials manufactured by AM techniques (Dahmen *et al*., 2021). Unlike conventional image analysis, which provides only two-dimensional information, tomography allows a complete three-dimensional reconstruction of the sample, enabling the exact quantification of total porosity and the differentiation between open and closed pores (Zhu *et al*., 2020).

The resolution of is fundamentally determined by the focal spot size of the X-ray source, the pixel size of the detector and the scanning geometry. Laboratory systems typically produce three-dimensional grids with volume elements ranging from 0.5 to 10 μm, which is sufficient

to detect pores relevant to fatigue behavior in binder jetted components, where critical pore sizes often exceed 5 μm (Dahmen et al., 2021; Wang; Miller, 2020.) A volume element, or the three-dimensional counterpart of a pixel, represents a discrete portion of the scanned material and contains the local X-ray attenuation value, allowing digital reconstruction of the internal structure. However, it is essential to distinguish between the nominal size of the volume element and the effective spatial resolution, which can be limited by factors such as beam divergence, detector blur and reconstruction artifacts (Maire; Withers, 2014.).

When configured correctly, Micro-CT allows reliable segmentation of closed and surface-connected pores, surpassing the capabilities of 2D methods in detecting internal defects critical to mechanical performance (Du Plessis *et al*., 2018.). It also allows the quantification of pore volume, pore connectivity and spatial distribution, which are essential for predicting fatigue life in porous metals. In the context of BJT, Micro-CT has been used to evaluate pore evolution during sintering and the effectiveness of SP routes such as HIP (Dahmen et al., 2021). Despite their advantages, limitations such as acquisition time, high equipment cost and partial volume effects persist. Even so, among non-destructive techniques, Micro-CT remains one of the most powerful tools for three-dimensional analysis of porosity in additively manufactured materials (Maire & Withers, 2014; du Plessis et al., 2016).

The principle of the technique is based on the differential absorption of X-rays as the sample is scanned in multiple directions. The acquired data are computationally processed to generate cross-sectional slices, which can be reconstructed into a detailed three-dimensional model (Mostafaei *et al*., 2018). This model allows the extraction of quantitative metrics such as total porosity volume, connectivity between voids and thickness of the material's internal walls (Holmberg *et al*., 2019).

Computed tomography has proven to be particularly useful in the characterization of sintered materials, in which the porosity distribution is not homogeneous and can directly influence mechanical properties (Muhammad *et al*., 2022). In studies on BJT, the technique has been used to evaluate sintering efficiency and the impact of parameters such as temperature and processing time on porosity reduction (Dahmen *et al.*, 2021). In addition, it allows investigating the influence of post-processing treatments, such as SP and HIP, on material densification. Although tomography offers a higher level of detail than other methods, its high cost and the need for specialized equipment limit its applicability in industrial environments. In addition, data interpretation requires advanced software and sophisticated segmentation techniques to differentiate true pores from artifacts generated during image reconstruction (Ziaee; Crane,

2019). For this reason, the technique has been more commonly employed in academic research and advanced studies on the characterization of additive materials.

The combination of computed tomography with other methods, such as image analysis and the Archimedes method, allows a more complete characterization of the density and porosity of metallic materials. While image analysis provides detailed information on the morphology of pores at a microscopic level, tomography allows a global three-dimensional visualization of the internal structure, making it an essential tool for the study of materials with complex porosity (Mostafaei *et al*., 2018).

2.3.2.5 Comparison of Density Measurement Methods

The characterization of the density of materials manufactured by BJT can be performed using different methods, each with specific advantages and limitations. Volumetric methods, such as mass per volume and Archimedes' principle, are widely used, but have limitations when applied to materials with high open porosity or complex internal structure. More advanced methods, such as image analysis and computed tomography (Micro-CT), offer greater precision and detail in the quantification of porosity, allowing direct visualization of voids and their distribution throughout the material. The Table 2-4 below presents a comparison between the main methods reviewed, highlighting their applicability, precision and limitations.

Table 2-4 - Comparison of Density Measurement Methods

Method	Accuracy	Applicability	Advantages	Limitations
Mass-to-Volume	Low	Homogeneous and dense materials	Simple and fast, suitable for non-porous materials where geometric dimensions can be measured accurately	Cannot detect internal porosity, may overestimate density; Sample roughness can lead to overestimation of geometric dimensions
Archimedes (ASTM B962-15)	Medium - High	Sintered materials with up to 2% open porosity	Standardized, complex geometries can be measured	Loses accuracy for materials with high interconnected porosity. Fluids penetrate open pores, altering density readings;
Image Analysis	Medium - High	Porous and sintered materials	Allows visualization and measurement of pores, tracks porosity evolution	Only two-dimensional, depends on sample representativity
Computed Tomography (Micro-CT)	Very High	Porous and sintered materials	Three-dimensional analysis, differentiates open and closed pores	High cost, requires specialized equipment

The mass-volume method, despite its limitations, remains a fast and practical approach when applied to homogeneous and dense materials with well-defined geometric dimensions and minimal surface roughness. However, when used for porous surfaces, it tends to produce artificially high-density values.

Similarly, Archimedes' principle is effective for moderately porous materials, but its accuracy decreases when fluids infiltrate interconnected pores, artificially increasing the measured density. Furthermore, bubble formation due to rough surfaces can distort the measurement, making it necessary to follow rigorous degassing and wetting procedures to improve repeatability.

On the other hand, image analysis and computed tomography allow a more accurate and detailed assessment of porosity, providing direct visualization of voids. Image analysis allows quantitative measurement of pores and tracking of their evolution, making it highly suitable for materials with complex porosity distributions.

Computed tomography offers the highest accuracy, as it reconstructs a complete three-dimensional model of the internal structure, allowing differentiation between open and closed porosity. However, due to the high cost, high time consumption and complexity of computed tomography, image analysis emerges as a viable alternative for density and quality control studies, especially when combined with automated segmentation algorithms to minimize operator influence.

2.3.3 Effects of Shot Peening Techniques on Fatigue Performance

Shot Peening (SP) is a surface treatment widely used in the manufacturing industry to improve the fatigue performance of mechanical components. This process induces compressive residual stresses on the surface of materials, retard crack nucleation and propagation. SP also improves surface hardness and, in some case, can reduce roughness, essential factors for increasing the service life of mechanical components subjected to cyclic loads (Almen; Black, 1963). While SP has been extensively applied in conventional manufacturing processes, its potential in AM, particularly in indirect techniques as BJT, has gained attention due to its ability to address porosity and surface integrity challenges. Criscuolo *et al.* (2023) experimentally investigated the use of SP for localized densification of surfaces in components manufactured by iSLS, highlighting the influence of peening parameters on density and residual stress state.

In the context of conventional gear manufacturing, processes as carburizing, quenching, and grinding are combined to produce components with high mechanical strength and durability. However, these steps can induce tensile residual stresses and surface irregularities, which negatively impact fatigue life. SP is integrated into the manufacturing chain to mitigate these issues. Through surface impaction with small metallic or ceramic particles, SP creates a compressive residual stress layer, reducing stress concentration points and improving fatigue

resistance. The experimental studies of Ünal *et al.* (2022) and du Plessis *et al*. (2019) showed that the application of SP can significantly reduce residual stress heterogeneity, improving surface uniformity and increasing fatigue resistance. SP has been shown to be effective in mitigating bending and contact fatigue failures in gears subjected to high levels of load.

Among the several manufacturing alternatives to control fatigue behavior, shot peening has stood as a widely accepted method for inducing beneficial surface residual stresses. The survey presented by Rego (2022) shows that fatigue life in gear root bending can be improved by 20% to 76%, while flank contact fatigue life increased from 10% to 55%. These improvements reinforce the importance of considering residual stress fields in gear design, particularly in regions subjected to rolling contact fatigue as seen in Figure 2-10.

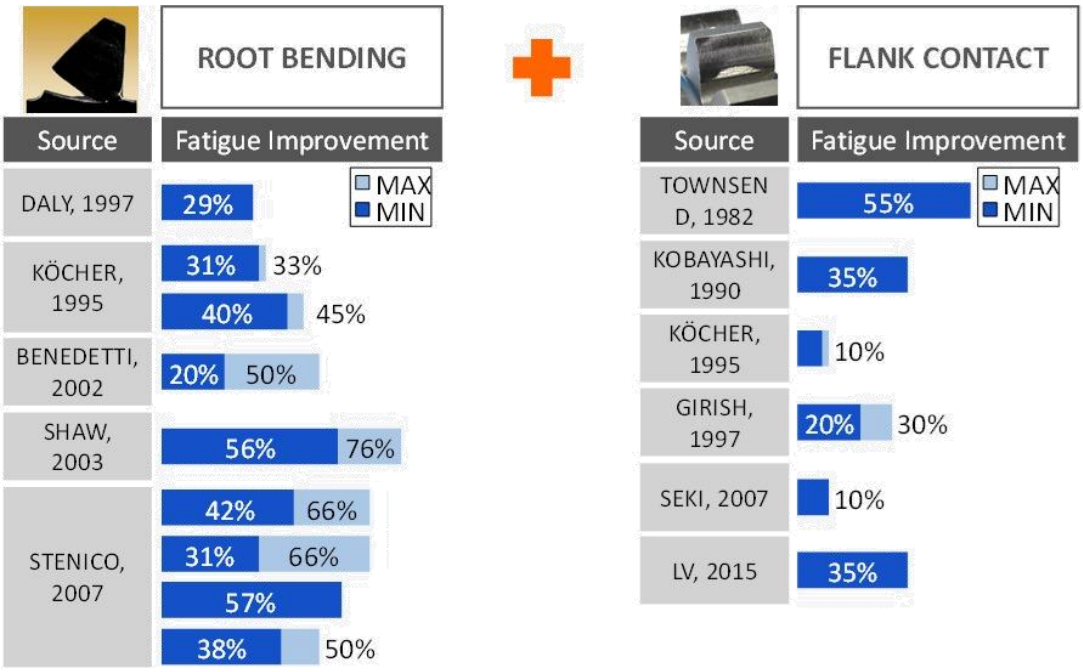

Figure 2-10: Effect of shot peening on fatigue improvement in gears. Survey compiled by Rego (2022) showing the range of fatigue life improvements observed in root bending and flank contact due to the introduction of compressive residual stresses.

Peyre *et al.* (1995) confirm the benefits of SP, especially in increasing fatigue resistance in metallic materials subjected to high load cycles. Okuniewski *et al.* (2024) highlighted that SP not only improves mechanical strength in alloys as Ti6Al4V, but also optimizes tribological and corrosion resistance properties, highlighting the importance of SP in modifying surface integrity.

In AM, especially in indirect techniques as BJT and iSLS (Indirect Selective Laser Sintering), challenges as intrinsic porosity and lower mechanical strength of components require innovative solutions. Criscuolo *et al*. (2023) explored how SP can densify surfaces of parts manufactured by iSLS, using a numerical and experimental approach to investigate the peening parameters and their impact on surface density, surface integrity, and residual stress state. However, the authors also observed that the energy required for pore closure during SP is so high that surface plastic deformation becomes predominant, relegating the induction of compressive residual stresses to a secondary role. As a result, the compressive residual stress values achieved in the samples are significantly lower than those observed in materials manufactured by conventional methods, as Figure 2-11 shown. Suwanpreecha *et al.* (2024) also demonstrated that SP, when combined with thermal treatments as aging, can generate significant improvements in fatigue performance, inducing surface nanocrystallization and compressive residual stresses.

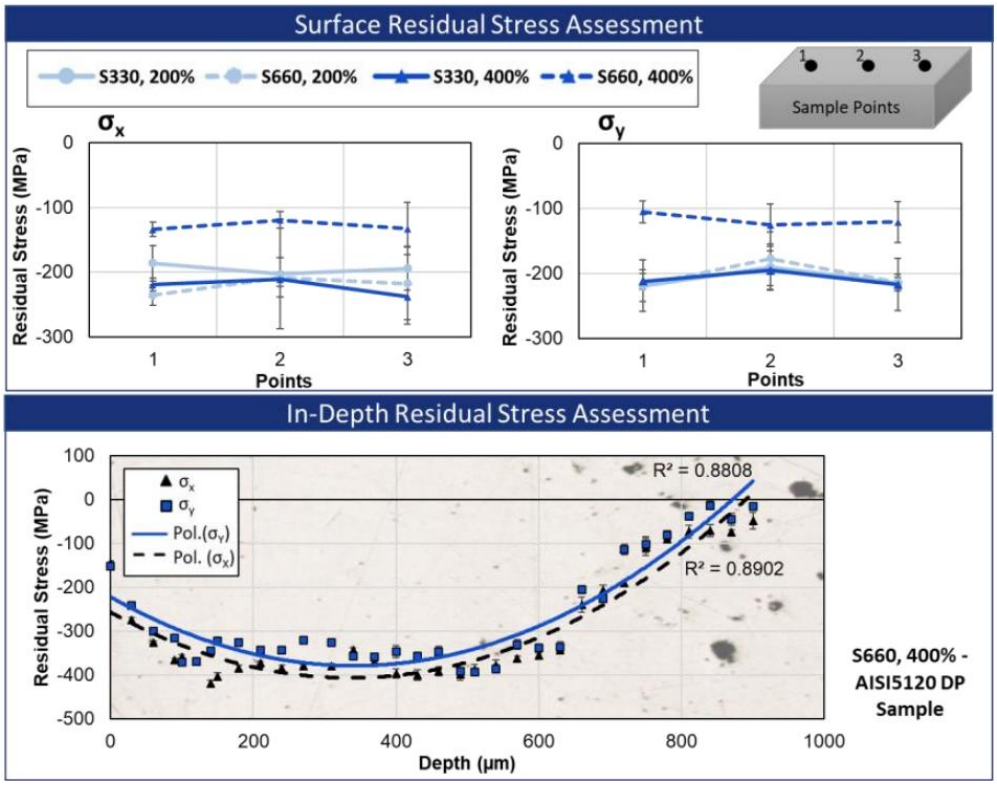

Figure 2-11 - Residual stress measurement was conducted on the surfaces and profile of densified samples (Criscuolo *et al*., 2023).

Another important aspect highlighted by Peyre *et al*. (1995) is the detailed analysis of the SP conditions, including the mechanical interaction generated by the shock waves and their

influence on the residual stress field. It was demonstrated that SP, when applied in an optimized manner, can reach significant depths of compressive stresses, contributing to the improvement of fatigue resistance and surface integrity. Okuniewski *et al*. (2024) reinforce that SP, combined with processes as electropolishing, offers an even greater potential for improvement in components manufactured by both conventional and AM methods.

Although there are numerous studies on the effects of SP in both conventional and AM manufacturing chains, there is an important gap in the literature regarding BJT. There are no articles that explore in an integrated application of SP, first as a method to promote surface densification while also, later in the production chain, to induce compressive residual stresses around the remaining pores, thereby preventing their opening under service conditions. This approach could provide significant advances in the production of components with high mechanical performance, combining the design flexibility of AM with targeted SP strategies.

2.4 State of the Art: Surface Finishing and Fatigue Behavior in Binder Jetting Components

This chapter presents a review of the current scientific literature addressing the influence of post-processing on the mechanical performance of porous metallic materials, with an emphasis on those produced by BJT. The main objective is to understand how surface treatments, particularly SP, can mitigate the limitations imposed by intrinsic porosity and improve fatigue resistance, especially under contact loading conditions. While the focus is on additively manufactured components, the scope also includes relevant findings from powder metallurgy (PM) and other sintering-based technologies, given their comparable porous microstructures and mechanical behavior.

Given the layer-by-layer nature of BJT and its sintering-based consolidation, components produced by this process exhibit high levels of porosity and irregular pore morphologies. These characteristics are known to adversely affect fatigue life, especially in high-load applications. The literature reviewed includes various metallic alloys, ranging from stainless steels and nickel-based superalloys to titanium and iron-based systems, highlighting how different material systems respond to similar post-processing strategies. SP techniques have been explored across these materials as potential methods for improving surface integrity, modifying residual stress states, and ultimately enhancing mechanical performance. While material-specific effects are discussed where relevant, the focus of this review remains on

understanding the role of SP in post-processed porous metallic components, regardless of exact alloy composition.

To evaluate the relevance and coverage of the topic in the literature, a bibliometric analysis was conducted using the Scopus database. Three groups of keywords were used in the search: “Binder Jetting OR Binder Jet,” “Finishing OR Finish,” and “Fatigue.” As shown in Figure 2-12, the search returned only a single study directly addressing the relationship between BJT, finishing techniques, and fatigue behavior. Furthermore, the inclusion of the keyword “Gear” yielded no relevant studies, highlighting a significant gap in the literature on contact fatigue performance in BJT components with complex post-processing chains.

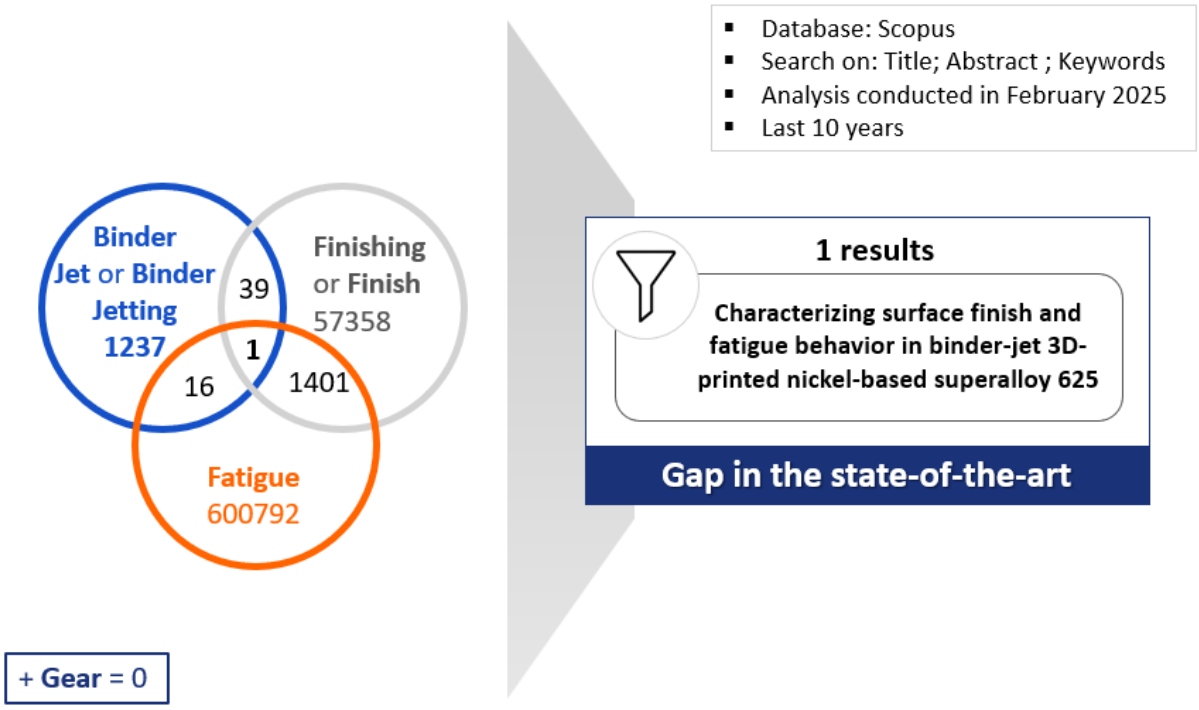

Figure 2-12: Bibliometrics research on BJT, finishing techniques and fatigue resistance.

Although no comprehensive studies were found focusing specifically on post-processing chains for BJT under rolling contact fatigue (RCF), some foundational works provide relevant insight into the behavior of porous metals. In the bibliometric analysis, the term “finishing” was intentionally adopted instead of more specific terms, such as “shot peening”, to cover a wider range of surface modification techniques potentially relevant to BJT components. This decision was made to avoid restricting the search too narrowly and ensured the inclusion of studies using a variety of finishing strategies, even if not explicitly labeled as “peening”. Holmberg et al. (2019) investigated the rolling contact fatigue life of powder

metallurgy steels with varying porosity levels, samples with different densities, 6.8 g/cm³ and 7.15 g/cm³, were tested, as well as a reference steel with full density, with centerless grinding and superfinishing. Their results demonstrated that density is the dominant factor limiting fatigue performance, with sintered steel of 7.15 g/cm³ having four times more fatigue life than 6.8 g/cm³ under the same contact pressure, and fatigue cracks initiating at subsurface pores located approximately 100 µm from the surface and propagate to the surface leading to material failure as presented in Figure 2-13. Despite the differences in surface finish, no significant influence was observed on fatigue life under purely rolling contact. While this study focused on powder metallurgy and not BJT, its relevance lies in its experimental methodology and emphasis on density as a fatigue-driving parameter.

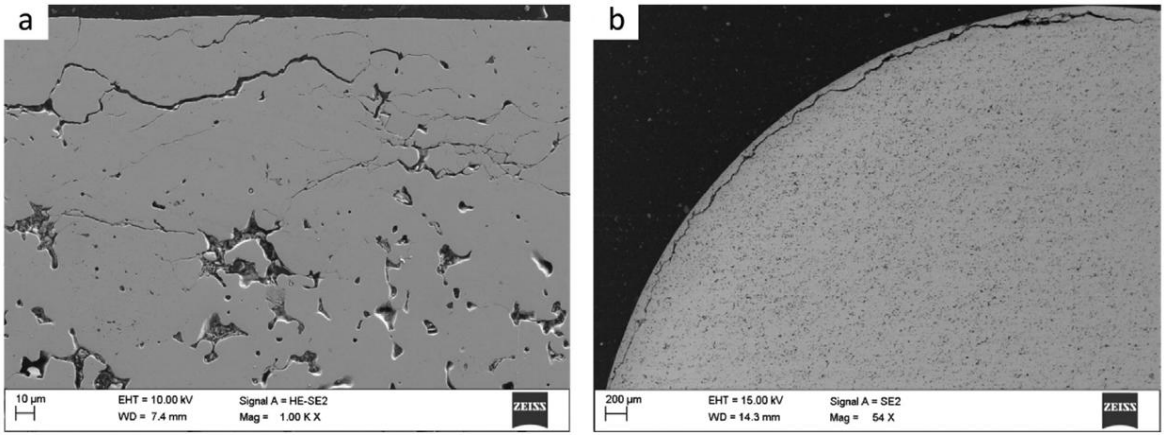

Figure 2-13 - SEM images of cross-sections reveal: (a) an extensive network of cracks beneath the surface and (b) a significant crack propagating approximately one-quarter of the sample's circumference after failure, occurring after 5×10^6 load cycles (Holmberg *et al*. 2019).

In the context of BJT, Mostafaei et al. (2018) evaluated the fatigue behavior of alloy 625 specimens produced via BJT under reversed tension-compression loading. Their results indicated that grinding significantly improved fatigue life by reducing surface roughness, increasing surface hardness, and inducing compressive residual stress as seem in Figure 2-14. However, the study did not address rolling contact fatigue or utilize shot peening for densification or stress induction, making it only partially relevant to the objectives of this work.

	111			200			220			311		
	2θ	d-spacing	FWHM	2θ	d-spacing	FWHM	2θ	d-spacing	FWHM	2θ	d-spacing	FWHM
As-sintered	43,56	2,08	0,18	50,44	1,81	0,1	74,67	1,27	0,39	90,52	1,08	0,96
Ground	43,41	2,09	0,43	50,37	1,81	0,55	74,32	1,28	0,55	90,16	1,09	1,15

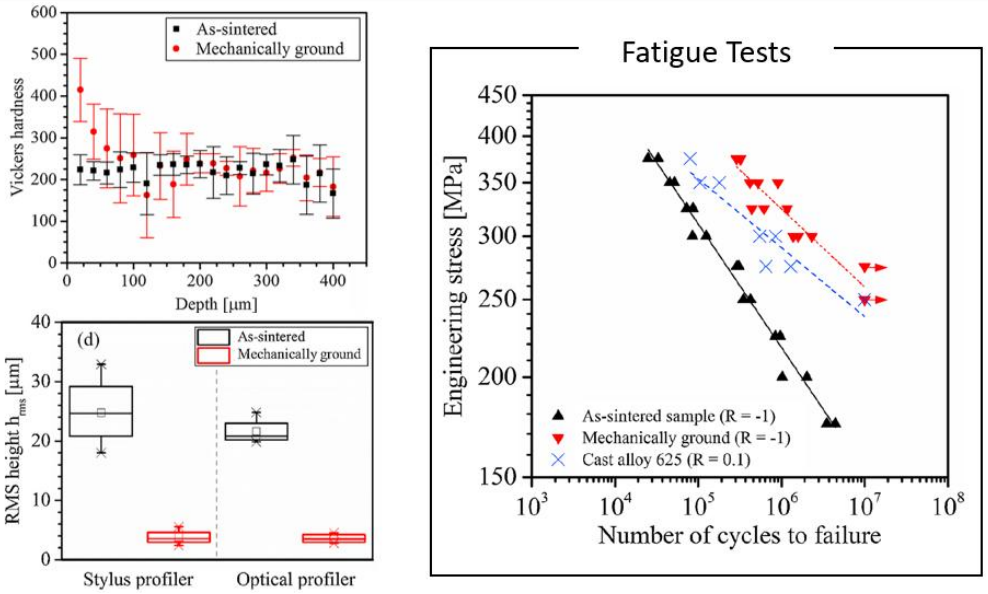

Figure 2-14: Results comparing as-sintered and mechanically ground samples in relation to microhardness, roughness, residual stress and fatigue (Mostafaei et al. 2018).

Muhammad et al. (2022) analyzed the microstructural variability of binder-jetted 316L steel under low-cycle fatigue conditions besides how different powder particle size distributions and post-processing heat treatments affect the microstructure and failure mechanisms. Findings indicate that primitive porosity lines, formed during the manufacturing process, are the main factor compromising fatigue life. These lines lead to the formation of elongated pores during sintering, reducing fatigue resistance. It has been shown that a minimum level of green density is required to minimize the occurrence of this interconnected porosity.

Although the study demonstrated that hot isostatic pressing (HIP) is effective in eliminating internal porosity, it also leads to significant grain growth, which can reduce the mechanical strength of the material and compromise fatigue resistance. Furthermore, HIP has a well-documented limitation, it is ineffective at closing surface-connected pores, particularly those exposed to the environment or located at geometric transitions. These open pores act as preferential sites for crack nucleation, especially under cyclic contact loading.

This observation underscores the need for alternative post-processing strategies capable of modifying the near-surface condition without detrimental microstructural coarsening. Shot peening (SP) emerges as a promising approach, offering both superficial densification and the ability to induce compressive residual stresses, particularly in the top 100–300 µm of the surface

layer, where fatigue cracks in porous materials often originate. These benefits can be achieved without the thermal side effects associated with HIP.

A more direct contribution to the current work is found in the study by Criscuolo et al. (2023). who investigated the use of shot peening to densify the surface of components produced by indirect Selective Laser Sintering (iSLS). Experimental data shows that SP densification varied according to the process parameters, reaching densified layers up to 943 µm deep. Increasing the coverage and size of the medium results in higher surface density but also increases roughness and reduces the induced compressive residual stresses, as shown in Figure 2-15. This is because part of the impact energy was dissipated in the plastic deformation required to close the pores, rather than being converted directly into residual stresses. In contrast to the study by Muhammad et al. (2022), which showed that HIP eliminates porosity but promotes excessive grain growth, SP proved to be an effective alternative, increasing surface density without compromising the material's microstructure.

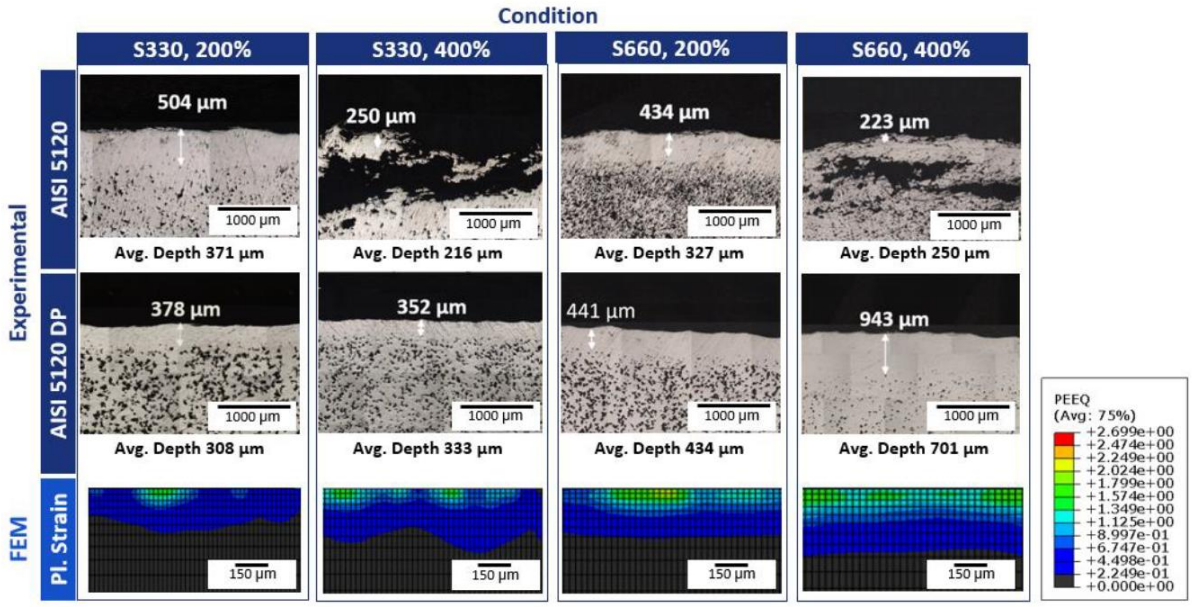

Figure 2-15: Matrix of representations (microscopy and simulation) of cross-sections of the densified surfaces. The first and second row refer to the experimental samples and the third to the FEM model. Each column represents one condition (Criscuolo et al., 2023).

Moreover, SP is a mechanical surface treatment concentrated on the surface layers, precisely where fatigue cracks are known to nucleate in gear components subjected to cyclic contact loads. This makes it particularly suitable for applications such as rolling contact fatigue, where subsurface shear stresses are highest in the first few hundred micrometers from the

surface. While the materials and AM route differ from BJT, the study provides valuable insight into the trade-offs between densification and stress induction in porous materials.

Suwanpreecha et al. (2024) further demonstrated that SP combined with aging heat treatments can generate nanocrystallized surface layers and significant compressive stresses, improving fatigue behavior in 17-4PH stainless steel produced by material extrusion. Although the AM process is different, the base material and the role of SP align closely with the scope of the present study.

Despite the growing attention to finishing treatments in AM, there is still a clear lack of studies investigating the combined use of SP for surface densification and residual stress induction in BJT. Even fewer papers explore the integration of multiple shot peening stages in the same post-processing chain or evaluate how this layered approach influences fatigue performance under rolling and sliding conditions.

Existing literature consistently identifies porosity as the main factor for crack initiation in porous metallic materials. Although HIP is a widely adopted strategy to reduce internal porosity, it often promotes grain growth, which can compromise fatigue strength, especially in surface-driven mechanisms. In addition, HIP is ineffective at eliminating surface-connected pores, which are often responsible for early-stage crack nucleation under contact loading. In contrast, shot peening operates directly on the surface region, which is precisely where fatigue failures usually initiate in gear components. By inducing plastic deformation, SP not only promotes localized densification, but also introduces compressive residual stresses in the upper surface layers, typically in the first few hundred micrometers, without modifying the overall microstructure. This dual function makes SP a promising alternative to conventional densification techniques, particularly when strategically applied in a multi-stage post-processing route for BJT parts.

This research aims to address this gap by systematically investigating the effect of dual stage shot peening on the surface integrity and fatigue resistance of BJT components. The originality lies in combining SP for densification and for residual stress induction within the same processing chain, evaluating their synergistic contribution to the mitigation of crack initiation and propagation under RCF.

The influence of finishing treatments on pore morphology modification and fatigue performance improvement remains inadequately understood. Addressing this gap, the subsequent chapter outlines the research objectives and hypotheses that will guide this study,

with a focus on systematically evaluating SP as a post-processing technique for BJT components.

3 Objective and Approach

The primary objective of this research is the assessment of the impact of SP on the surface integrity of components manufactured through BJT, specifically focusing on how SP exert influence on porosity morphology and compressive residual stress. This study aims to systematically assess how SP modifies the surface integrity properties of hardness, roughness, residual stress and porosity. By understanding the correlation between the SP and the surface integrity state, this study allows to design of an optimized manufacturing chain oriented to densification and residual stress state, which can improve the overall fatigue strength of binder jetted components. Figure 3-1 summarizes the hypothesis, objective, and approach of this study.

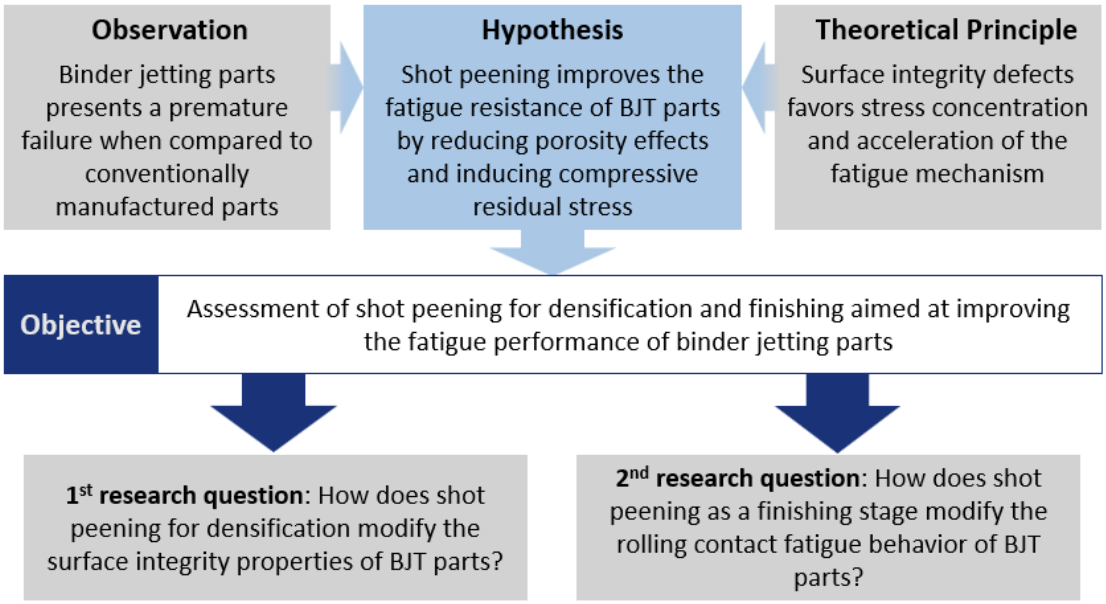

Figure 3-1 - The basis of the hypothesis, objective, and approach

In this research framework, two pivotal questions are delineated to direct the investigative process and systematically organize the outcomes:

1st Research question: How does shot peening for densification modify the surface integrity properties of BJT parts?

2nd Research question: How does shot peening as a finishing stage modify the rolling contact fatigue behavior of BJT parts?

The inherent characteristics of BJT, particularly its high porosity, present significant challenges for the mechanical integrity of manufactured components under fatigue loading conditions. Open and interconnected pores act as stress concentrators, weakening the material's surface integrity and facilitating crack initiation under cyclic loading. The lack of material continuity in these regions leads to localized stress amplification, accelerating the degradation of mechanical properties and compromising structural reliability over time. To address these surface integrity challenges, this study investigates SP as a densification method, as it is applied to close surface-connected pores. The plastic deformation caused by SP increases the densification of the material and modifies the surface roughness.

As a finishing stage, SP also plays a critical role in improving fatigue performance. By redistributing residual stresses, SP helps mitigate tensile stress accumulation, reducing the risk of crack propagation and improving overall fatigue resistance. The combination of these effects is expected to significantly enhance the durability and mechanical stability of BJT components subjected to repeated loading.

To validate these effects, rolling contact fatigue tests will be conducted to quantify the influence of SP on mechanical performance. The study aims to establish a quantitative relationship between densification, residual stress distribution, and fatigue resistance, offering a systematic assessment of shot peening parameters to enhance post-processing strategies for BJT components.

The evaluation of SP for densification and residual stress induction on surface integrity, specifically analyzing pore closure, residual stresses, and their correlation with fatigue behavior, constitutes the core objective of this study. By systematically investigating how SP modifies these properties, this research defines a strategy that enhances the mechanical reliability of BJT components, addressing a key limitation of this additive manufacturing technique.

Furthermore, this study contributes to the development of an optimized SP strategy for BJT, improving its applicability in demanding engineering fields, such as electric vehicle drivetrains and high-performance gear systems. The insights gained will provide valuable information regarding failure mechanisms in BJT, particularly under rolling contact fatigue conditions. By analyzing surface integrity evolution and its impact on fatigue performance, this research helps bridge the technological gap between conventional manufacturing and BJT. As consequence, it is expected that it will support the advancement of robust and durable components for industrial applications. The conclusions drawn are bounded by the

experimental conditions investigated, such as the material, the failure mode and the loading spectrum. They delineate the applicability of the proposed post-processing strategy, while they can also rise insights for further applications.

4 Materials and Methods

4.1 Overall Experimental Scope

Among the possibilities offered by AM and its post-processing, several analyses can be performed from different points of view within the gear manufacturing chain. The study presented here focuses on martensitic stainless steel, 17-4PH (equivalent to AISI 630), and evaluates three different post-processing chains. Route A omits shot peening entirely, relying only on heat treatment and grinding. Route B applies shot peening before aging, aiming primarily at densification. Route C builds on Route B by adding a second shot peening step after heat treatment to induce highly compressive residual stresses. All three routes include grinding and H900 heat treatment. The overview of these post-processing routes is illustrated in Figure 4-1.

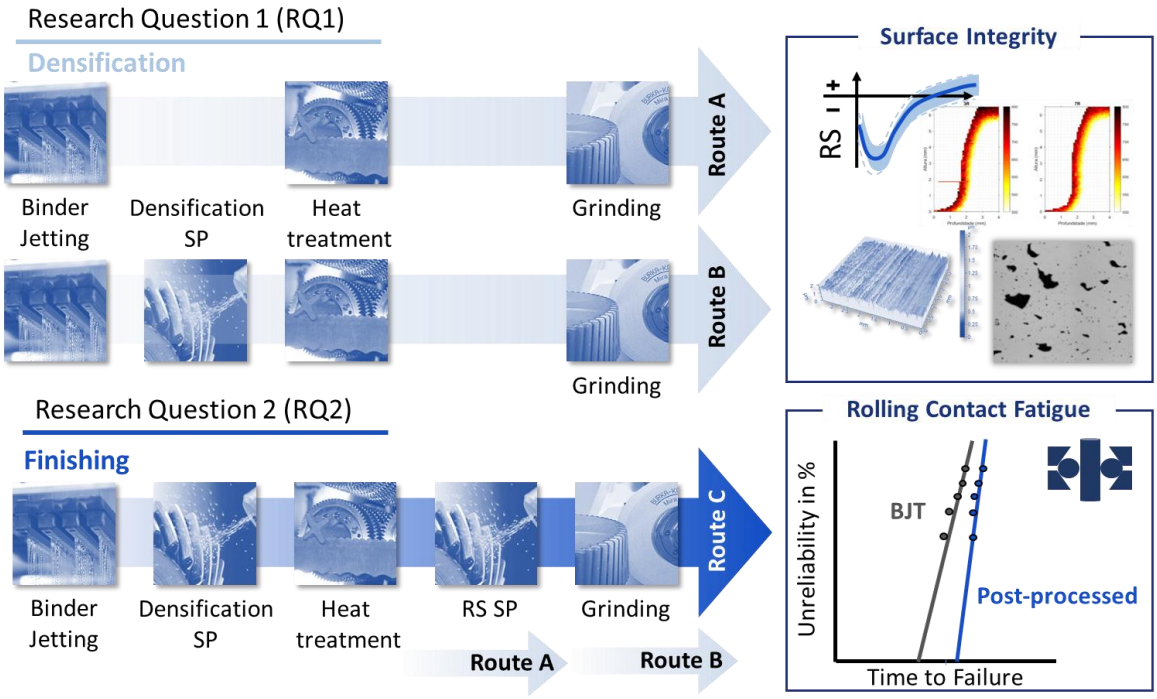

Figure 4-1: Overview of the post-processing routes evaluated for 17-4PH steel, comparing chains with and without SP. The assessments focus on surface integrity and rolling contact fatigue performance.

The 17-4 PH stainless steel was selected due to its combination of high mechanical strength, corrosion resistance and compatibility with AM and post-processing techniques. Although it is not normally used in high-torque industrial gear systems, 17-4 PH has proven to be suitable for gear components that operate under moderate loads and in environments where corrosion or aggressive media are present. Notable examples include gears in power tools, manufactured by powder compression molding for high dimensional accuracy and wear resistance (Neway Precision, 2025), as well as sun gears in planetary systems for drilling equipment, produced through extrusion-based metal AM and selected for their strength and resistance to environmental degradation (Proto3000, 2025). These applications illustrate the alloy's effectiveness in functional gear mechanisms, where both surface integrity and durability are critical. In addition, the alloy's precipitation hardening capability allows mechanical properties to be tailored to meet fatigue performance requirements in demanding conditions.

The base material used in the process was obtained by gas atomization, ensuring a spherical morphology which is essential for the correct packing of the powder and its fluidity within the deposition system. The particle size distribution was selected to align with BJT requirements, with particles mainly in the range of 9.2 µm to 25.4 µm, as depicted in Figure 4-2. Particles above 35 µm can hinder powder bed compaction and lower the final part's resolution, whereas too many fine particles below 9.2 µm can cause agglomeration and difficulties in material reuse (Klee et al. 2023).

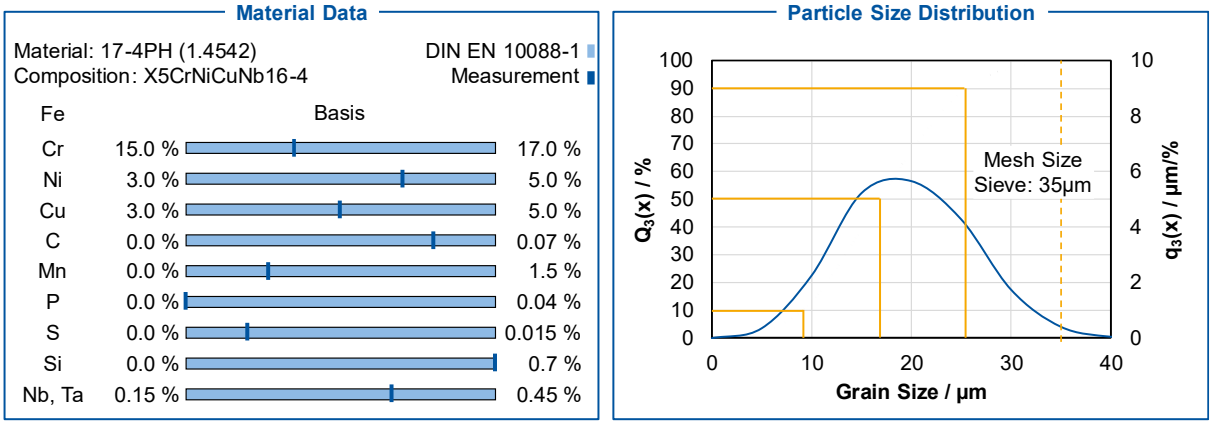

$Q_3(x)$ / %	10	50	90
Particle Size / µm	9.2	16.9	25.4

Figure 4-2: Powder analysis - control variables for the optimization of binder jetting (Klee; Brimmers; Berg, 2002)

All processes and parameters were carefully planned and kept constant to make sure that any differences seen during fatigue testing were caused by the different post-processing chains. Also, test specimens from the three chains were produced at the same time, to mitigate different thermomechanical loading conditions for the sample. Additionally, they were clearly identified to enable proper investigation in case of eventual variations between batches.

The samples were built using the BJT process on a *Digital Metal DM P2500* machine. After deposition, the samples were cured, debinded, and sintered. Next, pre-machining was done to adjust the geometry and surface of the specimens, followed by SP for densification.

The geometry of the printed specimens was designed as a solid cylinder, with 80 mm in length and 10 mm in diameter, printed horizontally to minimize distortion during sintering and ensure dimensional stability. This configuration also allows the application of surface treatments and fatigue tests under well-controlled contact conditions. A schematic drawing is presented in Figure 4-3, highlighting the regions of interest for post-processing and testing.

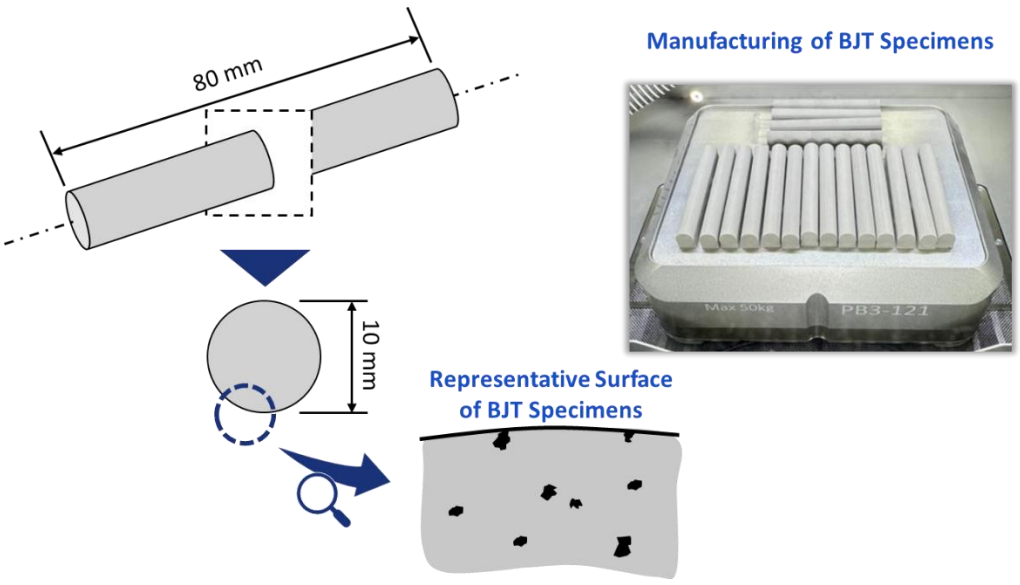

Figure 4-3: Geometry of BJT specimens and representative area for densification, alongside an image of the manufactured batch.

Finally, the specimens were heat treated using the H900 process and then ground. This production chain was chosen to study how porous materials treated with SP behave under rolling contact fatigue.

Route C is based on Route B, but adding another SP step after the heat treatment. This second SP step was conducted to induce a compressive residual stress state after the material

was already hardened and densified. This process was used to study how residual stress affects pre-densified materials and help to avoid primary failure modes.

Route A production chain omits SP, using only H900 heat treatment and grinding. This serves as a baseline to isolate the effects of SP by assessing material performance under rolling contact fatigue without shot peening.

Alongside these three production chains, a conventional manufacturing route was included for comparison with the BJT samples. This traditional chain involves 17-4 PH stainless steel processed through standard manufacturing methods, followed by SP to induce compressive RS, heat treatment using the H900 process, and final grinding. This reference is used to benchmark the performance of BJT-produced components against traditionally manufactured counterparts.

All manufacturing steps were carried out by industrial partners. The entire campaign of surface integrity assessment and fatigue testing of specimens was performed at CCM-ITA. The parameters for each test were set based on the specific features to be studied, while keeping consistency across the manufacturing steps. Selecting standard manufacturing processes and parameters, along with using the same batches for all specimens, helped reduce the number of test repetitions needed.

Since manufacturing processes involve high thermal and mechanical loads, components may experience different RS states during production. As shown by Rego (2016), the RS state created at each stage of the manufacturing process can affect fatigue life. Therefore, it is essential to understand how RS states change throughout each process.

Due to characteristics implicit in the BJT manufacturing process and its pore formation, the first SP step mainly causes plastic deformation, leading to surface densification. To better understand this behavior, pore morphology was studied using image techniques to show differences between the manufacturing chain.

The experimental plan for this study is summarized in Figure 4-1. The investigation focuses on a production chain for gears made with AM. Based on existing studies, it is also possible to estimate some aspects of dynamic performance, considering the final surface integrity of the parts.

Detailed manufacturing and post-processing procedures, including printing parameters, sintering profiles, and shot peening strategies, are described in Sections 4.2 and 4.3, respectively.

4.2 Specimens' Manufacturing

The samples were manufactured by BJT using the *Digital Metal DM P2500* printer and 17-4 PH stainless steel metal powders. The geometry of the samples was designed to be 80 mm long and 10 mm in diameter, all of which were printed in a horizontal position to assure greater dimensional stability and minimize distortions during sintering.

The printing process began with the controlled application of the powder, which was distributed layer by layer in the printer's buildbox. With each new layer, a deposition head selectively applied C20, a liquid binder based on organic solvents and ethoxylated surfactants, promoting adhesion between the particles and the formation of green parts. The layer thickness parameter was set at 42 μm, with a powder deposition speed of 50 mm/s and application of the binder set at dark level 1 (66.67% of the maximum possible). These parameters were selected based on the optimized process configuration described by Klee et al. (2023), which demonstrated that a 42 μm layer thickness combined with two-directional powder spreading at 50 mm/s and dark level 1 binder application ensures sufficient green density of approximately 51% with low variability, enhancing sintering reliability and minimizing crack formation. As no heat is applied during this stage, the parts could be handled as soon as the printing cycle was completed.

After printing, the samples underwent a thermal curing process to stabilize the binder bonds and prevent delamination during the following stages. This curing process was carried out in a *Digital Metal* curing furnace, under a controlled air atmosphere. The thermal cycle followed a gradual heating ramp of 10 hours up to 200°C, followed by an isothermal plateau of 8 hours at 200°C, ensuring partial removal of the solvent and greater mechanical resistance to the green parts This thermal profile was selected based on the standard *Digital Metal* workflow described by Klee et al. (2023), which ensures uniform binder curing, minimizes internal stresses, and prevents surface cracking before debinding.

Once curing was complete, the samples were removed from the powder bed and transferred to the debinding, which is essential to eliminate organic residues before sintering and avoid internal defects. This process was carried out in a *Carbolite Gero PDS 120* furnace, operating under an inert atmosphere of argon, preventing premature oxidation of the material. The thermal cycle consisted of a heating ramp of 2°C/min up to 500°C, followed by a 5-hour plateau at 500°C, with controlled cooling to 200°C and subsequent natural cooling inside the furnace.

The final stage of manufacturing was sintering, which was carried out to consolidate the metal particles and achieve a dense, homogeneous microstructure. The samples were treated in a *Carbolite Gero HTK 8 MO* furnace, under a controlled hydrogen atmosphere (H_2 5% in argon), promoting the removal of residual oxides and improving diffusion between the metal particles. The sintering thermal cycle followed a heating ramp of 5°C/min up to 1305°C, with a plateau time of 13 hours at this temperature to ensure complete coalescence of the particles. After this period, the samples were cooled in a controlled manner to 200°C under an inert atmosphere, followed by natural cooling inside the furnace.

During sintering, the samples underwent a predictable volumetric shrinkage due to the fusion of the metal particles. This high level of densification guarantees superior mechanical properties and a homogeneous structure suitable for subsequent contact fatigue studies.

4.3 Post-processing Stage

4.3.1 Soft Machining

Due to the distortions caused mainly by the sintering process, soft machining is necessary to adapt the test specimens dimensionally and geometrically for the subsequent stages of the manufacturing chain. This process was performed on a lathe, using low material removal rates, with the sole purpose of adjusting the test specimens.

The roughing stage was carried out at a cutting speed of 500 rpm with a feed rate of 0.299 mm/rev and a cutting depth of 0.2 mm. The finishing stage followed at 630 rpm with a feed rate of 0.135 mm/rev and a reduced depth of cut of 0.1 mm (Groover, 2013). This machining step was applied identically to all chains, ensuring that any potential interference affects them equally and does not compromise the comparison of downstream processes.

Since a grinding process is planned at the end of the chain, the resulting geometry after turning is not considered definitive. It is essential to maintain an adequate stock for removal during the grinding process. In this study, a stock allowance of 150 µm was utilized to account for the plastic deformation caused by the shot peening process, ensuring that sufficient material remains for the final grinding stage. This allowance surpasses the 80 µm typically recommended by Davis (2005) for gear manufacturing processes, owing to the more pronounced surface effects observed in additively manufactured components.

This process was designed to be predominantly mechanical, with low heat input. Furthermore, the resulting microstructure after this stage is expected to remain similar to that observed after sintering.

4.3.2 Shot Peening for Densification

The first SP process was used to increase the surface density of the samples. This mechanical treatment was performed using S660 steel media with 400% covering levels. A larger shot size was selected due to its larger impact area, allowing for greater plastic deformation of the surface. The selection of these parameters was guided by the experimental results presented by Criscuolo (2024), who demonstrated that higher coverage levels and larger media sizes lead to increased densification depth and improved surface integrity in AM steels. These conditions were selected to investigate the impact of increased density on surface compaction, promoting greater resistance to crack nucleation in subsurface layers, thus increasing the fatigue resistance of the treated samples.

The media used had diameters ranging from 1.40 to 2.0 mm. They were propelled with a controlled pressure of 6 bar, featuring an Almen intensity of 1.27 mm A, evaluated according to the procedures outlined in SAE J443 (2003). They were assessed through using a type C Almen strip. This setup was planned to provide sufficient kinetic energy to cause localized plastic deformations on the surface of the samples, without compromising the structural integrity of the material. The variation of parameters also allowed the evaluation of the influence of impact intensity on surface properties, such as roughness, densification and distribution of residual stresses .

The samples were fixed in a 3-jaws chuck inside the machine, as seen in Figure 4-4, thus enabling semi-automated use and rotation of the component during the process, homogenizing the SP across the entire surface of the test specimen.

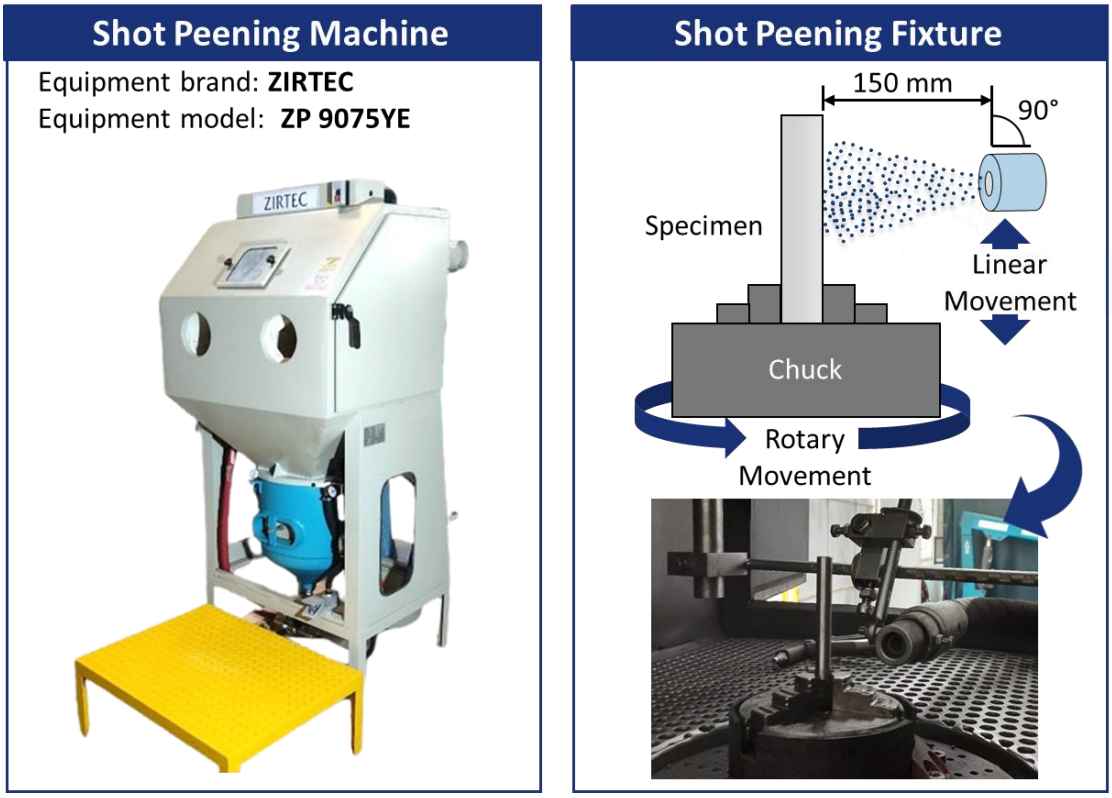

Figure 4-4: Shot peening machine and schematic of the shot peening setup used for specimen processing.

In addition to the primary test condition described above, preliminary tests were conducted using S460 steel specimens to evaluate the effect of smaller media on the surface response. These tests aimed to understand the influence of media geometry on surface densification.

Complementary tests were also carried out at a reduced operating pressure of 3 bar, using S660 and S460 17-4PH specimens, as seen in Table 4-1. These tests aimed to assess the sensitivity of the surface response to impact energy, allowing a comparative analysis of how lower pressure intensities influence porosity closure and induced residual stresses. Although they were not used in the final processing conditions, the results of these tests were valuable in defining the parameter window and verifying the reproducibility of surface effects under varying SP parameters.

Table 4-1 - Summarizes the preliminary shot peening conditions tested to evaluate the influence of pressure and media size on surface densification

Peening Media	Diameter (mm)	Pressure (Bar)	Coverage (%)	Nozzle Angle	Distance (mm)
S460	1.18 to 1.40	3	400	90°	150
S660	1.40 to 2.00	3	400	90°	150
S460	1.18 to 1.40	6	400	90°	150
S660	1.40 to 2.00	6	400	90°	150

4.3.3 Heat Treatment

The material used in this study was 17-4 PH stainless steel, known for its high mechanical strength and corrosion resistance. The samples, whose specific dimensions and geometries were previously defined, were subjected to a heat treatment consisting of solubilization followed by H900 aging. The H900 condition was selected because of its balance between hardness and toughness, providing greater fatigue resistance and dimensional stability, essential properties for rolling contact applications. This process aims to improve mechanical properties through controlled artificial aging. An electric furnace with precise temperature control was used to perform the heat treatment (Pellegrini *et al.,* 2023).

Preliminarily, the samples were subjected to a solubilization treatment before aging. This process consisted of heating the samples to 1040 °C with a tolerance of ± 5 °C, followed by holding them at that temperature for 60 minutes. After this step, rapid cooling in air was performed to promote the formation of a homogeneous microstructure and ensure the dissolution of the hardening precipitates. This procedure is essential to reestablish the solubility of the hardening elements before aging. (Merlin *et al.*, 2024).

As the available heat treatment furnace did not have a protective atmosphere, an alternative solution was implemented to prevent oxidation during exposure to high temperatures. A sealed stainless-steel casing, seen in Figure 4-5, was manufactured by welding and used to encapsulate the specimens. Inside this casing, titanium was also inserted along with the samples. Titanium was chosen because of its high chemical affinity for oxygen, it acts as an absorber, preferentially oxidizing and thus consuming the oxygen available within the closed system. This sacrificial oxidation mechanism helps to maintain a low partial pressure of oxygen inside the enclosure, preventing oxidation of the surface or decarburization of the samples during the solubilization process (Stout; Gibbons, 1955).

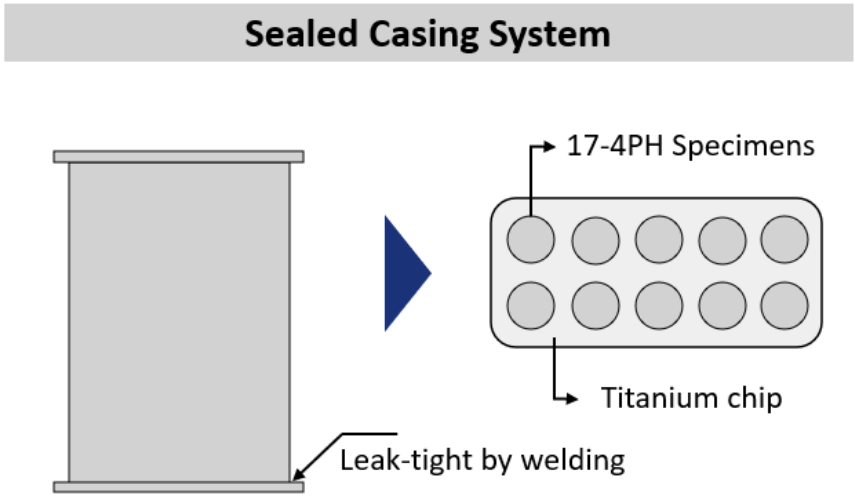

Figure 4-5: Schematic representation of the sealed casing system used to prevent oxidation during heat treatment.

After solubilization, the samples were placed inside the furnace preheated to 482 °C, with a tolerance of ± 5 °C. The heating rate was controlled at approximately 10 °C/min. After reaching the target temperature, the samples remained in aging condition for 60 minutes. This time was strictly monitored to ensure consistency in the mechanical properties obtained. Cooling was carried out in air to room temperature, ensuring the stabilization of the microstructure formed during the heat treatment (Pellegrini *et al.,* 2023).

All process parameters, including temperatures, times and cooling rates, were recorded to ensure traceability of the results.

4.3.4 Shot Peening to Induce Compressive Residual Stresses

For the second manufacturing route, a second SP process was applied with the aim of inducing a compressive residual stress state in the samples. Unlike the first SP treatment, which primarily targeted surface densification, this second treatment focused on modifying the residual stress profile to improve fatigue strength, particularly by inhibiting the propagation of pre-existing cracks or subsurface discontinuities. The mechanical treatment was carried out using S230 steel media, with particle diameters ranging from 0.50 mm to 0.71 mm, following the SAE J444 classification. The use of smaller shot sizes was intended to concentrate the residual stress field closer to the surface, particularly in regions already compacted by the previous SP stage (Lin *et al.,* 2020) Furthermore, as the surface layers were already hardened

in the first stage of SP, the use of larger media sizes can increase the risk of surface damage due to excessive plastic deformation, an effect known as overpeening (Cammett, 2007; Kirk, 2014).

The process was conducted using 98% coverage, which refers to the condition where every point on the surface has been impacted by at least one shot. This level of coverage is commonly adopted in industrial applications, as it ensures uniform treatment across the entire component and maximizes the introduction of beneficial compressive residual stresses (Wu *et al*., 2020; Miracle *et al*., 2001).

The SP equipment settings used in this second treatment were kept identical to those employed during the initial densification process. This includes the same clamping system, sample rotation method and enclosure configuration. The only changes implemented were the type of media and the coverage control.

In addition to the selected parameters, preliminary tests were carried out with S170 steel shot at both 3 bar and 6 bar pressures, as well as with S230 steel shot under the same conditions. These tests were carried out to assess the sensitivity of the surface to different impact energies and to determine the influence of shot size and pressure on residual stress. The results of these tests provided information on the effectiveness of the selected parameters and supported the final selection of S230 media at the pressure and coverage reported above.

This second SP stage, applied exclusively to Route C, was essential for establishing a multilayer residual stress profile. In Route B, the primary purpose of the SP treatment was to promote surface densification. In contrast, the second SP on Route C focused on inducing compressive residual stresses closer to the surface. . This synergistic distribution of residual stress is well known to increase fatigue life, both by preventing the nucleation of new cracks and by preventing the growth of existing ones (Schulze, 2006.; Torres; Voorwald, 2002). In this study, this strategy was adopted on the basis of these findings. However, the real effectiveness of this residual stress configuration has yet to be validated by the fatigue tests described in the following sections. Table 4-2 - Summarizes the shot peening conditions tested to evaluate the influence of pressure and media size on residual stress induction summarizes the conditions used for the process.

Table 4-2 - Summarizes the shot peening conditions tested to evaluate the influence of pressure and media size on residual stress induction

Shot Type	Diameter (mm)	Pressure (Bar)	Coverage (%)	Nozzle Angle	Distance (mm)
S230	0.58 to 0.71	3	98	90°	150
S170	0.43 to 0.50	3	98	90°	150
S230	0.58 to 0.71	6	98	90°	150
S170	0.43 to 0.50	6	98	90°	150

4.3.5 Grinding

Grinding was selected as the final finishing process for all the specimens, applied after the completion of each post-processing route. Depending on the manufacturing chain, this included heat treatment alone or a combination of heat treatment and a second SP step designed to induce compressive residual stresses. In all cases, grinding was responsible for providing the final geometry and surface condition required for the rolling contact fatigue test.

This process is a material removal technique based on the interaction between hard abrasive grains and the sample surface, allowing for high dimensional accuracy, geometric fidelity and low surface roughness. These attributes are essential for mechanical components operating under high-cycle fatigue conditions, where the quality of the surface and the distribution of residual stresses strongly influence the onset and propagation of fatigue. The thermal effects associated with grinding must be carefully controlled to avoid compromising the microstructural integrity of the material. Excessive heat input during the process can lead to phase transformations, tensile residual stresses or localized softening, all of which reduce fatigue performance. Efficient control of cutting and cooling parameters is therefore crucial (Youssef *et al.,* 2011).

For this purpose, a silicon carbide (SiC) grinding wheel was selected due to its high hardness, superior chemical stability and thermal conductivity, which are particularly advantageous when machining precipitation-hardened steels like 17-4 PH, as they minimize the risk of thermal damage and help preserve surface integrity (Marinescu et al., 2007). SiC abrasives are also effective in removing hardened layers while maintaining dimensional control.

The grinding wheel was operated at a rotation speed of 2300 rpm, corresponding to a moderate cutting speed that balances sufficient material removal with thermal stability, avoiding surface burns and microstructural changes. The cylindrical sample was rotated at 150 rpm, a value selected to ensure uniform exposure of the surface to the grinding wheel and consistent geometry. The feed rate was set at 1000 mm/min, chosen as a compromise between productivity and roughness control; higher feed rates may cause surface tearing, while lower rates increase heat input (Brinksmeier et al., 2010). These parameters were not only optimized to balance the preservation of surface integrity and the efficiency of material removal, but also to avoid inducing tensile residual stresses or excessive roughness prior to fatigue testing.

As in traditional gear manufacturing, grinding serves as the final operation in the BJT based production chain. The aim is to achieve the specified dimensional tolerances by refining the surface topography and removing any inconsistencies introduced during the previous stages. As this is the last stage before mechanical testing, any changes to the surface will directly influence the specimens fatigue behavior. The final surface condition obtained through grinding plays a fundamental role in the fatigue life of rolling contact components. Emphasize that surface roughness and residual stress profiles induced by grinding can significantly alter crack initiation behavior (Brinksmeier *et al*., 2010). Thus, proper control of this step is essential to ensure repeatability, minimize experimental uncertainty, and accurately isolate the effects of porosity and post-processing treatments on fatigue resistance.

4.4 Specimen's Test Assessment

All specimens were subjected to a campaign of surface integrity analysis. The purpose was to evaluate how different process kinematics and plastic deformation mechanisms influence the gear final surface integrity state. The evaluation included residual stress assessment, topographic and dimensional evaluations, hardness mapping and material characterization. The methodology for each approach is detailed in the following specifications.

4.4.1 Pores Investigation

The presence of open porosity resulting from the solid-state sintering process presents significant challenges when it comes to determining density. Traditional methods, such as the Archimedes principle, are unsuitable in this context, as they rely on immersing the sample in water to measure its apparent weight. In the case of highly porous materials, pores connected

to the surface allow fluid to infiltrate the internal volume, altering floatability and leading to inaccurate results (Spierings, 2011). Immersing the structure in water compromises the reliability of the measurement and makes this technique unfeasible for components with open porosity.

An alternative to the porosity characterization process was supported by a custom-developed algorithm implemented in *MATLAB®* using the *Image Processing Toolbox®*. This computational method was designed to quantify porosity-related metrics from metallographic images with high reliability and repeatability. The complete image processing routine is described in Figure 4-6 and comprises several sequential steps that guarantee the conversion of raw microscopy images into accurate quantitative data, the code is presented in appendix A.

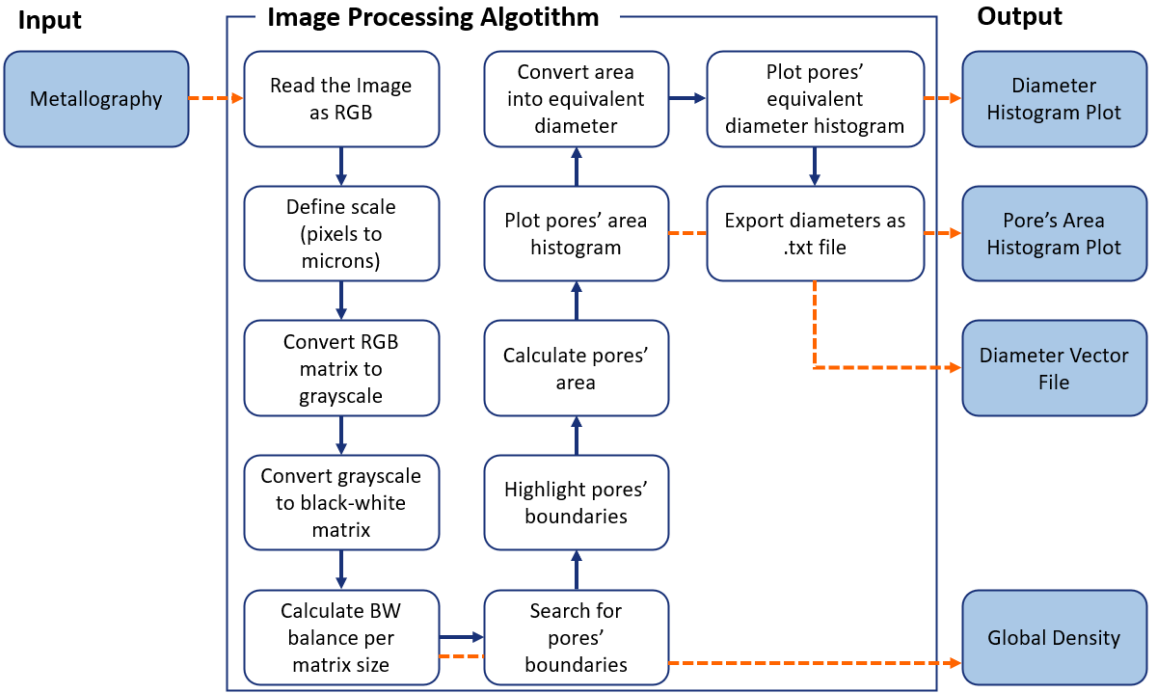

Figure 4-6 Developed MATLAB® algorithm for image processing. Metallography images are the given input. After processing, density data is obtained as histograms and as .txt files.

For image-based density measurement, each sample was sectioned perpendicularly to the functional surface, corresponding to the transverse plane relative to the direction of construction. From each section, three representative micrographs were acquired, distributed uniformly across the sample. This sampling strategy was adopted to capture local variations in pore morphology and quantify densification near the surface, particularly in areas most subject to mechanical loads.

Initially, the metallographic image is imported in RGB format. The spatial resolution is defined by setting the pixel-micron scale, calibrated according to the magnification used during image acquisition. The RGB image is then converted to grayscale, reducing the complexity of the data and maintaining the intensity gradients relevant to feature differentiation. A binarization step then takes place, converting the grayscale image into a black and white matrix. Unlike global thresholding methods, the algorithm applies an adaptive thresholding strategy, which determines local threshold values based on the regional properties of the image. This ensures better detection of pore boundary contours, particularly in heterogeneous images affected by illumination gradients or polishing artifacts (Zhao, 2000).

Once binarized, the algorithm calculates the proportion of black and white pixels in the matrix, generating the overall density. Pores are identified by searching for contiguous regions of black pixels, and each void detected is processed to calculate its area. The boundary of each pore is highlighted and stored, which allows both visual validation and additional geometric calculations.

To characterize pore morphology, two additional metrics are computed. The first is the equivalent diameter, D_{eq}, calculated from the pore area, A_{pore}, using the equation 4.1, which allows a normalized interpretation of pore size independent of shape elongation (Cipolloni *et al.,*2014).

$$D_{eq} = \sqrt{\frac{4A_{pore}}{\pi}} \tag{4.1}$$

The second metric is the perimeter-area ratio, C, which serves as an indicator of the circularity of the pore, calculated using the equation 4.2. In this expression, P_{pore} is the perimeter of the pore and A_{pore} is again the pore area. A perfectly circular pore will produce the minimum possible value for this ratio, while irregular and elongated pores produce larger ratios. This parameter is valuable for assessing the quality of the sintering process and detecting the effects of pore anisotropy or coalescence. The algorithm plots histograms for pore area and equivalent diameter and exports the calculated diameters to file for later statistical analysis or correlation with other mechanical properties.

$$C = \frac{4\pi A_{pore}}{P^2{}_{pore}} \tag{4.2}$$

In addition to the equivalent diameter and circularity, the aspect ratio (AR) was also calculated to quantify the elongation of each pore. This parameter is defined as the ratio between the shorter and longer sides of the bounding box surrounding each pore, computed as:

$$AR = \frac{\min(a, b)}{\max(a, b)} \tag{4.3}$$

Where a and b are the bounding box dimensions along the horizontal and vertical directions, respectively. This metric ranges from 0, highly elongated pore, to 1, perfectly equiaxed pore, and serves as a complementary indicator of pore anisotropy.

Figure 4-7 shows an example of the pore identification routine, showing the original image on the left and the processed image on the right, with the recognized pores marked in red and their equivalent diameters in blue.

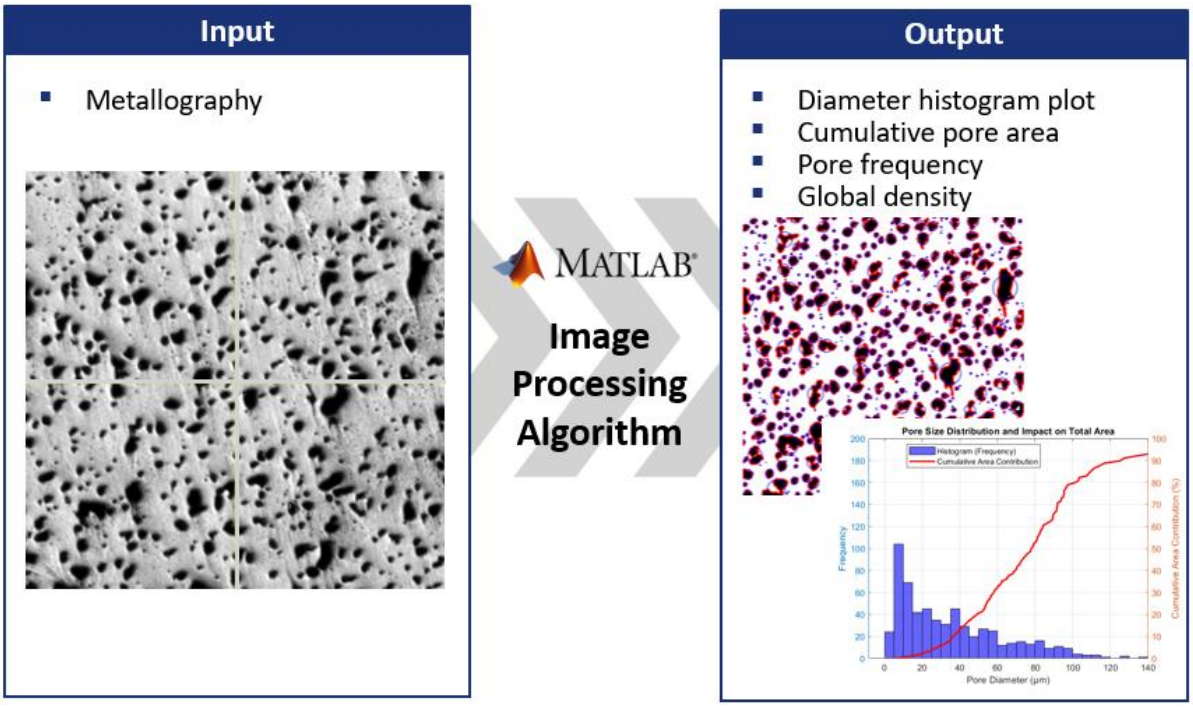

Figure 4-7: Developed MATLAB® algorithm for image processing. Input image and treated output image with porosity data extracted.

The microscope *Emco-Test DuraScan* used in this study was equipped with a 100x and 60x objective lens, which offers sufficient magnification and resolution to accurately detect and

measure the pores typically found in BJT components, which range from 5 to 80 μm in diameter (Mostafaei et al., 2018).

4.4.2 Residual Stress State Assessment

The most common and widely used method for assessing residual stress is X-ray diffraction (XRD) (Law; Luzin, 2011). Among the available techniques, XRD stands out as the most widely adopted approach for evaluating near-surface residual stresses in metallic components, especially in martensitic stainless steels such as 17-4 PH. Its widespread use in surface integrity investigations is due to its non-destructive nature, high sensitivity to micrometric stress gradients, and strong correlation with mechanical performance under fatigue (Fitzpatrick; Lodini, 2003; Prevéy, 2001).

X-ray diffraction operates on the principle that the wavelength of X-rays is comparable to the spacing between atomic planes in crystalline materials. When X-rays strike a crystalline structure, they are diffracted in specific directions defined by Bragg's Law, which relates the diffraction angle (2θ) to the interplanar spacing. Residual stress alters the atomic spacing, resulting in a measurable shift in the diffraction peak. Because of the complex orientation of grains in polycrystalline materials, accurate stress determination requires measurements at multiple angles, and cannot rely on a single diffraction geometry (Cullity, 1956; Fitzpatrick, 2005; Tanaka, 2019).

Once the theoretical basis of XRD was established, the specific technique used in this study was the cosα method, implemented through a *Pulstec MICRO-X360s* diffractometer. This method employs a two-dimensional detector to capture the Debye–Scherrer diffraction ring generated when an X-ray beam hits the sample surface. As shown in Figure 4-8, the method involves tilt angle ψ_0 and rotation angle φ_0, and the azimuthal angle α defines the direction of the diffraction vector relative to the ring (Taira et al., 1978; Sasaki & Hirose, 1995; Tanaka, 2019).

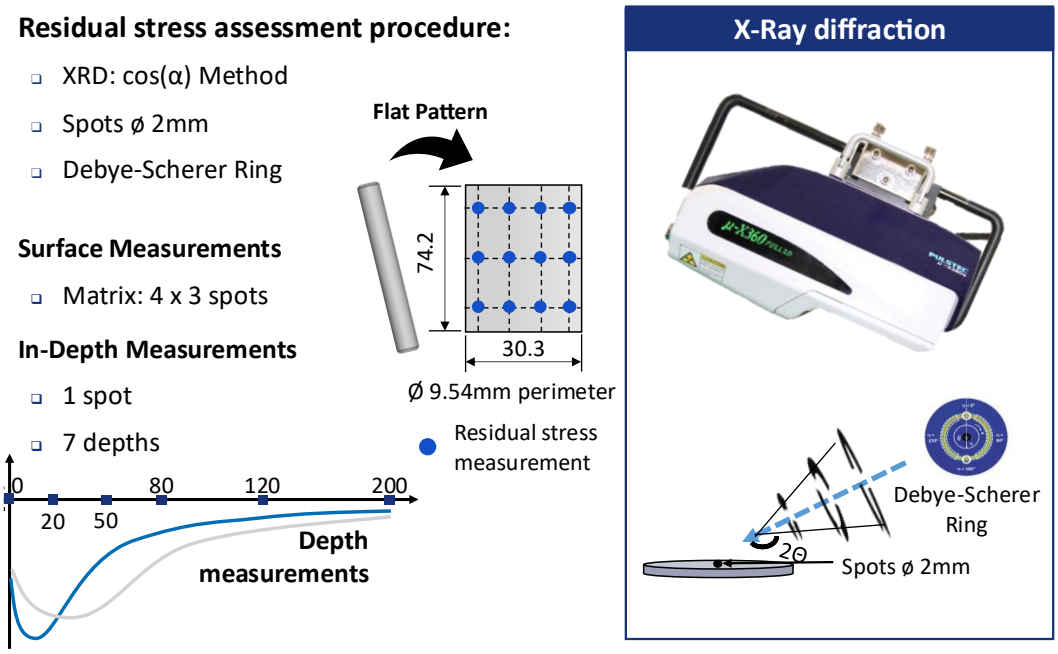

Figure 4-8: Residual stress assessment procedure

Compared to the traditional $\sin^2\psi$ method, the cosα method offers several advantages: it requires fewer mechanical adjustments, enables faster measurements, and is suitable for portable systems. The shifts in the diffraction ring, caused by elastic distortions of the crystal lattice, are directly correlated to the residual stress state and allow high-resolution stress mapping near the surface (Tanaka, 2018; Cullity, 1978).

The cos (α) method provides advantages in terms of speed, compact instrumentation, and the ability to assess residual stress with fewer angular adjustments compared to traditional $\sin^2\psi$ techniques. The diffraction angle shifts resulting from elastic lattice distortions are directly linked to stress values, allowing the mapping of stress states in treated or near-surface regions (Tanaka, 2018; Cullity, 1978).

To investigate how residual stresses evolve below the surface, successive material removal was performed on each specimen using an electrochemical etching method. This approach avoids the introduction of plastic deformation commonly associated with mechanical polishing (Pangborn; Weissmann; Kramer, 1981). The solution used was an acid mixture composed of 15 milliliters of nitric acid (65%), 8 milliliters of hydrofluoric acid (50%), and 1.3 grams of urea, diluted in distilled water to reach a total volume of 100 milliliters. This formulation, known as urea-based acid pickling, enables controlled anodic dissolution of the metallic surface.

The use of electrochemical removal is widely recognized in literature as an effective way to avoid stress redistribution during material thinning. Unlike abrasive techniques, the chemical attack selectively dissolves grain boundary material and exposed surfaces without inducing mechanical strain. This method provides uniform and controlled surface conditions and avoids the generation of residual stresses in material removal that would distort the original residual stress readings. The resulting surface is suitable for X-ray analysis, preserving the original stress distribution and enabling accurate depth profiling (Pangborn; Weissman; Kramer ,1981).

Etching was carried out by applying direct current using a bench power supply capable of delivering up to 30 amperes and 12 volts. The specimen served as the anode and was immersed in the solution along with a suitable counter-electrode. Each sample was etched sequentially, targeting depth levels of approximately 0, 20, 50, 80, 120 and 200 micrometers. These depths were defined based on typical ranges for residual stress gradients observed in surface-treated components. Particularly, it was considered the cases where processes including shot peening or grinding induce compressive residual stress. The location of each stress measurement is indicated in Figure 4-6, with mapping along the loading direction of the cylindrical specimen. All measurements were taken in the axial direction of the specimen, which corresponds to the principal loading direction in fatigue tests and is therefore the most relevant for assessing mechanical performance. This orientation is also perpendicular to the machining marks.

All residual stress measurements at different depths were carried out on the same specimen for each processing condition. A new specimen was only introduced when a different manufacturing condition was evaluated. This approach ensured continuity and comparability within each experimental group while allowing reliable assessment of stress evolution through the material thickness.

Surface mapping was carried out to assess the spatial uniformity of the residual stress distribution. Measurements were taken in a 4×3 matrix, with four points equidistant along the circumference and three along the height of the cylindrical specimen, totaling 12 measurement points per sample. This mapping strategy allows the assessment of potential heterogeneities introduced by anisotropies in the manufacturing process or localized effects of post-processing operations. All residual stress measurements were carried out on the same specimen for each processing condition.

The number of discrete RS measurement positions was defined considering experimental constraints and statistical reliability criteria. Based on classic experimental design principles (Montgomery, 2017; Box; Hunter; Hunter, 2005), the adequacy of the sample size can be assessed not in absolute terms, but in relation to the variability of the data. To this end, the coefficient of variation (CV) was used as a guiding parameter in defining the sampling plan. Under controlled measurement conditions, a CV below 15% is generally accepted as indicative of sufficient precision, allowing the use of a reduced number of observations without compromising the reliability of the average estimates. This criterion, also adopted in standards such as ISO 13528 (2022), supports the use of six depth positions and twelve surface points per specimen to characterize the residual stress field.

Through this method, it was possible to observe the relaxation and redistribution of residual stress across the subsurface region of the specimens, highlighting the influence of each post-processing step on the mechanical state of the material. The combination of electrochemical thinning and cos α X-ray diffraction proved to be a robust and reliable strategy for the residual stress evaluation in BJT components.

4.4.3 Topography and Dimensional Analysis

The evolution of dimensional characteristics throughout the post-processing stages is a key factor in determining the functional performance and integrity of the components produced by the binder jet. Surface irregularities can influence fatigue resistance, stress localization and the effectiveness of subsequent finishing processes. In this context, a detailed topographical analysis was conducted to characterize the surface condition at each stage and to assess the impact of different treatments on reducing surface roughness and uniformity.

Measurements were taken after each relevant stage of the manufacturing chain, including as-built, SP for densification, heat treatment, residual stress shot peening and after grinding. This sequential analysis made it possible to trace the evolution of the surface and understand how each process contributes to the regularity or irregularity of the surface.

Surface roughness measurements were carried out using a *Taylor Hobson Surtronic S-100 Series* contact profilometer. The direction of displacement of the needle was aligned with the direction of the load to be applied in the fatigue tests, i.e. transverse to the cylinder. To ensure spatial representativeness, a total of 3 points were measured on each specimen, in three different heights.

All measurements followed the recommendations of ISO 13565-2 (ISO, 1996). A *Gaussian* filter was applied to eliminate noise and account for surface waviness, with a cut-off value of 2.5 mm. The raw data were processed using *TalyMap Platinum* version 7.4, which enabled individualized analysis of topographic features.

From the measured profiles, the common roughness parameters Ra, Rq and Rz were extracted, providing a general description of the surface's amplitude. To improve functional understanding of the surface, additional parameters such as Rk, Rpk and Rvk were also obtained. These parameters provide insights into the potential fluid retention or contact behavior of the surface. In addition, *Abbott-Firestone* curves were generated to visualize the cumulative distribution of profile heights and help interpret the surface's functional performance (Stout; Blunt, 2000).

The complete methodology and topography results are summarized in Figure 4-9.

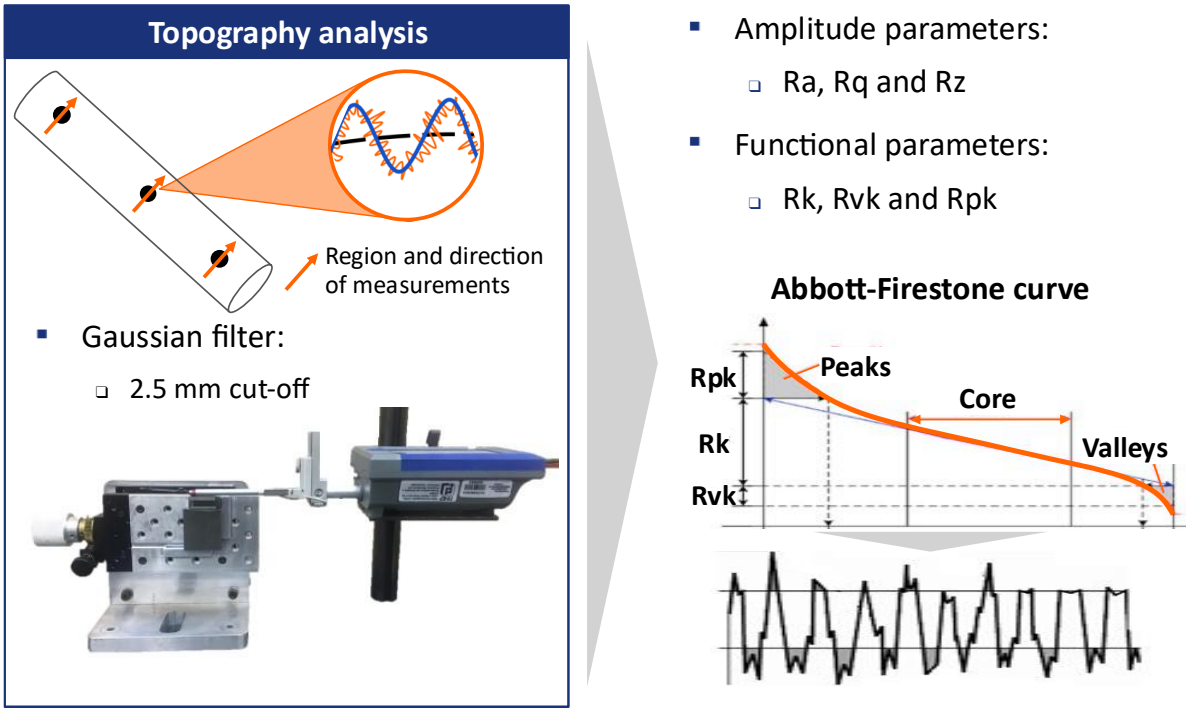

Figure 4-9: Topograpphy measurements: regions analyzed, equipment used and the main roughness metrics assessed from the *Abbott-Firestone* curve.

4.4.4 Microhardness Analysis

According to ISO 6336-5 (ISO, 2007), the fatigue life of components under cyclic loading conditions is correlated to their mechanical strength. The higher the mechanical strength, the greater the stress required to initiate a crack. Therefore, the mechanical strength of the component can be assessed by means of hardness mapping, which can be extrapolated to tensile and shear strength, properties associated with the contact fatigue failure mode.

In components produced by BJT, porosity is a critical factor that influences mechanical performance and difficult conventional measurement techniques. In this study, hardness mapping was carried out at several stages of the post-processing chain: as-built, SP for densification, heat treatment, SP for RS induction and after grinding. These measurements aimed to monitor the evolution of the mechanical response as the porosity changed throughout the process. The presence of pores interferes with the uniformity of plastic deformation during indentation. Indentations that coincide with pores can lead to irregular deformation fields and underestimated hardness values. Despite these challenges, hardness mapping remains an effective method for comparing process conditions and assessing the mechanical integrity of porous materials produced by indirect additive manufacturing.

The tests were performed using the *Vickers* method, according to ISO 6507-1 (ISO, 2018), which consists of applying a constant load through a diamond-shaped indenter and measuring the dimensions of the resulting impression. The higher the mechanical resistance, the lower the plastic deformation and, therefore, the lower the indentation lost after the load is removed. Thus, the hardness value can be derived from the size of the indentation mark (ISO, 2018). The equipment used was the *Emco-Test DuraScan 50* hardness tester, located at CCM-ITA.

A constant load of 0.1 kgf was applied for all indentations, as lower loads result in smaller indentation areas, thereby minimizing the potential influence of pores on the microhardness measurements. The samples were prepared using standard metallographic procedures. Microhardness was conducted in one direction in the cylindrical cross-section, with indentations spaced 0.1 mm apart. This configuration allowed a detailed assessment of the microhardness variations in the near-surface and subsurface regions.

Microhardness was used in this study to support the identification of regions potentially affected by porosity after each post-processing stage. Localized variations in microhardness can be associated with incomplete pore closure or heterogeneous densification, which compromises the mechanical uniformity of the component (Bai et al., 2017). This type of analysis has been

applied as an indirect indicator of surface integrity and processing consistency in porous AM materials (Mostafaei et al., 2018). Therefore, microhardness provides relevant spatial information that complements conventional porosity quantification methods, helping to validate the effectiveness of each stage in the manufacturing chain. The procedure adopted in this study is summarized in Figure 4-10.

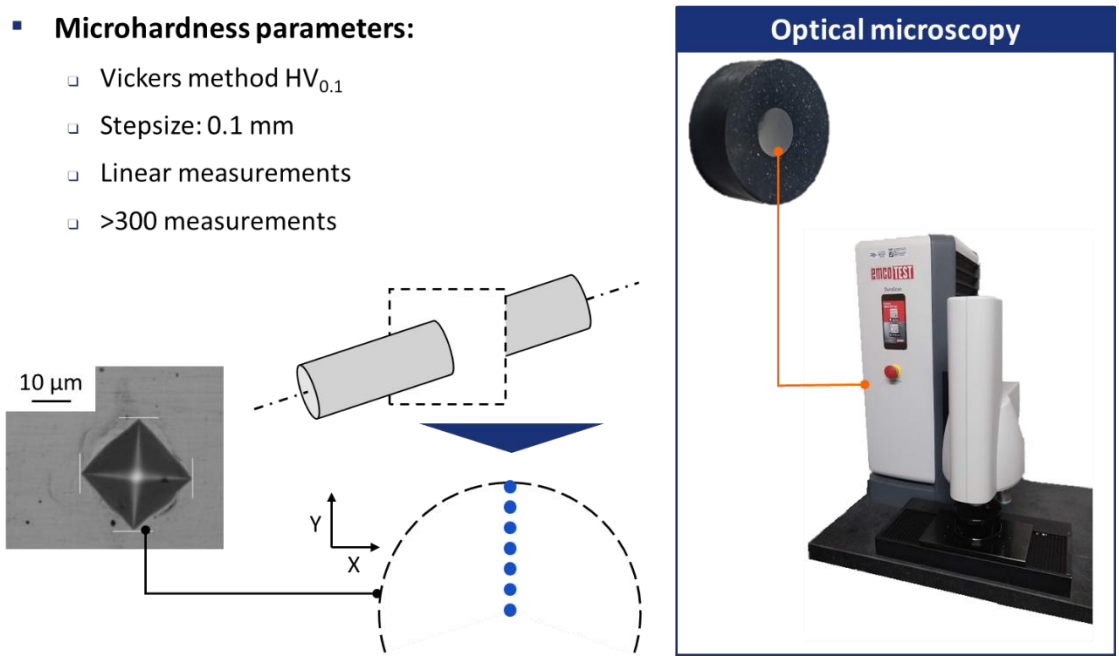

Figure 4-10: The microhardness analysis procedure

4.4.5 Rolling Contact Fatigue Tests

In this study, rolling contact fatigue (RCF) tests were carried out using a simplified test rig based on the ball-rod configuration. This configuration reproduces pure rolling contact conditions without controlled sliding, simulating the contact regime typically found in pitch line regions of gears and rolling element bearings. The system is based on the standard NTN RCF tester, as described by Glover (1982), and follows the principles described in ASTM STP 771. The device consists of three steel balls in continuous contact with a cylindrical rod, which rotates at a constant speed of 3600 rpm. The balls are pressed against the rod by compression springs, generating stable Hertzian contact. Figure 4-11 show the test rig.

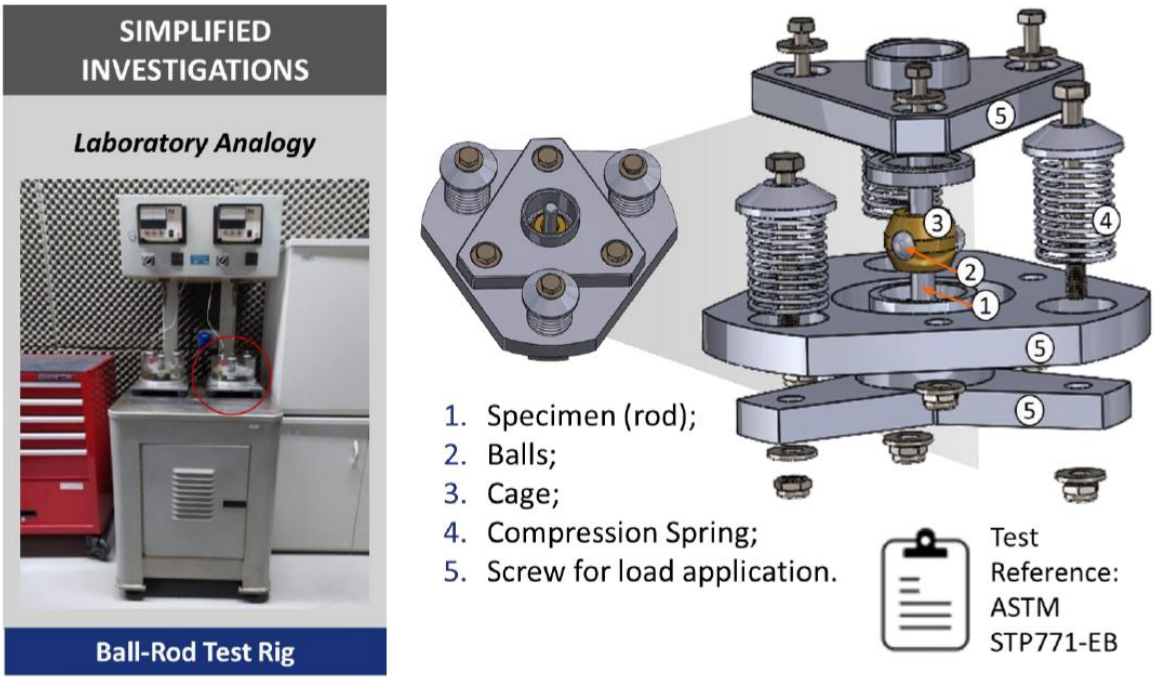

Figure 4-11: Schematic view and photograph of the Ball-Rod RCF test rig.

The contact conditions were selected to replicate realistic service stresses, while accelerating fatigue damage in a controlled and repeatable manner. Lubrication was ensured by the continuous application of ISO VG 100 oil, selected to provide an adequate lubricating film and prevent premature surface wear due to boundary contact. The load configuration was set to achieve maximum contact pressures of 2,79 GPa. This value is within the range used in contact fatigue studies on porous metals, such as the 1.82 GPa applied by Holmberg et al. (2019), reinforcing the relevance of the pressure level selected for evaluating contact fatigue by rolling in low-density materials.

Unlike fatigue tests with predefined cycle limits, the RCF does not have an actual fatigue limit. Failure is considered inevitable given enough stress cycles, as confirmed in previous studies (Glover, 1982). Therefore, in the present work, no maximum number of cycles was defined. The test was terminated when a significant increase in system vibration was detected, specifically, when the vibration amplitude exceeded 20% of the stabilized value, indicating the onset of surface crack propagation. An on-board accelerometer continuously monitored the dynamic response of the system. This 20% increase in vibration amplitude was used as a non-destructive failure criterion, allowing the onset of damage to be identified without the need to dismantle the component.

The evolution of the damage mechanism follows a multi-stage progression. Initially, contact occurs between clean, smooth surfaces, where the contact pressure is distributed according to *Hertzian* theory. This condition creates a stress field with a maximum located slightly below the surface. As the number of cycles increases, this region undergoes microplastic deformation, leading to the formation of localized wear marks, known as contact tracks. Over time, stress concentrations in this region initiate cracks, particularly in or near pre-existing pores or microstructural heterogeneities. These cracks propagate under repeated rolling contact, eventually reaching the surface and causing surface damage. The test bench allows this evolution to be observed, relating the vibration signature to the damage. Figure 4-12 show the failure evolution (Gohar; Rahnejat, 2018).

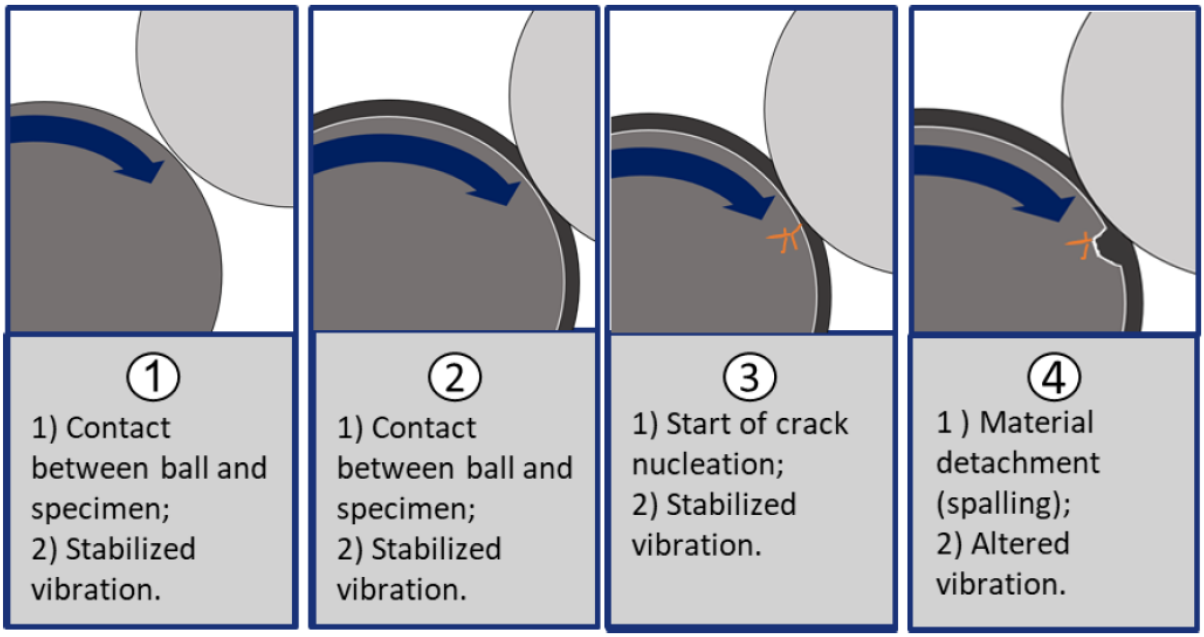

Figure 4-12: Typical progression of rolling contact fatigue: initial contact, track formation, crack nucleation, and final surface spalling (Glover, 1982).

To better quantify the state of stress in the contact zone, a simplified *Hertzian* model was adopted. The elastic contact between the ball and the rod was approximated by an elliptical contact area. The pressure distribution, contact dimensions and stress fields were calculated using analytical expressions derived from the contact mechanics framework of Johnson (1987). These parameters support the interpretation of failure mechanisms and help correlate experimental fatigue life with surface and subsurface characteristics such as residual stresses, porosity and finish quality.

The use of this test method allows the assessment of fatigue behavior in a controlled and accelerated environment, simulating key aspects of real applications. It is particularly relevant for materials produced by additive manufacturing techniques, where internal porosity, heterogeneous microstructures and non-uniform surface conditions influence fatigue performance. The test results obtained provide essential insights into the effectiveness of each post-processing route and help define the optimum combination of finishing processes to increase rolling contact fatigue life.

RCF tests were carried out to evaluate the mechanical strength of components produced by BJT under different post-processing routes. The study considered three post-processing conditions, identified as “Route A”, “Route B” and “Route C”. In addition, a conventionally manufactured reference, not produced with additive manufacturing, was tested totaling four experimental groups. Six valid tests were carried out for each condition. A single specimen was used per condition, with multiple contact tracks positioned along its length. To ensure statistical independence between the tests, a minimum spacing of 3 mm was maintained between the tracks, avoiding any mechanical interaction between neighboring failure zones (Gomes, 2023).

The validity of the test was established on the basis of three criteria applied sequentially: stability of contact and vibration at the start of the test, increase in vibration during the test and the presence of consistent failure mechanisms when compared to other tests within the same group (Glover, 1982). These criteria ensured that only failures representative of RCF were considered in the analysis.

The fatigue life data was treated statistically using a two-parameter *Weibull* distribution (Weibull, 1951). This model is widely adopted for fatigue analysis due to its ability to capture both the characteristic life (η) and the dispersion in failure behavior by means of the shape parameter (β). The construction of *Weibull* probability plots makes it possible to estimate the reliability and failure consistency of each processing route. This analytical approach is in line with established methodologies for fatigue testing, as found in standards such as ISO 281:2007 and in the work of Murakami (2002), supporting the comparative assessment of the durability of the different routes under investigation.

4.5 Summary

This study investigates the influence of different post-processing chains on the mechanical performance of BJT-manufactured components, with a focus on the evolution of surface integrity. All specimens were manufactured using 17-4 PH stainless steel processed on

a *Digital Metal DM P2500* printer, followed by curing, debinding and sintering. Three distinct post-processing routes were analyzed: one involving SP for densification, a second incorporating an additional SP stage to induce residual stress and a third reference chain without SP. All samples were subjected to heat treatment and H900 grinding, with a conventionally manufactured reference group included for comparison.

To ensure consistency and minimize variability, all samples were produced in a single batch and subjected to identical process parameters. Detailed analyses were carried out to characterize the evolution of porosity, residual stress, surface roughness and hardness throughout each post-processing stage. Image-based porosity measurements were implemented using a customized MATLAB® algorithm capable of quantifying pore area, equivalent diameter and shape factor, ensuring reliable analysis even in porous AM structures. Residual stresses were assessed using the X-ray diffraction technique through the cosα method. Depth profiles were obtained by removing the electrochemical layer, which preserved the original stress field.

Microhardness was carried out after each post-processing stage to detect heterogeneities related to incomplete pore closure or local densification variations. Topographic measurements were carried out according to ISO standards, following the evolution of roughness throughout the processing stages. Grinding, the final step in all routes, ensured dimensional conformity and low surface roughness, essential for rolling contact fatigue performance.

To assess mechanical strength, rolling contact fatigue tests were carried out using a pure rolling configuration based on the ball-rod principle. The tests simulated contact conditions representative of service, allowing accelerated damage accumulation under ISO VG 100 lubrication. Failure detection was carried out using an accelerometer, and the end of the test was defined by the start of the increase in vibration caused by crack propagation.

The integrated analysis of each processing route revealed the effects of densification, residual stress modification and finishing treatments on the fatigue performance of BJT components. This systematic approach allowed direct comparison of the routes and provided essential insights into the optimization of AM post-processing for high-performance applications.

5 Results and Discussion

The results of this study are presented in two main sections: Section 5.1, Surface Integrity Analysis, and Section 5.2, Fatigue Performance Analysis. Section 5.1 is dedicated to evaluating how different finishing processes affect the surface integrity of binder-jetted parts, considering parameters such as roughness, densification, and induced residual stresses. These surface characteristics play a crucial role in defining the functional performance and reliability of components, directly addressing the first research question regarding the influence of post-processing on surface integrity. Section 5.2 focuses on how such modifications reflect in the mechanical behavior of the components under cyclic loading, providing a fatigue life comparison across different processing routes. This section supports the second research question by assessing whether and to what extent the surface improvements introduced in Section 5.1 translate into enhanced fatigue performance. Taken together, these analyses offer a comprehensive understanding of the limitations of binder-jetted parts and demonstrate how post-processing techniques may compensate for or mitigate these intrinsic shortcomings.

5.1 Surface Integrity Analysis

5.1.1 Porosity Analysis

The porosity characteristics of the specimens were evaluated before and after the application of the densification treatment by shot peening. Figure 5-1shows the as-built surface condition, where a high density of pores distributed across both the surface and the bulk of the material is evident. In addition, the average volumetric porosity of the manufactured specimens was 16,98% with a standard deviation of 2,49%, reflecting the inherent characteristics of the BJT process and its influence on the mechanical properties of the component. These defects, typical of the BJT process, exhibit irregular morphologies and are frequently interconnected, creating preferential sites for crack nucleation under cyclic loading conditions. The presence of surface-connected pores, associated with incomplete particle bonding and local heterogeneities, significantly compromises the mechanical performance, especially under rolling contact fatigue scenarios, as extensively reported by Beretta et al. (2017) and Yadollahi and Shamsaei (2017).

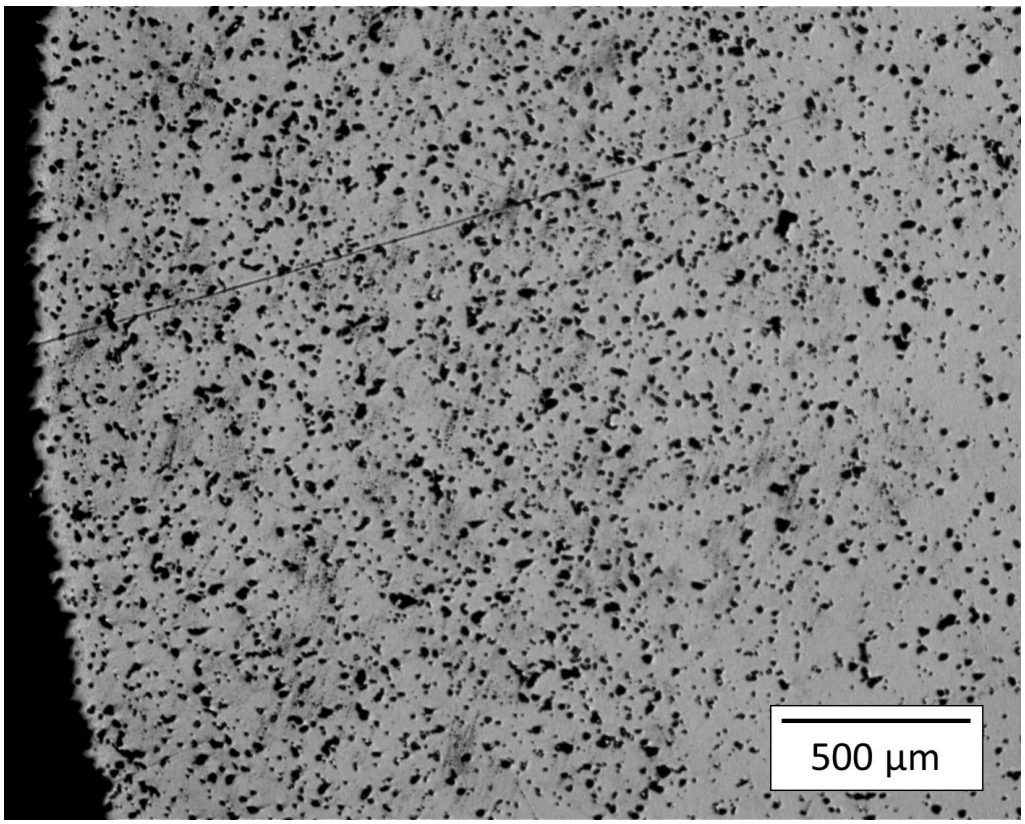

Figure 5-1: Surface condition BJT as built showing extensive porosity

This relative density is consistent with the range reported in Table 2-2 for sintered 17-4PH stainless steel components manufactured by BJT, where values between 80% and 88% are commonly observed depending on the processing route and material system. It is important to note that density values reported in the literature are strongly influenced by the measurement technique. Mass-to-volume methods, for example, often overestimate density by neglecting closed or unconnected pores. *Archimedes*-based methods tend to exhibit low accuracy in materials with high pore connectivity, as the fluid may infiltrate the porous network and distort the actual volume measurement. In contrast, image-based methods provide localized porosity quantification and are highly dependent on sample representativeness, requiring a larger number of analyzed sections to obtain statistically meaningful results. In the present study, localized density measurements are essential due to the presence of a densified surface layer, which cannot be accurately captured by the Archimedes method, as this technique averages the bulk density and overlooks near-surface variations.

Quantitative analyses of the as-built condition are presented in Figure 5-2 following the equations 4.1 and 4.2. The aspect ratio distribution shows a significant number of pores with low aspect ratio values, indicating elongated and irregular defect geometries, which are

mechanically detrimental due to their high local stress concentrations. The circularity distribution further highlights the irregular nature of the pore population, with a broad spread towards lower circularity values, suggesting a predominance of non-equiaxed pores. The equivalent diameter distribution reveals the presence of large pores contributing disproportionately to the total pore area, as also demonstrated by the cumulative area curve. The mean equivalent pore diameter in the as-built condition was approximately 14,63 µm with a standard deviation of 10,17 µm, reflecting the predominance of large, irregular defects typical of the BJT process and critical for fatigue performance.

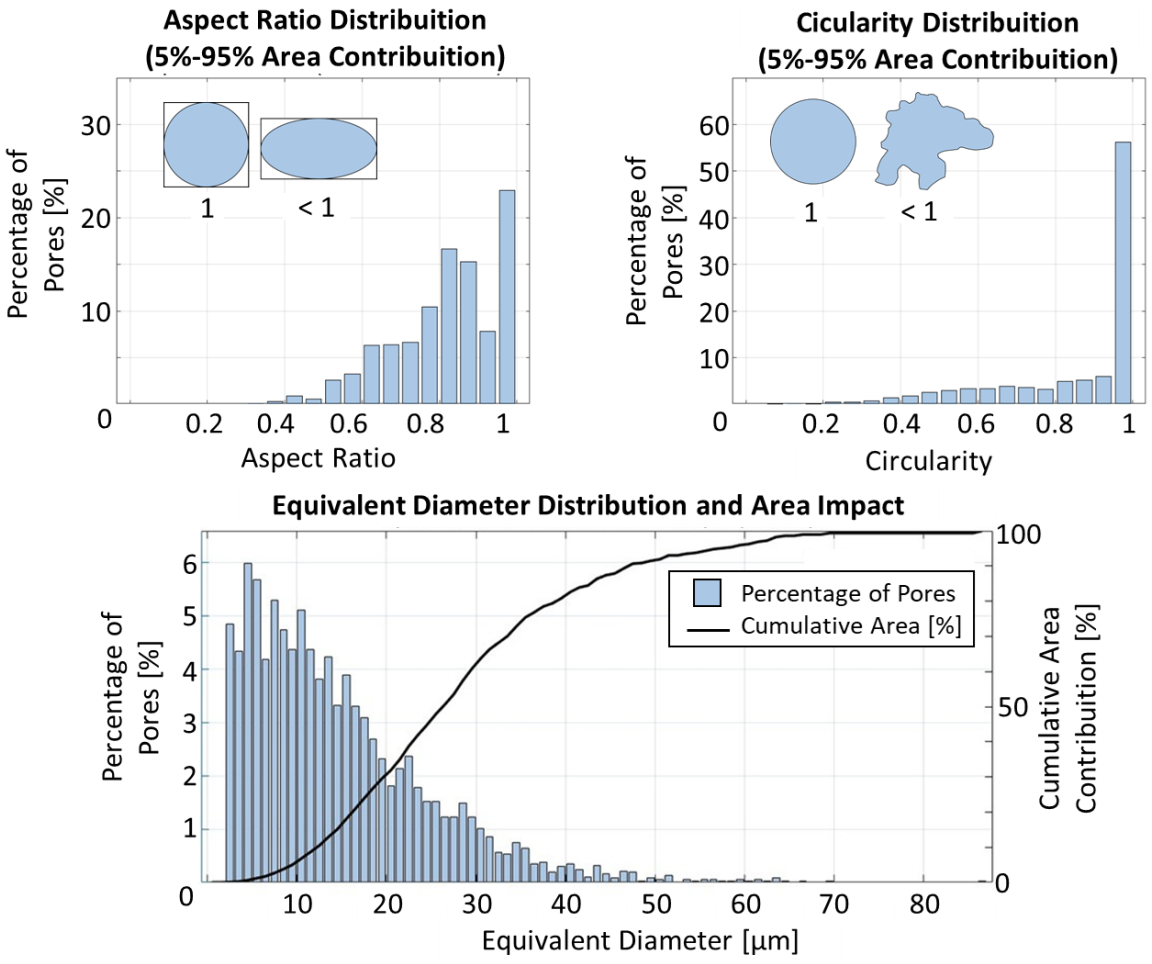

Figure 5-2: Quantitative characterization of pore morphology and size distribution for the as-built surface: (a) Aspect Ratio distribution, (b) Circularity distribution, (c) Equivalent diameter distribution and cumulative area contribution.

Similar values have been documented in the literature for BJT and other powder-based processes. Zhu et al. (2020) examined pores in binder-jetted copper samples and identified

average pore volumes around 10^4 μm³, resulting in equivalent diameters between 13 and 27 μm, depending on morphology. These pores were highly irregular in shape before post-processing, exhibiting low solidity and high eccentricity, which can negatively impact mechanical performance. Mostafaei et al. (2019) also detected persistent large and interconnected pores in binder-jetted Inconel 625 even after sintering, with sizes ranging from 10 to 30 μm. These comparisons indicate that the pore size and irregular morphology observed in the present study align with the common defect characteristics of binder jetting and highlight the importance of post-processing steps aimed at densification to mitigate fatigue sensitivity.

Following the characterization of the as-built surface, the same set of analyses was conducted for the specimens after shot peening densification. Figure 5-3 shows the surface condition after the application of shot peening, revealing a significant reduction in visible porosity and a more homogeneous and compacted microstructure. The surface irregularities associated with open pores were largely mitigated, and a densified layer approximately 350 μm thick was formed, as confirmed by metallographic cross-sections. This densified layer results from localized plastic deformation induced by the SP impacts, promoting the closure of interconnected surface pores and compacting near-surface regions without compromising the underlying bulk structure. The identification of this densified region was based on combined criteria: a notable reduction in the mean equivalent pore diameter to below 10 μm (Sangid *et al.,* 2020), a local increase in density exceeding 99% (Frech et al., 2018), indicative of effective plastic deformation and pore closure.

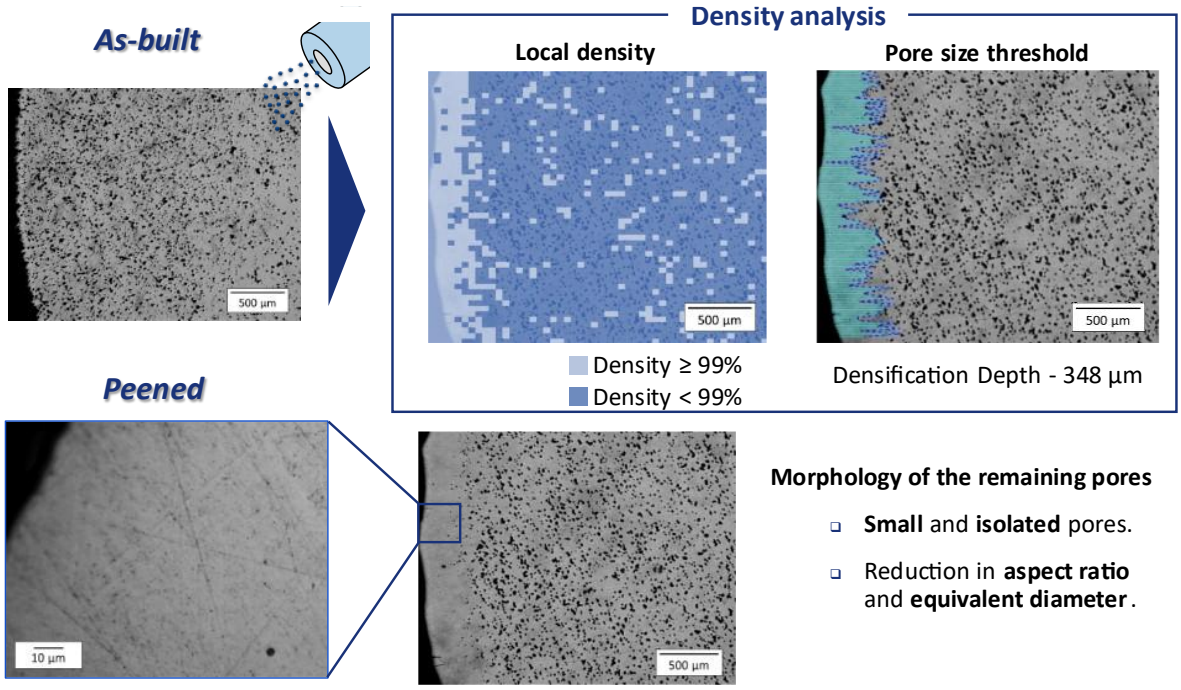

Figure 5-3: Density analysis workflow showing pore distribution characterization. From left to right: (A) initial metallographic image, (B) pore segmentation with local density map, and (C) density gradient across the densified layer. Bottom: (D) magnified view highlighting pore morphology and (E) representative region analyzed for density profiling.

The quantitative analysis of the densified specimens, presented in Figure 5-4, confirms the morphological evolution induced by shot peening. The aspect ratio distribution shifted towards higher values, with the majority of the pores presenting nearly equiaxed geometries, significantly reducing the defect-induced stress concentration potential. The circularity distribution became highly concentrated around values close to 1.0, indicating a prevalence of spherical pores, which are less mechanically critical. The equivalent diameter distribution shifted towards smaller values, and the cumulative area curve exhibited a steeper initial rise and faster saturation, reflecting the elimination of larger pores and a concentration of the porosity contribution into much smaller defects. For consistency and robustness in the statistical evaluation, the quantitative pore analysis focused on the central range of the cumulative area contribution, specifically from 5% to 95%, but this criterion was applied exclusively to the aspect ratio and circularity distributions. This approach was adopted because very small pores tend to be highly regular and nearly perfectly circular, which could artificially improve the statistical indicators of shape in these distributions. Conversely, extremely large pores are often isolated outliers that disproportionately influence the analysis. By excluding these two

extremes, the assessment more accurately characterizes the predominant pore morphology that is most relevant to mechanical performance. The equivalent diameter distribution, however, was evaluated across the full range of detected pores to capture the complete size variation induced by the shot peening treatment.

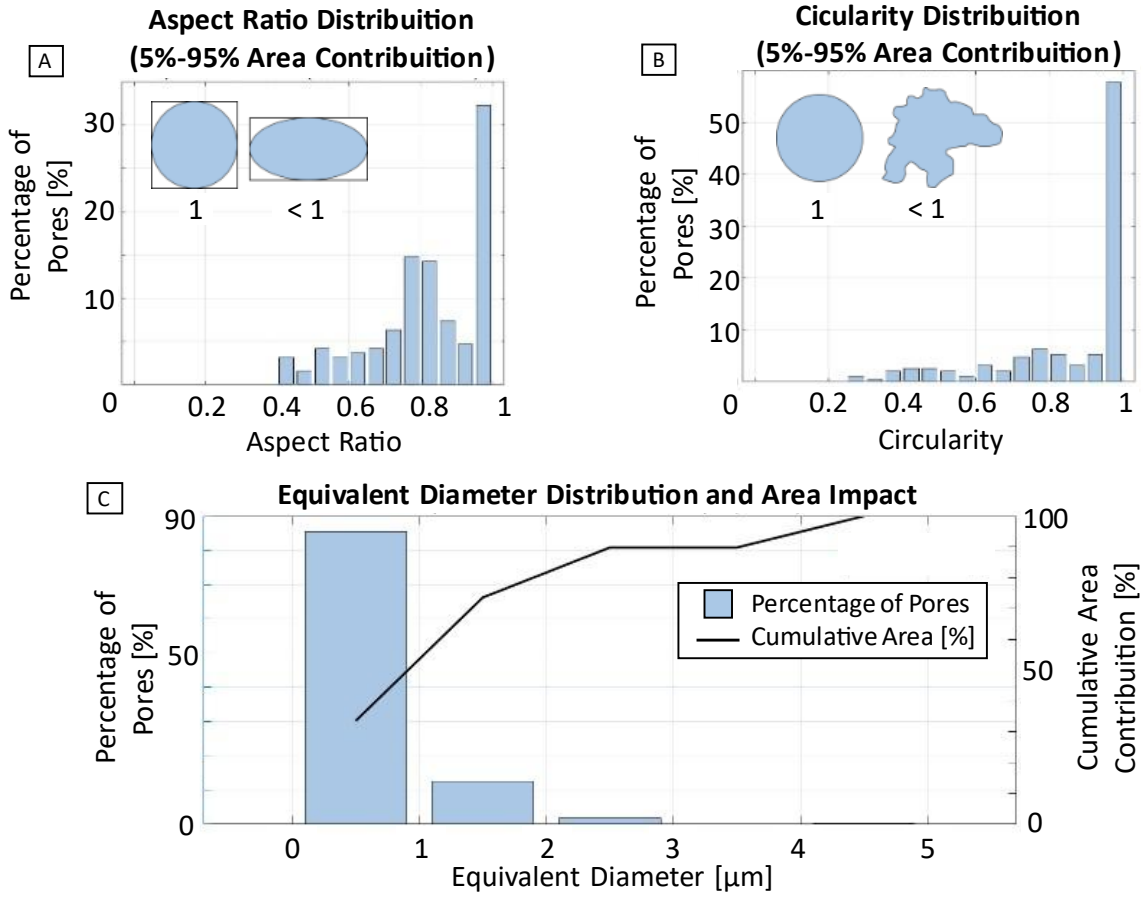

Figure 5-4: Quantitative characterization of pore morphology and size distribution for the densified surface: (a) Aspect Ratio distribution, (b) Circularity distribution, (c) Equivalent diameter distribution and cumulative area contribution.

A direct comparison between the as-built and densified conditions highlights the effectiveness of the shot peening process in modifying the surface integrity. In the as-built specimens, elongated, irregular pores with large equivalent diameters dominated the surface condition, while in the densified specimens, the pore morphology evolved towards compact, spherical shapes with reduced dimensions. Quantitatively, in the densified layer the average equivalent diameter decreased from 14,63 µm to 0,58 µm, and the proportion of pores with aspect ratio above 0.8 and circularity above 0.9 significantly increased. These morphological

changes are fundamental for improving the load-bearing capacity of the surface under cyclic stresses, as the reduction in defect severity directly mitigates the risk of early crack initiation, increasing the durability and reliability of the component (Cunningham et al., 2017).

Despite the improvements achieved, it is important to note that a population of small residual pores persisted within the densified layer. While these defects are significantly less critical compared to the original as-built porosity, their presence cannot be entirely disregarded. Particularly in high-cycle fatigue regimes, even small and isolated pores may eventually act as nucleation sites under prolonged cyclic exposure. The successful formation of a densified surface layer, combined with the morphological evolution of the pore population, confirms the potential of SP as a viable strategy to enhance the surface integrity of BJT components. The correlation between the densified layer characteristics, the residual stress profiles induced by shot peening, and the subsequent mechanical performance will be addressed in the following sections.

Additional metallographic analyses were conducted on cross sections extracted along different planes of the cylindrical specimens, as shown in Figure 5-5. These evaluations reveal that the pores exhibit a preferential orientation following the layer-by-layer deposition pattern inherent to the BJT. Specifically, in the longitudinal sections, XZ and YZ planes, elongated and aligned pores are observed, with some regions exhibiting clear defect clustering. In contrast, the cross section, XY plane, shows a more equiaxial and isotropic distribution of pores. These findings indicate an anisotropic porosity morphology, with directional characteristics aligned with the printing layers. This directional behavior not only reflects the influence of layer consolidation and binder saturation mechanisms but also suggests that fatigue crack propagation may be facilitated along certain paths, especially in planes parallel to the build direction.

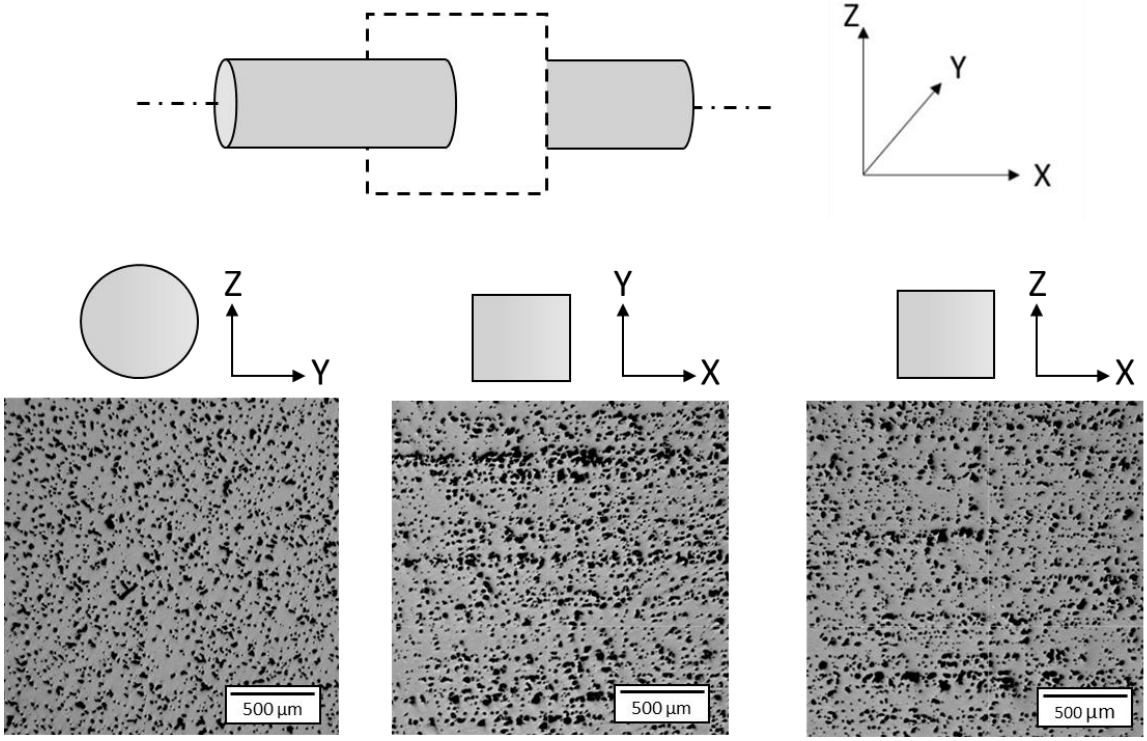

Figure 5-5: Pore morphology observed in three orthogonal planes (XY, XZ, YZ) of a cylindrical specimen. Elongated pores aligned with the build direction and pore clustering are evident, reflecting the layer-wise deposition of the BJT

5.1.2 Residual Stress Analysis

This subsection presents the analysis of the RS induced in the samples manufactured by BJT after different post-processing routes, with emphasis on the application of SP as a densification method and, subsequently, as a treatment for inducing compressive RS. The evolution of RS was assessed both on the surface and in depth, using X-ray diffraction measurements. The results allow to understand how each stage of processing influences the stress state of the samples, directly impacting on surface integrity and mechanical performance under fatigue conditions.

5.1.2.1 Surface Distribution

The evaluation of surface RS for different post-processing routes applied to BJT components revealed key trends in relation to the evolution of surface integrity. This stage of the study directly addresses the first research question, which investigates how SP for

densification, and other subsequent treatments, modify the mechanical stability of the surface on BJT fabricated parts shown in Figure 5-6.

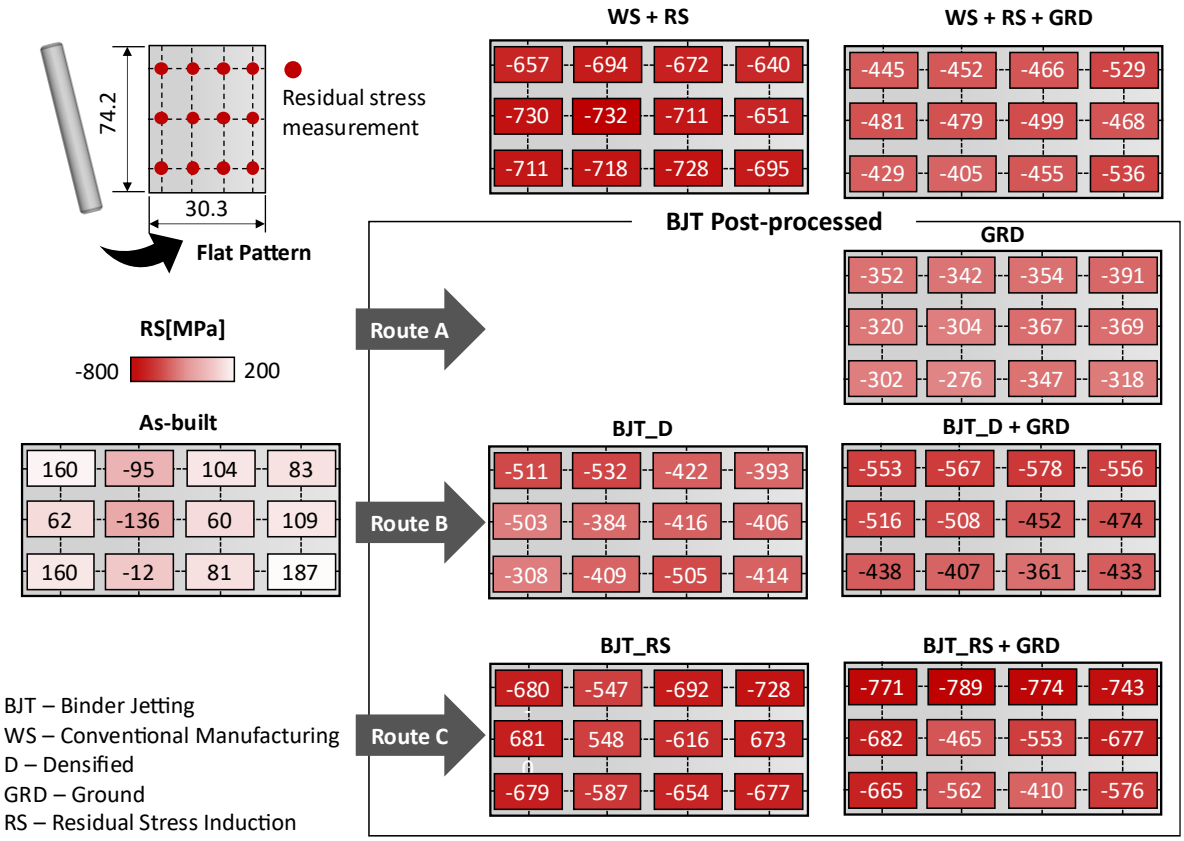

Figure 5-6: Residual stress maps measured by X-ray diffraction for BJT and conventional manufacturing samples subjected to different post-processing routes. Routes A, B, and C represent distinct combinations of surface treatments. Color scale indicates the magnitude of residual stress.

The WS condition, representing the conventionally manufactured reference, exhibited a uniformly compressive RS state. The stress distribution was consistent across the evaluated surface, indicating a relatively stable and homogeneous mechanical state. This behavior reflects the benefits of a fully dense and microstructurally uniform substrate, typical of conventional manufacturing routes, where RS are primarily influenced by machining-induced plastic deformation rather than by thermal or structural heterogeneities.

In the as-built condition, RS values varied widely, alternating between tensile and compressive regimes, with a mean value of 59 MPa, standard deviation of 95 MPa and a mean shear stress of -7 MPa. This high level of heterogeneity is a direct consequence of the inherent

porosity and non-uniform sintering behavior of the BJT process, which generates localized shrinkage and thermal gradients that affect the residual stress distribution. Such behavior has been widely observed in iSLS-fabricated components, where the removal of the polymer binder during sintering leads to a network of voids that compromises mechanical uniformity, emphasizing the need for corrective post-processing strategies (Mostafaei et al., 2019).

Route A, involving only the final grinding of the as-built BJT components, resulted in a modest compressive RS state. Despite the material removal and improvement in surface finish, the RS values remained relatively low in intensity. Grinding alone did not significantly alter the stress field to counteract the effects of sintering. The remaining influence of underlying porosity and sintering-induced distortions likely limits the mechanical stabilization achievable through grinding. Route A represents a minimal intervention strategy, offering basic surface conformity without effectively enhancing the fatigue-resistant RS state.

In Route B, the application of SP for densification in BJT samples led to a substantial increase in the intensity of compressive residual stresses relative to the as-built condition. The average RS reached -433 MPa, with values ranging from -532 MPa to -308 MPa, standard deviation of 65 MPa and a shear stress of -22 MPa. In contrast to the high variability observed in the as-built condition, the standard deviation observed here indicates a notable improvement in the homogeneity of the residual stress field, suggesting that SP was able to partially overcome the heterogeneity imposed by the initial porosity and microstructural irregularities.

Criscuolo et al. (2023), applied SP to components produced by iSLS, it is evident that the compressive RS obtained in the present work are substantially higher in surface. In that study, maximum RS values after peening remained around −250 MPa, even under severe SP conditions. One notable distinction lies in the initial density and porosity of the substrates: while iSLS parts exhibited relative lower density levels. While the iSLS samples from Criscuolo et al. (2023) ranged from 50% to 75%, also with extensive interconnected porosity, the herein investigated BJT parts presented a more consolidated structure with relative porosity of 16,98%. This likely influenced the energy partition during peening, with the more porous iSLS material converting a larger fraction of the impact energy as plastic deformation, whereas the BJT surface was able to store a greater portion of that energy in the form of RS. This difference may explain both the higher compressive values and the improved stress uniformity observed here.

Route C uses the application of SP specifically for the induction of residual stresses further intensified the compressive residual stress field. In this condition, the maximum compressive RS reached values close to -728 MPa, with a standard deviation of 58 MPa, a

consistent distribution over the entire surface, in addition to a shear stress of -39 MPa. The greater energy input and the optimized parameters applied during SP for RS were fundamental in achieving these levels of compression, effectively surpassing those obtained with SP alone for densification.

Although these results demonstrate a substantial improvement over the BJT as-built condition, the maximum compressive RS achieved in Route C remain lower than those observed in conventionally manufactured and SP case-hardened steels. Jbily, Amar and Simonneau (2024) shows that RS levels can exceed 1200 MPa near the surface, with compressive RS extending to depths greater than 60 µm. This discrepancy reflects not only the intrinsic limitations imposed by the lower density and porosity of AM parts, but also the influence of material composition, heat treatment, and SP parameterization.

After the final grinding of the BJT_RS condition, the residual stresses remained entirely compressive, albeit with a slight reduction in magnitude due to the removal of material and the thermal and mechanical input to the process. Even after this finishing stage, the compressive RS values remained well above those of the SP for densification condition, confirming the effectiveness of BJT_RS as beneficial treatment for inducing surface compressive stresses even in a porous component.

Compared to the conventionally manufactured WS samples, Route C demonstrated superior results, in the perspective of the requirements for rolling contact fatigue strength. While the WS+RS condition presented compressive RS magnitudes similar to BJT_RS, the subsequent grinding step in WS+RS+GRD caused a substantial drop, with values often below –500 MPa. This contrast highlights the advantage of performing a second SP step after densification and thermal treatment in the BJT route. The hardened and densified subsurface better accommodates plastic deformation, allowing the energy of SP to be effectively retained and resulting in a more intense, although less uniform, compressive RS field.

These results collectively demonstrate that the combination of surface densification via SP, heat treatment and finishing by SP for induction of RS is capable of significantly improving the surface integrity of BJT components. These processes not only increase the magnitude of the compressive residual stress, which is known to delay crack initiation under cyclic loading, but also ensure a stable and uniform stress field across the entire surface of the component. This is a critical condition for applications subject to rolling contact fatigue, in which residual pores and stress concentrations are known initiators of subsurface cracks. The positive effect of each sequential post-treatment step validates the hypothesis that BJT-produced parts can achieve

surface mechanical properties comparable to those manufactured by conventional means, provided that a customized and synergistic post-processing chain is applied.

Further supporting this analysis, Appendix B presents detailed measurement reports for both residual stress and retained austenite. The retained austenite content was found to be approximately 2%, indicating the effectiveness of the applied heat treatment in achieving a predominantly martensitic microstructure.

5.1.2.2 In-depth Profile Distribuition

The initial application of SP on the samples manufactured by BJT had the main objective of promoting surface densification, reducing the presence of pores in the surface and subsurface layers. Although the introduction of compressive RS is a natural side effect of the process, at this stage the focus was on improving its surface integrity.

The sample subjected only to SP for densification, prior to heat treatment, presented a maximum RS value in deep profile of –682 MPa, indicating the effectiveness of the process in generating beneficial stresses associated with the densification of the surface layer.

Following the processing chain, grinding was performed to meet the requirements of dimensional tolerance and topographic quality, with the controlled removal of 100 μm of the surface. This operation resulted in the removal of material, and consequently of part of the RS curve induced by the previous process, resulting in a maximum compressive RS of -623 MPa. The comparison between the residual stress profiles before and after grinding, presented in Figure 5-7, shows that, although part of the densified layer was removed, the compressive regime was largely preserved, which is beneficial for fatigue resistance. The surface mapping and depth profiling were performed on distinct specimens processed under identical conditions.

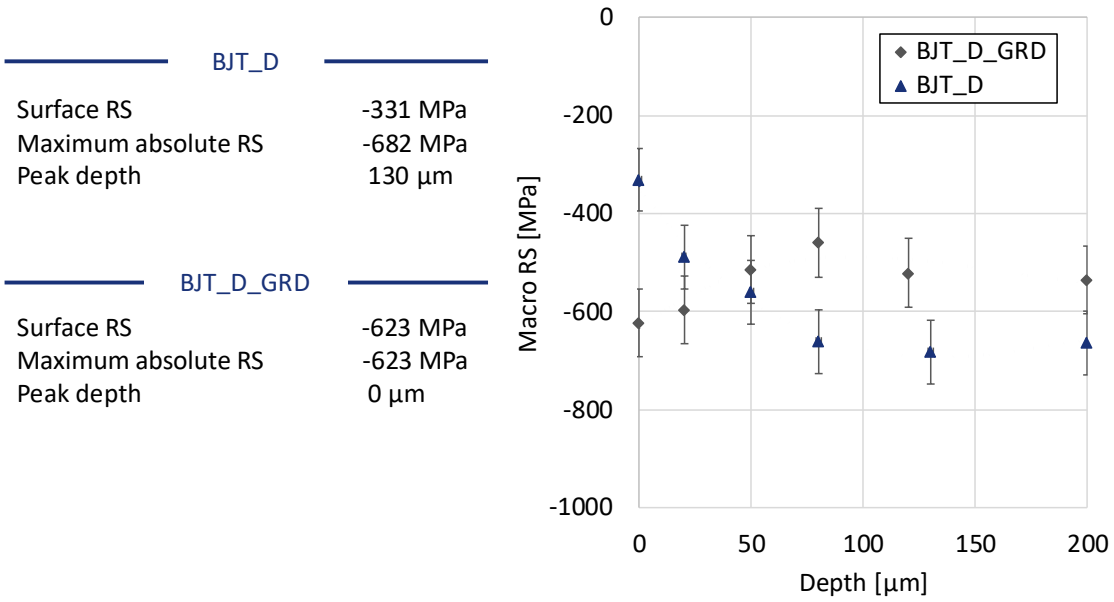

Figure 5-7: Residual stress profiles for BJT_D and BJT_D_GRD conditions, highlighting the reduction in peak depth and increase in surface compression after grinding. Numerical values indicate surface stress, maximum compression, and peak depth for each condition.

These results are in line with recent literature. Criscuolo et al. (2023) demonstrated that SP applied in indirect AM, such as iSLS, is capable of inducing deep compressive RS, associated with the formation of a densified layer close to the surface. In their experiments with densified 20MnCr5 steel, the generation of relevant compressive stresses was observed up to approximately 900 µm in depth, even in materials with porous internal regions. These results indicate that the closure of surface and subsurface pores was able to store sufficient energy to maintain relevant compressive RS, even in porous materials subject to plastic deformation processes.

In addition, finishing processes such as grinding have a direct impact on the stress state. As discussed by Griffiths (2001), grinding can both relax pre-existing RS, due to the removal of the plasticized layer, and induce new residual stresses due to the thermal and mechanical conditions of the process. Similarly, Rego (2016) analyzed the interaction of residual stresses in gears throughout the manufacturing chain and highlighted that, when machining occurs after a treatment that has already induced RS, the resulting RS is a combination of the pre-existing stresses with those introduced by the previous process. This superposition effect can, depending on the conditions, partially preserve the benefits of the original compressive state or modify its distribution profile and depth. Therefore, it is noted that after material removal, the RS peak

induced by BJT_D becomes practically the surface RS, remaining compressive and beneficial for fatigue life. A correct understanding of this interaction between processes is essential for controlling surface integrity and optimizing the fatigue life of components manufactured by indirect additive manufacturing routes, such as BJT.

Complementing the surface densification step described above, the samples were subjected to a second application of SP, this time with the explicit objective of inducing compressive RS in samples that had already undergone surface plastic deformation. The main purpose of this second application was not only to increase surface compression, but especially to protect the densified layer against the opening and propagation of cracks that use residual pores as stress concentrators during loading.

After BJT_RS, a maximum compressive stress value of -918 MPa was recorded. Then, the grinding step was performed, with removal of approximately 100 µm of the surface. Even after this removal step, the compressive residual stresses remained high, reaching -778 MPa in the final condition, as shown in Figure 5-8.

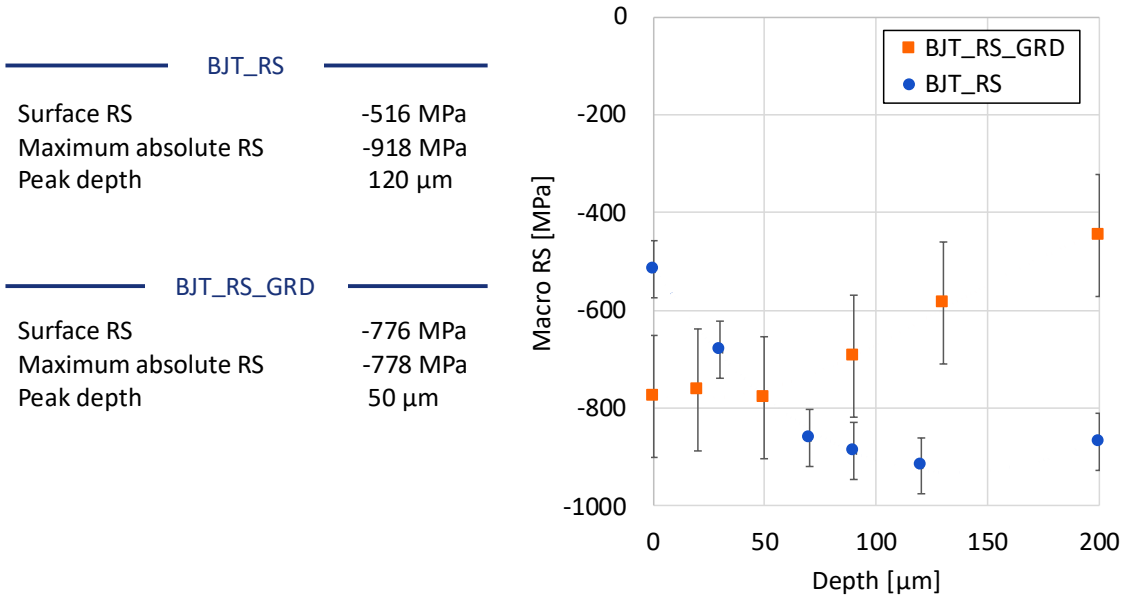

Figure 5-8: Residual stress profiles for BJT_RS and BJT_RS_GRD conditions, showing the effect of grinding on stress magnitude and depth distribution. Numerical values indicate surface stress, maximum compression, and peak depth for each case.

This preservation of compressive RS is particularly relevant in light of the known failure mechanisms for porous materials under contact fatigue. According to Holmberg et al. (2019),

failures in sintered steels under rolling contact fatigue tend to initiate at a depth of approximately 100 μm. The presence of residual pores in the densified region, however, still acts as a critical trigger for crack nucleation.

Therefore, the maintenance of compressive stresses of approximately -700 MPa in this critical layer even after grinding is a highly positive result, indicating that the double application strategy of SP was effective not only in densifying the surface, but also in structurally protecting the region most vulnerable to fatigue damage.

This observation also highlights a key distinction when comparing BJT components to conventionally manufactured ones. In carburized or nitrided steels subjected to SP the maximum compressive RS often reach values between –1000 and –1400 MPa and are typically located at shallow depths, around 20 to 80 μm (Girish; Mayuram; Krishnamurthy, 1997; Stenico, 2007). In contrast, for the BJT_RS condition, the peak compressive stress of –918 MPa is found at a depth of approximately 120 μm. This inversion in the RS profile suggests that, while AM parts may not achieve the same peak intensity, they tend to exhibit deeper penetration of the stress field. This behavior may come from the lower initial hardness and greater deformability of the porous material, sintered microstructure, which facilitates subsurface plastic deformation during SP and results in a broader compressive zone. This mechanism is characteristic of ductile materials, in which plastic deformation can be effectively accommodated beneath the surface under mechanical impact.

Another point to be considered is that the improvement of the surface condition and the induction of compressive stresses contribute synergistically to delay the propagation of subsurface cracks. As demonstrated by Ziaee et al. (2019), interconnected porosity in binder-jetted materials promotes crack propagation between adjacent defects located in regions of maximum shear stress, being accelerated by the presence of preferential fracture trajectories. By reducing the surface pore density and introducing a local compression state, the risk of crack formation and coalescence is considerably reduced.

This protective effect is particularly important for resisting failure mechanisms that originate below the surface under cyclic loading conditions, such as those illustrated in Figure 2-3. In these cases, cracks tend to initiate beneath the surface and propagate along shear planes (Mode II) before eventually reaching the surface and transitioning to opening mode (Mode I), leading to material detachment. Preserving a compressive stress field in the subsurface region, especially near the depth of maximum shear stress, helps prevent this bifurcation and reduces the risk of catastrophic failure.

These results reinforce the importance of a controlled combination of post-treatment processes for components produced with BJT, where the high initial porosity makes surface protection even more critical to ensure resistance in applications subject to cyclic loading.

Figure 5-9 shows the comparison of RS profiles for samples subjected only to SP for densification and for samples that underwent the complete sequence of treatments, consisting of SP for densification, heat treatment and SP for induce RS.

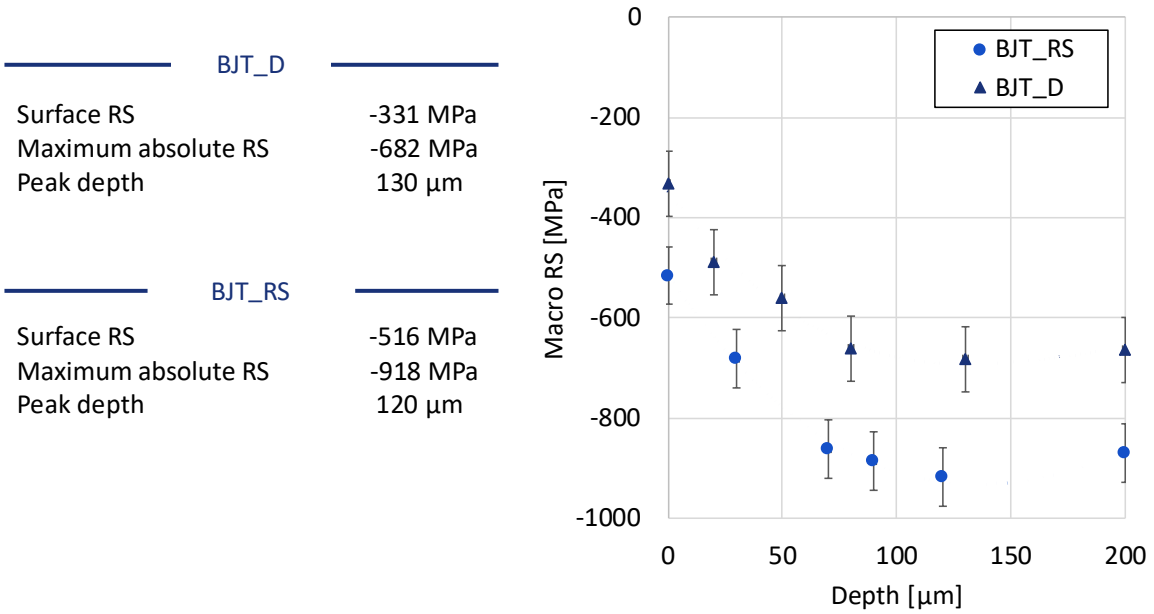

Figure 5-9: Residual stress profiles for BJT_D and BJT_RS conditions, showing higher compressive magnitude and shallower peak depth for BJT_RS. Numerical values summarize surface stress, maximum compression, and peak depth for each treatment.

It can be observed that the second SP, after densification and heat treatment, resulted in a significant increase in the magnitude of compressive RS along the depth. This behavior confirms that the objective of intensifying the compressive state was achieved.

The already densified surface provided a favorable condition for the new induction of compressive RS. The surface layer, having undergone plastic deformation during the first SP, presented a structure less susceptible to plastic deformation, being more conducive to additional RS induction. Furthermore, the subsequent heat treatment promoted the hardening of this layer, increasing its resistance to surface deformation and, consequently, its capacity to store plastic energy in the form of RS.

The synergistic combination between initial densification and heat treatment allowed the second SP to induce higher residual stress levels compared to the values obtained when

densification was applied alone. This evolution of properties is extremely relevant, as it acts directly on the protection of the critical layer close to 100 μm in depth, a region described by Martin et al. (2022) as critical for strain localization and crack formation in heterogeneous microstructures.

Therefore, the adopted strategy not only consolidated the surface integrity necessary for operation under severe cyclic loads, but also extended the potential service life of components manufactured through BJT, even under critical stress conditions. This effect is consistent with the literature, which indicates that the introduction of compressive residual stresses acts to delay crack initiation and propagation, resulting in a significant increase in fatigue resistance (Schijve, 2003; Totten, 2002).

In this context, both porosity and RS profiles play a central role in establishing surface integrity. However, these parameters alone may not be sufficient to guarantee the fatigue performance of BJT components. Surface topography also governs the distribution of contact stress, and sharp features or rough textures may promote localized stress concentrations. Therefore, to fully assess the potential of the proposed post-processing strategies, it is crucial to evaluate the evolution of surface roughness and its implications for fatigue life.

5.1.3 Roughness Analysis

The evaluation of surface roughness parameters throughout the manufacturing chain revealed a significant evolution in surface integrity, critical for applications involving severe contact fatigue conditions, such as gears. According to Liu et al. (2019), lower *Rvk* values suggest a reduced probability of fatigue contact failure. Lower *Rpk* values, which correspond to the peaks that wear at the start of operation, and *Rk* values, which define the load-bearing core of the surface, allow for better load distribution. This reduces the concentrations of contact stresses and, consequently, the probability of failure (Brecher; Renkens; Löpenhaus, 2016). These observations highlight the functional importance of controlling not only the average roughness, but also the complete profile of the support area curve.

Figure 5-10 illustrates the behavior of the main roughness parameters throughout the successive processing stages: BJT, Turning, SP for densification, SP for residual stress, and grinding. Due to the excessive scale of the as-built surface profile, its Abbott–Firestone curve was omitted from the comparative plot to preserve the visual clarity of the remaining processing stages.

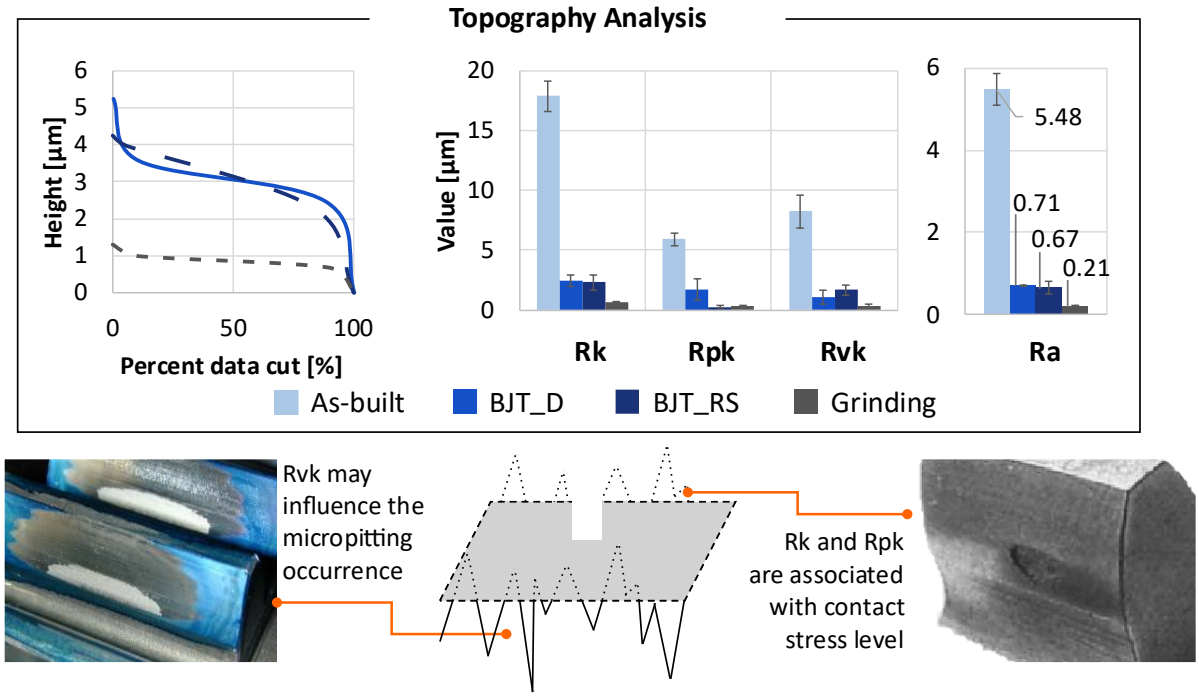

Figure 5-10: Topography analysis across processing stages, showing *Abbott–Firestone* curves and roughness parameters. Schematics illustrate peak–core–valley interpretation and surface evolution from as-built to ground condition.

As expected, the surfaces in the as built BJT condition presented the highest roughness values. The inherent layer-by-layer manufacturing process, coupled with the incomplete densification typical of BJT, led to significant surface irregularities. These results are consistent with previous studies on BJT, where *Ra* values typically range from 8 to 12 µm depending on powder size and binder saturation (Bai; Wagner; Williams, 2017). This condition is particularly detrimental in contact fatigue applications, since high levels of roughness introduce localized stress concentrations and limit the actual contact area available for load distribution (Kato, 2000; Johnson, 1985). According to classical contact mechanics, rougher surfaces result in higher stress intensities at the asperity tips, thus accelerating crack initiation mechanisms.

The turning operation was mainly applied as a preparatory machining step, with the aim of removing the most external irregularities from the printed surface and allowing the proper application of subsequent finishing processes. Although not investigated in this study, this step contributed to an initial reduction in surface roughness, facilitating the effectiveness of subsequent densification and stress induction strategies.

After turning, the specimens were subjected to the first SP treatment, with the main objective of promoting surface densification. Although this process induced localized plastic

deformation that helped close pores connected to the surface, a slight increase in roughness parameters as *Ra* and *Rvk* was observed. This behavior aligns with Denkena and Biermann (2014), who reported that although shot peening improves subsurface conditions, it can lead to surface asperities and increased roughness. In the present case, the rise in *Rvk* may indicate deeper valleys potentially associated with either partially closed porosities or newly formed impact-related depressions. The mechanical implication of this increase should be interpreted with caution, as it may introduce local stress concentrators depending on the contact conditions. A high *Rvk* may increase the lubricant retention capability in dynamic contacts, but can also be detrimental in rolling contact fatigue since deep valleys can act as crack initiation sites (Marinescu *et al.,* 2006). Despite this increase, the step is essential for preparing the surface for subsequent modification of the stress field, while still contributing to smoother micro-asperities compared to the as-built condition.

The second shot peening step was applied with a distinct set of parameters, specifically designed to maximize the induction of compressive residual stresses rather than further enhance surface densification. Considering the reduced trend of the now densified surface to further move inward, the roughness parameters such as *Rk* and *Rvk* remained relatively stable compared to the previous stage. However, a slight reduction in *Rpk* was observed, indicating a possible flattening of surface peaks due to the modified peening conditions. Similar behavior has been observed by Guagliano (2001), who reported that peening conditions optimized for residual stress can flatten peaks, reduced *Rpk*, while maintaining valley morphology. This subtle change suggests that, while the process did not significantly alter the global topography, it may have contributed to a more uniform surface texture. However, given that a final grinding operation was planned, ensuring precise dimensional and surface finishing, the slight variation or maintenance of roughness at this stage was not critical. In scenarios where shot peening constitutes the final processing step, excessive roughness could reintroduce localized stress concentrators detrimental to contact fatigue resistance (Sakai et al., 1995). In the present case, the subsequent grinding step ensured the removal of surface summits and the homogenization of the contact surface, preserving the beneficial effects of the induced residual stresses.

Finally, the grinding operation culminated in the manufacturing sequence, providing the smoothest surfaces among all processing conditions. Grinding effectively eliminated residual roughness, achieving low values of *Ra*, *Rk*, *Rpk* and *Rvk*. Tung and McMillan (2004) suggested that surfaces with $Ra < 0.3$ μm significantly improve fatigue performance under rolling contact, which is in agreement with the values achieved in this work. The final surface state ensures a

uniform and continuous load-bearing area, reducing peak contact stresses and contributing significantly to improving fatigue life under rolling and sliding conditions. In agreement with previous studies, fine surface finishes obtained by grinding are directly associated with extended fatigue life in contact applications (Griffiths, 1980; Waterhouse, 1972).

Among the analyzed parameters, *Rvk* plays a particularly important role in contact fatigue, as it represents the valley depth and may be associated with lubricant retention or crack initiation sites under cyclic loading.

In summary, the progressive reduction of surface roughness throughout the manufacturing chain is essential for the mechanical performance of components. In particular, for applications under cyclic contact loading, controlling surface parameters such as *Ra*, *Rk*, *Rpk*, and *Rvk* is essential to reduce crack initiation points, distribute loads more evenly and maximize component durability.

5.1.4 Hardness Analysis

At the end of the manufacturing chain, the specimens were evaluated in terms of microhardness. The microhardness profiles were measured along the longitudinal cross section of the samples and are shown in Figure 5-11. These measurements were intended to evaluate the effects of the post-processing strategies adopted for the BJT_D, and BJT_RS conditions. They provided insights into how surface densification and the additional shot peening step influence the hardness near the surface and its gradient toward the core, which is relevant to fatigue initiation mechanisms.

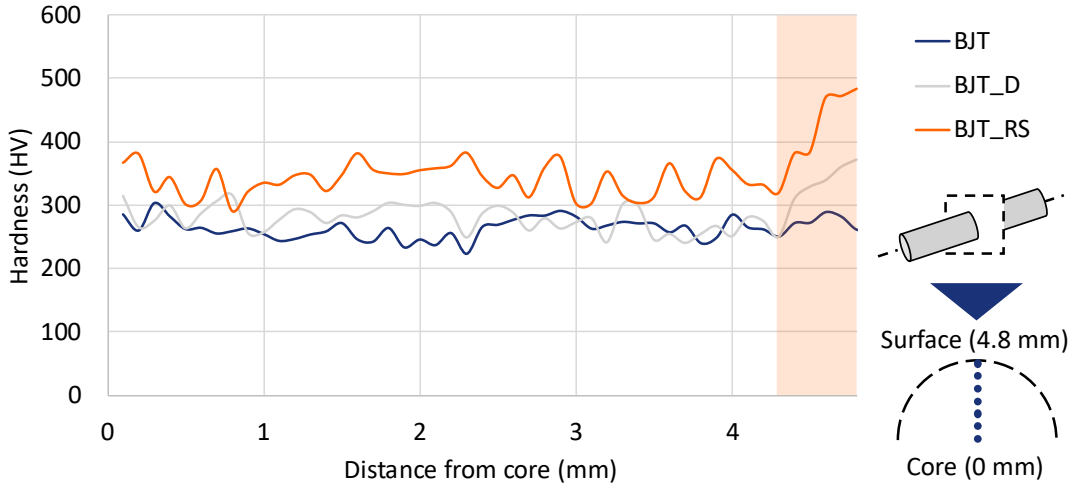

Figure 5-11: Hardness profiles across the cross-sections of the ball rod for BJT, BJT_D, and BJT_RS conditions. Surface hardening increases progressively from BJT to BJT_D due to densification, and reaches higher values in BJT_RS, likely as a result of the heat treatment and the surface work hardening promoted by consecutive SP.

Figure 5-11 shows the hardness maps obtained for the three manufacturing routes. The BJT condition, representing the as-built, exhibits a highly heterogeneous hardness distribution, with values typically ranging from 250 to 350 HV. This irregularity is attributed to the intrinsic porosity of the parts. Notably, no distinct hardened layer is formed in this condition, indicating insufficient reinforcement near the surface.

In contrast, the BJT_D condition, which includes a surface densification step by SP, shows a clear improvement in hardness distribution. A more continuous hardened region is observed along the outer perimeter, with values reaching approximately 450 HV. This behavior confirms the effectiveness of shot peening in promoting localized plastic deformation and densification, contributing to increased hardness near the surface.

The BJT_RS condition exhibits distinct behavior. In this case, a marked increase in hardness is observed not only near the surface but also throughout the cross-section, with mean value of 347 HV. This is explained by the fact that BJT_RS is the only condition subjected to a heat treatment step before the final shot peening, which is not applied to the other samples. Unlike the previous conditions, the elevated hardness in the core is primarily attributed to the application of a heat treatment, which promotes precipitation hardening in the 17-4PH steel. Therefore, the overall hardening effect results from the synergistic contribution of both precipitation mechanisms and surface plastic deformation. The additional increase observed

near the surface is then attributed to the second SP process, which introduces localized plastic deformation and compressive RS, resulting in a reinforced surface layer.

These results confirm that the combined application of heat treatment, densification, and shot peening acts synergistically to improve both the bulk and surface mechanical properties of binder jetting components, especially in terms of hardness and likely fatigue performance.

5.1.5 Summary

This section addressed the first research question (RQ1) by evaluating how each post-processing stage modifies the surface integrity of BJT parts. The results demonstrate that each treatment step contributed progressively to enhancing key surface characteristics, improving the functional performance of the material.

The as-built condition presented a surface integrity characterized by high porosity, irregular pore morphology, a neutral RS state, high roughness and lack of surface hardening. All the referred factors are known to reduce fatigue strength. SP for densification produced a compacted surface layer, reducing porosity and shifting the pore morphology to spherical and equiaxial shapes. This morphological refinement mitigated stress concentration sites and led to a measurable increase in hardness near the surface. In addition, a compressive residual stress state was induced, contributing to greater mechanical stability.

A second SP step, specifically configured to maximize compressive RS induction, further increased the compressive RS, especially in the subsurface region. This treatment deepened the compressive layer, preserving a significant magnitude of RS even after the final manufacturing stage of grinding.

Surface roughness evolved throughout the treatments, initially increasing due to the impacts of SP. Iy was, however, minimized by the grinding step, which produced a uniform and smooth surface with low Rk, Rpk, and Rvk values. This final condition favors the uniform distribution of contact stresses and reduces potential local crack initiation sites. At the same time, microhardness measurements confirmed a progressive hardening effect from the as-built to the post-processed state, particularly in the densified surface region, evidencing localized plastic deformation.

In summary, the combination of shot peening for densification and RS induction, followed by grinding, significantly improved the surface integrity of the BJT parts. These improvements, quantified by reductions in porosity and roughness, increases in hardness, and the establishment of the compressive RS state, validate the effectiveness of the proposed post-

processing strategy in modifying and improving the surface integrity properties of BJT components under the specific conditions investigated.

5.2 Fatigue Performance Analysis

After characterizing the post-processed surfaces in terms of their physical and geometric modifications, the next section of the Results and Discussion chapter presents the functional performance evaluation, with a specific focus on RCF. This analysis addresses the second research question, investigating how different post-processing strategies influence the fatigue behavior of components subjected to BJT. The analysis begins with a comparison between WS and BJT, with the aim of evaluating the difference in performance and confirming the tendency for premature failure of BJT parts compared to conventionally manufactured components.

Subsequently, the two post-processed BJT conditions are analyzed using the untreated BJT as a reference. The aim is to assess whether the incorporation of SP, first as a densification step and then as a residual stress inducing treatment, can improve the fatigue performance of BJT parts. To this end, RCF tests were carried out and the results were analyzed using *Weibull* statistics to quantify both the characteristic useful life and the dispersion of failures in each condition.

5.2.1 Fatigue Behavior – WS

This subsection presents the fatigue behavior under WS conditions, which serves as the reference performance level for this study. The WS samples were manufactured by conventional means, involving machining, heat treatment, grinding, and SP step to induce compressive RS. The results were statistically analyzed using a two-parameter *Weibull* distribution, allowing for the evaluation of both the characteristic life and the variability in failure behavior.

Under the RCF conditions tested, the WS samples exhibited a characteristic life (η) of approximately 214,090 cycles, with a *Weibull* slope (β) of 2.4, as shown in Figure 5-12. These values reflect fatigue resistance combined with a moderate level of variability, representative of robust but industrially realistic conditions.

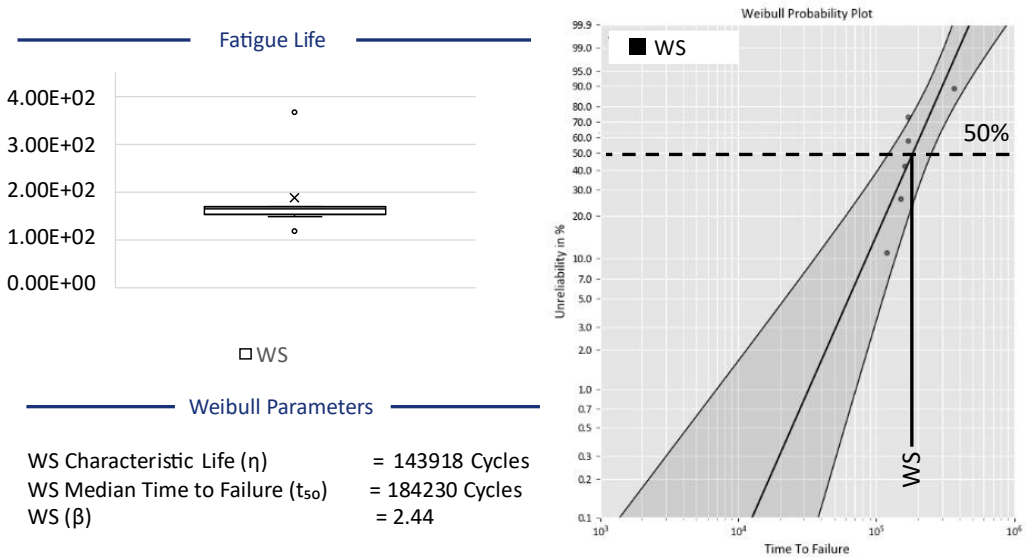

Figure 5-12: Fatigue life distribution and corresponding *Weibull* probability plot for WS samples.

The observed performance is attributed to the combination of factors achieved through this conventional processing route: a fully dense and homogeneous microstructure, resulting from hot rolling and controlled heat treatment, and the presence of compressive RS. Together, these characteristics contribute to the delay in crack initiation and the stabilization of crack propagation under cyclic loading conditions.

As noted in Section 5.1, the WS condition exhibited low surface roughness, consistent hardness, and the absence of surface defects, resulting in a favorable surface integrity profile for RCF applications.

In the context of this work, the WS condition serves as a technologically consolidated benchmark, establishing the target fatigue performance for comparison with additively manufactured components. The following sections investigate whether post-processing strategies applied to BJT parts can approach or exceed this reference in terms of fatigue life and structural reliability under rolling contact conditions.

5.2.2 Fatigue Behavior – Route A

The fatigue response of components manufactured by BJT without SP, route A, was evaluated under rolling contact conditions. Figure 5-13 shows route A exhibited a characteristic life (ɳ) of approximately 143,920 cycles, with a *Weibull* slope (β) of 3.2, indicating moderate

dispersion in failure occurrences. Although this slope suggests consistency among the samples, the overall fatigue life remained limited.

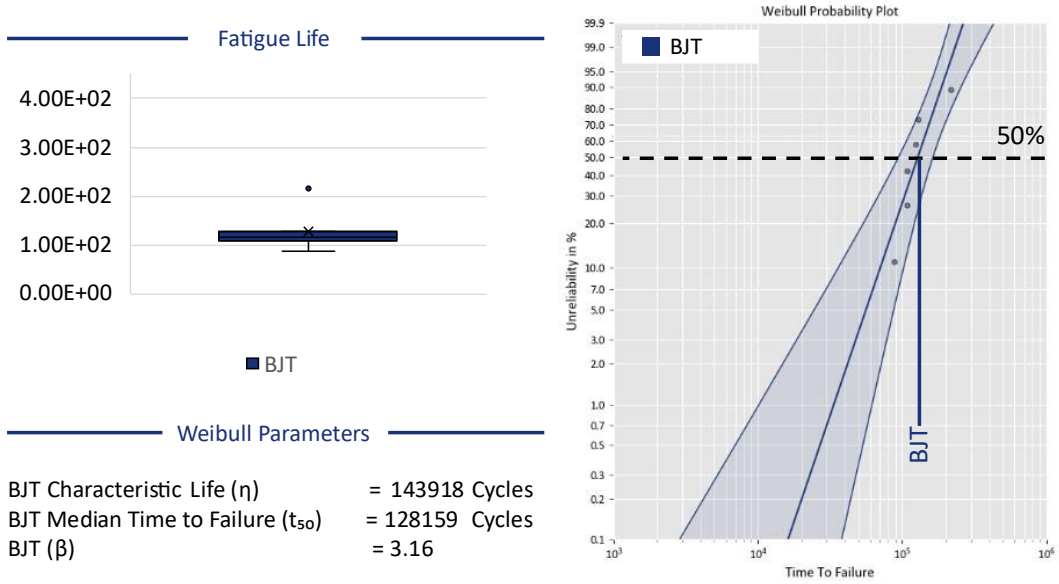

Figure 5-13: Fatigue life distribution and corresponding *Weibull* probability plot for BJT samples.

This behavior is in line with the results of the surface integrity analysis discussed in Section 5.1, where BJT samples exhibited high subsurface porosity, with irregular, interconnected pores. The absence of SP left these defects unchanged, resulting in a microstructure prone to high stress concentration and early crack initiation.

This trend is also corroborated by the literature, which identifies porosity as the main limiting factor in the fatigue life of components produced by powder metallurgy and AM. Dahmen et al. (2021) demonstrated that materials with lower density exhibit early crack nucleation at the edges of pores, followed by accelerated propagation under cyclic loading. These mechanisms lead to premature failure, even under pure rolling conditions. Similarly, Mostafaei et al. (2018) observed inferior fatigue performance in components manufactured by BJT, with significantly earlier failures compared to cast and post-processed counterparts. The authors attributed this reduced fatigue resistance to the presence of surface-connected pores, high roughness, and the absence of post-processing heat or mechanical treatments.

The absence of SP resulted in low surface hardness and no meaningfully beneficial RS state. Combined with porosity, these characteristics created ideal conditions for early crack nucleation and unstable propagation. Thus, the fatigue observed here reinforces the need for

customized post-processing strategies to improve surface integrity and enhance the functional performance of BJT components.

5.2.3 Fatigue Behavior – Route B

Route B, BJT_D condition, refers to components subjected to mechanical surface treatment by SP prior to heat treatment, with the main objective of promoting surface densification. This process aims to reduce the severity and connectivity of surface and subsurface porosity without altering the core of the material.

As shown in Figure 5-14, the application of this treatment resulted in a characteristic life ($\hat{\eta}$) of approximately 197,441 cycles, reflecting an increase of 37% compared to the untreated BJT condition. In addition, the *Weibull* slope increased from $\beta = 3.2$ to $\beta = 5.5$, indicating a notable reduction in the variability of failure times and suggesting improved uniformity in surface integrity among the samples.

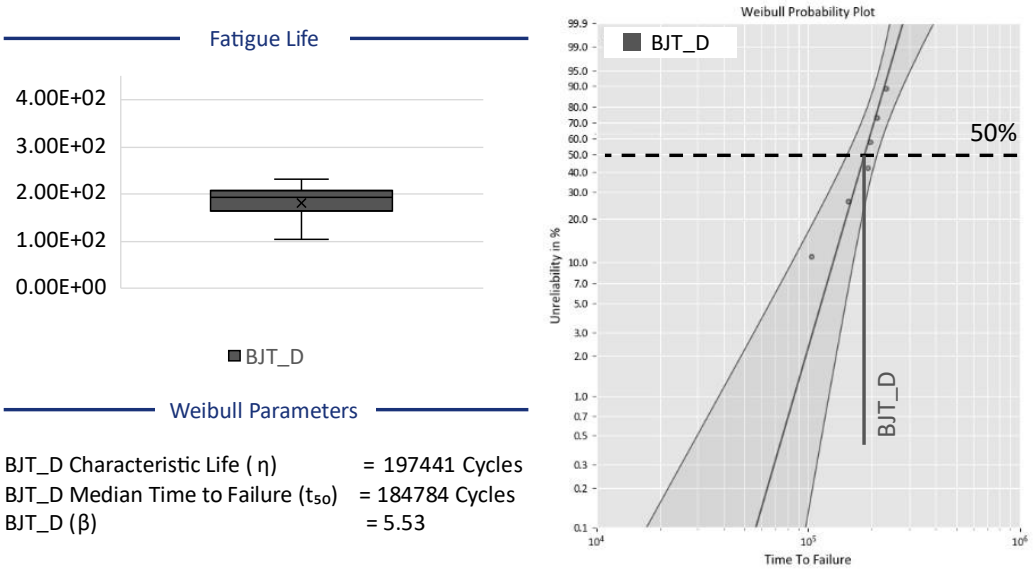

Figure 5-14: Fatigue life distribution and *Weibull* probability plot for BJT_D samples. The analysis shows improved consistency and increased characteristic life after densification.

Although the shot peening process in this case was not primarily intended to induce compressive RS, it induced substantial localized plastic deformation. This led to a set of beneficial surface modifications: closure of surface and near-surface pores, reduction of discontinuities inherited from the sintering process, and a measurable increase in surface hardness. These combined effects act to mitigate stress concentration factors and delay the onset

of fatigue cracks, which is particularly important in components produced by BJT, which are characterized by heterogeneous defect distributions.

This behavior is consistent with previous findings in the literature. Harding et al. (2017) reported a 29% increase in rotary bending fatigue resistance after SP, attributing it to both the modification of the topography and the secondary effect of compressive RS, even without material removal. Denti et al. (2019), used Ti6Al4V parts produced by AM, observed an increase of up to 150% in fatigue life due to pore closure, reduced roughness, and surface hardening. Uzan et al. (2018) similarly demonstrated that SP contributed to more consistent fatigue behavior in LPBF-manufactured AlSi10Mg samples by reducing roughness and improved RS state.

In the present study, the increase in fatigue life and the reduction in failure variability confirm that surface densification alone is capable of significantly altering the fatigue behavior of BJT parts. The greater homogeneity among the samples likely results from the mitigation of pore size variability and morphological irregularities, along with the improvement of surface mechanical properties.

However, the performance of route B remains inferior to that of the WS condition, suggesting that surface densification, while effective, does not completely overcome the structural limitations imposed by the BJT process. These results reinforce the importance of exploring complementary strategies, to further improve fatigue performance.

5.2.4 Fatigue Behavior – Route C

Route C, the BJT_RS condition, builds upon Route B by incorporating a second SP step applied after heat treatment, this time explicitly designed to induce compressive RS. While the first SP stage focused on surface densification through localized plastic deformation, the second was intended to refine the RS state near the surface, aiming to enhance fatigue resistance by reducing the effective tensile stresses acting on critical subsurface regions where crack nucleation typically occurs.

Figure 5-15 shows the fatigue results for this condition. The application of a second stage of SP led to a moderate increase in characteristic life, from $\hat{\eta}$ = 197,441 cycles (BJT_D) to $\hat{\eta}$ = 226,895 cycles in BJT_RS. When compared to the untreated route A, BJT condition, this represents an overall improvement of 57%. Notably, this is also the only BJT-based condition that surpassed the fatigue life of the conventionally manufactured WS reference. These findings

confirm that additional mechanical processing can further extend the service life of the component under RCF, especially when surface and subsurface properties are synergistically optimized. However, this gain was accompanied by a sharp decline in the *Weibull* slope, from $\beta = 5.5$ to $\beta = 2.2$, indicating a significant increase in the variability of failure times.

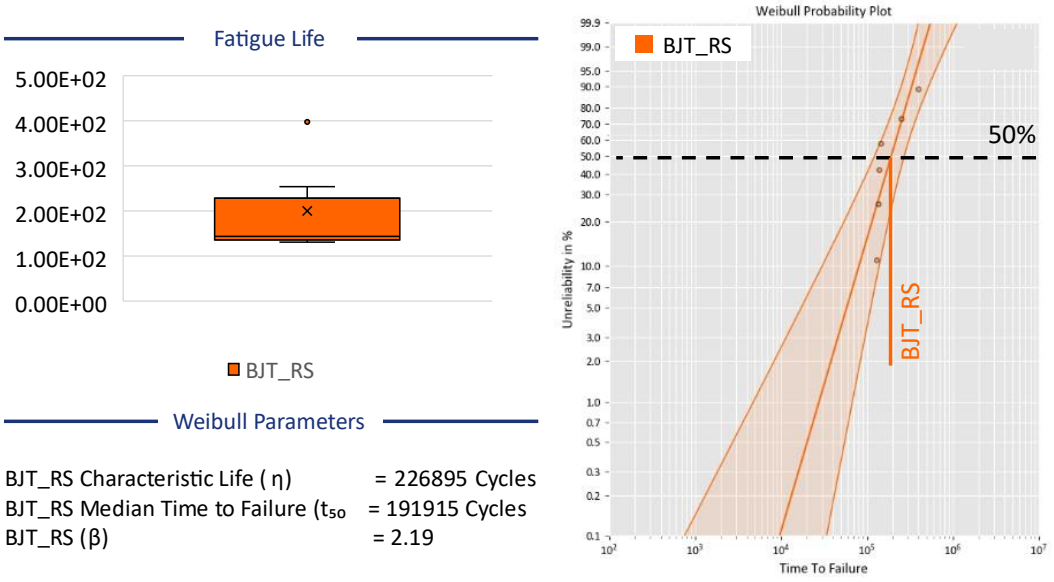

Figure 5-15: Fatigue life distribution and *Weibull* probability plot for BJT_RS samples. The data reveal enhanced fatigue performance and reduced scatter following residual stress treatment.

This behavior highlights a critical point in fatigue analysis. Resistance to RCF is governed by a complex interaction of factors, and the presence of compressive RS alone is not sufficient to guarantee improved or reliable performance.

As discussed in Section 5.1, the second stage of SP did not further densify the surface, nor did it alter the hardness values compared to the BJT_D condition. Its main contribution is the redistribution and reinforcement of compressive RS.

This reinforces what has been widely observed in literature. Fatigue in AM materials is a multifactorial phenomenon, sensitive not only to the presence of compressive RS but also to its compatibility with other surface and subsurface characteristics. Uzan et al. (2018) demonstrated that the beneficial effects of SP on LPBF parts were consistent only when the process also reduced roughness and alter pore morphology. Similarly, Denti et al. (2019) concluded that SP was only effective in improving the fatigue life of PBF samples when it acted synergistically on multiple parameters, including pore morphology and hardness. Harding et al.

(2017) also warned that RS may not produce positive effects if it is not properly integrated into the microstructural response of the material. Martin et al. (2022) further emphasized the importance of synergy in surface treatment, especially in porous structures.

In the present study, route C showed the highest average life among the three BJT-based processing chains, demonstrating the potential of layered mechanical treatments to progressively improve fatigue behavior. However, the increase in dispersion highlights a trade-off, while some regions may benefit from RS state refinement, others may accumulate local incompatibilities.

This result suggests that, although the application of multiple SP stages may be beneficial, strict control of process uniformity and surface integrity is essential. Unlike route B, where the impact of surface densification was relatively homogeneous, route C appears to be more sensitive to processing variability, where surface properties evolve from a porous and mechanically non-uniform baseline.

In summary, Route C demonstrated that additional mechanical post-processing can significantly increase the average fatigue life of BJT components. Most importantly, it was the only condition that outperformed the conventional WS reference, revealing that a well-designed combination of densification and residual stress induction can surpass even established industrial manufacturing routes in rolling contact fatigue resistance. This highlights the practical potential of such post-processing strategies for demanding applications in high-performance components.

5.2.5 Rolling Contact Fatigue Damage Morphology

While the previous section addressed the statistical analysis of fatigue life using *Weibull* distributions, this section focuses on the damage characteristics associated with RCF. By examining the failure surfaces of tested specimens, it is possible to identify differences in damage morphology and infer dominant crack initiation mechanisms for each manufacturing route. These observations provide a microstructural perspective on the failure processes and complement the quantitative fatigue life data. Figure 5-16 shows representative images of the regions of fatigue failure due to rolling contact in the different manufacturing routes studied.

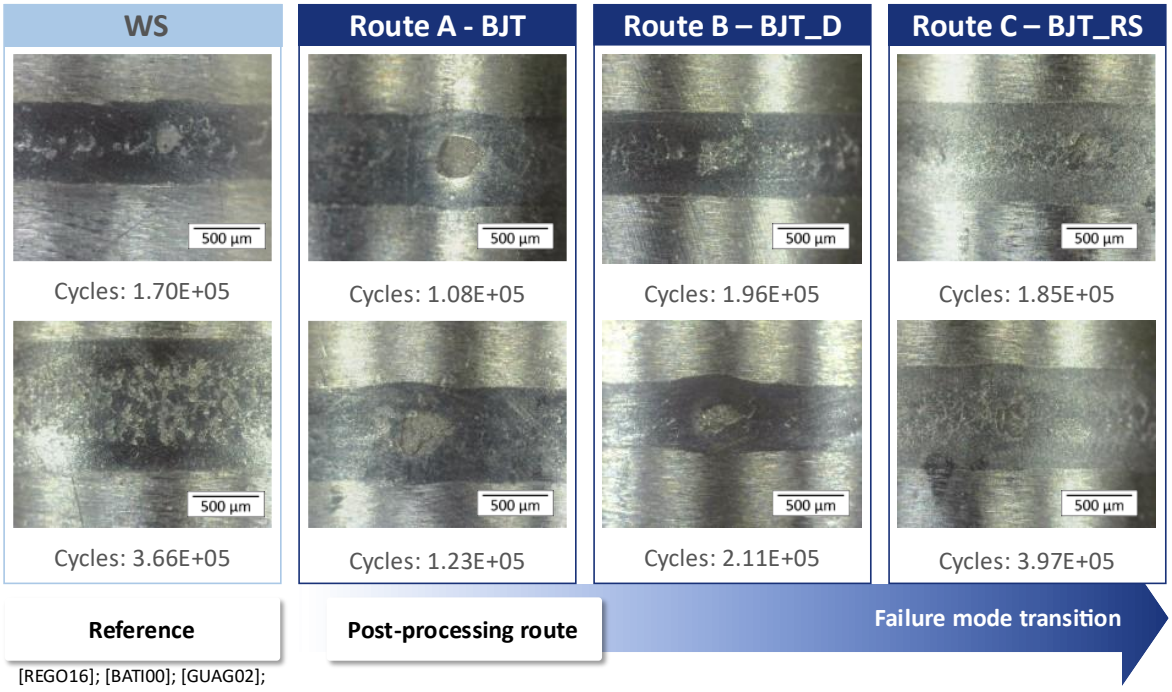

Figure 5-16: Optical images of rolling contact fatigue failure regions and corresponding number of cycles to failure for each manufacturing route. The upper and lower images represent two distinct tested samples for each condition, selected to illustrate the variability in failure morphology within the same route.

In the optical images shown in Figure 5-16, the darkened bands represent the regions subjected to rolling contact during the RCF tests. These bands concentrate the surface damage and mark the zone of highest mechanical interaction between the component and the counterbody.

The width of the contact band did not show a consistent correlation with fatigue life or hardness. Although it was initially expected that Route A would have the widest band, due to the absence of densified layer and consequently lower hardness, this was not observed. In fact, Route C, which had the longest average fatigue life, also had relatively wide damage bands. A plausible explanation is that Route A failed too early to fully develop an extensive contact track, while Route C withstood more cycles and, despite its harder surface, underwent more progressive accumulation of plastic deformation.

In route A, larger fractures were observed, with irregular edges and characteristics compatible with subsurface nucleation. Although the exact depth of the crack origin cannot be determined solely from optical images, in porous materials, nucleation typically occurs around 100 µm below the surface under cyclic contact loading conditions (Holmberg *et al.* 2019). The

damage observed suggests that the internal pores acted as crack initiators, leading to localized structural collapse, characterized by abrupt and catastrophically concentrated failures.

With the introduction of surface densification by SP on route B, a significant transformation is observed in both the morphology and location of the failures. As shown in Figure 5-3, the surface region becomes substantially more compact, with more than 99% densification. Although the densified layer is not entirely free of porosity, the remaining pores are smaller, less irregular, and more uniformly distributed compared to route A.

This densified layer is upper 300 μm and alters the conditions for crack initiation. It reduces the prevalence of large, interconnected pores in the 100 μm subsurface zone. As a result, the classic subsurface initiation mechanism becomes less dominant, and failure tends to originate closer to the surface, potentially from smaller residual pores still present in the densified layer.

In addition, SP induces localized plastic deformation that leads to an increase in surface hardness, increasing resistance to crack initiation under cyclic contact stresses. Consequently, a change in the damage is observed: cracks originate at shallower depths, propagate more gradually, and lead to longer fatigue lives compared to route A.

In route C, which combines surface densification and the induction of compressive RS, the damage observed is even further reduced. Although the failures are not visually identical to those observed in the WS condition, they are more similar in terms of distribution and extent, with a clear mitigation of the subsurface damage observed in route A. The combination of the densified layer with the compressive RS field acts synergistically to contain crack nucleation and growth. This containment not only delays the onset of failure but also modifies its nature, instead of localized and deep failures, more homogeneous surface damage is observed along the bearing track.

This transition in failure behavior has important implications for component reliability. Catastrophic fatigue failure, observed in route A, abruptly compromises the integrity of the component. In route B and route C, however, failure occurs progressively, with increasing surface damage, which allows for greater predictability and potential for preventive maintenance. This progressive damage observed in the peened conditions is consistent with the literature on shot-peened components. As shown in Figure 5-17, the damage patterns observed in Routes B and C resemble those reported by Batista *et al.* (2000), Guagliano, Riva and Guidetti (2002), and Lv, Lei and Sun (2015), where surface treatments promote a transition from deep, localized failures to more distributed and superficial damage. The similarities

between the present results and these references reinforce the effectiveness of the mechanisms applied here, namely pore closure and compressive residual stress induction, in altering the failure behavior.

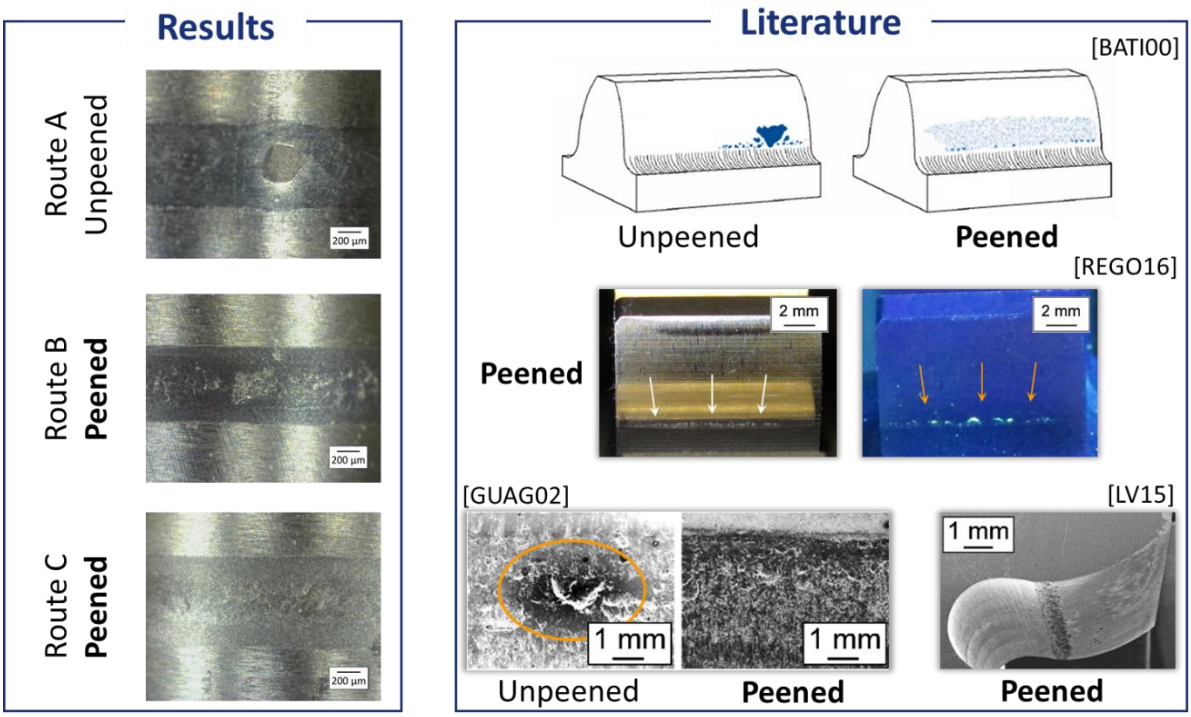

Figure 5-17: Comparative damage morphology between experimental results and literature references. On the left, damage progression across Routes A, B, and C; on the right, representative failure patterns from unpeened and peened surfaces as reported by Rego (2016), Batista *et al.* (2000), Guagliano et al. (2002) and Lv *et al*. (2015).

These experimental results demonstrate that Route C not only improved fatigue life among the BJT conditions, but also outperformed the WS reference, confirming that the mitigation mechanisms applied can surpass conventional manufacturing benchmarks in terms of contact fatigue resistance.

As a consolidated hypothesis, it is proposed that the closure of pores by surface densification prevents the emergence of the deep and critical damage, while the induction of compressive RS stabilizes the remaining pores, preventing their coalescence and limiting the propagation of cracks. This combination alters the damage of the component, promoting greater durability, greater failure predictability, and, consequently, greater structural reliability for gears manufactured by BJT.

5.2.6 Integrated Discussion

The results of the RCF tests across all investigated conditions demonstrate the progressive influence of each post-processing strategy on both the average fatigue life and the consistency of failure behavior. Figure 5-18 summarizes fatigue life distributions for each condition using a box plot, allowing for a direct and intuitive comparison of central tendency and variability.

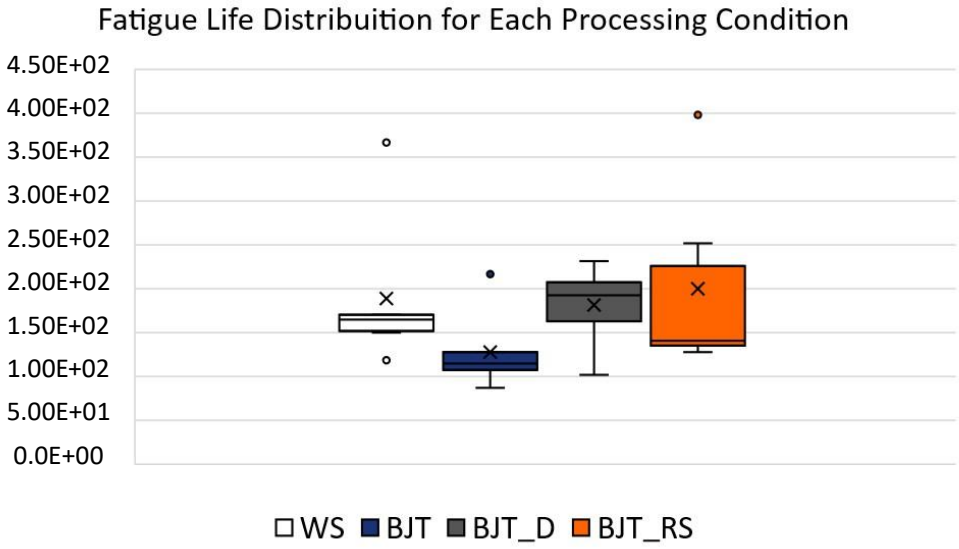

Figure 5-18: Box plot of fatigue life distribution for each processing condition

The WS condition served as a performance reference. It demonstrated a characteristic life of approximately 214,090 cycles and a Weibull slope of $\beta = 2.4$, reflecting a combination of fatigue resistance and moderate dispersion. This performance is attributed to its refined microstructure, low porosity, and controlled heat treatment and finishing processes, which together ensure a stable surface condition with minimized defects.

In contrast, route A, showed a substantial reduction in fatigue life and a slightly higher slope. The lower fatigue resistance is directly linked to the porosity, and the absence of compressive residual stresses. The relatively narrow β value, despite the low performance, reflects the consistently poor surface integrity in all route A samples.

The introduction of surface densification in route B significantly improved the durability and reliability of the components. The characteristic life increased to $\hat{\eta} = 197{,}441$ cycles and

the slope to $\beta = 5.5$, indicating a highly uniform fatigue response among the samples. This result confirms the effectiveness of localized plastic deformation in closing pores, reducing discontinuities, and improving hardness. The narrower failure distribution suggests a homogenization of surface integrity, even in a material originally characterized by a heterogeneous defect network.

Route C, incorporating a second SP step, achieved the highest mean fatigue life. However, this improvement came at the cost of a significant increase in dispersion. While some specimens clearly benefited from the refinement of the compressive RS state, others exhibited premature failures. This suggests that the second SP introduced or amplified local variability, possibly due to interactions with preexisting surface heterogeneities or inconsistent stress redistribution.

These results confirm that the fatigue behavior of BJT components is governed by the collective effect of surface integrity parameters, including porosity, hardness, RS, and their spatial distribution. Densification through SP has been shown to be a key factor in improving performance, with measurable benefits in both crack resistance and statistical reliability. The additional gain observed in route C reinforces the relevance of RS manipulation but also serves as a cautionary example of the complexity involved in applying sequential treatments to materials with non-uniform microstructures.

From a design perspective, these findings suggest that the optimal processing route depends not only on achieving the highest mean life, but also on controlling variability to ensure predictable in-service performance. Route B offered the most consistent results, while route C revealed the greatest potential when process control is adequate. Route A, in contrast, clearly lacks the surface quality necessary for reliable operation under RCF conditions, corroborating the broader consensus that post-processing is essential in the AM of functional components. These findings collectively demonstrate that AM components, when subjected to tailored, multi-step post-processing, can achieve and even exceed the fatigue resistance of parts produced by mature, conventional manufacturing chains.

The combination of the box plot presented in Figure 5-18 and the *Weibull* probability in analysis Figure 5-19, reinforces the conclusion that fatigue performance in AM components is not governed by a single factor, but rather by the complex interaction between surface integrity parameters such as porosity, hardness, roughness, and RS. These methods provide both intuitive and statistical perspectives, allowing for a clear comparison of the characteristic life and the dispersion of failure behavior across all processing routes.

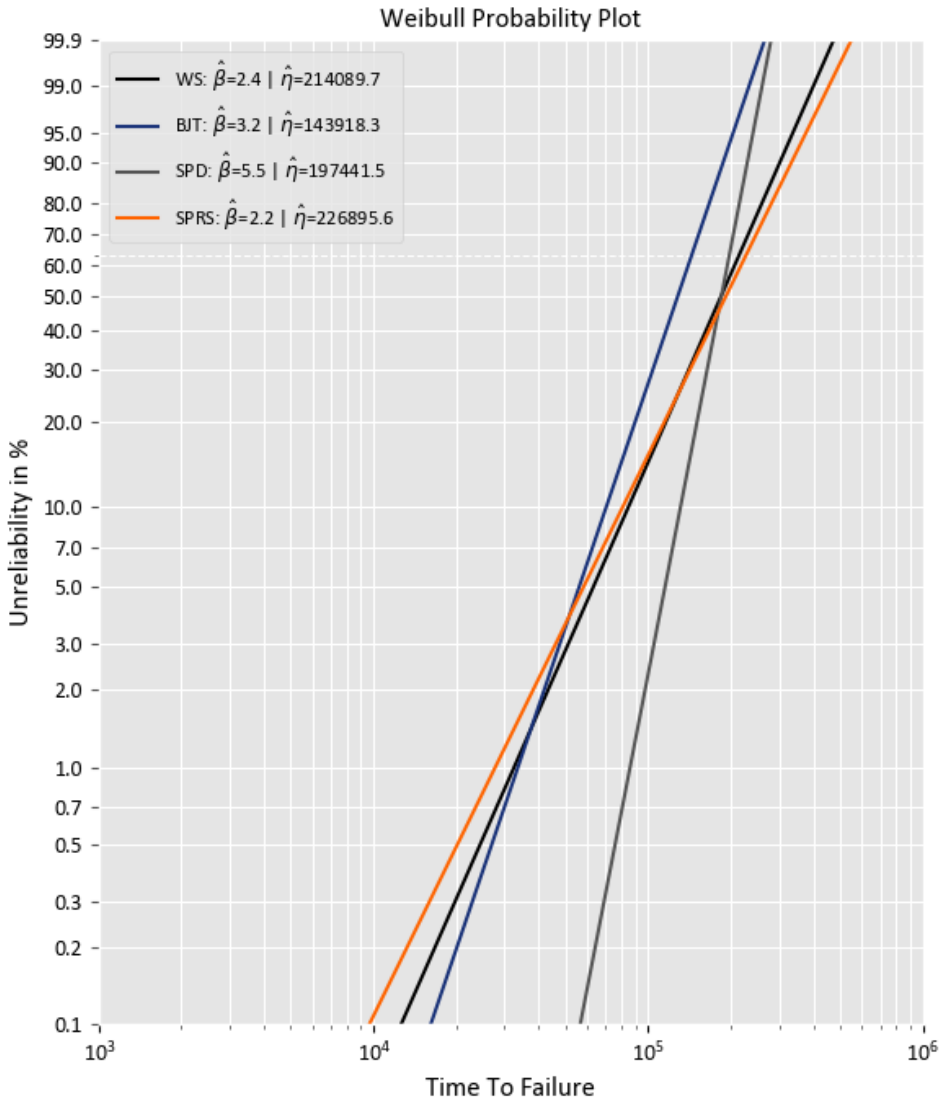

Figure 5-19: Statistical approach to the results based on *Weibull* distribution method.

6 Conclusion and Outolooks

This study aimed to evaluate how SP strategies could improve the mechanical performance of components produced by BJT, with particular emphasis on surface integrity and RCF resistance. It was expected that the application of SP in distinct stages, aimed at surface densification and residual stress induction, would mitigate the deleterious effects of porosity, improving fatigue performance.

The hypothesis of this study stated that SP could improve the fatigue resistance of BJT parts by addressing their two main limitations: surface-connected porosity and lack of beneficial RS states. The hypothesis that a customized sequence of SP treatments would reduce the mechanical effects of porosity and induce compressive RS near the surface, both of which retard crack nucleation and slow down crack growth. This approach aimed to transform inherently fragile BJT components into structurally viable parts suitable for demanding contact fatigue applications.

The results confirmed these expectations. The SP for densification effectively reduced pore size and increased circularity, contributing to a more resistant surface. The second application of SP to the production chain, although not intended to alter porosity, fulfilled its designed purpose of enhancing the compressive RS state. This improvement built upon the initial RS state already induced by the first SP process. These effects were most prominent in the BJT_RS condition, which exhibited the highest characteristic life among all BJT samples. However, both SP conditions also showed a noticeably higher failure dispersion when compared to the WS and as-built BJT conditions. This indicates that, although SP improved average fatigue performance, it also introduced greater variability. Such inconsistency highlights the sensitivity of post-processing outcomes to initial part quality and reinforces the need for tighter process control to ensure reliable performance gains.

When the results from each section are integrated, a broader understanding becomes evident. Surface densification and RS induction are not independent phenomena. Surface integrity analysis and fatigue tests converge to show that post-processing routes must be designed considering not only geometric correction or local reinforcement, but systemic modification of the failure scenario.

This work therefore presents a transversal synthesis that articulates localized improvements with overall enhancements of fatigue performance. The partial results derived from each analytical stage converge to support a central conclusion: the effectiveness of post-

processing resides not in the optimization of individual surface or subsurface parameters. They must consider the integrated contribution to altering the fundamental mechanisms that govern crack initiation and propagation in additively manufactured components.

This study offers both technological and scientific contributions. Technologically, it establishes a replicable post-processing route that significantly enhances the mechanical performance of low-density steel components produced via BJT. Scientifically, it increases the understanding of surface integrity evolution in indirect AM, providing experimental evidence that supports a comprehensive approach to post-processing. By integrating surface densification and RS optimization, the results indicate a promising strategy for the functional qualification of porous AM components and potentially extending its applicability beyond the BJT process.

Future research should consider optimizing the second stage of SP, including a systematic evaluation of process parameters to maximize the combined effects of surface densification and RS induction. The exploration of surface treatments, capable of tailoring subsurface properties in a spatially controlled manner, could also lead to further improvements in fatigue resistance. In addition, assessing the long-term stability of induced RS under realistic service conditions would provide critical insights into the durability of post-processed components.

Based on the current results, future studies could extend the investigation to actual gear geometries, validating the effectiveness of the proposed strategies under more representative mechanical and geometrical conditions. These developments would help bridge the gap between fundamental specimen-scale characterization and real-world applications, particularly within the context of durability in transmission components.

Complementary to the post-processing route, improvements in the manufacturing chain itself may be pursued through the optimization of powder deposition and sintering parameters. Improvements in the uniformity of the green part and the sintered density could extend the benefits of subsequent treatments. Furthermore, the integration of SP with additional finishing methods may offer hybrid surface engineering solutions capable of addressing both roughness and defect morphology in an efficient and scalable manner. These advances are particularly promising for applications in the field of electromobility, which demand scalable manufacturing of lightweight and high-performance components capable of withstanding severe mechanical conditions.

In summary, the results of this thesis validate the hypothesis that strategic post-processing can overcome critical limitations of BJT manufacturing. By understanding and

manipulating the relationship between surface integrity and fatigue behavior, this research contributes not only to the advancement of finishing practices in additive manufacturing, but also to the broader field of durability engineering for AM.

References

ALBAN, L.E. Failure of Gears. In: ASM Handbook Vol 11 "**Failure Analysis and Prevention**". Materials Park: ASM International, 2002. P. 2558-2603

ALMANGOUR, Bandar; YANG, Jenn-Ming. **Improving the surface quality and mechanical properties by shot-peening of 17-4 stainless steel fabricated by additive manufacturing**. Materials & Design, v. 110, p. 914-924, 2016.

ALMEN, J. O., & BLACK, P. H. (1963). **Residual Stresses and Fatigue in Metals**. McGraw-Hill.

ALTAN, T., NGAILE, G., & SHEN, G. (2005). **Cold and Hot Forging: Fundamentals and Applications.** ASM International.

ASLANTAŞ, K.; TAŞGETIREN, S. **A study of spur gear pitting formation and life prediction**. Wear, v. 257, n. 11, p. 1167-1175, 2004.

ASTM International. (2023). **B962-23: Standard Test Methods for Density of Compacted or Sintered Powder Metallurgy (PM) Products Using Archimedes' Principle**.

ANTOINE, F.; BESSON, J.M. **Simplified Modellization of gear micropitting**. In: Proceedings of the Institution of Mechanical Engineers Vol. 216. Aerospace Engineering, 2002. p. 291-302.

BAI, Yun; WAGNER, Grady; WILLIAMS, Christopher B. **Effect of particle size distribution on powder packing and sintering in binder jetting additive manufacturing of metals**. Journal of Manufacturing Science and Engineering, v. 139, n. 8, p. 081019, 2017.

BATISTA, A. C.; DIAS, A. M.; LEBRUN, J. L.; LE FLOUR, J. C.; INGLEBERT, G. **Contact fatigue of automotive gears: evolution and effects of residual stresses introduced by surface treatments.** Fatigue & Fracture of Engineering Materials & Structures, Vol. 23. Wiley, 2000. p. 217–228.

BEHRENS, B.-A. et al. **Numerical investigations on the fatigue failure of forging tools due to thermo-mechanical cyclic loading**. International Journal of Material Forming, v. 3, p. 339-342, 2010.

BERGMAN, Ola; BERGMARK, Anders. **Influence of microstructure on the fatigue performance of PM steels.** Advances in Powder Metallurgy and Particulate Materials, n. 7, p. 7-270, 2003.

BLANCO, L. et al. **Quantitative evaluation of porosity effects in sintered and heat treated high performance steels**. Powder metallurgy, v. 48, n. 4, p. 315-322, 2005.

BOSTON CONSULTING GROUP. **Mobility in the Public Sector**. Available at: https://www.bcg.com/industries/public-sector/mobility. Acess on: 04/02/2025.

BOSTON CONSULTING GROUP. **Rewiring the Auto Industry for the Electric, Connected Future**. Available at: https://www.bcg.com/publications/2023/rewiring-auto-industry-electric-connected-future. Access on: 22/07/24.

BOX, George E. P.; HUNTER, J. Stuart; HUNTER, William G. **Statistics for experimenters: design, innovation, and discovery**. 2nd ed. Hoboken: Wiley-Interscience, 2005. 672 p. ISBN 978-0-471-71813-0.

BRECHER, C.; RENKENS, D.; LÖPENHAUS, C. **Method for Calculating Normal Pressure Distribution of High Resolution and Large Contact Area**. Journal of Tribology, v. 138, n. 011402, p. 1–9, Jan. 2016.

BRINKSMEIER, E. et al. **Ultra-precision grinding**. CIRP annals, v. 59, n. 2, p. 652-671, 2010

BUDINSKI, K. G., & BUDINSKI, M. K. (2010). **Engineering Materials: Properties and Selection (9th ed.).** Pearson.

CAMMETT, J. **Shot peening coverage – the real deal**. *The Shot Peener*, v. 21, n. 3, p. 8–14, Summer 2007. Available at: https://www.shotpeener.com/magazine/2007/07/Summer-2007.pdf. Accessed on: May 7, 2025

CAMPBELL, J. (2015). **Complete Casting Handbook: Metal Casting Processes, Metallurgy, Techniques and Design (2nd ed.).** Butterworth-Heinemann.

CRISCUOLO, I., CARNEIRO, F., GUIMARÃES, G., MASCHERONI, J., & REGO, R. (2023). **Indirect selective laser sintering: Modeling and analysis of surface densification by SP**. In International Conference on Gears 2023 (pp. 1681-1698).

CIPOLLONI, Giulia et al. **A quantitative characterisation of porosity in a Cr–Mo sintered steel using image analysis**. Materials characterization, v. 94, p. 58-68, 2014.

DAHMEN, T. et al. **Densification, microstructure, and mechanical properties of heat-treated MAR-M247 fabricated by Binder Jetting**. Additive Manufacturing, v. 39, p. 101912, 2021.

DALAEI, Kamellia; KARLSSON, Birger; SVENSSON, L.-E. Stability of SP induced residual stresses and their influence on fatigue lifetime. **Materials Science and Engineering: A**, v. 528, n. 3, p. 1008-1015, 2011.

DAVIS, J. R. (Ed.). (1998). **Metals Handbook Desk Edition (2nd ed.).** ASM International.

DEBROY, T., Wei, H. L., Zuback, J. S., Mukherjee, T., Elmer, J. W., Milewski, J. O., ... & Zhang, W. (2018). **Additive manufacturing of metallic components—Process, structure, and properties.** Progress in Materials Science, 92, 112–224

DEL GIUDICE, Lorenzo; VASSILIOU, Michalis F. **Mechanical properties of 3D printed material with binder jet technology and potential applications of additive manufacturing in seismic testing of structures.** Additive Manufacturing, v. 36, p. 101714, 2020.

DENKENA, B.; BIERMANN, D. **Cutting edge geometries**. CIRP annals, v. 63, n. 2, p. 631-653, 2014.

DENTI, Lucia; SOLA, Antonella. **On the effectiveness of different surface finishing techniques on A357. 0 parts produced by laser-based powder bed fusion: surface roughness and fatigue strength.** Metals, v. 9, n. 12, p. 1284, 2019.

DO, Truong; KWON, Patrick; SHIN, Chang Seop. **Process development toward full-density stainless steel parts with binder jetting printing.** International Journal of Machine Tools and Manufacture, v. 121, p. 50-60, 2017.

DOSSETT, Jon L.; TOTTEN, George E. (Ed.). **Steel heat treating fundamentals and processes**. Asm International, 2013.

DOURANDISH, Mahdi; GODLINSKI, Dirk; SIMCHI, Abdolreza. **3D printing of biocompatible PM-materials**. In: Materials science forum. Trans Tech Publications Ltd, 2007. p. 453-456.

DOYLE, Michael et al**. Effect of layer thickness and orientation on mechanical behavior of binder jet stainless steel 420+ bronze parts**. Procedia Manufacturing, v. 1, p. 251-262, 2015.

DU PLESSIS, Anton et al. **X-ray microcomputed tomography in additive manufacturing: a review of the current technology and applications.** 3D Printing and Additive Manufacturing, v. 5, n. 3, p. 227-247, 2018.).

DU PLESSIS, A., Glaser, D., Möller, H., Mathe, N., Tshabalala, L., Mfusi, B., & Mostert, R. (2019). **Pore closure effect of laser shock peening of additively manufactured AlSi10Mg**. 3D Printing and Additive Manufacturing, 6(5), 245-252.

DU, Wenchao et al. **Binder jetting additive manufacturing: Effect of particle size distribution on density.** Journal of Manufacturing Science and Engineering, v. 143, n. 9, p. 091002, 2021.

DUDLEY, D. W. (1994). **Handbook of Practical Gear Design**. CRC Press.

DUNSTAN, Matthew K.; PARAMORE, James D.; FANG, Z. Zak. **The effects of microstructure and porosity on the competing fatigue failure mechanisms in powder metallurgy Ti-6Al-4V.** International Journal of Fatigue, v. 116, p. 584-591, 2018.

EDER, Stefan J. et al. **Thermostat influence on the structural development and material removal during abrasion of nanocrystalline ferrite**. ACS applied materials & interfaces, v. 9, n. 15, p. 13713-13725, 2017.

EMADI, A. **Advanced Electric Drive Vehicles**. CRC Press, 2014.

FITZPATRICK, Michael E.; LODINI, Alain (Ed.). **Analysis of residual stress by diffraction using neutron and synchrotron radiation**. CRC Press, 2003.

FORD, Simon; DESPEISSE, Mélanie. **Additive manufacturing and sustainability: an exploratory study of the advantages and challenges**. Journal of cleaner Production, v. 137, p. 1573-1587, 2016.

FRAZIER, W. E. (2014). **Metal additive manufacturing: A review**. Journal of Materials Engineering and Performance, 23(6), 1917–1928

GIRISH, D. V.; MAYURAM, M. M.; KRISHNAMURTHY, S. **Influence of shot peening on the surface durability of thermomechanically treated En 24 steel spur gears**. Tribology International, v. 30, n. 12, p. 865-870, 1997.

GLOBAL WIND ENERGY COUNCIL. (2021). **Global Wind Report 2021**. Retrieved from https://gwec.net/global-wind-report-2021/.

GOHAR, Ramsey; RAHNEJAT, Homer. **Fundamentals of tribology**. World Scientific, 2018.

GOMES, Gilberto Martins de Oliveira. **The interaction between grinding and isotropic superfinishing in the gear manufacturing chain**. 2023. 132 f. Dissertation of Master of Science in Materials, Manufacturing, and Automation – Instituto Tecnológico de Aeronáutica, São José dos Campos.

GRIFFITHS, Brian. **Manufacturing surface technology: surface integrity & functional performance**. CRC Press, 2001

GROOVER, M. P. (2013). **Fundamentals of Modern Manufacturing: Materials, Processes, and Systems (5th ed.)**. John Wiley & Sons.

GUAGLIANO, M. (2001). **Relating Almen intensity to residual stresses induced by shot peening: A numerical approach.** Journal of Materials Processing Technology, 110(3), 277–286.

GUAGLIANO, M.; RIVA, E.; GUIDETTI, M. **Contact fatigue failure analysis of shot-peened gears**. Engineering Failure Analysis, Vol. 9. Elsevier Science Ltd., 2002. p. 147–158.

HOLMBERG, Anders; ANDERSSON, Michael; RUDOLPHI, Åsa Kassman. **Rolling fatigue life of PM steel with different porosity and surface finish.** Wear, v. 426, p. 454-461, 2019.

HSIAO, C. N.; CHIOU, C. S.; YANG, J. R. **Aging reactions in a 17-4 PH stainless steel**. Materials Chemistry and Physics, v. 74, n. 2, p. 134-142, 2002.

HUBER, Daniel; VOGEL, Lucas; FISCHER, Alfons. **The effects of sintering temperature and hold time on densification, mechanical properties and microstructural characteristics of binder jet 3D printed 17-4 PH stainless steel**. Additive Manufacturing, v. 46, p. 102114, 2021.

IEA. (2021). **Global EV Outlook 2021**, IEA, Paris https://www.iea.org/reports/global-ev-outlook-2021.

IEA. (2023), **Global EV Outlook 2023**, IEA, Paris https://www.iea.org/reports/global-ev-outlook-2023, Licence: CC BY 4.0

IMARC GROUP. **Gear Manufacturing Market by Product (Worm Gear, Bevel Gear, and Others), End User (Oil and Gas industry, Power Industry, Automotive, and Others), and Region 2024-2032.** Available at: https://www.imarcgroup.com/gear-manufacturing-market. Access on: 22/07/24.

IMARC GROUP. **Transmission Gear Manufacturing Plant Project Report 2024: Industry Trends, Plant Setup, Machinery, Raw Materials, Investment Opportunities, Cost and Revenue.** Available at: https://www.imarcgroup.com/transmission-gear-manufacturing-plant-project-report. Access on: 22/07/24.

INTERNATIONAL ORGANIZATION FOR STANDARDIZATION. ISO 13528:2022 – **Statistical methods for use in proficiency testing by interlaboratory comparison**. Geneva: ISO, 2022.

INTERNATIONAL ORGANIZATION FOR STANDARDIZATION. **ISO 281:2007 – Rolling bearings — Dynamic load ratings and rating life**. Geneva: ISO, 2007.

JBILY, Ing Dalia; AMAR, Ing Luc; SIMONNEAU, Ing André. **Experimental and Analytical Study of the Effect of Shot Peening on Gear Micropitting and Contact Fatigue Failure**. GEAR TECHNOLOGY, p. 43, 2024.

J.P. MORGAN. **Automotive Innovation.** Available at: https://www.jpmorgan.com/insights/global-research/autos/automotive-innovation. Access on: 22/07/24.

KALPAKJIAN, S., & Schmid, S. R. (2014). **Manufacturing Processes for Engineering Materials (6th ed.).** Pearson.

KELLENS, Karel et al. **Environmental impact of additive manufacturing processes: does AM contribute to a more sustainable way of part manufacturing?.** Procedia Cirp, v. 61, p. 582-587, 2017.

KIRK, D. **Quantification of shot peening coverage**. *The Shot Peener*, v. 28, n. 4, p. 22–34, Fall 2014. Available at: https://www.shotpeener.com/magazine/2014/04/Fall-2014.pdf. Accessed on: May 7, 2025.

KLEE L, BRIMMERS J, BERGS T. **Tooth root load capacity of additive manufactured gears**. In: Brecher C, Bergs T (eds) 9th WZL Gear Conference USA. Elgin, IL/ USA: Reishauer USA, July 21st/22nd 2022, pp 3–1–3–19, 2022.

KLEE, Lukas; BERGS, Thomas; SOLF, Mareike; BRIMMERS, Jens. **Binder jetting in gears**. Forschung im Ingenieurwesen, v. 87, p. 779–791, 2023.

LANGE, K. (1985). **Handbook of Metal Forming**. McGraw-Hill.

LAW, M.; LUZIN, V. **Effect of spatial variation of stress-free lattice spacings on measured residual stresses.** *Journal of Strain Analysis for Engineering Design*, v. 46, n. 8, p. 837–841, 2011.

LEUDERS, S., et al. (2013). **On the mechanical behaviour of titanium alloy TiAl6V4 manufactured by selective laser melting**. International Journal of Fatigue, 48, 300–307

LIN, Qinjie et al. **Effects of different shot peening parameters on residual stress, surface roughness and cell size.** Surface and Coatings Technology, v. 398, p. 126054, 2020.

LIU, H. et al. **A Review on Micropitting Studies of Steel Gears**. Coatings, v. 9, n. 1, p. 1–42, Jan. 2019.

LIU, Z. Y.; HE, Y.; FU, J.; QIN, J.; MA, Y. **The influence of layer thickness on the pore characteristics of binder jetting additive manufactured parts.** Materials, v. 10, p. 1124, 2017.

LV, Y.; LEI, L.; SUN, L. **Effect of shot peening on the fatigue resistance of laser surface melted 20CrMnTi steel gear.** Materials Science & Engineering A, Vol. 629. Elsevier Science Ltd., 2015. p. 8–15.

MARINESCU, Ioan D. et al. **Handbook of machining with grinding wheels**. Crc Press, 2006.

MAIRE, Eric; WITHERS, Philip John. **Quantitative X-ray tomography. Internation almaterials reviews**, v. 59, n. 1, p. 1-43, 2014

MCKINSEY & COMPANY. **Global Gear Manufacturing Market Overview**. Apr 2025. Available at: https://www.marketresearchfuture.com/reports/gear-manufacturing-market-31427. Access on: 10/04/2025.

MAITRA, G. M. (1994). **Handbook of Gear Design.** Tata McGraw-Hill Education.

MARTIN, Noémie et al. **Correlation between microstructure heterogeneity and multi-scale mechanical behavior of hybrid LPBF-DED Inconel 625**. Journal of Materials Processing Technology, v. 303, p. 117542, 2022.

MERLIN, Mattia et al. **Influence of Heat Treatment Parameters on the Microstructure of 17-4 PH Single Tracks Fabricated by Direct Energy Deposition**. Applied Sciences, v. 14, n. 2, p. 700, 2024.

MCKINSEY & COMPANY. **Shared mobility, sustainable cities, shared destinies**. 05 Jan. Available at: https://www.mckinsey.com/industries/automotive-and-assembly/our-insights/shared-mobility-sustainable-cities-shared-destinies. Access on: 05/12/2024.

MCKINSEY & COMPANY. **The mainstreaming of additive manufacturing.** 15 Mar. 2022. Available at: https://www.mckinsey.com/capabilities/operations/our-insights/the-mainstreaming-of-additive-manufacturing. Accessed on: 11 Dec. 2024.

MCKINSEY & COMPANY. **Why the automotive future is electric**. Available at: https://www.mckinsey.com/industries/automotive-and-assembly/our-insights/why-the-automotive-future-is-electric. Access on: 04/02/2025.

MICHAELS, Steven; SACHS, Emanuel M.; CIMA, Michael J. **Metal parts generation by three dimensional printing.** 1992

MIRACLE, Daniel B. et al. **ASM handbook**. Materials Park, OH: ASM international, 2001.

MITSUBAYASHI, Masahiko; MIYATA, Takashi; AIHARA, Hideo. **Phenomenal analysis of shot peening: analysis of fatique strength by fracture mechanics for shot-peened steel**. JSAE Review, v. 15, n. 1, p. 67-71, 1994.

MIYANAJI, Hadi. **Binder jetting additive manufacturing process fundamentals and the resultant influences on part quality**. 2018.

MONTGOMERY, Douglas C. **Design and analysis of experiments**. John wiley & sons, 2017.

MOSTAFAEI, Amir et al. **Characterizing surface finish and fatigue behavior in binder-jet 3D-printed nickel-based superalloy 625.** Additive Manufacturing, v. 24, p. 200-209, 2018.

MUHAMMAD, Waqas et al. **Effect of binder jetting microstructure variability on low cycle fatigue behavior of 316L.** Materials Science and Engineering: A, v. 839, p. 142820, 2022.

NEZHADFAR, P. D. et al. **Effect of heat treatment on the tensile behavior of 17-4 PH stainless steel additively manufactured by metal binder jetting**. 2021.

NEWAY PRECISION WORKS LTD. **17-4 PH Stainless Steel Powder Compression Molding Custom Power Tool Gears. 2025**. Available at: https://www.newayprecision.com/study-cases/17-4-ph-stainless-steel-powder-compression-molding-custom-power-tool-gears. Accessed on: May 6, 2025.

NICOLETTO, Gianni. **Smooth and notch fatigue behavior of selectively laser melted Inconel 718 with as-built surfaces.** International Journal of Fatigue, v. 128, p. 105211, 2019.

NGO, Tuan D. et al. Additive manufacturing (3D printing): A review of materials, methods, applications and challenges. **Composites Part B: Engineering**, v. 143, p. 172-196, 2018.

OLVER, A. V. **The mechanism of rolling contact fatigue: an update.** Proceedings of the Institution of Mechanical Engineers, Part J: Journal of Engineering Tribology, v. 219, n. 5, p. 313-330, 2005.

PANGBORN, R. N.; WEISSMANN, S.; KRAMER, I. R. **Dislocation distribution and prediction of fatigue damage.** *Metallurgical Transactions A*, v. 12A, p. 109–120, 1981.

PELLEGRINI, Alessandro et al. **Influence of aging treatments on 17–4 PH stainless steel parts realized using material extrusion additive manufacturing technologies**. The International Journal of Advanced Manufacturing Technology, v. 126, n. 1, p. 163-178, 2023.

PREVÉY, Paul S. **X-ray diffraction characterization of residual stresses produced by shot peening**. Shot Peener(USA), v. 15, n. 1, p. 4-8, 2001.

PROTO3000**. 17-4 PH Stainless Steel – Robust Metal 3D Printing Material.** 2025. Available at: https://proto3000.com/materials/17-4-ph-stainless-steel-dm-studiop-system/. Accessed on: May 6, 2025.

RACK, H. J.; KALISH, David. The strength, fracture toughness, and low cycle fatigue behavior of 17-4 PH stainless steel. **Metallurgical Transactions**, v. 5, n. 7, p. 1595-1605, 1974.

RADHAKRISHNAN, Jayaraj et al. **Microstructure and tensile properties of binder jet printed 17–4 precipitation hardened martensitic stainless steel.** Materials Science and Engineering: A, v. 860, p. 144270, 2022.

RAO, TV Ramana. **Metal casting: Principles and practice**. New Age International, 2007.

REGO, R. R. **A Call to the Gear Community: Addressing Residual Stresses in Design Standards.** Aachen Conference on Gear Production: Gear finishing technology and quality inspection, November 2022.

REGO, R**. Influência do uso de distribuição bimodal de classes de granalha no processo de shot peening sobre o perfil de tensões residuais de engrenagens**. Faculdade De Tecnologia SENAI Cimatec, 2016.

REGO, R. **Residual stress interaction in-between processes of the gear manufacturing chain**. Instituto Tecnológico de Aeronáutica, 2016.

SAE – SOCIETY OF AUTOMOTIVE ENGINEERS. ***SAE J443: Procedures for Using Standard Shot Peening Test Strip*****.** Warrendale, PA: SAE International, 2003.

SANGID, Michael D. et al. **ICME approach to determining critical pore size of IN718 produced by selective laser melting**. Jom, v. 72, p. 465-474, 2020.

SCHOINOCHORITIS, Babis; CHANTZIS, Dimitrios; SALONITIS, Konstantinos. **Simulation of metallic powder bed additive manufacturing processes with the finite element method: A critical review**. Proceedings of the Institution of Mechanical Engineers, Part B: Journal of Engineering Manufacture, v. 231, n. 1, p. 96-117, 2017.

SCHULZE, Volker. **Modern mechanical surface treatment: states, stability, effects**. John Wiley & Sons, 2006.

SELUGA, Kristopher Joseph. **Three dimensional printing by vector printing of fine metal powders**. 2001. Tese de Doutorado. Massachusetts Institute of Technology.

SCHIJVE, Jaap. **Fatigue of structures and materials in the 20th century and the state of the art**. International Journal of fatigue, v. 25, n. 8, p. 679-702, 2003.

SHIVPURI, R. et al. **Microstructure-mechanics interactions in modeling chip segmentation during titanium machining**. CIRP annals, v. 51, n. 1, p. 71-74, 2002.

STEFANESCU, Doru Michael. **Science and engineering of casting solidification**. Springer, 2015.

STENICO, Alessandro. **Werkstoffmechanische Untersuchungen zur Zahnfußtragfähigkeit einsatzgehärteter Zahnräder**. 2007. Tese de Doutorado. Technische Universität München.

STOUT, Ken J.; BLUNT, Liam. **Three dimensional surface topography**. Elsevier, 2000.

STOUT, Virgil L.; GIBBONS, Martin D. **Gettering of gas by titanium**. Journal of applied physics, v. 26, n. 12, p. 1488-1492, 1955

SUN, Li et al. **Densification and properties of 420 stainless steel produced by three-dimensional printing with addition of Si 3 N 4 powder**. 2009.

SUWANPREECHA, Chanun et al. **Effects of aging and shot peening on surface quality and fatigue properties of material extrusion additive manufactured 17-4PH stainless steel.** Materials & Design, v. 241, p. 112939, 2024.

TANG, Yunlong et al. **Elastic modulus of 316 stainless steel lattice structure fabricated via binder jetting process**. Materials Science and Technology, v. 32, n. 7, p. 648-656, 2016.

TAO, Yijie et al. **Simulation of tooth surface topography in continuous generating grinding based on the transient analogy model**. Journal of Materials Processing Technology, v. 312, p. 117833, 2023.

TERNERO, Fátima et al. **Influence of the total porosity on the properties of sintered materials —A review**. Metals, v. 11, n. 5, p. 730, 2021.

TORRES, M. A. S.; VOORWALD, H. J. C. **An evaluation of shot peening, residual stress and stress relaxation on the fatigue life of AISI 4340 steel**. International Journal of fatigue, v. 24, n. 8, p. 877-886, 2002.

TOTTEN, George E. (Ed.). **Handbook of residual stress and deformation of steel**. ASM international, 2002.

TOTTEN, George E.; XIE, Lin; FUNATANI, Kiyoshi. **Handbook of mechanical alloy design**. CRC press, 2003.

TUNG, Simon C.; MCMILLAN, Michael L. **Automotive tribology overview of current advances and challenges for the future**. Tribology international, v. 37, n. 7, p. 517-536, 2004.

VERLEE, Bruno; DORMAL, Thierry; LECOMTE-BECKERS, Jacqueline. **Density and porosity control of sintered 316L stainless steel parts produced by additive manufacturing**. 2012.

VISWANATHAN, U. K.; BANERJEE, S.; KRISHNAN, R. **Effects of aging on the microstructure of 17-4 PH stainless steel.** Materials Science and Engineering: A, v. 104, p. 181-189, 1988.

WANG, Y.; MILLER, J. D. **Current developments and applications of micro-CT for the 3D analysis of multiphase mineral systems in geometallurgy**. Earth-Science Reviews, v. 211, p. 103406, 2020

WEIBULL, Waloddi. **A statistical distribution function of wide applicability**. Journal of applied mechanics, 1951.

WU, Jizhan et al. **Effect of shot peening coverage on residual stress and surface roughness of 18CrNiMo7-6 steel.** International Journal of Mechanical Sciences, v. 183, p. 105785, 2020.

WULPI, Donald J. **Understanding how components fail**. ASM international, 2013.

YADROITSEV, Igor et al. (Ed.). **Fundamentals of laser powder bed fusion of metals**. Elsevier, 2021.

YOUSSEF, S. et al. **Residual stresses and metallurgic transformations induced by grinding.** International Journal of Machining and Machinability of Materials, v. 9, n. 3-4, p. 223-232, 2011.

ZAFOŠNIK, B.; GLODEŽ, S.; ULBIN, M.; FLAŠKER, J. **A fracture mechanics model for the analysis of micro-pitting in regard to lubricated rolling–sliding contact problems**. In: International Journal of Fatigue Vol. 29. Elsevier Science Ltd., 2007. p. 1950-1958.

ZAGO, Marco et al. **Analysis of the causes determining dimensional and geometrical errors in 316L and 17-4PH stainless steel parts fabricated by metal binder jetting.** The International Journal of Advanced Manufacturing Technology, v. 132, n. 1, p. 835-851, 2024.

ZHAN, K.; JIANG, C. H.; JI, V. **Uniformity of residual stress distribution on the surface of S30432 austenitic stainless steel by different shot peening processes**. Materials Letters, v. 99, p. 61-64, 2013.

ZIAEE, M.; CRANE, N. B. **Binder jetting: A review of process, materials, and methods**. Additive Manufacturing, v. 28, p. 781–801, 2019.

ZIAEE, Mohsen; TRIDAS, Eric M.; CRANE, Nathan B. **Binder-jet printing of fine stainless steel powder with varied final density.** Jom, **v**. 69, p. 592-596, 2017.

ZHOU, Yuhaowei et al. **The verification of the mechanical properties of binder jetting manufactured parts by instrumented indentation testing**. Procedia Manufacturing, v. 1, p. 327-342, 2015.

ZHU, Yunhui et al. **Unraveling pore evolution in post-processing of binder jetting materials: X-ray computed tomography, computer vision, and machine learning**. Additive Manufacturing, v. 34, p. 101183, 2020.

Appendix A – Image Processing Code

```
clear all
close all
clc

%%% Seleção da imagem e definição da escala
[file, path] = uigetfile({'*.jpeg;*.jpg;*.png'}, 'Select the image file');
if isequal(file, 0)
    disp('User selected Cancel');
    return;
end

[~, filename_base, ext] = fileparts(file);
rgb = imread(fullfile(path, file));

imshow(rgb)
ref_scale = drawline;
x = defScale(ref_scale); % pixels/µm
fprintf('Scale set at %.4f pixel/µm.\n', x);
close Figure 1
clear ref_scale

%%% Perguntar onde salvar
output_folder_base = uigetdir(path, 'Select folder to save the results');
if isequal(output_folder_base, 0)
    disp('User selected Cancel');
    return;
end
output_folder = fullfile(output_folder_base, [filename_base '_Results']);
mkdir(output_folder);

%%% Processamento de imagem
gray_image = rgb2gray(rgb);
imgBW = imbinarize(gray_image, 'adaptive', 'Sensitivity', .85);
imgBW = ~imgBW;

%%% Remover baquelite
L_temp = bwlabel(imgBW);
stats_temp = regionprops(L_temp, 'Area');
[~, idx_largest] = max([stats_temp.Area]);
imgBW(L_temp == idx_largest) = 0;

imgNoBaquelite = imgBW;
mask_amostra = (L_temp ~= idx_largest);
mask_amostra = logical(mask_amostra);

[B, L] = bwboundaries(imgNoBaquelite, 'noholes');

%%% Criar imagem: peça branca, poros pretos
contoured_image = uint8(255 * ones(size(imgBW)));
contoured_image(imgNoBaquelite == 1) = 0;

figure;
imshow(contoured_image); hold on;
for k = 1:length(B)
```

```
    boundary = B{k};
    plot(boundary(:,2), boundary(:,1), 'r', 'LineWidth', 1);
end
title('Pores Detection');
hold off;
saveas(gcf, fullfile(output_folder, [filename_base '_Pores_Detected.png']));
savefig(fullfile(output_folder, [filename_base '_Pores_Detected.fig']));
close

%%% Cálculo de parâmetros dos poros
stats = regionprops(L, 'Area', 'BoundingBox');
FA = zeros(length(stats), 1);
FF = zeros(length(stats), 1);
diameters = zeros(length(stats), 1);
areas_real = zeros(length(stats), 1);
valid_pores = true(length(stats), 1);

for i = 1:length(stats)
    area = stats(i).Area;
    boundingBox = stats(i).BoundingBox;

    a = boundingBox(3);
    b = boundingBox(4);

    FA(i) = min(b, a) / max(a, b);
    FA(i) = min(FA(i), 1);

    boundary = B{i};
    perimeter = sum(sqrt(sum(diff(boundary).^2, 2)));

    FF(i) = (4 * pi * area) / (perimeter^2);
    FF(i) = min(FF(i), 1);

    diameters(i) = sqrt(4 * (area / (x^2)) / pi);
    areas_real(i) = area / (x^2);

    if FA(i) < 0.3
        valid_pores(i) = false;
    end
end

FA = FA(valid_pores);
FF = FF(valid_pores);
diameters = diameters(valid_pores);
areas_real = areas_real(valid_pores);

%%% Calcular Porosidade
total_valid_pixels = sum(mask_amostra(:));
total_area_um2 = total_valid_pixels / (x^2);

pores_area_um2 = sum(areas_real);
porosity = (pores_area_um2 / total_area_um2) * 100;
fprintf('Porosity equals to %.2f%%.\n', porosity);

%%% Seleção 5%-95% cumulative area
[areas_sorted, idx_sorted] = sort(areas_real, 'descend');
cumulative_area_sorted = cumsum(areas_sorted) / sum(areas_sorted) * 100;
selected_idx = (cumulative_area_sorted >= 5) & (cumulative_area_sorted <= 95);
```

```
FA_selected = FA(idx_sorted(selected_idx));
FF_selected = FF(idx_sorted(selected_idx));
diameters_selected = diameters(idx_sorted(selected_idx));

%%% Exportar para Excel
T_data = table(diameters, FA, FF, 'VariableNames', {'Equivalent_Diameter_um',
'Aspect_Ratio', 'Circularity'});
T_data_selected = table(diameters_selected, FA_selected, FF_selected,
'VariableNames', {'Equivalent_Diameter_um', 'Aspect_Ratio', 'Circularity'});

stats_labels = {'Mean'; 'Median'; 'Standard_Deviation'};
T_stats = table(stats_labels, ...
    [mean(diameters); median(diameters); std(diameters)], ...
    [mean(FA); median(FA); std(FA)], ...
    [mean(FF); median(FF); std(FF)], ...
    'VariableNames', {'Statistic', 'Equivalent_Diameter_um', 'Aspect_Ratio',
'Circularity'});

T_stats_selected = table(stats_labels, ...
    [mean(diameters_selected); median(diameters_selected);
std(diameters_selected)], ...
    [mean(FA_selected); median(FA_selected); std(FA_selected)], ...
    [mean(FF_selected); median(FF_selected); std(FF_selected)], ...
    'VariableNames', {'Statistic', 'Equivalent_Diameter_um', 'Aspect_Ratio',
'Circularity'});

writetable(T_data, fullfile(output_folder, [filename_base '.xlsx']), 'Sheet',
'All_Pores');
writetable(T_stats, fullfile(output_folder, [filename_base '.xlsx']), 'Sheet',
'Statistics_All_Pores');
writetable(T_data_selected, fullfile(output_folder, [filename_base '.xlsx']),
'Sheet', 'Pores_5to95');
writetable(T_stats_selected, fullfile(output_folder, [filename_base '.xlsx']),
'Sheet', 'Statistics_5to95');

%%% Gráficos
light_blue = [170/255, 200/255, 230/255];

edges_FA = 0:0.05:1;
edges_FF = 0:0.05:1;
edges_diam = 0:1:max(diameters)+1;
bin_centers_diam = edges_diam(1:end-1) + diff(edges_diam)/2;

% Aspect Ratio (All)
figure;
counts_FA = histcounts(FA, edges_FA);
percent_FA = counts_FA / sum(counts_FA) * 100;
bar(edges_FA(1:end-1)+0.025, percent_FA, 'FaceColor', light_blue, 'EdgeColor',
'black');
xlabel('Aspect Ratio');
ylabel('Percentage of Pores (%)');
title('Aspect Ratio Distribution (All Pores)');
grid on;
saveas(gcf, fullfile(output_folder, [filename_base '_Aspect_Ratio_All.png']));
savefig(fullfile(output_folder, [filename_base '_Aspect_Ratio_All.fig']));
close

% Circularity (All)
figure;
```

```
counts_FF = histcounts(FF, edges_FF);
percent_FF = counts_FF / sum(counts_FF) * 100;
bar(edges_FF(1:end-1)+0.025, percent_FF, 'FaceColor', light_blue, 'EdgeColor',
'black');
xlabel('Circularity');
ylabel('Percentage of Pores (%)');
title('Circularity Distribution (All Pores)');
grid on;
saveas(gcf, fullfile(output_folder, [filename_base '_Circularity_All.png']));
savefig(fullfile(output_folder, [filename_base '_Circularity_All.fig']));
close

% Aspect Ratio (5%-95%)
figure;
counts_FA_sel = histcounts(FA_selected, edges_FA);
percent_FA_sel = counts_FA_sel / sum(counts_FA_sel) * 100;
bar(edges_FA(1:end-1)+0.025, percent_FA_sel, 'FaceColor', light_blue, 'EdgeColor',
'black');
xlabel('Aspect Ratio');
ylabel('Percentage of Pores (%)');
title('Aspect Ratio Distribution (5%-95% Area Contribution)');
grid on;
saveas(gcf, fullfile(output_folder, [filename_base '_Aspect_Ratio_5to95.png']));
savefig(fullfile(output_folder, [filename_base '_Aspect_Ratio_5to95.fig']));
close

% Circularity (5%-95%)
figure;
counts_FF_sel = histcounts(FF_selected, edges_FF);
percent_FF_sel = counts_FF_sel / sum(counts_FF_sel) * 100;
bar(edges_FF(1:end-1)+0.025, percent_FF_sel, 'FaceColor', light_blue, 'EdgeColor',
'black');
xlabel('Circularity');
ylabel('Percentage of Pores (%)');
title('Circularity Distribution (5%-95% Area Contribution)');
grid on;
saveas(gcf, fullfile(output_folder, [filename_base '_Circularity_5to95.png']));
savefig(fullfile(output_folder, [filename_base '_Circularity_5to95.fig']));
close

% Equivalent Diameter + Cumulative Area
figure;
[counts_diam, ~] = histcounts(diameters, edges_diam);
percent_diam = counts_diam / sum(counts_diam) * 100;

area_by_bin_diam = zeros(length(edges_diam)-1, 1);
for i = 1:length(diameters)
    d = diameters(i);
    a = areas_real(i);
    bin_idx = find(d >= edges_diam(1:end-1) & d < edges_diam(2:end), 1, 'first');
    if ~isempty(bin_idx)
        area_by_bin_diam(bin_idx) = area_by_bin_diam(bin_idx) + a;
    end
end
cumulative_area_diam = cumsum(area_by_bin_diam) / sum(area_by_bin_diam) * 100;

yyaxis left
bar(bin_centers_diam, percent_diam, 'FaceColor', light_blue, 'EdgeColor',
'black');
```

```
ylabel('Percentage of Pores (%)');

yyaxis right
plot(bin_centers_diam, cumulative_area_diam, '-', 'Color', 'k', 'LineWidth', 2);
ylabel('Cumulative Area Contribution (%)', 'Color', 'k');
ylim([0 100]);
set(gca, 'YColor', 'k');

xlabel('Equivalent Diameter (µm)');
title('Equivalent Diameter Distribution and Area Impact (All Pores)');
legend('Percentage of Pores', 'Cumulative Area (%)', 'Location', 'northwest');
grid on;
saveas(gcf, fullfile(output_folder, [filename_base
'_Diameter_Distribution_All.png']));
savefig(fullfile(output_folder, [filename_base
'_Diameter_Distribution_All.fig']));
close

%%% --- Gerar arquivo resumo .txt ---
summary_filename = fullfile(output_folder, [filename_base '_Summary.txt']);
fid = fopen(summary_filename, 'w');
fprintf(fid, 'Image analyzed: %s%s\n', filename_base, ext);
fprintf(fid, 'Scale: %.4f pixels/µm\n', x);
fprintf(fid, 'Porosity: %.2f%%\n', porosity);
fclose(fid);

%%% --- Função auxiliar ---
function scale_value = defScale(scale)
    scale_pos = scale.Position;
    diff_scale = diff(scale.Position);
    scale_ref = hypot(diff_scale(1), diff_scale(2));
    prompt = "Set actual dimension of the defined line (µm): ";
    x = input(prompt);
    scale_value = scale_ref / x; % pixels/µm
end
```

Appendix B – X-ray diffraction measurement report

X-ray residual stress measurement system
μ-X360 Ver. 3. 2. 2. 0

Measurement information

Measurement time	2025/05/01 12:58 - 13:00
Comment 1	10_BJT2_000
Comment 2	
Folder	Rubik

Sample information

Item	Analyisis 1
Name	αFe(211)
Lattice constant(a)	2,8664 A
Lattice constant(b)	---
Lattice constant(c)	---
Wavelength	K-Alpha
Diffraction angle(2Theta)	156,396 deg
Diffraction lattice angle(2Eta)	23,604 deg
Interplanar spacing(d)	1,170
Diffraction plane(h,k,l)	2, 1, 1
Crystal structure	B.C.C
Young's modulus(E)	224,000 GPa
Poisson's ratio(v)	0,280
Sigma(x) stress constant(K)	-465,097 GPa
Tau(xy) stress constant(K)	380,985 GPa
Sigma(y) stress constant(K)	-2091,661 GPa

Camera image

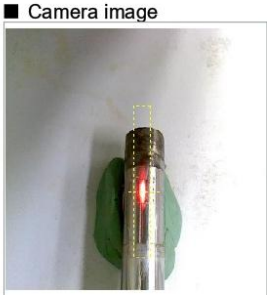

FWHM

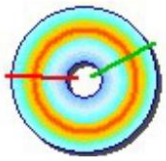

FWHM 3,73 deg
(3,68 - 3,80 deg)
Alpha(Max) 273,60 deg
Alpha(Min) 61,92 deg

Measurement condition

Measurement area	All (5,000 - 40,500 mm)
Pitch	100 um
X-ray irradiation time(Setup)	15 sec
X-ray irradiation time(Meas.)	15 sec
X-ray irradiation time(Max)	46 sec
X-ray tube current	1,50 mA
X-ray tube voltage	30,00 kV
Sample distance(Monitor)	51,000 mm
Sample distance(Analysis)	53,274 mm
X-ray incidence angle	35,0 deg
Offset of alpha angle	0 deg
X-ray wavelength (K-Alpha)	2,29093[A (Cr)
X-ray wavelength (K-Beta)	2,08480 A (Cr)
Total measurement count	39639
Oscillation count	207
X-ray tube total use time	304,35 h (1095664 sec)
Detection sensitivity	26,6 % (228377)
Peak strength (Ave)	211k
Level of ambient light	0,3 %
Temperature	33,13 deg C
K-Beta cut filter	Unused
Valid range of alpha angle	18,00 <---> 90,00 deg
Peak analysis method	Fitting Lorentz
Correction coefficient (Stress)	0,000xx + 1,000x + 0,000
Correction coefficient (FWHM)	0,000xx + 1,000x + 0,000
Rejection coefficient (R.Gamma)	0,000xx + 1,435x + 0,206
Austenite calculation method	Integrated intensity ratio
R-value (Alpha)	---
R-value (Gamma)	---
Collimator size	Phi1,0

FWHM graph

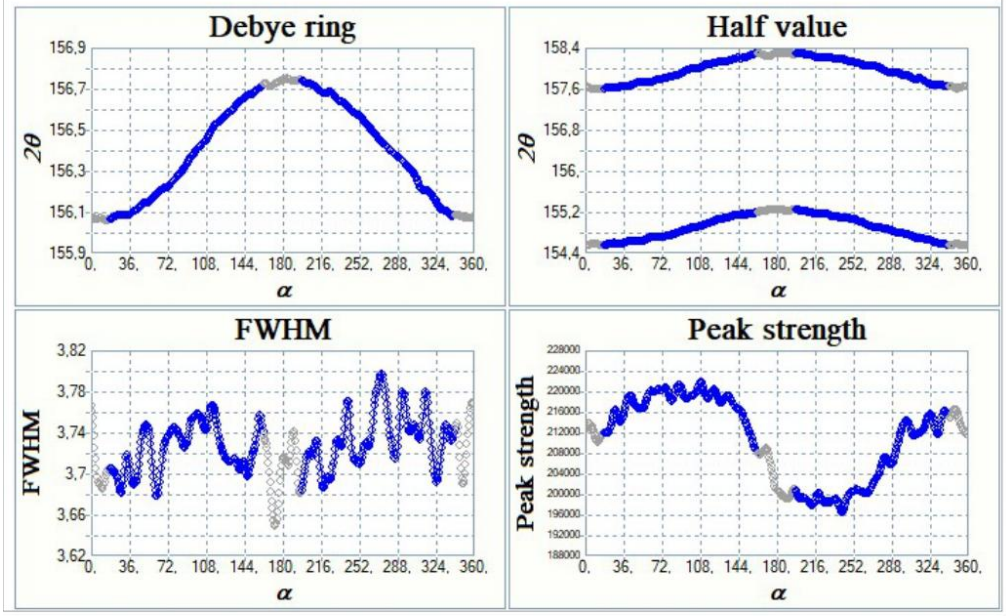

X-ray residual stress measurement system
μ-X360 Ver. 3. 2. 2. 0

Measurement information

Measurement time 2025/05/01 12:58 - 13:00

Comment 1 10_BJT2_000
Comment 2
Folder Rubik

Sample information

Item	Analyisis 1
Name	αFe(211)
Lattice constant(a)	2,8664 A
Lattice constant(b)	---
Lattice constant(c)	---
Wavelength	K-Alpha
Diffraction angle(2Theta)	156,396 deg
Diffraction lattice angle(2Eta)	23,604 deg
Interplanar spacing(d)	1,170
Diffraction plane(h,k,l)	2, 1, 1
Crystal structure	B.C.C
Young's modulus(E)	224,000 GPa
Poisson's ratio(v)	0,280
Sigma(x) stress constant(K)	-465,097 GPa
Tau(xy) stress constant(K)	380,985 GPa
Sigma(y) stress constant(K)	-2091,661 GPa

Camera image

Residual stress

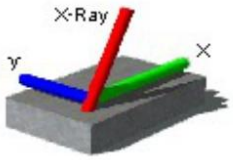

Sigma(x) -623 MPa
(Std. Dev. 5 MPa)
(Slope 0,001340)

Tau(xy) 73 MPa
(Std. Dev. 11 MPa)
(Slope 0,000193)

Measurement condition

Measurement area	All (5,000 - 40,500 mm)
Pitch	100 um
X-ray irradiation time(Setup)	15 sec
X-ray irradiation time(Meas.)	15 sec
X-ray irradiation time(Max)	46 sec
X-ray tube current	1,50 mA
X-ray tube voltage	30,00 kV
Sample distance(Monitor)	51,000 mm
Sample distance(Analysis)	53,274 mm
X-ray incidence angle	35,0 deg
Offset of alpha angle	0 deg
X-ray wavelength (K-Alpha)	2,29093[A (Cr)
X-ray wavelength (K-Beta)	2,08480 A (Cr)
Total measurement count	39639
Oscillation count	207
X-ray tube total use time	304,35 h (1095664 sec)
Detection sensitivity	26,6 % (228377)
Peak strength (Ave)	211k
Level of ambient light	0,3 %
Temperature	33,13 deg C
K-Beta cut filter	Unused
Valid range of alpha angle	18,00 <---> 90,00 deg
Peak analysis method	Fitting Lorentz
Correction coefficient (Stress)	0,000xx + 1,000x + 0,000
Correction coefficient (FWHM)	0,000xx + 1,000x + 0,000
ection coefficient (R.Gamma)	0,000xx + 1,435x + 0,206
Austenite calculation method	Integrated intensity ratio
R-value (Alpha)	---
R-value (Gamma)	---
Collimator size	Phi1,0

Residual stress graph

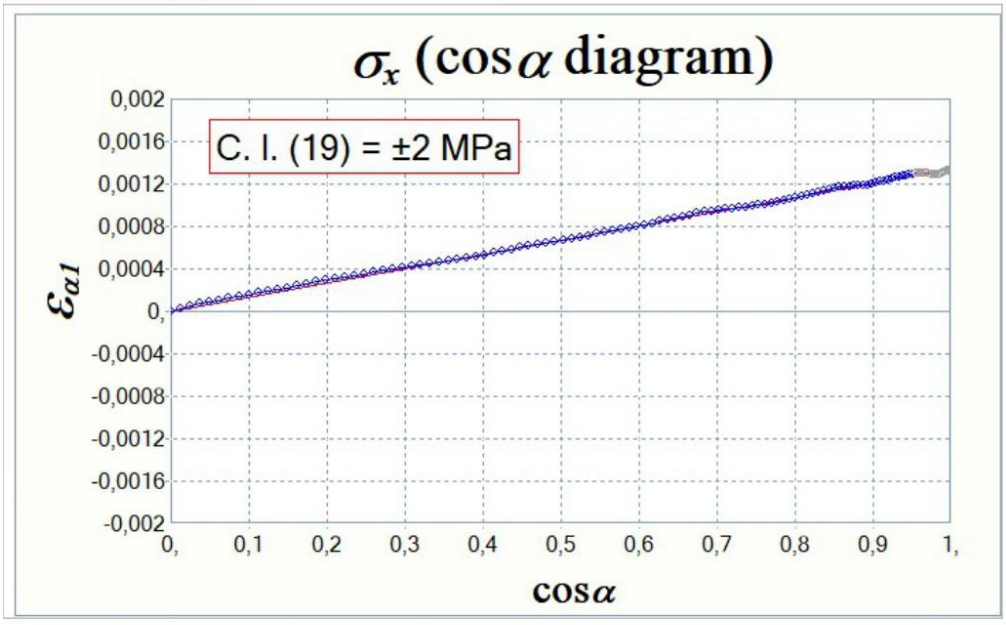

X-ray residual stress measurement system
μ-X360 Ver. 3. 2. 2. 0

Measurement information

Measurement time 2025/05/01 12:58 - 13:00

Comment 1 10_BJT2_000
Comment 2
Folder Rubik

Sample information

Item	Analyisis 1
Name	αFe(211)
Lattice constant(a)	2,8664 A
Lattice constant(b)	---
Lattice constant(c)	---
Wavelength	K-Alpha
Diffraction angle(2Theta)	156,396 deg
Diffraction lattice angle(2Eta)	23,604 deg
Interplanar spacing(d)	1,170
Diffraction plane(h,k,l)	2, 1, 1
Crystal structure	B.C.C
Young's modulus(E)	224,000 GPa
Poisson's ratio(v)	0,280
Sigma(x) stress constant(K)	-465,097 GPa
Tau(xy) stress constant(K)	380,985 GPa
Sigma(y) stress constant(K)	-2091,661 GPa

Camera image

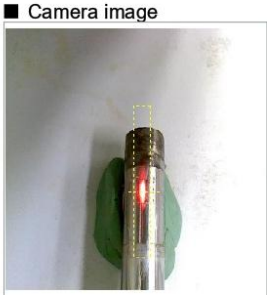

Map

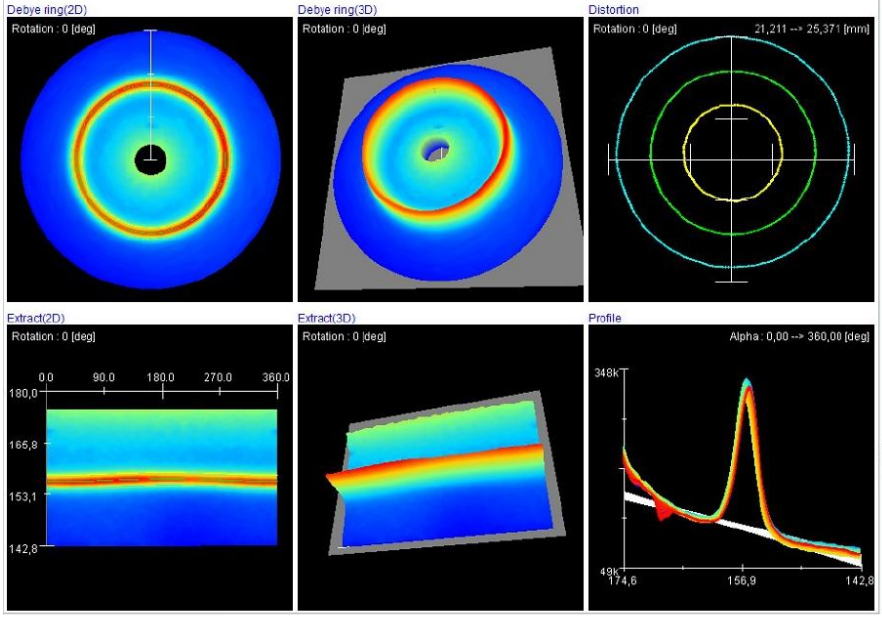

Measurement condition

Measurement area	All (5,000 - 40,500 mm)
Pitch	100 um
X-ray irradiation time(Setup)	15 sec
X-ray irradiation time(Meas.)	15 sec
X-ray irradiation time(Max)	46 sec
X-ray tube current	1,50 mA
X-ray tube voltage	30,00 kV
Sample distance(Monitor)	51,000 mm
Sample distance(Analysis)	53,274 mm
X-ray incidence angle	35,0 deg
Offset of alpha angle	0 deg
X-ray wavelength (K-Alpha)	2,29093[A (Cr)
X-ray wavelength (K-Beta)	2,08480 A (Cr)
Total measurement count	39639
Oscillation count	207
X-ray tube total use time	304,35 h (1095664 se
Detection sensitivity	26,6 % (228377)
Peak strength (Ave)	211k
Level of ambient light	0,3 %
Temperature	33,13 deg C
K-Beta cut filter	Unused
Valid range of alpha angle	18,00 <---> 90,00 deg
Peak analysis method	Fitting Lorentz
Correction coefficient (Stress)	0,000xx + 1,000x + 0,
Correction coefficient (FWHM)	0,000xx + 1,000x + 0,
ection coefficient (R.Gamma)	0,000xx + 1,435x + 0,
Austenite calculation method	Integrated intensity ra
R-value (Alpha)	---
R-value (Gamma)	---
Collimator size	Phi1,0

Residual stress

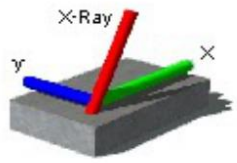

Sigma(x) -623 MPa
(Std. Dev. 5 MPa)
Tau(xy) 73 MPa
(Std. Dev. 11 MPa)

FWHM

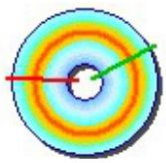

FWHM 3,73 deg
(3,68 - 3,80 deg)
Alpha(Max) 273,60 deg
Alpha(Min) 61,92 deg

Residual stress graph

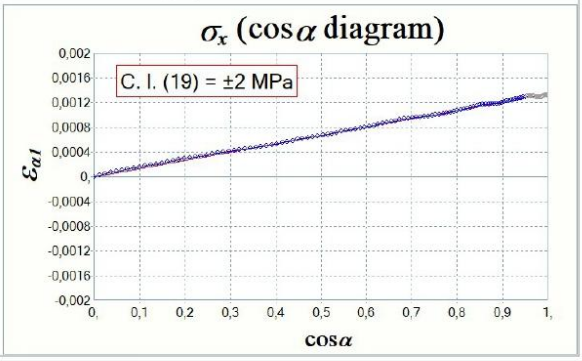

FWHM graph

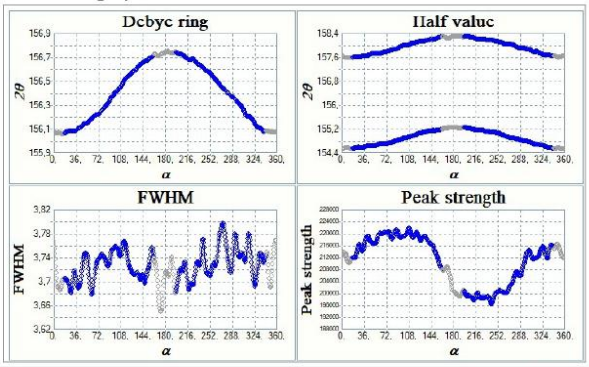

Measurement information

Measurement time 2025/05/02 11:02 - 11:03

Comment 1 06_BJT_000
Comment 2
Folder Rubik

Sample information

Item	Analyisis 1
Name	αFe(211)
Lattice constant(a)	2,8664 A
Lattice constant(b)	---
Lattice constant(c)	---
Wavelength	K-Alpha
Diffraction angle(2Theta)	156,396 deg
Diffraction lattice angle(2Eta)	23,604 deg
Interplanar spacing(d)	1,170
Diffraction plane(h,k,l)	2, 1, 1
Crystal structure	B.C.C
Young's modulus(E)	224,000 GPa
Poisson's ratio(v)	0,280
Sigma(x) stress constant(K)	-465,097 GPa
Tau(xy) stress constant(K)	380,985 GPa
Sigma(y) stress constant(K)	-2091,661 GPa

Camera image

Retained austenite

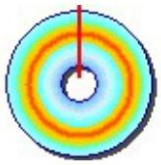

γ_{Ri} --- %

(--- %)

Alpha(Max) --- deg

Alpha(Min) --- deg

Measurement condition

Measurement area	All (5,000 - 40,500 mm)
Pitch	100 um
X-ray irradiation time(Setup)	15 sec
X-ray irradiation time(Meas.)	15 sec
X-ray irradiation time(Max)	56 sec
X-ray tube current	1,50 mA
X-ray tube voltage	30,00 kV
Sample distance(Monitor)	51,000 mm
Sample distance(Analysis)	53,169 mm
X-ray incidence angle	35,0 deg
Offset of alpha angle	0 deg
X-ray wavelength (K-Alpha)	2,29093[A (Cr)
X-ray wavelength (K-Beta)	2,08480 A (Cr)
Total measurement count	39664
Oscillation count	207
X-ray tube total use time	304,46 h (1096064 sec)
Detection sensitivity	21,6 % (185447)
Peak strength (Ave)	134k
Level of ambient light	0,3 %
Temperature	30,56 deg C
K-Beta cut filter	Unused
Valid range of alpha angle	18,00 <---> 90,00 deg
Peak analysis method	Fitting Lorentz
Correction coefficient (Stress)	0,000xx + 1,000x + 0,000
Correction coefficient (FWHM)	0,000xx + 1,000x + 0,000
ection coefficient (R.Gamma)	0,000xx + 1,435x + 0,206
Austenite calculation method	Integrated intensity ratio
R-value (Alpha)	---
R-value (Gamma)	---
Collimator size	Phi1,0

Retained austenite graph

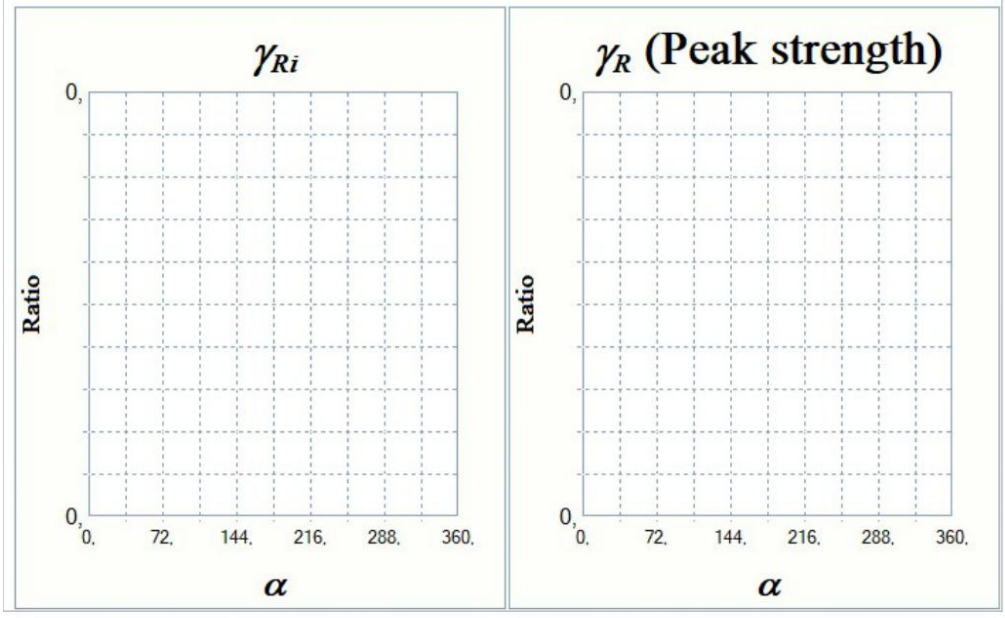

Measurement information

Measurement time 2025/05/02 11:02 - 11:03

Comment 1 06_BJT_000
Comment 2
Folder Rubik

Sample information

Item	Analyisis 1
Name	αFe(211)
Lattice constant(a)	2,8664 A
Lattice constant(b)	---
Lattice constant(c)	---
Wavelength	K-Alpha
Diffraction angle(2Theta)	156,396 deg
Diffraction lattice angle(2Eta)	23,604 deg
Interplanar spacing(d)	1,170
Diffraction plane(h,k,l)	2, 1, 1
Crystal structure	B.C.C
Young's modulus(E)	224,000 GPa
Poisson's ratio(v)	0,280
Sigma(x) stress constant(K)	-465,097 GPa
Tau(xy) stress constant(K)	380,985 GPa
Sigma(y) stress constant(K)	-2091,661 GPa

Camera image

FWHM

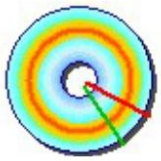

FWHM 4,64 deg
(4,50 - 4,77 deg)
Alpha(Max) 117,36 deg
Alpha(Min) 145,44 deg

Measurement condition

Measurement area	All (5,000 - 40,500 mm)
Pitch	100 um
X-ray irradiation time(Setup)	15 sec
X-ray irradiation time(Meas.)	15 sec
X-ray irradiation time(Max)	56 sec
X-ray tube current	1,50 mA
X-ray tube voltage	30,00 kV
Sample distance(Monitor)	51,000 mm
Sample distance(Analysis)	53,169 mm
X-ray incidence angle	35,0 deg
Offset of alpha angle	0 deg
X-ray wavelength (K-Alpha)	2,29093[A (Cr)
X-ray wavelength (K-Beta)	2,08480 A (Cr)
Total measurement count	39664
Oscillation count	207
X-ray tube total use time	304,46 h (1096064 sec)
Detection sensitivity	21,6 % (185447)
Peak strength (Ave)	134k
Level of ambient light	0,3 %
Temperature	30,56 deg C
K-Beta cut filter	Unused
Valid range of alpha angle	18,00 <---> 90,00 deg
Peak analysis method	Fitting Lorentz
Correction coefficient (Stress)	0,000xx + 1,000x + 0,000
Correction coefficient (FWHM)	0,000xx + 1,000x + 0,000
Rection coefficient (R.Gamma)	0,000xx + 1,435x + 0,206
Austenite calculation method	Integrated intensity ratio
R-value (Alpha)	---
R-value (Gamma)	---
Collimator size	Phi1,0

FWHM graph

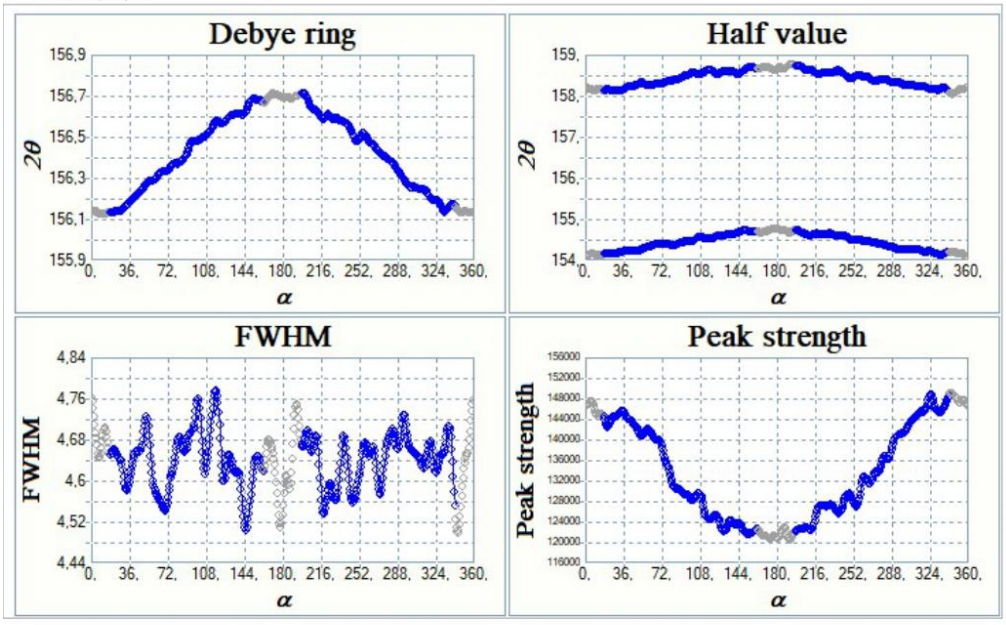

■ Measurement information

Measurement time 2025/05/02 11:02 - 11:03

Comment 1 06_BJT_000
Comment 2
Folder Rubik

■ Sample information

Item	Analyisis 1
Name	αFe(211)
Lattice constant(a)	2,8664 A
Lattice constant(b)	---
Lattice constant(c)	---
Wavelength	K-Alpha
Diffraction angle(2Theta)	156,396 deg
Diffraction lattice angle(2Eta)	23,604 deg
Interplanar spacing(d)	1,170
Diffraction plane(h,k,l)	2, 1, 1
Crystal structure	B.C.C
Young's modulus(E)	224,000 GPa
Poisson's ratio(v)	0,280
Sigma(x) stress constant(K)	-465,097 GPa
Tau(xy) stress constant(K)	380,985 GPa
Sigma(y) stress constant(K)	-2091,661 GPa

■ Camera image

■ Residual stress

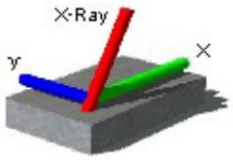

Sigma(x) -516 MPa
(Std. Dev. 16 MPa)
(Slope 0,001110)

Tau(xy) -13 MPa
(Std. Dev. 12 MPa)
(Slope -0,000033)

■ Measurement condition

Measurement area	All (5,000 - 40,500 mm)
Pitch	100 um
X-ray irradiation time(Setup)	15 sec
X-ray irradiation time(Meas.)	15 sec
X-ray irradiation time(Max)	56 sec
X-ray tube current	1,50 mA
X-ray tube voltage	30,00 kV
Sample distance(Monitor)	51,000 mm
Sample distance(Analysis)	53,169 mm
X-ray incidence angle	35,0 deg
Offset of alpha angle	0 deg
X-ray wavelength (K-Alpha)	2,29093[A (Cr)
X-ray wavelength (K-Beta)	2,08480 A (Cr)
Total measurement count	39664
Oscillation count	207
X-ray tube total use time	304,46 h (1096064 sec)
Detection sensitivity	21,6 % (185447)
Peak strength (Ave)	134k
Level of ambient light	0,3 %
Temperature	30,56 deg C
K-Beta cut filter	Unused
Valid range of alpha angle	18,00 <---> 90,00 deg
Peak analysis method	Fitting Lorentz
Correction coefficient (Stress)	0,000xx + 1,000x + 0,000
Correction coefficient (FWHM)	0,000xx + 1,000x + 0,000
ection coefficient (R.Gamma)	0,000xx + 1,435x + 0,206
Austenite calculation method	Integrated intensity ratio
R-value (Alpha)	---
R-value (Gamma)	---
Collimator size	Phi1,0

■ Residual stress graph

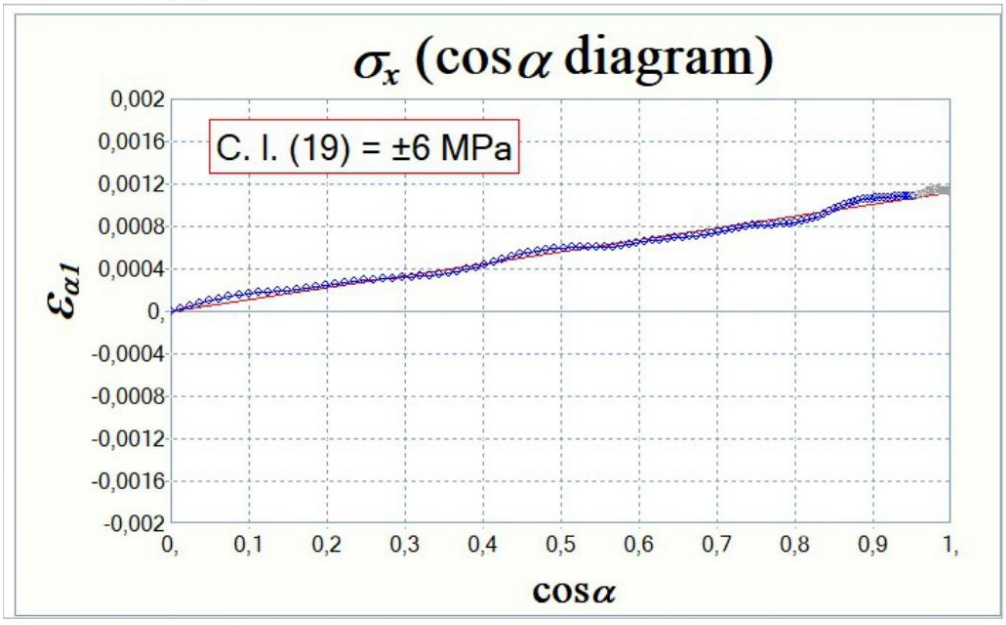

X-ray residual stress measurement system
μ-X360 Ver. 3. 2. 2. 0

Measurement information

Measurement time 2025/05/02 11:02 - 11:03

Comment 1 06_BJT_000
Comment 2
Folder Rubik

Sample information

Item	Analyisis 1
Name	αFe(211)
Lattice constant(a)	2,8664 A
Lattice constant(b)	---
Lattice constant(c)	---
Wavelength	K-Alpha
Diffraction angle(2Theta)	156,396 deg
Diffraction lattice angle(2Eta)	23,604 deg
Interplanar spacing(d)	1,170
Diffraction plane(h,k,l)	2, 1, 1
Crystal structure	B.C.C
Young's modulus(E)	224,000 GPa
Poisson's ratio(v)	0,280
Sigma(x) stress constant(K)	-465,097 GPa
Tau(xy) stress constant(K)	380,985 GPa
Sigma(y) stress constant(K)	-2091,661 GPa

Camera image

Map

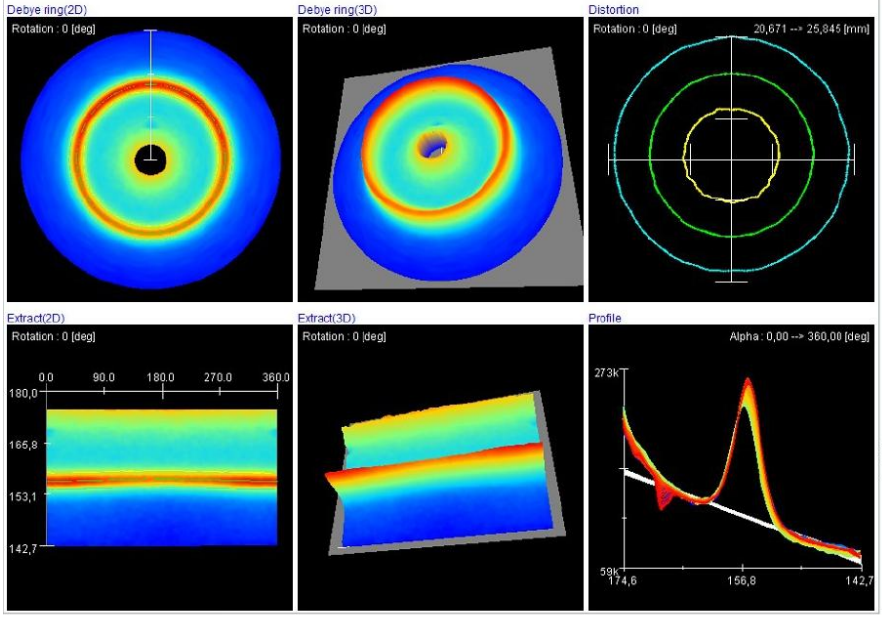

Measurement condition

Measurement area	All (5,000 - 40,500 mm)
Pitch	100 um
X-ray irradiation time(Setup)	15 sec
X-ray irradiation time(Meas.)	15 sec
X-ray irradiation time(Max)	56 sec
X-ray tube current	1,50 mA
X-ray tube voltage	30,00 kV
Sample distance(Monitor)	51,000 mm
Sample distance(Analysis)	53,169 mm
X-ray incidence angle	35,0 deg
Offset of alpha angle	0 deg
X-ray wavelength (K-Alpha)	2,29093[A (Cr)
X-ray wavelength (K-Beta)	2,08480 A (Cr)
Total measurement count	39664
Oscillation count	207
X-ray tube total use time	304,46 h (1096064 se
Detection sensitivity	21,6 % (185447)
Peak strength (Ave)	134k
Level of ambient light	0,3 %
Temperature	30,56 deg C
K-Beta cut filter	Unused
Valid range of alpha angle	18,00 <---> 90,00 deg
Peak analysis method	Fitting Lorentz
Correction coefficient (Stress)	0,000xx + 1,000x + 0,
Correction coefficient (FWHM)	0,000xx + 1,000x + 0,
ection coefficient (R.Gamma)	0,000xx + 1,435x + 0,
Austenite calculation method	Integrated intensity ra
R-value (Alpha)	---
R-value (Gamma)	---
Collimator size	Phi1,0

Residual stress

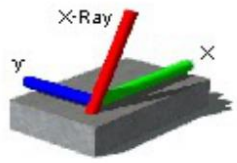

Sigma(x) -516 MPa
(Std. Dev. 16 MPa)
Tau(xy) -13 MPa
(Std. Dev. 12 MPa)

FWHM

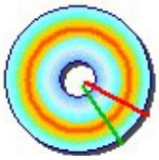

FWHM 4,64 deg
(4,50 - 4,77 deg)
Alpha(Max) 117,36 deg
Alpha(Min) 145,44 deg

Residual stress graph

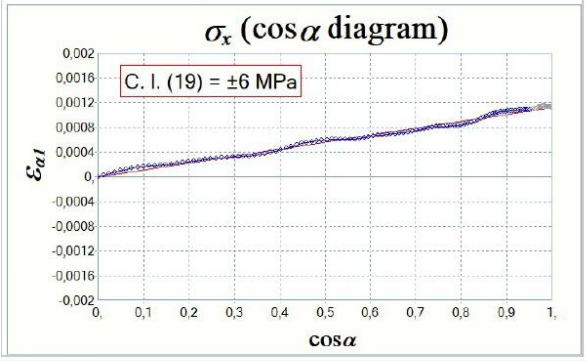

FWHM graph

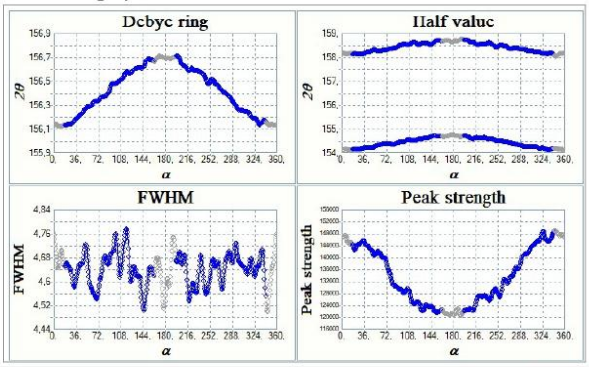

Measurement information

Measurement time 2025/05/01 10:32 - 10:33

Comment 1 01_BJT_000
Comment 2
Folder Rubik

Sample information

Item	Analyisis 1
Name	αFe(211)
Lattice constant(a)	2,8664 A
Lattice constant(b)	---
Lattice constant(c)	---
Wavelength	K-Alpha
Diffraction angle(2Theta)	156,396 deg
Diffraction lattice angle(2Eta)	23,604 deg
Interplanar spacing(d)	1,170
Diffraction plane(h,k,l)	2, 1, 1
Crystal structure	B.C.C
Young's modulus(E)	224,000 GPa
Poisson's ratio(v)	0,280
Sigma(x) stress constant(K)	-465,097 GPa
Tau(xy) stress constant(K)	380,985 GPa
Sigma(y) stress constant(K)	-2091,661 GPa

Camera image

Retained austenite

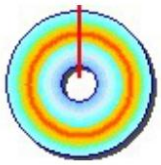

γ_{Ri} --- %

(--- %)

Alpha(Max) --- deg

Alpha(Min) --- deg

Measurement condition

Measurement area	All (5,000 - 40,500 mm)
Pitch	100 um
X-ray irradiation time(Setup)	15 sec
X-ray irradiation time(Meas.)	15 sec
X-ray irradiation time(Max)	45 sec
X-ray tube current	1,50 mA
X-ray tube voltage	30,00 kV
Sample distance(Monitor)	51,000 mm
Sample distance(Analysis)	53,415 mm
X-ray incidence angle	35,0 deg
Offset of alpha angle	0 deg
X-ray wavelength (K-Alpha)	2,29093[A (Cr)
X-ray wavelength (K-Beta)	2,08480 A (Cr)
Total measurement count	39615
Oscillation count	207
X-ray tube total use time	304,24 h (1095280 sec)
Detection sensitivity	27,0 % (232405)
Peak strength (Ave)	207k
Level of ambient light	0,3 %
Temperature	26,50 deg C
K-Beta cut filter	Unused
Valid range of alpha angle	18,00 <---> 90,00 deg
Peak analysis method	Fitting Lorentz
Correction coefficient (Stress)	0,000xx + 1,000x + 0,000
Correction coefficient (FWHM)	0,000xx + 1,000x + 0,000
ection coefficient (R.Gamma)	0,000xx + 1,435x + 0,206
Austenite calculation method	Integrated intensity ratio
R-value (Alpha)	---
R-value (Gamma)	---
Collimator size	Phi1,0

Retained austenite graph

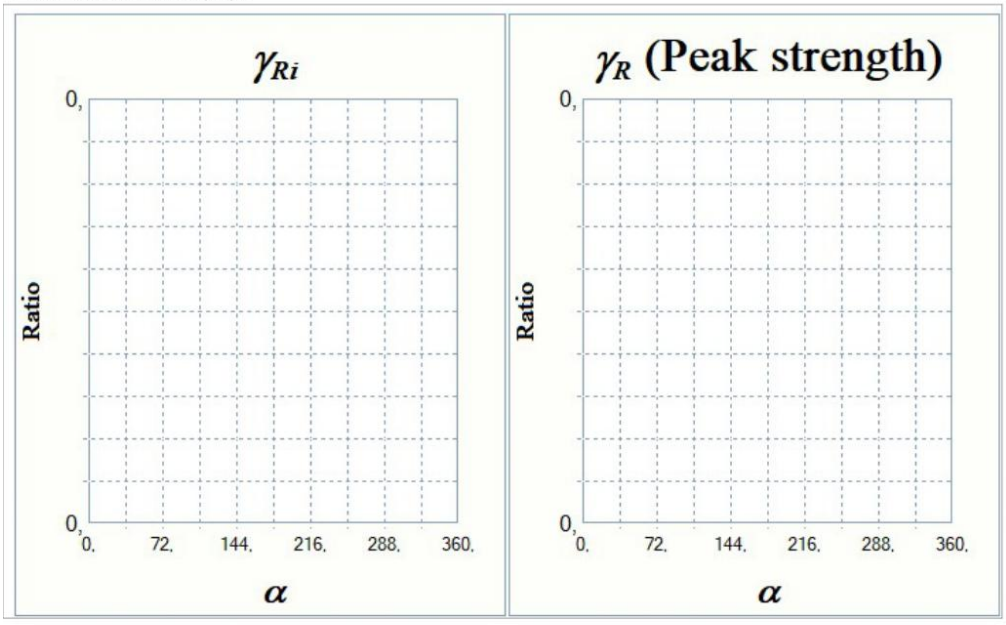

X-ray residual stress measurement system
μ-X360 Ver. 3. 2. 2. 0

Measurement information

Measurement time	2025/05/01 10:32 - 10:33
Comment 1	01_BJT_000
Comment 2	
Folder	Rubik

Sample information

Item	Analyisis 1
Name	αFe(211)
Lattice constant(a)	2,8664 A
Lattice constant(b)	---
Lattice constant(c)	---
Wavelength	K-Alpha
Diffraction angle(2Theta)	156,396 deg
Diffraction lattice angle(2Eta)	23,604 deg
Interplanar spacing(d)	1,170
Diffraction plane(h,k,l)	2, 1, 1
Crystal structure	B.C.C
Young's modulus(E)	224,000 GPa
Poisson's ratio(v)	0,280
Sigma(x) stress constant(K)	-465,097 GPa
Tau(xy) stress constant(K)	380,985 GPa
Sigma(y) stress constant(K)	-2091,661 GPa

Camera image

FWHM

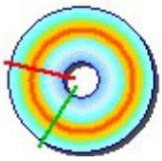

FWHM 3,92 deg

(3,85 - 4,02 deg)

Alpha(Max) 283,68 deg

Alpha(Min) 212,40 deg

Measurement condition

Measurement area	All (5,000 - 40,500 mm)
Pitch	100 um
X-ray irradiation time(Setup)	15 sec
X-ray irradiation time(Meas.)	15 sec
X-ray irradiation time(Max)	45 sec
X-ray tube current	1,50 mA
X-ray tube voltage	30,00 kV
Sample distance(Monitor)	51,000 mm
Sample distance(Analysis)	53,415 mm
X-ray incidence angle	35,0 deg
Offset of alpha angle	0 deg
X-ray wavelength (K-Alpha)	2,29093[A (Cr)
X-ray wavelength (K-Beta)	2,08480 A (Cr)
Total measurement count	39615
Oscillation count	207
X-ray tube total use time	304,24 h (1095280 sec)
Detection sensitivity	27,0 % (232405)
Peak strength (Ave)	207k
Level of ambient light	0,3 %
Temperature	26,50 deg C
K-Beta cut filter	Unused
Valid range of alpha angle	18,00 <---> 90,00 deg
Peak analysis method	Fitting Lorentz
Correction coefficient (Stress)	0,000xx + 1,000x + 0,000
Correction coefficient (FWHM)	0,000xx + 1,000x + 0,000
Rejection coefficient (R.Gamma)	0,000xx + 1,435x + 0,206
Austenite calculation method	Integrated intensity ratio
R-value (Alpha)	---
R-value (Gamma)	---
Collimator size	Phi1,0

FWHM graph

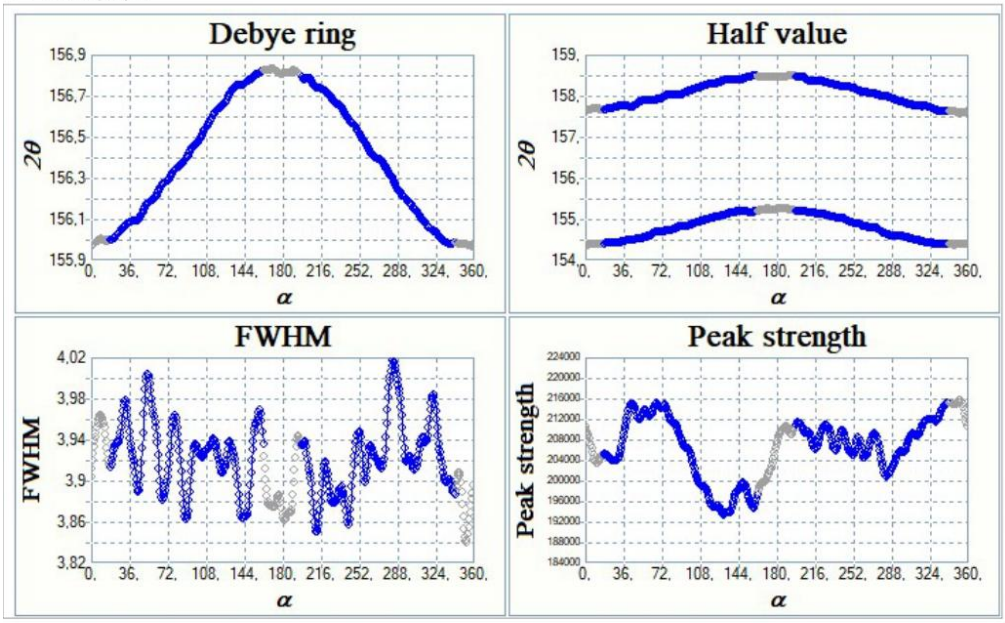

■ Measurement information

Measurement time 2025/05/01 10:32 - 10:33

Comment 1 01_BJT_000
Comment 2
Folder Rubik

■ Sample information

Item	Analyisis 1
Name	αFe(211)
Lattice constant(a)	2,8664 A
Lattice constant(b)	---
Lattice constant(c)	---
Wavelength	K-Alpha
Diffraction angle(2Theta)	156,396 deg
Diffraction lattice angle(2Eta)	23,604 deg
Interplanar spacing(d)	1,170
Diffraction plane(h,k,l)	2, 1, 1
Crystal structure	B.C.C
Young's modulus(E)	224,000 GPa
Poisson's ratio(v)	0,280
Sigma(x) stress constant(K)	-465,097 GPa
Tau(xy) stress constant(K)	380,985 GPa
Sigma(y) stress constant(K)	-2091,661 GPa

■ Camera image

■ Residual stress

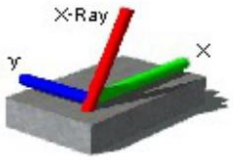

Sigma(x) -776 MPa
(Std. Dev. 10 MPa)
(Slope 0,001669)

Tau(xy) -34 MPa
(Std. Dev. 10 MPa)
(Slope -0,000089)

■ Measurement condition

Measurement area	All (5,000 - 40,500 mm)
Pitch	100 um
X-ray irradiation time(Setup)	15 sec
X-ray irradiation time(Meas.)	15 sec
X-ray irradiation time(Max)	45 sec
X-ray tube current	1,50 mA
X-ray tube voltage	30,00 kV
Sample distance(Monitor)	51,000 mm
Sample distance(Analysis)	53,415 mm
X-ray incidence angle	35,0 deg
Offset of alpha angle	0 deg
X-ray wavelength (K-Alpha)	2,29093[A (Cr)
X-ray wavelength (K-Beta)	2,08480 A (Cr)
Total measurement count	39615
Oscillation count	207
X-ray tube total use time	304,24 h (1095280 sec)
Detection sensitivity	27,0 % (232405)
Peak strength (Ave)	207k
Level of ambient light	0,3 %
Temperature	26,50 deg C
K-Beta cut filter	Unused
Valid range of alpha angle	18,00 <---> 90,00 deg
Peak analysis method	Fitting Lorentz
Correction coefficient (Stress)	0,000xx + 1,000x + 0,000
Correction coefficient (FWHM)	0,000xx + 1,000x + 0,000
ection coefficient (R.Gamma)	0,000xx + 1,435x + 0,206
Austenite calculation method	Integrated intensity ratio
R-value (Alpha)	---
R-value (Gamma)	---
Collimator size	Phi1,0

■ Residual stress graph

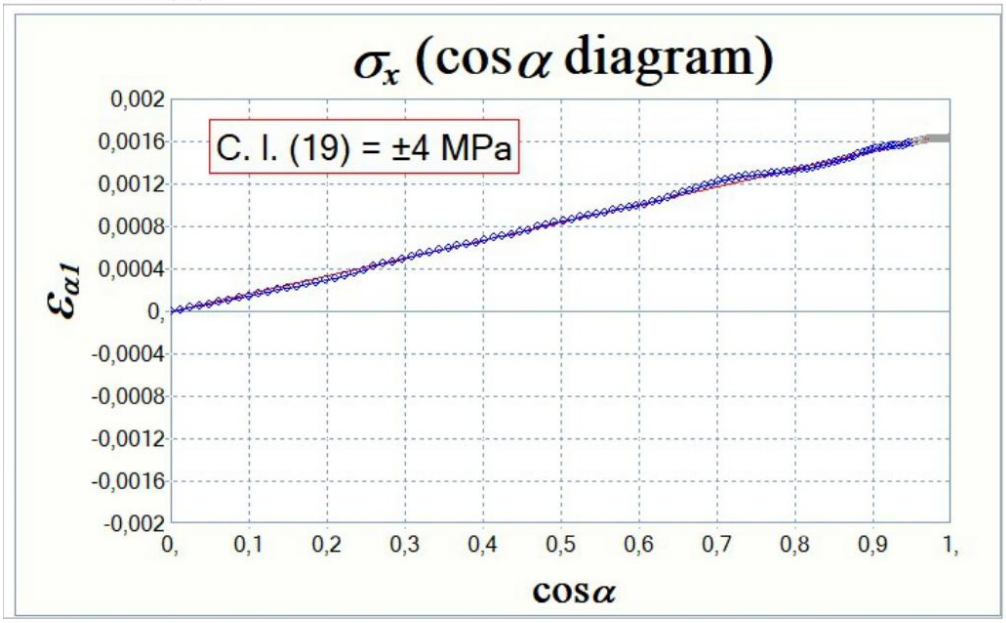

X-ray residual stress measurement system
μ-X360 Ver. 3. 2. 2. 0

Measurement information

Measurement time 2025/05/01 10:32 - 10:33

Comment 1 01_BJT_000
Comment 2
Folder Rubik

Sample information

Item	Analyisis 1
Name	αFe(211)
Lattice constant(a)	2,8664 A
Lattice constant(b)	---
Lattice constant(c)	---
Wavelength	K-Alpha
Diffraction angle(2Theta)	156,396 deg
Diffraction lattice angle(2Eta)	23,604 deg
Interplanar spacing(d)	1,170
Diffraction plane(h,k,l)	2, 1, 1
Crystal structure	B.C.C
Young's modulus(E)	224,000 GPa
Poisson's ratio(v)	0,280
Sigma(x) stress constant(K)	-465,097 GPa
Tau(xy) stress constant(K)	380,985 GPa
Sigma(y) stress constant(K)	-2091,661 GPa

Camera image

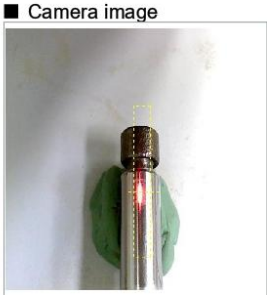

Map

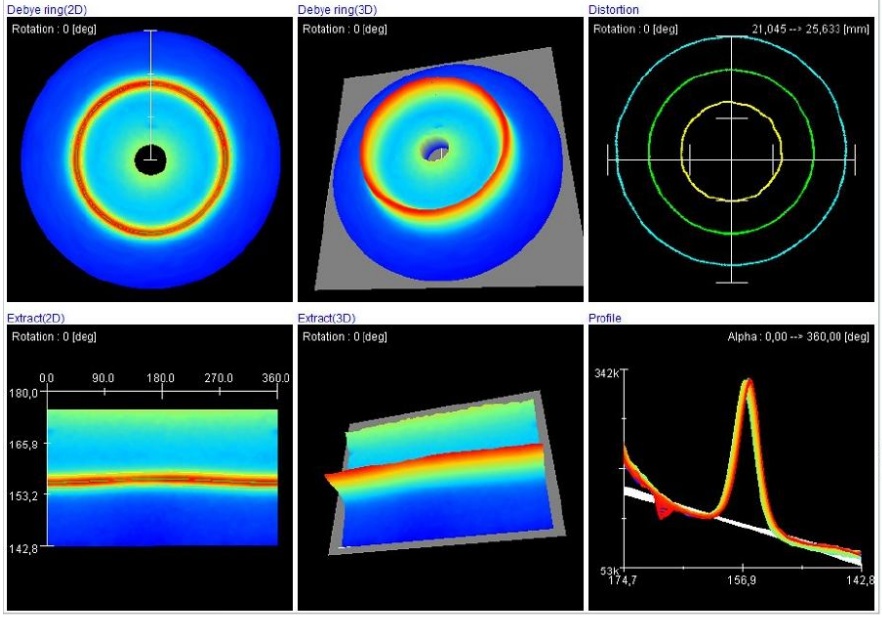

Measurement condition

Measurement area	All (5,000 - 40,500 mm)
Pitch	100 um
X-ray irradiation time(Setup)	15 sec
X-ray irradiation time(Meas.)	15 sec
X-ray irradiation time(Max)	45 sec
X-ray tube current	1,50 mA
X-ray tube voltage	30,00 kV
Sample distance(Monitor)	51,000 mm
Sample distance(Analysis)	53,415 mm
X-ray incidence angle	35,0 deg
Offset of alpha angle	0 deg
X-ray wavelength (K-Alpha)	2,29093[A (Cr)
X-ray wavelength (K-Beta)	2,08480 A (Cr)
Total measurement count	39615
Oscillation count	207
X-ray tube total use time	304,24 h (1095280 se
Detection sensitivity	27,0 % (232405)
Peak strength (Ave)	207k
Level of ambient light	0,3 %
Temperature	26,50 deg C
K-Beta cut filter	Unused
Valid range of alpha angle	18,00 <---> 90,00 deg
Peak analysis method	Fitting Lorentz
Correction coefficient (Stress)	0,000xx + 1,000x + 0,
Correction coefficient (FWHM)	0,000xx + 1,000x + 0,
ection coefficient (R.Gamma)	0,000xx + 1,435x + 0,
Austenite calculation method	Integrated intensity ra
R-value (Alpha)	---
R-value (Gamma)	---
Collimator size	Phi1,0

Residual stress

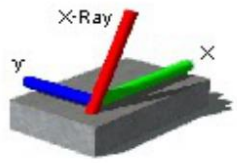

Sigma(x) -776 MPa
(Std. Dev. 10 MPa)
Tau(xy) -34 MPa
(Std. Dev. 10 MPa)

FWHM

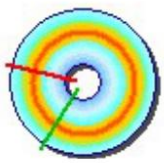

FWHM 3,92 deg
(3,85 - 4,02 deg)
Alpha(Max) 283,68 deg
Alpha(Min) 212,40 deg

Residual stress graph

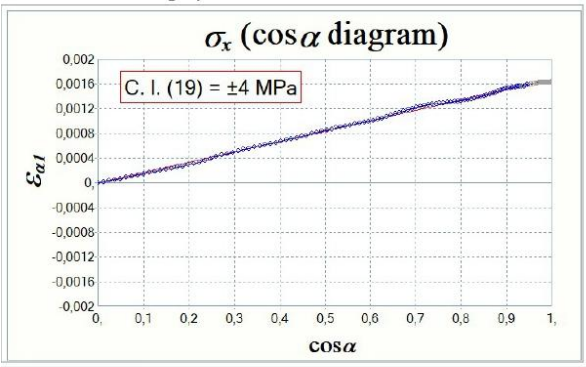

FWHM graph

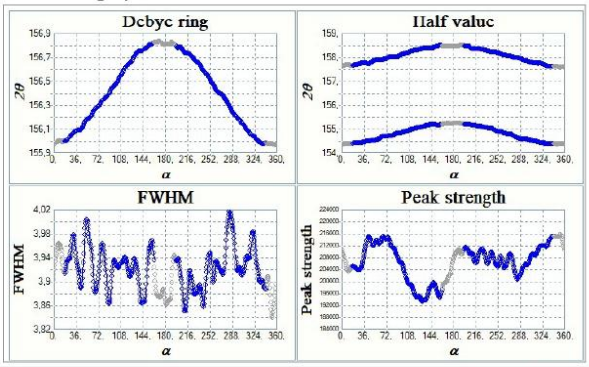

X-ray residual stress measurement system
μ-X360 Ver. 3. 2. 2. 0

Measurement information

Measurement time 2025/05/01 12:58 - 13:00

Comment 1 10_BJT2_000
Comment 2
Folder Rubik

Sample information

Item	Analyisis 1
Name	αFe(211)
Lattice constant(a)	2,8664 A
Lattice constant(b)	---
Lattice constant(c)	---
Wavelength	K-Alpha
Diffraction angle(2Theta)	156,396 deg
Diffraction lattice angle(2Eta)	23,604 deg
Interplanar spacing(d)	1,170
Diffraction plane(h,k,l)	2, 1, 1
Crystal structure	B.C.C
Young's modulus(E)	224,000 GPa
Poisson's ratio(v)	0,280
Sigma(x) stress constant(K)	-465,097 GPa
Tau(xy) stress constant(K)	380,985 GPa
Sigma(y) stress constant(K)	-2091,661 GPa

Camera image

Retained austenite

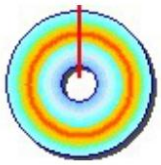

γ_{Ri} --- %

(--- %)

Alpha(Max) --- deg

Alpha(Min) --- deg

Measurement condition

Measurement area	All (5,000 - 40,500 mm)
Pitch	100 um
X-ray irradiation time(Setup)	15 sec
X-ray irradiation time(Meas.)	15 sec
X-ray irradiation time(Max)	46 sec
X-ray tube current	1,50 mA
X-ray tube voltage	30,00 kV
Sample distance(Monitor)	51,000 mm
Sample distance(Analysis)	53,274 mm
X-ray incidence angle	35,0 deg
Offset of alpha angle	0 deg
X-ray wavelength (K-Alpha)	2,29093[A (Cr)
X-ray wavelength (K-Beta)	2,08480 A (Cr)
Total measurement count	39639
Oscillation count	207
X-ray tube total use time	304,35 h (1095664 sec)
Detection sensitivity	26,6 % (228377)
Peak strength (Ave)	211k
Level of ambient light	0,3 %
Temperature	33,13 deg C
K-Beta cut filter	Unused
Valid range of alpha angle	18,00 <---> 90,00 deg
Peak analysis method	Fitting Lorentz
Correction coefficient (Stress)	0,000xx + 1,000x + 0,000
Correction coefficient (FWHM)	0,000xx + 1,000x + 0,000
ection coefficient (R.Gamma)	0,000xx + 1,435x + 0,206
Austenite calculation method	Integrated intensity ratio
R-value (Alpha)	---
R-value (Gamma)	---
Collimator size	Phi1,0

Retained austenite graph

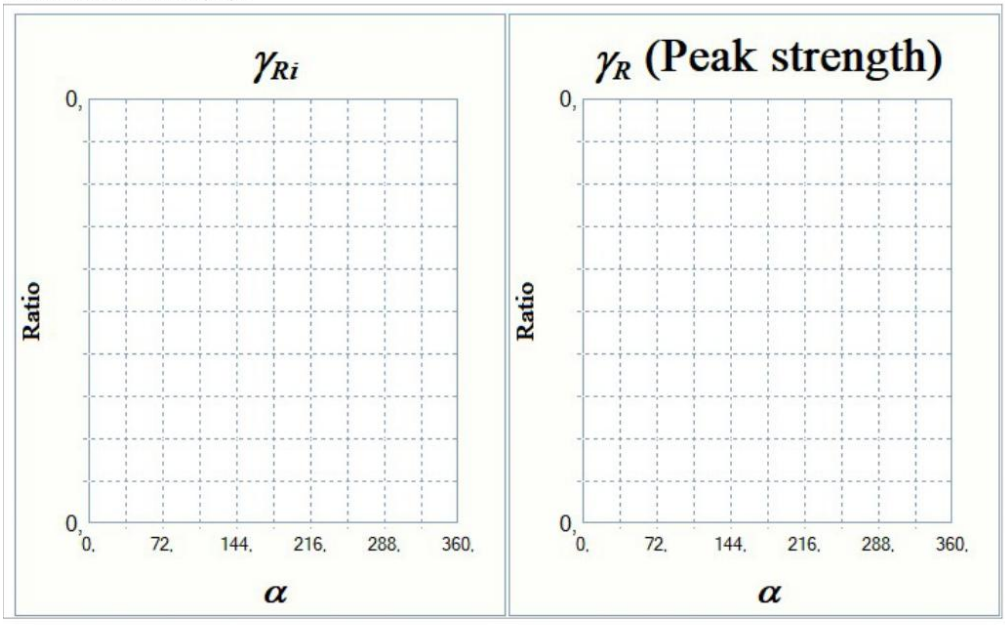

■ Measurement information

Measurement time 2025/07/25 09:48 - 09:50

Comment 1 Raustenite3
Comment 2
Folder RUBIK

■ Sample information

Item	Analyisis 1
Name	αFe(211)
Lattice constant(a)	2,8664 A
Lattice constant(b)	---
Lattice constant(c)	---
Wavelength	K-Alpha
Diffraction angle(2Theta)	156,396 deg
Diffraction lattice angle(2Eta)	23,604 deg
Interplanar spacing(d)	1,170
Diffraction plane(h,k,l)	2, 1, 1
Crystal structure	B.C.C
Young's modulus(E)	224,000 GPa
Poisson's ratio(v)	0,280
Sigma(x) stress constant(K)	---
Tau(xy) stress constant(K)	---
Sigma(y) stress constant(K)	-2091,661 GPa

■ Camera image

■ FWHM

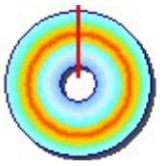

FWHM ---deg
(---deg)
Alpha(Max) ---deg
Alpha(Min) ---deg

■ Measurement condition

Measurement area	All (5,000 - 40,500 mm)
Pitch	50 um
X-ray irradiation time(Setup)	30 sec
X-ray irradiation time(Meas.)	30 sec
X-ray irradiation time(Max)	30 sec
X-ray tube current	1,00 mA
X-ray tube voltage	30,00 kV
Sample distance(Monitor)	27,000 mm
Sample distance(Analysis)	28,461 mm
X-ray incidence angle	0,0 deg
Offset of alpha angle	0 deg
X-ray wavelength (K-Alpha)	2,29093[A (Cr)
X-ray wavelength (K-Beta)	2,08480 A (Cr)
Total measurement count	43004
Oscillation count	207
X-ray tube total use time	343,34 h (1236031 sec)
Detection sensitivity	31,2 % (268286)
Peak strength (Ave)	429k
Level of ambient light	0,3 %
Temperature	26,25 deg C
K-Beta cut filter	Used
Valid range of alpha angle	0,00 <---> 90,00 deg
Peak analysis method	Fitting Lorentz
Correction coefficient (Stress)	0,000xx + 1,000x + 0,000
Correction coefficient (FWHM)	0,000xx + 1,000x + 0,000
ection coefficient (R.Gamma)	0,000xx + 1,435x + 0,206
Austenite calculation method	Integrated intensity ratio
R-value (Alpha)	---
R-value (Gamma)	---
Collimator size	Phi1,0

■ FWHM graph

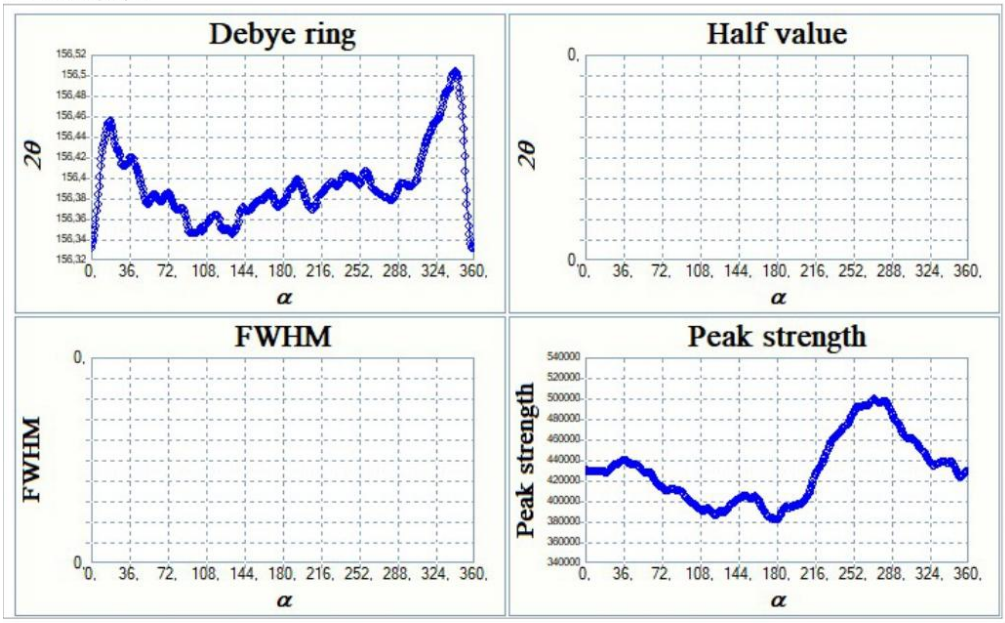

X-ray residual stress measurement system
μ-X360 Ver. 3. 2. 2. 0

■ Measurement information

Measurement time 2025/07/25 09:48 - 09:50

Comment 1 Raustenite3
Comment 2
Folder RUBIK

■ Sample information

Item	Analyisis 1
Name	αFe(211)
Lattice constant(a)	2,8664 A
Lattice constant(b)	---
Lattice constant(c)	---
Wavelength	K-Alpha
Diffraction angle(2Theta)	156,396 deg
Diffraction lattice angle(2Eta)	23,604 deg
Interplanar spacing(d)	1,170
Diffraction plane(h,k,l)	2, 1, 1
Crystal structure	B.C.C
Young's modulus(E)	224,000 GPa
Poisson's ratio(v)	0,280
Sigma(x) stress constant(K)	---
Tau(xy) stress constant(K)	---
Sigma(y) stress constant(K)	-2091,661 GPa

■ Camera image

■ Residual stress

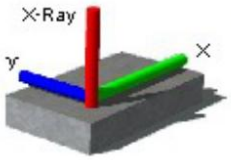

Sigma(x) --- MPa
(Std. Dev. --- MPa)
(Slope ---)

Tau(xy) --- MPa
(Std. Dev. --- MPa)
(Slope ---)

■ Measurement condition

Measurement area	All (5,000 - 40,500 mm)
Pitch	50 um
X-ray irradiation time(Setup)	30 sec
X-ray irradiation time(Meas.)	30 sec
X-ray irradiation time(Max)	30 sec
X-ray tube current	1,00 mA
X-ray tube voltage	30,00 kV
Sample distance(Monitor)	27,000 mm
Sample distance(Analysis)	28,461 mm
X-ray incidence angle	0,0 deg
Offset of alpha angle	0 deg
X-ray wavelength (K-Alpha)	2,29093[A (Cr)
X-ray wavelength (K-Beta)	2,08480 A (Cr)
Total measurement count	43004
Oscillation count	207
X-ray tube total use time	343,34 h (1236031 sec)
Detection sensitivity	31,2 % (268286)
Peak strength (Ave)	429k
Level of ambient light	0,3 %
Temperature	26,25 deg C
K-Beta cut filter	Used
Valid range of alpha angle	0,00 <---> 90,00 deg
Peak analysis method	Fitting Lorentz
Correction coefficient (Stress)	0,000xx + 1,000x + 0,000
Correction coefficient (FWHM)	0,000xx + 1,000x + 0,000
ection coefficient (R.Gamma)	0,000xx + 1,435x + 0,206
Austenite calculation method	Integrated intensity ratio
R-value (Alpha)	---
R-value (Gamma)	---
Collimator size	Phi1,0

■ Residual stress graph

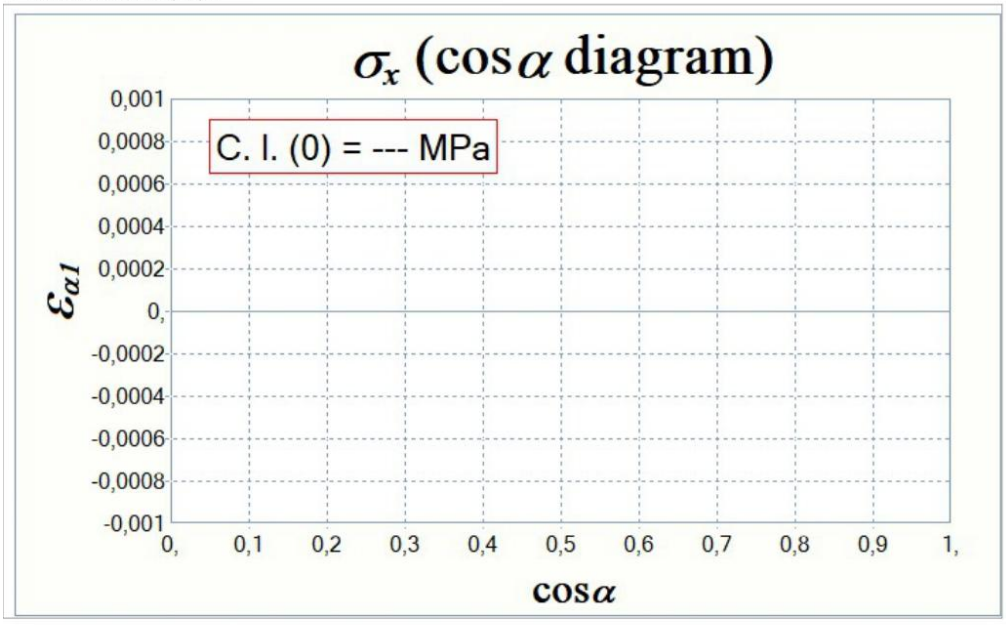

X-ray residual stress measurement system
μ-X360 Ver. 3. 2. 2. 0

Measurement information

Measurement time 2025/07/25 09:48 - 09:50

Comment 1 Raustenite3
Comment 2
Folder RUBIK

Sample information

Item	Analyisis 1
Name	αFe(211)
Lattice constant(a)	2,8664 A
Lattice constant(b)	---
Lattice constant(c)	---
Wavelength	K-Alpha
Diffraction angle(2Theta)	156,396 deg
Diffraction lattice angle(2Eta)	23,604 deg
Interplanar spacing(d)	1,170
Diffraction plane(h,k,l)	2, 1, 1
Crystal structure	B.C.C
Young's modulus(E)	224,000 GPa
Poisson's ratio(v)	0,280
Sigma(x) stress constant(K)	---
Tau(xy) stress constant(K)	---
Sigma(y) stress constant(K)	-2091,661 GPa

Camera image

Map

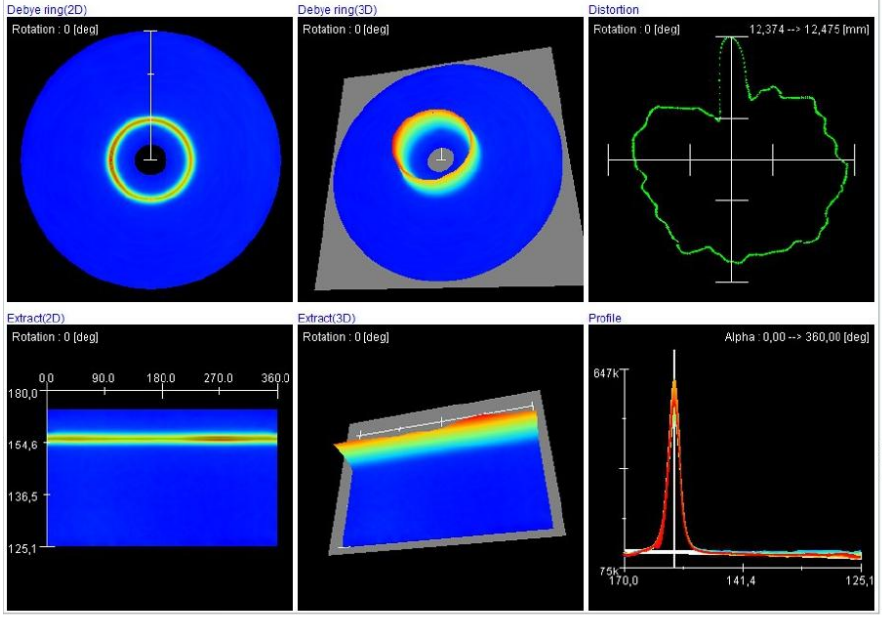

Measurement condition

Measurement area	All (5,000 - 40,500 mm)
Pitch	50 um
X-ray irradiation time(Setup)	30 sec
X-ray irradiation time(Meas.)	30 sec
X-ray irradiation time(Max)	30 sec
X-ray tube current	1,00 mA
X-ray tube voltage	30,00 kV
Sample distance(Monitor)	27,000 mm
Sample distance(Analysis)	28,461 mm
X-ray incidence angle	0,0 deg
Offset of alpha angle	0 deg
X-ray wavelength (K-Alpha)	2,29093[A (Cr)
X-ray wavelength (K-Beta)	2,08480 A (Cr)
Total measurement count	43004
Oscillation count	207
X-ray tube total use time	343,34 h (1236031 se
Detection sensitivity	31,2 % (268286)
Peak strength (Ave)	429k
Level of ambient light	0,3 %
Temperature	26,25 deg C
K-Beta cut filter	Used
Valid range of alpha angle	0,00 <---> 90,00 deg
Peak analysis method	Fitting Lorentz
Correction coefficient (Stress)	0,000xx + 1,000x + 0,
Correction coefficient (FWHM)	0,000xx + 1,000x + 0,
ection coefficient (R.Gamma)	0,000xx + 1,435x + 0,
Austenite calculation method	Integrated intensity ra
R-value (Alpha)	---
R-value (Gamma)	---
Collimator size	Phi1,0

Residual stress

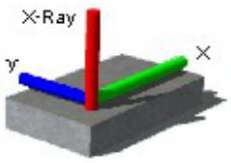

Sigma(x) --- MPa
(Std. Dev. --- MPa)
Tau(xy) --- MPa
(Std. Dev. --- MPa)

FWHM

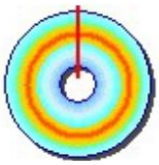

FWHM --- deg
(--- deg)
Alpha(Max) --- deg
Alpha(Min) --- deg

Residual stress graph

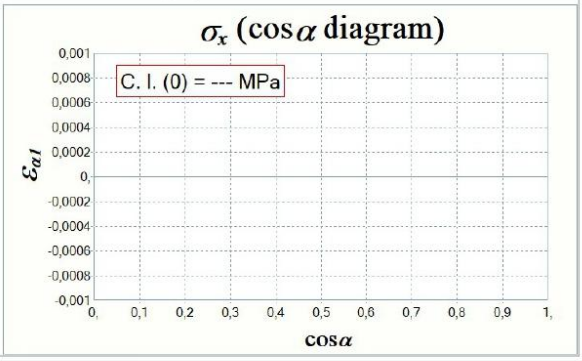

FWHM graph

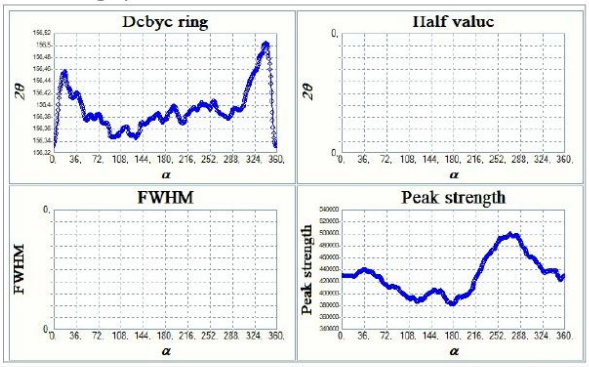

■ Measurement information

Measurement time	2025/07/25 09:47 - 09:48
Comment 1	Raustenite2
Comment 2	
Folder	RUBIK

■ Sample information

Item	Analyisis 1
Name	αFe(211)
Lattice constant(a)	2,8664 A
Lattice constant(b)	---
Lattice constant(c)	---
Wavelength	K-Alpha
Diffraction angle(2Theta)	156,396 deg
Diffraction lattice angle(2Eta)	23,604 deg
Interplanar spacing(d)	1,170
Diffraction plane(h,k,l)	2, 1, 1
Crystal structure	B.C.C
Young's modulus(E)	224,000 GPa
Poisson's ratio(v)	0,280
Sigma(x) stress constant(K)	---
Tau(xy) stress constant(K)	---
Sigma(y) stress constant(K)	-2091,661 GPa

■ Camera image

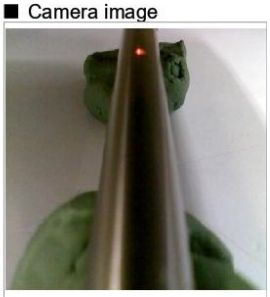

■ Retained austenite

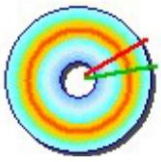

γ_{Ri} 1,8 %

(0,6 - 5,3 %)

Alpha(Max) 59,04 deg

Alpha(Min) 79,92 deg

■ Measurement condition

Measurement area	All (5,000 - 40,500 mm)
Pitch	50 um
X-ray irradiation time(Setup)	30 sec
X-ray irradiation time(Meas.)	30 sec
X-ray irradiation time(Max)	30 sec
X-ray tube current	1,00 mA
X-ray tube voltage	30,00 kV
Sample distance(Monitor)	27,000 mm
Sample distance(Analysis)	28,798 mm
X-ray incidence angle	0,0 deg
Offset of alpha angle	0 deg
X-ray wavelength (K-Alpha)	2,29093[A (Cr)
X-ray wavelength (K-Beta)	2,08480 A (Cr)
Total measurement count	43003
Oscillation count	207
X-ray tube total use time	343,33 h (1236000 sec)
Detection sensitivity	30,9 % (265901)
Peak strength (Ave)	430k
Level of ambient light	0,3 %
Temperature	24,94 deg C
K-Beta cut filter	Used
Valid range of alpha angle	0,00 <---> 90,00 deg
Peak analysis method	Fitting Lorentz
Correction coefficient (Stress)	0,000xx + 1,000x + 0,000
Correction coefficient (FWHM)	0,000xx + 1,000x + 0,000
ection coefficient (R.Gamma)	0,000xx + 1,435x + 0,206
Austenite calculation method	Integrated intensity ratio
R-value (Alpha)	---
R-value (Gamma)	---
Collimator size	Phi1,0

■ Retained austenite graph

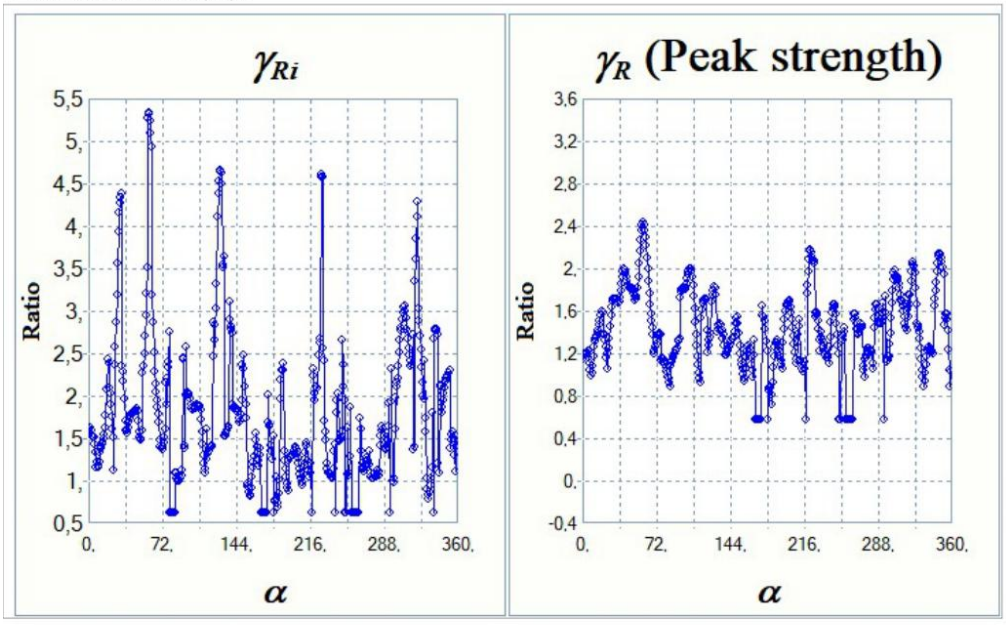

■ Measurement information

Measurement time	2025/07/25 09:47 - 09:48
Comment 1	Raustenite2
Comment 2	
Folder	RUBIK

■ Sample information

Item	Analyisis 1
Name	αFe(211)
Lattice constant(a)	2,8664 A
Lattice constant(b)	---
Lattice constant(c)	---
Wavelength	K-Alpha
Diffraction angle(2Theta)	156,396 deg
Diffraction lattice angle(2Eta)	23,604 deg
Interplanar spacing(d)	1,170
Diffraction plane(h,k,l)	2, 1, 1
Crystal structure	B.C.C
Young's modulus(E)	224,000 GPa
Poisson's ratio(v)	0,280
Sigma(x) stress constant(K)	---
Tau(xy) stress constant(K)	---
Sigma(y) stress constant(K)	-2091,661 GPa

■ Camera image

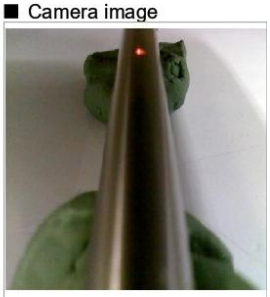

■ FWHM

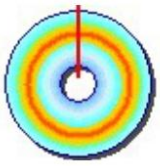

FWHM ---deg

(---deg)

Alpha(Max) ---deg

Alpha(Min) ---deg

■ Measurement condition

Measurement area	All (5,000 - 40,500 mm)
Pitch	50 um
X-ray irradiation time(Setup)	30 sec
X-ray irradiation time(Meas.)	30 sec
X-ray irradiation time(Max)	30 sec
X-ray tube current	1,00 mA
X-ray tube voltage	30,00 kV
Sample distance(Monitor)	27,000 mm
Sample distance(Analysis)	28,798 mm
X-ray incidence angle	0,0 deg
Offset of alpha angle	0 deg
X-ray wavelength (K-Alpha)	2,29093[A (Cr)
X-ray wavelength (K-Beta)	2,08480 A (Cr)
Total measurement count	43003
Oscillation count	207
X-ray tube total use time	343,33 h (1236000 sec)
Detection sensitivity	30,9 % (265901)
Peak strength (Ave)	430k
Level of ambient light	0,3 %
Temperature	24,94 deg C
K-Beta cut filter	Used
Valid range of alpha angle	0,00 <---> 90,00 deg
Peak analysis method	Fitting Lorentz
Correction coefficient (Stress)	0,000xx + 1,000x + 0,000
Correction coefficient (FWHM)	0,000xx + 1,000x + 0,000
ection coefficient (R.Gamma)	0,000xx + 1,435x + 0,206
Austenite calculation method	Integrated intensity ratio
R-value (Alpha)	---
R-value (Gamma)	---
Collimator size	Phi1,0

■ FWHM graph

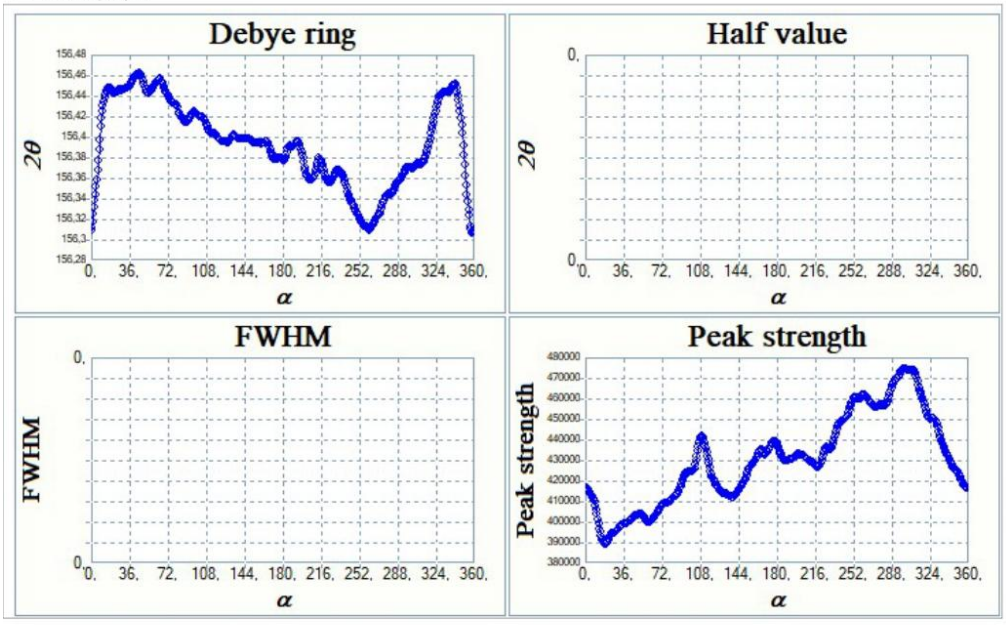

■ Measurement information

Measurement time 2025/07/25 09:47 - 09:48

Comment 1 Raustenite2
Comment 2
Folder RUBIK

■ Sample information

Item	Analyisis 1
Name	αFe(211)
Lattice constant(a)	2,8664 A
Lattice constant(b)	---
Lattice constant(c)	---
Wavelength	K-Alpha
Diffraction angle(2Theta)	156,396 deg
Diffraction lattice angle(2Eta)	23,604 deg
Interplanar spacing(d)	1,170
Diffraction plane(h,k,l)	2, 1, 1
Crystal structure	B.C.C
Young's modulus(E)	224,000 GPa
Poisson's ratio(v)	0,280
Sigma(x) stress constant(K)	---
Tau(xy) stress constant(K)	---
Sigma(y) stress constant(K)	-2091,661 GPa

■ Camera image

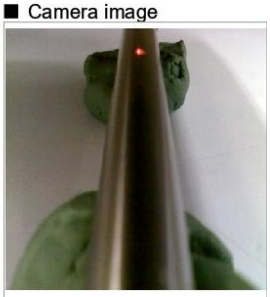

■ Residual stress

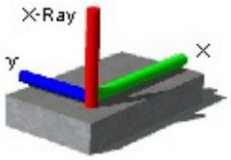

Sigma(x) --- MPa
(Std. Dev. --- MPa)
(Slope ---)

Tau(xy) --- MPa
(Std. Dev. --- MPa)
(Slope ---)

■ Measurement condition

Measurement area	All (5,000 - 40,500 mm)
Pitch	50 um
X-ray irradiation time(Setup)	30 sec
X-ray irradiation time(Meas.)	30 sec
X-ray irradiation time(Max)	30 sec
X-ray tube current	1,00 mA
X-ray tube voltage	30,00 kV
Sample distance(Monitor)	27,000 mm
Sample distance(Analysis)	28,798 mm
X-ray incidence angle	0,0 deg
Offset of alpha angle	0 deg
X-ray wavelength (K-Alpha)	2,29093[A (Cr)
X-ray wavelength (K-Beta)	2,08480 A (Cr)
Total measurement count	43003
Oscillation count	207
X-ray tube total use time	343,33 h (1236000 sec)
Detection sensitivity	30,9 % (265901)
Peak strength (Ave)	430k
Level of ambient light	0,3 %
Temperature	24,94 deg C
K-Beta cut filter	Used
Valid range of alpha angle	0,00 <---> 90,00 deg
Peak analysis method	Fitting Lorentz
Correction coefficient (Stress)	0,000xx + 1,000x + 0,000
Correction coefficient (FWHM)	0,000xx + 1,000x + 0,000
ection coefficient (R.Gamma)	0,000xx + 1,435x + 0,206
Austenite calculation method	Integrated intensity ratio
R-value (Alpha)	---
R-value (Gamma)	---
Collimator size	Phi1,0

■ Residual stress graph

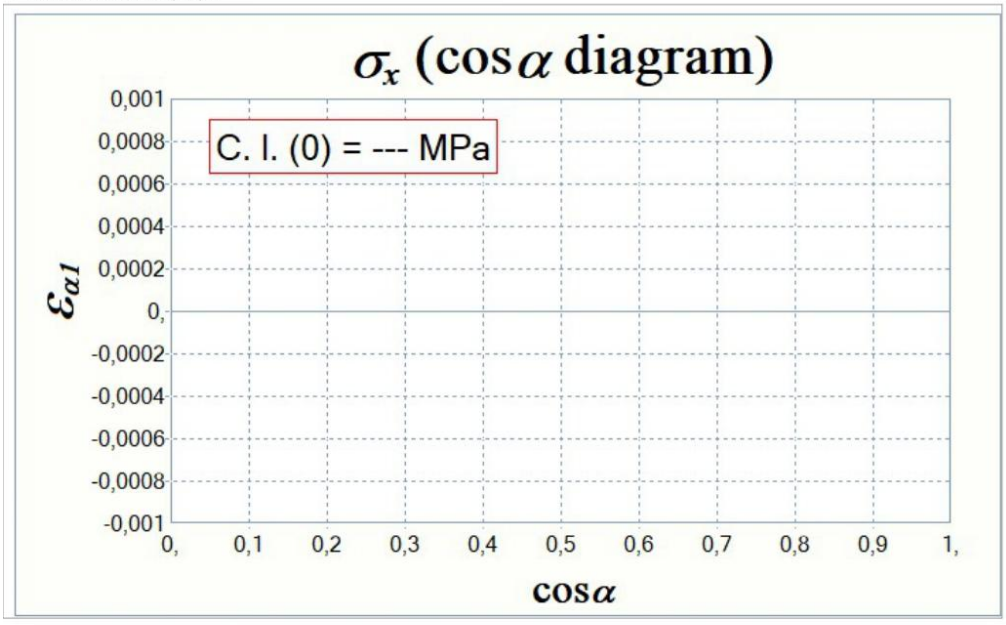

X-ray residual stress measurement system
μ-X360 Ver. 3. 2. 2. 0

Measurement information

Measurement time 2025/07/25 09:47 - 09:48

Comment 1 Raustenite2
Comment 2
Folder RUBIK

Sample information

Item	Analyisis 1
Name	αFe(211)
Lattice constant(a)	2,8664 A
Lattice constant(b)	---
Lattice constant(c)	---
Wavelength	K-Alpha
Diffraction angle(2Theta)	156,396 deg
Diffraction lattice angle(2Eta)	23,604 deg
Interplanar spacing(d)	1,170
Diffraction plane(h,k,l)	2, 1, 1
Crystal structure	B.C.C
Young's modulus(E)	224,000 GPa
Poisson's ratio(v)	0,280
Sigma(x) stress constant(K)	---
Tau(xy) stress constant(K)	---
Sigma(y) stress constant(K)	-2091,661 GPa

Camera image

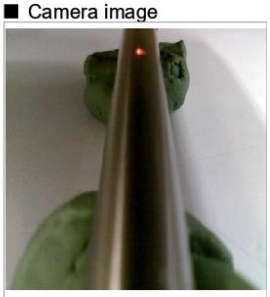

Map

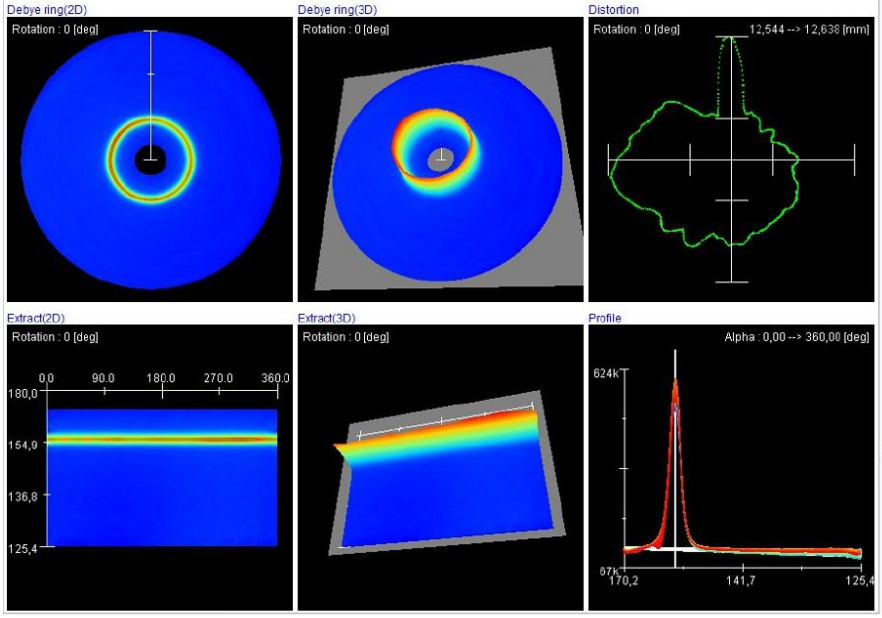

Measurement condition

Measurement area	All (5,000 - 40,500 mm)
Pitch	50 um
X-ray irradiation time(Setup)	30 sec
X-ray irradiation time(Meas.)	30 sec
X-ray irradiation time(Max)	30 sec
X-ray tube current	1,00 mA
X-ray tube voltage	30,00 kV
Sample distance(Monitor)	27,000 mm
Sample distance(Analysis)	28,798 mm
X-ray incidence angle	0,0 deg
Offset of alpha angle	0 deg
X-ray wavelength (K-Alpha)	2,29093[A (Cr)
X-ray wavelength (K-Beta)	2,08480 A (Cr)
Total measurement count	43003
Oscillation count	207
X-ray tube total use time	343,33 h (1236000 se
Detection sensitivity	30,9 % (265901)
Peak strength (Ave)	430k
Level of ambient light	0,3 %
Temperature	24,94 deg C
K-Beta cut filter	Used
Valid range of alpha angle	0,00 <---> 90,00 deg
Peak analysis method	Fitting Lorentz
Correction coefficient (Stress)	0,000xx + 1,000x + 0,
Correction coefficient (FWHM)	0,000xx + 1,000x + 0,
ection coefficient (R.Gamma)	0,000xx + 1,435x + 0,
Austenite calculation method	Integrated intensity ra
R-value (Alpha)	---
R-value (Gamma)	---
Collimator size	Phi1,0

Residual stress

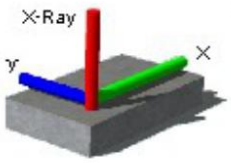

Sigma(x) --- MPa
(Std. Dev. --- MPa)
Tau(xy) --- MPa
(Std. Dev. --- MPa)

FWHM

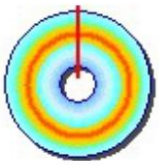

FWHM --- deg
(--- deg)
Alpha(Max) --- deg
Alpha(Min) --- deg

Residual stress graph

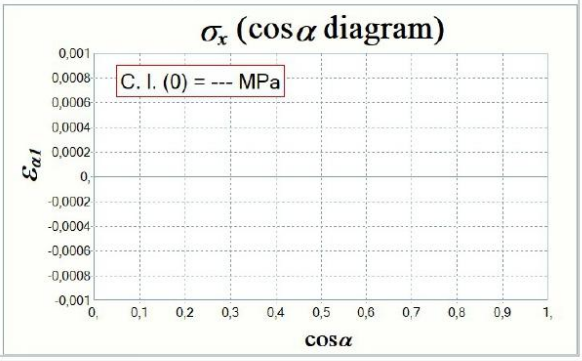

FWHM graph

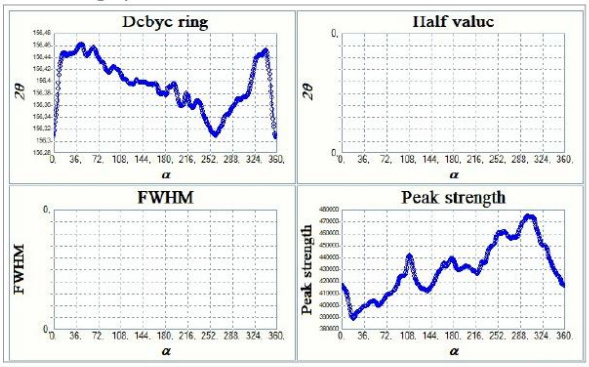

X-ray residual stress measurement system
μ-X360 Ver. 3. 2. 2. 0

Measurement information

Measurement time 2025/07/25 09:41 - 09:46

Comment 1 Raustenite
Comment 2
Folder RUBIK

Sample information

Item	Analyisis 1
Name	αFe(211)
Lattice constant(a)	2,8664 A
Lattice constant(b)	---
Lattice constant(c)	---
Wavelength	K-Alpha
Diffraction angle(2Theta)	156,396 deg
Diffraction lattice angle(2Eta)	23,604 deg
Interplanar spacing(d)	1,170
Diffraction plane(h,k,l)	2, 1, 1
Crystal structure	B.C.C
Young's modulus(E)	224,000 GPa
Poisson's ratio(v)	0,280
Sigma(x) stress constant(K)	---
Tau(xy) stress constant(K)	---
Sigma(y) stress constant(K)	-2091,661 GPa

Camera image

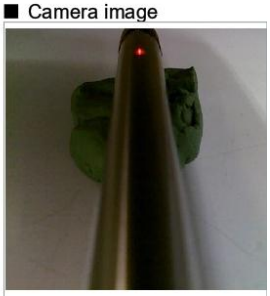

Retained austenite

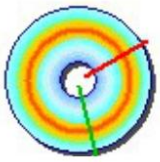

γ_{Ri} 2,0 %

(0,7 - 5,4 %)

Alpha(Max) 60,48 deg

Alpha(Min) 166,32 deg

Measurement condition

Measurement area	All (5,000 - 40,500 mm)
Pitch	50 um
X-ray irradiation time(Setup)	30 sec
X-ray irradiation time(Meas.)	30 sec
X-ray irradiation time(Max)	30 sec
X-ray tube current	1,00 mA
X-ray tube voltage	30,00 kV
Sample distance(Monitor)	27,000 mm
Sample distance(Analysis)	28,944 mm
X-ray incidence angle	0,0 deg
Offset of alpha angle	0 deg
X-ray wavelength (K-Alpha)	2,29093[A (Cr)
X-ray wavelength (K-Beta)	2,08480 A (Cr)
Total measurement count	43002
Oscillation count	207
X-ray tube total use time	343,32 h (1235969 sec)
Detection sensitivity	30,6 % (262880)
Peak strength (Ave)	428k
Level of ambient light	0,3 %
Temperature	23,38 deg C
K-Beta cut filter	Used
Valid range of alpha angle	0,00 <---> 90,00 deg
Peak analysis method	Fitting Lorentz
Correction coefficient (Stress)	0,000xx + 1,000x + 0,000
Correction coefficient (FWHM)	0,000xx + 1,000x + 0,000
ection coefficient (R.Gamma)	0,000xx + 1,435x + 0,206
Austenite calculation method	Integrated intensity ratio
R-value (Alpha)	---
R-value (Gamma)	---
Collimator size	Phi1,0

Retained austenite graph

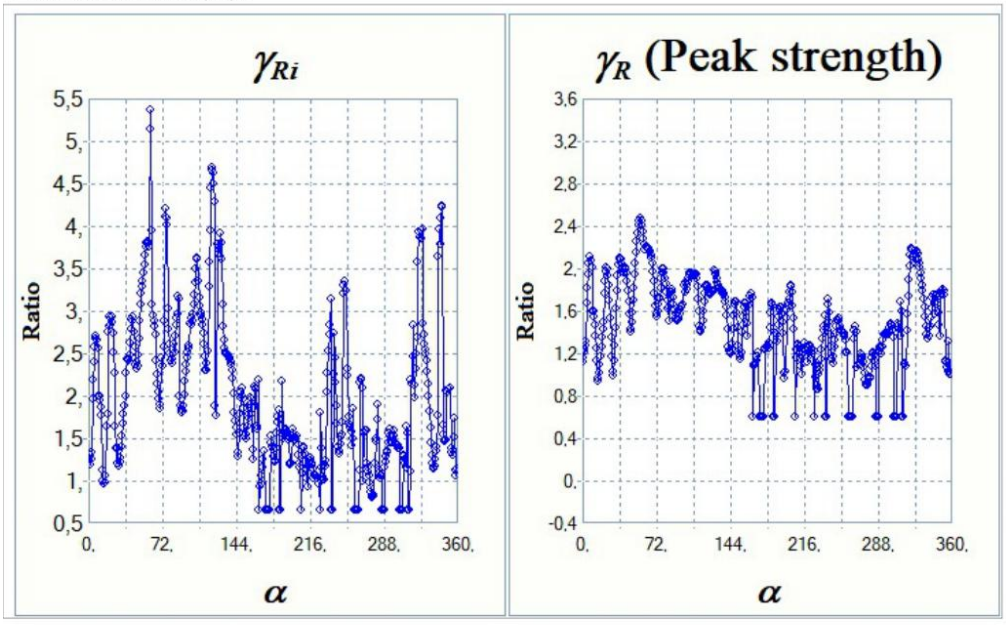

X-ray residual stress measurement system
μ-X360 Ver. 3. 2. 2. 0

Measurement information

Measurement time 2025/07/25 09:41 - 09:46

Comment 1 Raustenite
Comment 2
Folder RUBIK

Sample information

Item	Analyisis 1
Name	αFe(211)
Lattice constant(a)	2,8664 A
Lattice constant(b)	---
Lattice constant(c)	---
Wavelength	K-Alpha
Diffraction angle(2Theta)	156,396 deg
Diffraction lattice angle(2Eta)	23,604 deg
Interplanar spacing(d)	1,170
Diffraction plane(h,k,l)	2, 1, 1
Crystal structure	B.C.C
Young's modulus(E)	224,000 GPa
Poisson's ratio(v)	0,280
Sigma(x) stress constant(K)	---
Tau(xy) stress constant(K)	---
Sigma(y) stress constant(K)	-2091,661 GPa

Camera image

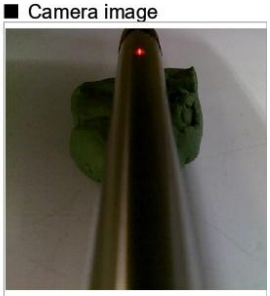

FWHM

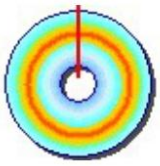

FWHM ---deg
(---deg)
Alpha(Max) ---deg
Alpha(Min) ---deg

Measurement condition

Measurement area	All (5,000 - 40,500 mm)
Pitch	50 um
X-ray irradiation time(Setup)	30 sec
X-ray irradiation time(Meas.)	30 sec
X-ray irradiation time(Max)	30 sec
X-ray tube current	1,00 mA
X-ray tube voltage	30,00 kV
Sample distance(Monitor)	27,000 mm
Sample distance(Analysis)	28,944 mm
X-ray incidence angle	0,0 deg
Offset of alpha angle	0 deg
X-ray wavelength (K-Alpha)	2,29093[A (Cr)
X-ray wavelength (K-Beta)	2,08480 A (Cr)
Total measurement count	43002
Oscillation count	207
X-ray tube total use time	343,32 h (1235969 sec)
Detection sensitivity	30,6 % (262880)
Peak strength (Ave)	428k
Level of ambient light	0,3 %
Temperature	23,38 deg C
K-Beta cut filter	Used
Valid range of alpha angle	0,00 <---> 90,00 deg
Peak analysis method	Fitting Lorentz
Correction coefficient (Stress)	0,000xx + 1,000x + 0,000
Correction coefficient (FWHM)	0,000xx + 1,000x + 0,000
ection coefficient (R.Gamma)	0,000xx + 1,435x + 0,206
Austenite calculation method	Integrated intensity ratio
R-value (Alpha)	---
R-value (Gamma)	---
Collimator size	Phi1,0

FWHM graph

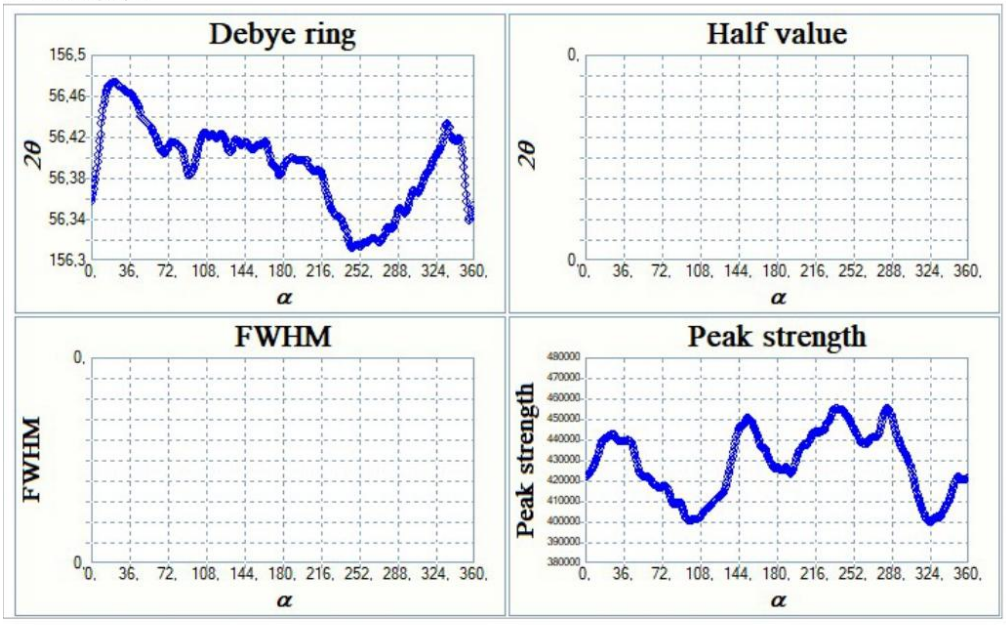

■ Measurement information

Measurement time 2025/07/25 09:41 - 09:46

Comment 1 Raustenite
Comment 2
Folder RUBIK

■ Sample information

Item	Analyisis 1
Name	αFe(211)
Lattice constant(a)	2,8664 A
Lattice constant(b)	---
Lattice constant(c)	---
Wavelength	K-Alpha
Diffraction angle(2Theta)	156,396 deg
Diffraction lattice angle(2Eta)	23,604 deg
Interplanar spacing(d)	1,170
Diffraction plane(h,k,l)	2, 1, 1
Crystal structure	B.C.C
Young's modulus(E)	224,000 GPa
Poisson's ratio(v)	0,280
Sigma(x) stress constant(K)	---
Tau(xy) stress constant(K)	---
Sigma(y) stress constant(K)	-2091,661 GPa

■ Camera image

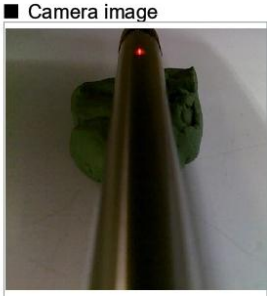

■ Residual stress

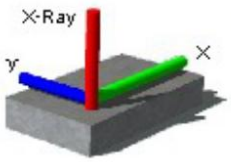

Sigma(x) --- MPa
(Std. Dev. --- MPa)
(Slope ---)

Tau(xy) --- MPa
(Std. Dev. --- MPa)
(Slope ---)

■ Measurement condition

Measurement area	All (5,000 - 40,500 mm)
Pitch	50 um
X-ray irradiation time(Setup)	30 sec
X-ray irradiation time(Meas.)	30 sec
X-ray irradiation time(Max)	30 sec
X-ray tube current	1,00 mA
X-ray tube voltage	30,00 kV
Sample distance(Monitor)	27,000 mm
Sample distance(Analysis)	28,944 mm
X-ray incidence angle	0,0 deg
Offset of alpha angle	0 deg
X-ray wavelength (K-Alpha)	2,29093[A (Cr)
X-ray wavelength (K-Beta)	2,08480 A (Cr)
Total measurement count	43002
Oscillation count	207
X-ray tube total use time	343,32 h (1235969 sec)
Detection sensitivity	30,6 % (262880)
Peak strength (Ave)	428k
Level of ambient light	0,3 %
Temperature	23,38 deg C
K-Beta cut filter	Used
Valid range of alpha angle	0,00 <---> 90,00 deg
Peak analysis method	Fitting Lorentz
Correction coefficient (Stress)	0,000xx + 1,000x + 0,000
Correction coefficient (FWHM)	0,000xx + 1,000x + 0,000
ection coefficient (R.Gamma)	0,000xx + 1,435x + 0,206
Austenite calculation method	Integrated intensity ratio
R-value (Alpha)	---
R-value (Gamma)	---
Collimator size	Phi1,0

■ Residual stress graph

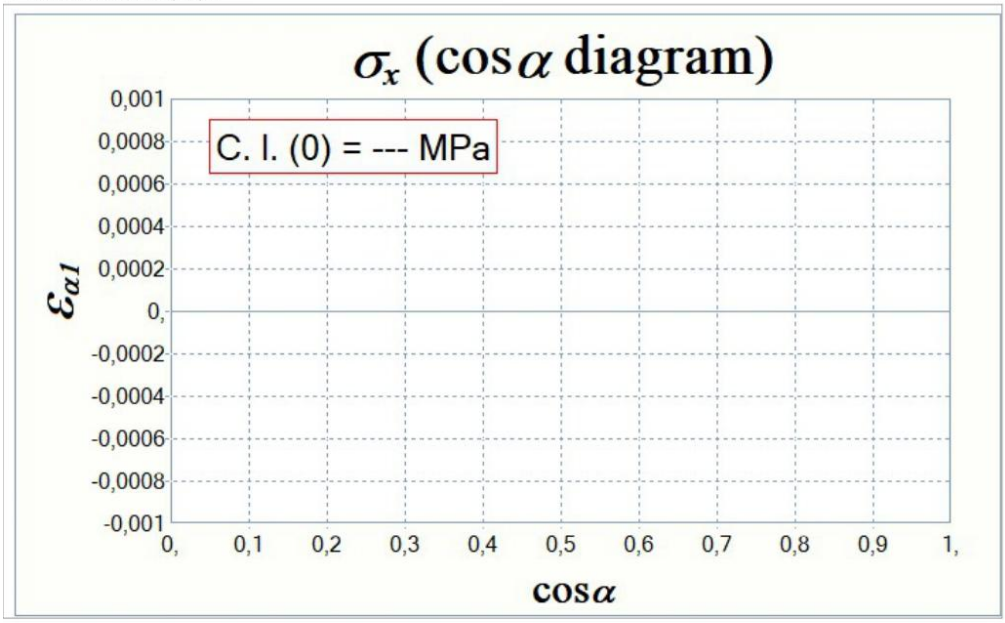

X-ray residual stress measurement system
μ-X360 Ver. 3. 2. 2. 0

Measurement information

Measurement time	2025/07/25 09:41 - 09:46
Comment 1	Raustenite
Comment 2	
Folder	RUBIK

Sample information

Item	Analyisis 1
Name	αFe(211)
Lattice constant(a)	2,8664 A
Lattice constant(b)	---
Lattice constant(c)	---
Wavelength	K-Alpha
Diffraction angle(2Theta)	156,396 deg
Diffraction lattice angle(2Eta)	23,604 deg
Interplanar spacing(d)	1,170
Diffraction plane(h,k,l)	2, 1, 1
Crystal structure	B.C.C
Young's modulus(E)	224,000 GPa
Poisson's ratio(v)	0,280
Sigma(x) stress constant(K)	---
Tau(xy) stress constant(K)	---
Sigma(y) stress constant(K)	-2091,661 GPa

Camera image

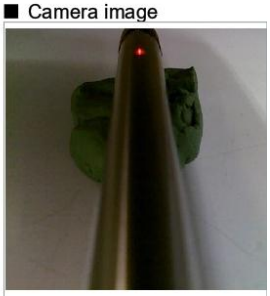

Map

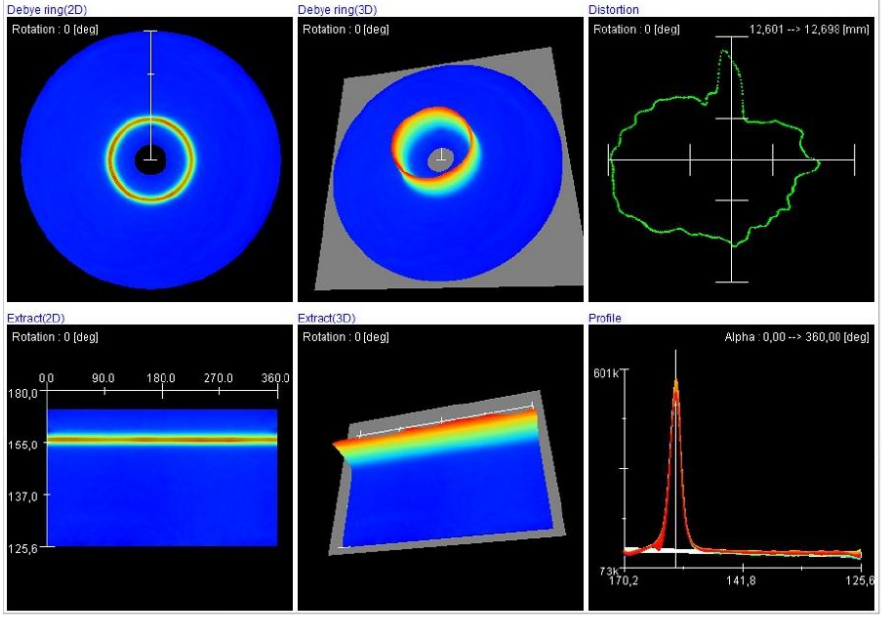

Measurement condition

Measurement area	All (5,000 - 40,500 mm)
Pitch	50 um
X-ray irradiation time(Setup)	30 sec
X-ray irradiation time(Meas.)	30 sec
X-ray irradiation time(Max)	30 sec
X-ray tube current	1,00 mA
X-ray tube voltage	30,00 kV
Sample distance(Monitor)	27,000 mm
Sample distance(Analysis)	28,944 mm
X-ray incidence angle	0,0 deg
Offset of alpha angle	0 deg
X-ray wavelength (K-Alpha)	2,29093[A (Cr)
X-ray wavelength (K-Beta)	2,08480 A (Cr)
Total measurement count	43002
Oscillation count	207
X-ray tube total use time	343,32 h (1235969 se
Detection sensitivity	30,6 % (262880)
Peak strength (Ave)	428k
Level of ambient light	0,3 %
Temperature	23,38 deg C
K-Beta cut filter	Used
Valid range of alpha angle	0,00 <---> 90,00 deg
Peak analysis method	Fitting Lorentz
Correction coefficient (Stress)	0,000xx + 1,000x + 0,
Correction coefficient (FWHM)	0,000xx + 1,000x + 0,
ection coefficient (R.Gamma)	0,000xx + 1,435x + 0,
Austenite calculation method	Integrated intensity ra
R-value (Alpha)	---
R-value (Gamma)	---
Collimator size	Phi1,0

Residual stress

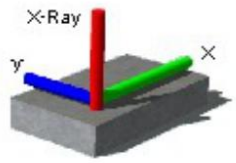

Sigma(x) --- MPa
(Std. Dev. --- MPa)
Tau(xy) --- MPa
(Std. Dev. --- MPa)

FWHM

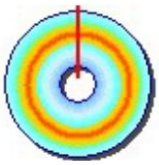

FWHM --- deg
(--- deg)
Alpha(Max) --- deg
Alpha(Min) --- deg

Residual stress graph

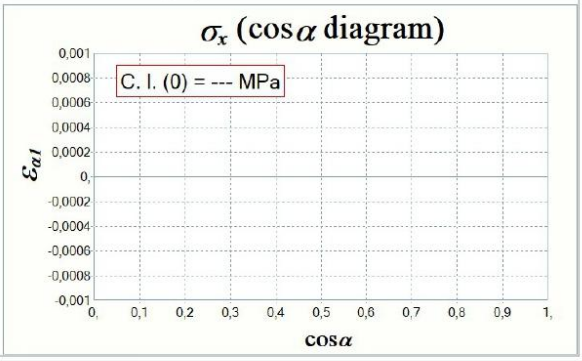

FWHM graph

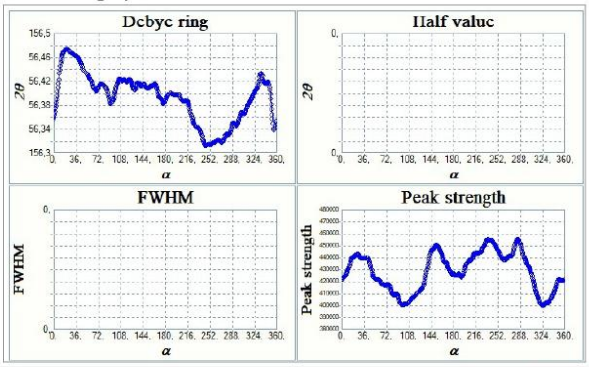

X-ray residual stress measurement system
μ-X360 Ver. 3. 2. 2. 0

Measurement information

Measurement time 2025/07/25 09:48 - 09:50

Comment 1 Raustenite3
Comment 2
Folder RUBIK

Sample information

Item	Analyisis 1
Name	αFe(211)
Lattice constant(a)	2,8664 A
Lattice constant(b)	---
Lattice constant(c)	---
Wavelength	K-Alpha
Diffraction angle(2Theta)	156,396 deg
Diffraction lattice angle(2Eta)	23,604 deg
Interplanar spacing(d)	1,170
Diffraction plane(h,k,l)	2, 1, 1
Crystal structure	B.C.C
Young's modulus(E)	224,000 GPa
Poisson's ratio(v)	0,280
Sigma(x) stress constant(K)	---
Tau(xy) stress constant(K)	---
Sigma(y) stress constant(K)	-2091,661 GPa

Camera image

Retained austenite

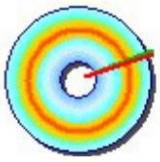

γ_{Ri} 1,7 %

(0,6 - 4,7 %)

Alpha(Max) 70,56 deg

Alpha(Min) 68,40 deg

Measurement condition

Measurement area	All (5,000 - 40,500 mm)
Pitch	50 um
X-ray irradiation time(Setup)	30 sec
X-ray irradiation time(Meas.)	30 sec
X-ray irradiation time(Max)	30 sec
X-ray tube current	1,00 mA
X-ray tube voltage	30,00 kV
Sample distance(Monitor)	27,000 mm
Sample distance(Analysis)	28,461 mm
X-ray incidence angle	0,0 deg
Offset of alpha angle	0 deg
X-ray wavelength (K-Alpha)	2,29093[A (Cr)
X-ray wavelength (K-Beta)	2,08480 A (Cr)
Total measurement count	43004
Oscillation count	207
X-ray tube total use time	343,34 h (1236031 sec)
Detection sensitivity	31,2 % (268286)
Peak strength (Ave)	429k
Level of ambient light	0,3 %
Temperature	26,25 deg C
K-Beta cut filter	Used
Valid range of alpha angle	0,00 <---> 90,00 deg
Peak analysis method	Fitting Lorentz
Correction coefficient (Stress)	0,000xx + 1,000x + 0,000
Correction coefficient (FWHM)	0,000xx + 1,000x + 0,000
ection coefficient (R.Gamma)	0,000xx + 1,435x + 0,206
Austenite calculation method	Integrated intensity ratio
R-value (Alpha)	---
R-value (Gamma)	---
Collimator size	Phi1,0

Retained austenite graph

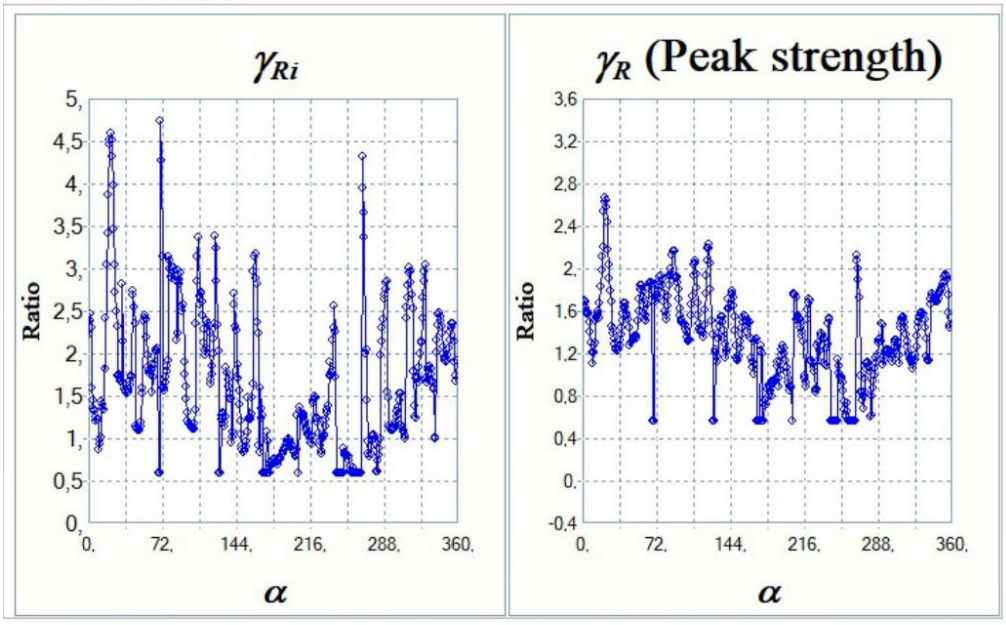

FOLHA DE REGISTRO DO DOCUMENTO

1. CLASSIFICAÇÃO/TIPO	2. DATA	3. REGISTRO N°	4. N° DE PÁGINAS
DM	04 de agosto de 2025	DCTA/ITA/DM-045/2025	175

5. TÍTULO E SUBTÍTULO:

Shot peening-based strategy for densification and residual stress enhancement in binder jetting

6. AUTOR(ES):

Matheus Rubik

7. INSTITUIÇÃO(ÕES)/ÓRGÃO(S) INTERNO(S)/DIVISÃO(ÕES):

Instituto Tecnológico de Aeronáutica - ITA

8. PALAVRAS-CHAVE SUGERIDAS PELO AUTOR:

1. Gears 2. Shot Peening 3.Binder Jetting 4. Manufacturing 6. Mechanical Engineering

9.PALAVRAS-CHAVE RESULTANTES DE INDEXAÇÃO:

Engragens; Processamento de materias a laser; Manufatura; Tensão residual; Resistência à fadiga; Engenharia mecânica.

10. APRESENTAÇÃO: **(X) Nacional** **( ) Internacional**

ITA, São José dos Campos. Curso de Mestrado. Programa de Pós-Graduação em Engenharia Aeronáutica e Mecânica. Área de Materiais, Manufatura e Automação. Orientador: Ronnie Rodrigo Rego. Defesa em 10/07/2025. Publicada em 2025

11. RESUMO:

Additive manufacturing by binder jetting has emerged as a promising technology to produce complex metal components, with the potential to reduce costs, material waste, and promote scalability. However, challenges related to high porosity limit its application in systems subject to contact fatigue, such as gears. In this context, the objective of this study was to investigate the sequential application of shot peening as a post-processing strategy to optimize surface integrity and improve the fatigue performance of components manufactured by binder jetting. The investigation focused on the detailed characterization of the surface integrity resulting from shot peening applied in two stages: the first dedicated to surface densification and the second to the induction of compressive residual stresses. Parameters such as hardness, porosity, roughness, and residual stress state were evaluated. The first shot peening stage promoted 99% surface density up to a depth of 350 µm, accompanied by a 37% increase in surface hardness and a notable improvement in roughness parameters, establishing a favorable condition for subsequent treatments. The second stage induced compressive residual stresses exceeding –900 MPa at depths of approximately 100 µm, aligned with profiles typically associated with improved fatigue resistance. Rolling contact fatigue tests showed that both treatments significantly extended fatigue life. The combination of densification and stress induction led to an increase of up to 54% in fatigue life compared to the as-built condition. The most significant gains were associated with the suppression of critical surface pores and the stabilization of compressive stress fields. These results indicate that combining densification and residual stress modification strategies is essential to mitigate the intrinsic limitations of binder jetting, promoting improvements in fatigue resistance without compromising part geometry. This study contributes to the advancement of integrated manufacturing routes, combining additive processes and mechanical treatments, with potential application in the production of gears and other critical components, including emerging applications in electromobility, as in sectors such as automotive, as well as in aerospace applications. As a continuation, the validation of these strategies in real geometries under representative operating conditions is proposed.

12. GRAU DE SIGILO:

(X) OSTENSIVO **( ) RESERVADO** **( ) SECRETO**